Investigations of the Analysis and Modelling of Magnetotelluric Data

by
Jandyr de Menezes Travassos

Thesis presented for the degree of
Doctor of Philosophy of the
University of Edinburgh
1987

Para
meu pai
Wandinha e
Renatinha

Abstract

Several distinct investigations of analysis, modeling and interpretation of magnetotelluric (MT and AMT) data are carried out using one synthetic data and two data sets collected in two distinct tectonically active regions. Both single site (SS) and remote reference (RR) techniques are employed to estimate the impedance tensor $\underline{\underline{Z}}$, with frequencies covering the range 1kHz-1mHz. Two biased SS estimates of $\underline{\underline{Z}}$ are used to compare the performance of 5 coherence-based acceptance criteria. It is demonstrated that the RR predicted coherence between local fields can be used for selecting data windows, and provides a necessary assessment on the reliability of a given RR estimate. It is demonstrated that the RR variance depends strongly on the local signal-to-noise ratios (monitored by the predicted coherence) and depends weakly on the number of data windows as long as coherences are above a moderate threshold. Although an estimate of $\underline{\underline{Z}}$ obtained using a remote electric field is grossly inaccurate, its associated predicted coherence is as efficient in selecting low noise level data windows as its counterpart, obtained using a remote magnetic field. The relation between SS and RR predicted coherences, the latter estimated using both electric and magnetic fields is investigated. A hybrid technique that uses a remote electric field is suggested. The topographic effect of slope having angles between 0° and 90° is investigated using 2D models for both E- and H-polarization cases (EPOL and HPOL). The validity of models obtained using topographically distorted data is investigated using a 1D inversion. Results obtained are also compared against an analytical approximation. Investigation on a data set from a 12 site traverse suggests the occurrence of near-surface inhomogeneities and topographical effects in several sites. The presence of near-surface inhomogeneities is discussed using previuosly published 3D results, while a 2D slope model is used in discussing the topography. It is suggested that changes in the azimuths of rotation may be used to derive an "azimuth depth" which may be associated to a structural change in the subsurface. The EP responses are assessed accordingly to a strictly 2D situation. Data interpretation is done using models obtained through 1D inversions of EPOL and HPOL responses.

Acknowledgements

I gratefully acknowledge the stimulating scientific discussions I had with Dr. D. Beamish, my supervisor, during the years I have spent in the Geomagnetism Research Group (GRG) at British Geological Survey (BGS), Edinburgh. I am also indebted to him by his decisive and invaluable assistance, which I regard as of paramount importance, when I joined his induction group. I also wish to thank him for all the suggestions given during the preparation of this dissertation; a great deal of its readability is a direct consequence of his comments. I also acknowledge the guidance given by Dr. V.R.S. Hutton (co-supervisor) during the first year I was working with her induction group, at the Geophysics Department (GD) of the University of Edinburgh. I wish to thank members of both the GRG and GSU at BGS and the GD, staff and research students, for the friendly and stimulating atmosphere during my stay in Edinburgh. I acknowledge the friendly guidance given by G. Dawes during my work in the GD. I acknowledge the diligent efforts of T. Harinarayama in calculating the results I needed for inclusion in chapter V. I acknowledge the patient and kind efforts of W. L. Campelo on typing the entire manuscript and on helping in the edition of this dissertation. I gratefully acknowledge the fruitful discussions and encouragement given by Dr. A.C.B. Pires during my career as geophysicist and his influence in my decision of undertaking this PhD. This work was entirely supported by a grant from CNPq-Conselho Nacional de Desenvolvimento Cientifico e Tecnologico, Brasil.

Contents

CHAPTER I
Introduction

I.1. Scope of the Work

The magnetotelluric (MT) method, is employed to obtain estimates of the so called earth response functions. These estimates are functions of frequency and of the earth's electrical structure and are usually presented as sounding curves. The end product of the MT method is the interpretation of the sounding curves in terms of a given geoelectric model which describes, to some extent, the earth's internal electric structure. The work considered in this thesis covers several distinct investigations of both the analysis and theoretical modeling of magnetotelluric data. No fieldwork was performed so that the instrumentation for magnetotelluric work is treated only briefly. Data sets collected in two distinct tectonically active regions are used in the investigations described below in chapters III and VI.

The first data set was collected in Turkey. The full experiment, to which only brief reference is given here, obtained simultaneous magnetotelluric recordings during a period of 6 months. The magnetotelluric instruments operated alongside three-component seismometers. The full experiment is referred to as the Turkish Dilatancy Project 3 (TDP3). The experimental data are primarily intended for investigations of crustal parameters in relation to recurrent local earthquake swarms. The full aspects of the data set are not considered here and only a data subset collected at two sites is considered. Since time-dependent magnetotelluric quantities were required to investigate possible time-dependent crustal processes, the methods of determining accurate magnetotelluric response estimates from experimental data constitute a major concern. This first set of data is strictly magnetotelluric in its period range; the field components being sampled at 5s intervals. To perform an investigation into the methods of determining MT response estimates, data collected continuously at two sites over a 7 day period were chosen as a "test" data set. A time length of 7 days can be considered a "typical" time-scale for much long-period MT work. Furthermore the 7 days provide a large number of degrees of freedom for the analysis at short periods. The period range investigated in this study covers the period range 10-10000s but the statistics for the range 1000-10000s are very limited even using 7 days of data so the results of the investigation presented here are confined to periods less than 1000s. The investigations carried out using this test data set are

described in Chapter III.

The second data set was collected as an experiment in 1982 involving the Universities of Alberta and Edinburgh, in the region of the Rocky Mountains Trench in western Canada near 53°N. The complete study is composed of 25 sites distributed along three profiles, one following the Trench and two perpendicular to it. In contrast to the first data set, the Canadian data covers a period range from 0.001s (1000Hz) to 100s and can therefore be described as a combination of audiomagnetotelluric (frequency <1s) and magnetotelluric (frequency >1s) data. Techniques for processing both frequency ranges are identical but it is worth noting that the inducing (source) fields are very different for the two cases. The work performed on this data set did not consist of analytic investigations. A standard package of programs used in the Department of Geophysics at the University of Edinburgh was used to routinely estimate MT sounding parameters along a selected 12-site profile perpendicular to the Trench. Site separations along this profile are nearly all less than 5 kilometres. A cluster of sites had site separations of 1km or less. The relatively broad-band nature of the sounding curves obtained along the profile should, in theory at least, allow a detailed assessment of the geoelectric structure through the whole crust beneath the profile. The sounding curves obtained have been used, in conjunction with other data of the experiment, to provide a more complete appraisal of the geoelectric structure of the region (Hutton et al., 1987). The work reported in this dissertation therefore does not attempt a complete investigation of the region using the spatially limited data from the 12-site profile. These data and their interpretation are considered in Chapter VI.

In order to fully understand the magnetotelluric method the fundamental relationships obeyed by electromagnetic fields must be considered. The theory behind the method is reviewed in Chapter II. Beginning with Maxwell's equations for the complete vector fields, a fundamental assumption concerning the neglect of displacement currents at the frequencies used in magnetotelluric sounding is established. By restricting the dimensionality of the Earth's geoelectric structure, Maxwell's equations can be simplified. The first obvious step is to assume that the conductivity distribution, within the Earth, varies only in depth, the 1D case. The relationships between the field components for this case are considered in Chapter II. This simple case, still much used for interpretation, allows the basis of the magnetotelluric method to be described in a relatively straightforward way. Chapter II is

completed by a discussion of the field relationships that are obeyed when the conductivity distribution is two dimensional. Three dimensional models of electromagnetic induction are not discussed apart from certain particular cases which arise in the interpretation of sounding curves.

As already mentioned, chapter III describes a detailed investigation of the methods of obtaining accurate MT response using a test data set. These estimates are computed by stacking spectral powers estimated via FFT. Both single site and remote reference techniques are used in investigation. Although the objective of that chapter is to investigate methods of data analysis, a simple approximate one-dimensional interpretation is also given at the end.

Having considered methods of processing MT data and the production of MT sounding curves from experimental data, it is necessary to provide some background to understand how such curves may be interpreted. Chapter IV considers both modeling and data inversion where "data" is regarded as MT sounding curves obtained at a particular location(s). Forward modeling numerical procedures exist for a fairly broad class of geoelectric structures ranging from the 1D case to various 3D formulations. Because of the large complexities introduced by the 3D case, only a few large data sets can "benefit" from forward 3D modeling studies applied directly to model the observations. Therefore only 1D and 2D cases are considered in Chapter IV.

At the present time a great deal of work has been applied to the problem of inverting MT data in the 1D case (e.g., Parker, 1983). This cannot be said of 2D and 3D cases. The 1D case, despite the limitations imposed by actual data which may not display 1D characteristics, appears to be a frequently employed interpretation procedure. Chapter IV considers the background to three 1D methods for inverting MT data which have been used in this work. The first method is one of a number of approximate heuristic schemes and is referred to as the Schmucker transformation. This method is applied to the data in Chapter III. The second method considered involves a parametrization of the earth in terms of a finite series of discrete layers. The method used forms a solution based on local linearization and is referred to as linearized inversion. This method is used on data obtained from the 2D forward modeling study in Chapter V and on the data of Chapter VI. Discrete layers are again a feature of the third method considered in Chapter IV. The Monte Carlo method attempts to avoid the linearization inherent in the second method. In this method a very large number

of 1D profiles is generated at random; each one is tested to check if it satisfies the observations and, if it does, the model is saved. The main advantage of the Monte Carlo process is that no approximation is needed in deriving a "population" of solutions, the main disadvantage is the extreme difficulty in generating an adequately large set of solutions (Parker, 1983). An example of such a difficulty is given in Chapter IV. The Monte Carlo procedure was also used extensively to examine the solutions to the Canadian data considered in Chapter VI. Chapter IV also contains a summary description of the two-dimensional forward modeling scheme used in this thesis. The computational scheme is based on a published and available coding of a finite-difference program described in the literature (Brewitt-Taylor and Weaver, 1976). The numerical performance of the installed version is compared with that due to a published analytical solution.

Chapter V deals with a particular case of 2D modeling, namely an evaluation of the topographic effect on MT data. It has been suggested that as MT data techniques, as described in Chapter III, improve and provide increasingly accurate response curves, the effect of a known topography should be estimated and removed when the data is modelled. The simplest way to remove topographic effects is to model the topography incorporating surface elevations, or depressions, into the forward model. The 2D finite difference scheme was modified to allow for such behaviour. Such a scheme allows the model results and observations to be compared along a profile. This is not always the case and topography may, as in fact it nearly always does, vary on a more rapid lateral scale than profile observations. In order to understand the effect of topography on MT data it is useful to consider the degree and characteristics of the effect of a simple slope on a uniform earth. It is then used to define the spatial and frequency characteristics introduced in the simplest case of a topographical distortion. The introduction of additional features such as other slopes (e.g., a graben) or a superimposed geoelectric structure would greatly complicate the problem due to electromagnetic coupling effects which would necessarily be a function of frequency. The single slope, or half-graben, is probably the simplest class of general near-surface, or "at-surface", distortions that may affect MT data (Menvielle and Szarka, 1986). Several models are considered by varying the inclination angle of the slopes.

The period range considered for the slope models goes from 0.005s (200Hz) to 100s (0.01Hz), i.e. both audio and magnetotelluric observations are considered. The elevation

separation of the slope is fixed at a "throw" of 1000m and slope angles range from 0 to 90 degrees. Both the spatial and frequency distortions due to the slope are considered in detail. At a particular location the distorting effect of the slope may be to introduce a false gradient into an otherwise 1D sounding curve. The topographic distortion introduced is investigated by applying a 1D inverse procedure to the results obtained. The way in which false layers may be introduced to the geoelectric section by topographic distortions is illustrated. An analytic solution to the simple topographic problem considered in Chapter V is available for the purely DC case. The DC case may be approximated by the quasi-static mode in magnetotellurics at sufficiently low frequencies. Results obtained for the DC solutions are compared with the equivalent results obtained from the numerical 2D solutions to conclude Chapter V.

Chapter VI describes the work done on a profile of 12 sites which is perpendicular to the Rocky Mountains Trench near Tête Jaune Cache. This profile is part of a more extensive survey composed of three profiles with a total of 25 sites. The data bandwidth covers a range from 1000Hz to 100s. Although Chapter VI comes at the end of the dissertation, most of the work described there was done before the other chapters. Only the section on data interpretation of that chapter was partly done after the other material presented below. In chapter VI both data acquisition and data analysis are described briefly. Results for all sites are shown rotated to the geological strike, represented by the Rocky Mountains Trench. Only the skew is used as a dimensionality indicator. The influence of topography is evaluated using a two-dimensional model. The relevance of the topography as modelled with respect to the Canadian data is discussed. The relative continuity of the E-polarization case along the traverse in contrast to the "discontinuous" behaviour expected for the H-polarization case is also discussed. Distortions caused by superficial inhomogeneities are discussed and exemplified using the results. The effect of these superficial 3D features is analysed in conjunction with one-dimensional inversions.

I.2. Phenomenological Basis of the Magnetotelluric Method

The magnetotelluric sounding method, MTS or simply MT, probes deep inside the earth using the time variations of the natural electromagnetic field as a source. As this primary field diffuses through the earth, electric (telluric) currents are induced by an emf following Faraday's law

$$emf = - \frac{d\Phi}{dt} \qquad (I.1)$$

where Φ is the magnetic flux through a surface $\underline{S}$ which encloses a conductive volume V. By definition this flux is given by

$$\Phi = \int_S \underline{B}_o \cdot d\underline{S} \qquad (I.2)$$

where $\underline{B}$ is the magnetic induction vector. The current flowing across the area $\underline{S}$ is described by the current density vector $\underline{j}$. Those currents in turn induce a secondary magnetic field which, at a point, described by the radius vector $\underline{r}$, is given by the Biot-Savart law

$$\underline{B} = \frac{\mu}{4\pi} \int_V \frac{\underline{j} \times \underline{r}}{r^3} dV \qquad (I.3)$$

where $\underline{r}$ is measured from the element of integration V and μ gives the permeability of the medium within the volume V.

An observer on the surface of the earth measures the variations of the magnetic field and also of the telluric field. The alternating currents tend to concentrate near the surface, a phenomenon known as the skin effect. Although the fields are source dependent, the ratio of the electric to the magnetic field is a characteristic measure of the conductivity of the medium, the earth,

$$Z = \mu \frac{E_x}{B_y} = -\mu \frac{E_y}{B_x} \qquad (I.4)$$

where Ex, Ey are the electric field horizontal components and Bx and By are the magnetic field horizontal components. Relation (I.4) is valid for a horizontally layered earth. The impedance Z is measured at various periods and, by using the skin effect, one is able to infer the conductivity distribution with depth below the observation point (Tikhonov, 1950; Cagniard, 1953).

I.3. Electrical Properties of Earth Materials

While the physical basis of the magnetotelluric method is rooted in the Faraday and Biot-Savart laws of induction, its geophysical basis is found in the electrical properties of rocks. The physical parameter of interest is the rock resistivity or conversely its electrical conductivity. The geophysical importance of the resistivity lies on its relation to a series of other

physical, compositional and structural parameters. These constitute a wealth of factors, most of them being more or less dependent on others such as temperature, partial pressure or oxygen fugacity, transition metal content, porosity and crack content, fluid content, amount of melt and other factors (Keller and Frischknechkt, 1970; Shankland, 1975).

The electrical conductivity of rocks is determined both in the field by the magnetotelluric method or other resistivity methods and in the laboratory. Usually field conductivities are found to be much higher than the the ones obtained with dry laboratory specimens. In both cases fluid content and temperature are singled out as the two most important parameters affecting rock conductivity, at least for the lower crust and upper mantle (Shankland and Ander, 1983). Nevertheless this fact does not simplify the interpretation of a given set of conductivity data since it depends on several factors which can in turn influence similar changes. At shallower depths and consequently lower temperatures, i.e. in the upper crust, the electrical properties of rocks are strongly dependent on the aqueous solution that fills pores and cracks inside the rocks (Keller and Frischknechkt, 1970). Water-bearing rock conductivity will depend on the amount of water, salinity, and pore structure, i.e. on the way water is distributed within the rock. At lower crust and upper mantle depths where higher temperatures prevail, stronger temperature effects are observed. Nevertheless other factors must be taken into consideration when interpreting conductivity anomalies. Usually bulk rock conductivities are explained in terms of an insulating silicate matrix with a conductive material permeating it. Again aqueous solutions are regarded as the principal source of crustal conductivity (Gough, 1986c). Crustal conductivities are explained also in terms of partial melting, hydrated minerals including clays and serpentine, graphite and sulphur (Shankland and Ander, 1983).

The electrical conductivity of crust and upper mantle inferred from field measurements can be divided into at least three regions: 1)a surface layer (SCL) of high conductivity associated with sediments and ground-water; 2) a lower conductivity layer (LCL) associated with the basement and 3) a lower crustal high conductivity layer (HCL) (Shankland and Ander, 1983). It is possible that the mechanism behind this conductivity differentiation is inextricably linked to the presence or absence of aqueous solutions. It is known that the presence of even a small weight percentage of water can increase electrical conductivity several orders of magnitude for a certain temperature level (Olhoeft, 1981).

Assigning the same conductivity mechanism, i.e. water, to all three layers suggests that the key factor probably resides in structural factors such as quantity of fluids and ionic content or whether fluids are more or less confined in voids or permeate the whole rock matrix as free water (Olhoeft, 1981; Shankland and Ander, 1983; Gough, 1986c). Resistivity values for the HCL are less than 50 Ω.m at 12-40km depths with an inferred temperature of 500°-850°C, while the LCL resistivities are greater than 100 Ω.m at 3-25km with temperatures ranging 200°-700°C in tectonically active regions (Shankland and Ander, 1983).

Although water is present in both the upper and lower crust it is suggested that higher upper crustal resistivities are explained in terms of isolated fractures. Due to stress field characteristics at LCL depths, fluids tend to be isolated in cavities, giving bulk resistivities only slightly below that of dry rock (Gough, 1986c). The high bulk conductivity at lower crustal depths is again explained most frequently by the presence of free water, but in this case the water is not isolated inside voids but probably permeates the whole rock matrix (Gough, 1986c). Partial melting is another possible explanation for the existence of a HCL in tectonically active regions although, within the accuracy of field data, it is possible to accept the hypothesis of water as a conductivity mechanism for both the LCL and HCL (Shankland and Ander, 1983). In active crustal environments the mechanisms to explain the build up and retention of the necessary volume of fluid has been suggested in terms of deep thrust fault zones (Etheridge et al., 1983; Kerrich et al., 1984) or in terms of the subduction of the oceanic crust (Fyfe, 1986).

CHAPTER II
Theory

II.1. The External Inducing Fields

The magnetotelluric method uses the variations of the electromagnetic field to probe the Earth's geoelectric structure. Under given assumptions, the interpretation of the relationships between field components can yield an image of the electrical conductivity distribution with depth. The spatial resolution of the geoelectric structure is limited by the diffusion of electromagnetic waves through the earth, while depth penetration is limited by an exponential absorption of energy. Due to the period range used in this work, depth penetration should fall well short of 500km.

Geomagnetic variations in the frequency range which are considered here are of both external and internal origin. The primary part is of external origin and is caused by transient electric current systems in the ionosphere and magnetosphere. The secondary part, of internal origin, comes from induced eddy currents within the earth. Assuming that the conductivity changes only with depth the induced currents would flow in sheets through the various layers, producing a secondary field which resembles the primary source field.

In this work frequencies ranging from 10^{3} Hz to 10^{-3} Hz are considered. Within this range variations in the electromagnetic field have a variety of causes. Above 1Hz the main contributions are from meteorological activity (sferics) and of man-made origin. The man-made fraction comes from power distribution networks and radio transmitters. They are narrow band contributions which usually dominate the natural spectrum at their frequencies. The natural fraction originates mainly from lightning discharges associated with thunderstorms. Its energy propagates between the earth's surface and the ionosphere which acts as a wave-guide. Distant thunderstorms provide a nearly uniform source. Descriptions of both man-made (e.g., Adam et al., 1986) and natural (e.g., Keller and Frischknechkt, 1970, pp.200-203) can be found in the literature.

Below 1Hz the natural electromagnetic field originates from interations between the Earth's magnetic field and solar plasma. Of considerable importance at those frequencies are the geomagnetic pulsations which appear as small, quasi-sinusoidal fluctuations or as trains of damped sine waves. Descriptions of magnetospheric disturbances can be found elsewhere (Parkinson, 1983). Geomagnetic

pulsations are classified according to continuity and period. Some have a steady or regular fluctuating amplitude, called Pc's, others show damped characteristics with between 5 and 20 cycles, the Pi's. The Pi's pulsations are generated in the development process of a substorm. For instance Pi2 pulsations are associated with the explosive phase of a substorm. The pulsations which fall inside the frequency range considered here are: Pc1 (0.2-5s); Pi1 (1-40s); Pc2 (5-10s) ; Pi2 (40-150s); Pc3 (10-45s); Pi3 ($\geq$150s); Pc4 (5-150s) and Pc5 (150-600s).

II.2. Fundamental Relations Obeyed by Electromagnetic Fields

The electromagnetic field elements obey Maxwell equations

$$\begin{aligned} \text{curl } \underline{H} &= \frac{\partial \underline{D}}{\partial t} + \underline{j} \\ \text{curl } \underline{E} &= -\frac{\partial \underline{B}}{\partial t} \\ \text{div } \underline{B} &= 0 \\ \text{div } \underline{D} &= q \end{aligned} \qquad \text{(II.1)}$$

which are complemented by the constitutive relations

$$\begin{aligned} \underline{D} &= \varepsilon \underline{E} \\ \underline{B} &= \mu \underline{H} \\ \underline{j} &= \sigma \underline{E} \end{aligned} \qquad \text{(II.2)}$$

with the medium parameters ε , μ and σ independent of time and of the field vectors. In this work SI units are used throughout. The quantities in equations (II.1) and (II.2) are expressed in units of:

magnetic field strength	$[\ H\ ]=A.m^{-1}$
magnetic induction	$[\ B\ ]=T$
electric induction	$[\ D\ ]=C.m^{-2}$
electric field strength	$[\ E\ ]=V.m^{-1}$
current density	$[\ j\ ]=A.m^{-2}$
conductivity	$[\ \sigma\ ]=S.m^{-1}$
charge density	$[\ q\ ]=C.m^{-3}$
permitivity (free space)	$\varepsilon_o = 1/(36\pi \times 10^{9})\ F.m^{-1}$
permeability (free space)	$\mu_o = 4\pi \times 10^{-7}\ H.m^{-1}$

The constitutive parameters, σ , ε and μ are expressed as tensors in anisotropic media and may vary with time; they can depend on the frequency and intensity of an applied field. In this work it is

assumed that all media may be considered as isotropic and that any dependency of the constitutive parameters with respect to time or to the applied field may be neglected. It is also assumed that $\mu=\mu_o$ for earth materials. Description of electromagnetic units and their conversions can be easily found in the literature (e.g., Payne, 1981).

The first term on the right hand side of the first of Maxwell equations

$$\underline{j}^d = \frac{\partial \underline{D}}{\partial t}$$

gives the displacement current. Assuming harmonic fields with a time dependence exp(-iwt), the ratio between displacement and conduction currents can be written as

$$\xi = \frac{j^d}{j} = \frac{\omega \epsilon}{\sigma} \cong \frac{\rho}{T} \times 10^{-10}$$

where $\rho = \sigma^{-1}$ is the resistivity, $w=2\pi/T$ is the angular frequency and T, the period in seconds. In this work the shortest period used is $>10^{-3}$ s thus $\xi < 10^{-3}$ for the resistivity range found in the earth. Therefore there is a quasi-stationary field which is described by equations (II.1) and (II.2), with the first equation of (II.1) re-written as

$$\text{curl } \underline{H} = \underline{j} \qquad \text{(II.3)}$$

, i.e. only conduction currents are considered.

Perform the curl operation on the second equation of (II.1) and use the second relation of (II.2) to re-write $\underline{H}$ in terms of $\underline{E}$ using (II.3) and the last relation of (II.2) to arrive at

$$\nabla^2 \underline{E} - \text{grad div } \underline{E} = \mu\sigma \frac{\partial \underline{E}}{\partial t}$$

but unless there are sources of currents or charges in the medium, div $\underline{E}$=0. This leads to the diffusion equation

$$\nabla^2 \underline{E} = \mu\sigma \frac{\partial \underline{E}}{\partial t} \qquad \text{(II.4)}$$

where $\mu = \mu_o$. Above the earth σ =0, so (II.4) simplifies to Laplace's equation

$$\nabla^2 \underline{E} = 0 \qquad \text{(II.5)}$$

The above discussion demonstrates that the magnetotelluric method deals with a diffusion of a quasi-static field through the earth.

II.3. Electromagnetic Induction in Layered Structures

Assume an Earth where conductivity varies only with depth. Consider the z-axis directed along the vertical, and pointing downwards so that $\sigma = \sigma(z)$. Such a situation is referred to as the one dimensional earth or the 1D case, for short. It is assumed that a primary electromagnetic field which is a function only of z, is generated by a horizontal current sheet located above the surface of the earth. The x-axis is aligned with the current direction j_x.

The current sheet generates a uniform magnetic field Hy. The vortex primary electric field directed along the x-axis induces electric currents in the conductive earth which in turn generate a secondary field. No charges accumulate on the interfaces since the electric field does not intersect boundaries. Fields are assumed harmonic so their time dependence is written as

$$T(t) = \exp(i\omega t) \qquad \text{(II.6)}$$

this assumption generates time derivatives which may be read as $\partial/\partial t \to i\omega$, so the second equation of (II.1) can be rewritten as

$$\mathrm{curl}\ \underline{E} = -i\omega \underline{B} \qquad \text{(II.7)}$$

while the diffusion equation (II.4) now reads

$$\nabla^2 \underline{E} - i\omega\mu\sigma \underline{E} = 0 \qquad \text{(II.8)}$$

which together with the relevant boundary conditions describes the 1D magnetotelluric problem.

Boundary conditions govern the horizontal fields across interfaces between two different media. Assume the horizontal boundary between two layers is cut perpendicularly by a rectangle with horizontal sides l_1, in a medium 1, $l_2 = l_1$ in another medium 2 and lateral sides $l_l < l_1, l_2$. This rectangle cuts the plane boundary along the x-direction through a line $l_o = l_1 = l_2$. Take as positive the sense of following the outline $l_1, l_l, l_2, l_l^{anti}$ clockwise. The rectangle area is described by the vector $\underline{S}$. Integrate equation (II.7) over the surface $\underline{S}$,

$$\int_S \text{curl}\, \underline{E} \cdot d\underline{S} = -i\omega \int_S \underline{B} \cdot d\underline{S} \qquad \text{(II.9)}$$

The left hand side of this equation may be transformed by Stokes' Theorem and since Ex and l_1 are perpendicular, i.e.

$$\int_{2l_1} \underline{E} \cdot d\underline{l} = 0$$

the left hand side can be written as

$$\int_S \text{curl}\, \underline{E} \cdot d\underline{S} = \left(E_x^{(1)} - E_x^{(2)} \right) l_0$$

where $E_x^{(1)}$ and $E_x^{(2)}$ are the electric fields in medium 1 and medium 2, respectively. The right hand side of (II.9) is

$$-i\omega \int_S \underline{B} \cdot d\underline{S} = B_y S (-i\omega)$$

and so (II.9) may be re-written as

$$\left(E_x^{(1)} - E_x^{(2)} \right) l_0 = B_y S (-i\omega)$$

Let the rectangle collapse towards the interface, $l_1 \to 0$ and $S \to 0$. As l_0 remains finite,

$$E_x^{(1)} = E_x^{(2)} \qquad \text{(II.10)}$$

i.e. the tangential electric field is continuous across the boundary.

The continuity of $\underline{H}$ across a boundary also needs to be investigated. For this rotate the rectangle l_1, l_1, l_2, l_1 along the y-direction. Integrate (II.3) to give

$$\int_S \text{curl}\, \underline{H} \cdot d\underline{S} = \int_S \underline{j} \cdot d\underline{S} \qquad \text{(II.11)}$$

where the right hand side is just the current that flows perpendicular to $\underline{S}$,

$$\int_S \underline{j} \cdot d\underline{S} = j\, l_0 l_1$$

The left hand side of (II.11) is treated in a similar manner as (II.9),

$$\int_S \text{curl}\, \underline{H} \cdot d\underline{S} = \left(H_y^{(1)} - H_y^{(2)} \right) l_0$$

and making $l_\ell \to 0$,

$$\left(H_y^{(1)} - H_y^{(2)} \right) l_0 = j l_0 l_\ell \longrightarrow 0$$

provided the current density j remains finite. Thus,

$$H_y^{(1)} = H_y^{(2)} \qquad \text{(II.12)}$$

i.e. the tangential magnetic field is continuous across the boundary.

First assume a homogeneous half-space. As the combination (Ex,Hy) has already been chosen to represent the incoming field, it is desirable to simplify the notation dropping the sub-indexes from the field components. Equation (II.8) now reads

$$\frac{d^2 E}{dz^2} - i\omega\sigma E = 0 \qquad \text{(II.13)}$$

with a harmonic time dependence assumed throughout. The solution to (II.13) is

$$E(z) = A \exp(-kz) + B \exp(kz)$$

where

$$k = \sqrt{i\omega\mu\sigma} = (1+i)\sqrt{\omega\mu\sigma/2} \qquad \text{(II.14)}$$

is the wavenumber. This solution represents a sum of two plane waves travelling downwards with amplitude A.exp(-kz) and upwards with amplitude B.exp(kz). But B=0 since the electric field must remain finite when $z \to \infty$. The full solution is therefore

$$E(z,\omega) = A \exp(-z/\delta) \exp(-i(z/\delta - \omega t)) \qquad \text{(II.15)}$$

where

$$\delta = \sqrt{2/\omega\mu\sigma} \qquad \text{(II.16)}$$

The electric field decays as it diffuses through the earth. The quantity δ defined in (II.16), is called skin depth, gives the depth where the field amplitude attenuates to 1/e of its surface value.

Expanding the curl in equation (II.7),

$$H = \frac{i}{\omega\mu}\,\frac{dE}{dz}$$

or

$$H(z,\omega) = \frac{\sqrt{2}}{1+i}\,\gamma\sqrt{\frac{\sigma}{\omega\mu}}\,E(z,\omega) \qquad \text{(II.17)}$$

and then at the surface

$$H(0,\omega) = \frac{\sqrt{2}}{1+i}\,\gamma\sqrt{\frac{\sigma}{\omega\mu}}\,A$$

putting z=0 in (II.15).

The fields (II.15) and (II.17) are the sum of the primary field and a secondary field caused by the induced currents. So the term A carries field information to the quantities measured at the surface, E(0,w) and H(0,w). The amplitude of the inducing field may be removed by defining the plane wave impedance, or just impedance, of the uniform medium as

$$Z_{xy} = \frac{E_x(0,\omega)}{H_y(0,\omega)} = \gamma\sqrt{\frac{i\omega\mu}{\sigma}} \qquad \text{(II.18)}$$

or as the pair (Ey,Hx) could have been chosen,

$$Z_{yx} = -\frac{E_y(0,\omega)}{H_x(0,\omega)} = Z_{xy}$$

Another important response function is given by (Weidelt, 1972),

$$C(\omega) = -\frac{E_y(0,\omega)}{E_y'(0,\omega)} = -\frac{E_x(0,\omega)}{E_x'(0,\omega)} \qquad \text{(II.19)}$$

where the primes stand for the derivative with respect to z. The impedance has units of ohms,

$$[Z] = \frac{[E]}{[H]} = \frac{V\cdot m^{-1}}{A\cdot m^{-1}} = \Omega$$

while Weidelt's response (II.19) is expressed in meters as is the skin depth (II.16). Usually one chooses to express the earth response function as apparent resistivity

$$\rho_{ij}(\omega) = \frac{1}{\omega\mu} |Z_{ij}|^2 \qquad \text{(II.20)}$$

and phase

$$\varphi_{ij}(\omega) = \text{Arg}(Z_{ij}) \qquad \text{(II.21)}$$

with i,j=x,y. In the case of a half space, $\rho_{ij}(w)=1/\sigma$ and $\varphi_{ij}(w)=\pi/4$.

Consider an earth with a resistivity distribution $\sigma=\sigma(z)$ which be parameterized with n discrete layers. A layer is characterized by its conductivity $\sigma_j=\sigma(z_j)$ and thickness. The first boundary is the earth's surface while the (n+1)-th layer is considered as a half-space of uniform conductivity. Choose an i-th layer as a reference. The electric field there will be given by the sum of waves travelling in both downward and upward directions

$$E_j(z,\omega) = A_j \exp(k_j(z_{j-1}-z)) + B_j \exp(-k_j(z_{j-1}-z))$$

$$H_j(z,\omega) = \frac{\sqrt{2}}{1+i}\sqrt{\frac{\sigma_j}{\omega\mu}}\left[A_j \exp(k_j(z_{j-1}-z)) - B_j \exp(-k_j(z_{j-1}-z))\right]$$

In the next layer solutions are similar with the substitution of j by j+1. Apply now the boundary conditions (II.10) and (II.12) at the interface $z=z_j$. Thus noting that $h_j=z_j-z_{j-1}$, i.e. the layer thickness,

$$A_j \exp(-k_j h_j) + B_j \exp(k_j h_j) = A_{j+1} + B_{j+1}$$

$$k_j(A_j \exp(-k_j h_j) - B_j \exp(k_j h_j)) = k_{j+1}(A_{j+1} - B_{j+1})$$

From these relations one can obtain a recursive solution that begins at the top of the half-space and gives Bj/Aj at the surface. As before B =0 for the half-space. It is convenient to define the reflection coefficient

$$r_{j,j+1} = \frac{k_j - k_{j+1}}{k_j + k_{j+1}}$$

in terms of which a recursive relation can be written

$$\frac{B_j}{A_j} = \frac{r_{j,j+1} + B_{j+1}/A_{j+1}}{1 + r_{j,j+1} B_{j+1}/A_{j+1}} \exp(-2 k_j h_j) \qquad \text{(II.22)}$$

The impedance on the surface is given by

$$Z_{xy}(0,\omega) = \frac{1+i}{\sqrt{2}} \sqrt{\frac{\omega\mu}{\sigma_1}} \frac{1 + B_1/A_1}{1 - B_1/A_1}$$

where B_1/A_1 is calculated from (II.22). Further discussion of 1D models can be found in chapters II, IV, V and VI.

II.4. Induction in Two-Dimensional Structures

Consider an earth where the conductivity is invariant along the x-direction, $\sigma = \sigma(y,z)$. Along this direction the partial derivatives are zero. In this case Maxwell's equations (II.3) and (II.7) decouple into two distinct modes. For this conductivity distribution, the field components obey the following relationships,

$$\frac{\partial H_z}{\partial y} - \frac{\partial H_y}{\partial z} = \sigma E_x$$

$$\frac{\partial H_x}{\partial z} = \sigma E_y \qquad \text{(II.23)}$$

$$-\frac{\partial H_x}{\partial y} = \sigma E_z$$

and

$$\frac{\partial E_z}{\partial y} - \frac{\partial E_y}{\partial z} = i\omega\mu H_x$$

$$\frac{\partial E_x}{\partial z} = -i\omega\mu H_y \qquad \text{(II.24)}$$

$$\frac{\partial E_x}{\partial y} = i\omega\mu H_z$$

Note that the first equation of (II.23) and the last two of (II.24) involve Ex,Hy and Hz while the remainder involve Ey,Ez and Hx. This is a convenient separation since in the first case the field is expressed by the triplet (Ex,Hy,Hz) with the electric field parallel to any discontinuity and in the second case the field is (Hx,Ey,Ez), where the magnetic field is parallel to the discontinuities. The first case is called the E-polarization case while the second is the H-polarization case.

The E-polarization set can be used to eliminate Hx and Hz and obtain a scalar Helmholtz equation in terms of Ex,

$$\frac{\partial^2 E_x}{\partial y^2} + \frac{\partial^2 E_x}{\partial z^2} - i\omega\mu\sigma E_x = 0 \qquad \text{(II.25)}$$

and repeating this process using the H-polarization set another Helmholtz equation is obtained

$$\frac{\partial^2 H_x}{\partial y^2} + \frac{\partial^2 H_x}{\partial z^2} + \frac{1}{\sigma}\left(\frac{\partial\sigma}{\partial y}\frac{\partial H_x}{\partial y} + \frac{\partial\sigma}{\partial z}\frac{\partial H_x}{\partial z}\right) - i\omega\mu\sigma H_x = 0 \qquad \text{(II.26)}$$

In the non-conducting air layer, $z<0$, $\sigma=0$ and then the right hand side of the last two equations in (II.23) vanish indicating that the magnetic field does not depend on either y or z. In other words Hx is constant along the earth's surface irrespective of the conductivity distribution inside the earth. This fact simplifies the problem for the H-polarization case. Nevertheless electric currents may cross interfaces and superficial charges appear where currents meet interfaces. The effect of these charges is known as the galvanic effect (Rokityansky, 1982, p.53).

Apart from a few simple conductitvity configurations equations (II.25) and (II.26) cannot be solved analytically. The forward problem can be solved numerically by one of several methods currently being used. Further discussion on 2D modeling can be found in chapters IV, V and VI.

II.5. Final Remarks

For a three-dimensional earth, $\sigma = \sigma(x,y,z)$, Maxwell's equations cannot be reduced to a simpler form and no analytical result is available. Again numerical solutions are available. Although three-dimensional modelling does not form part of this

work, 3D effects are, however, apparent on a number of response functions which are considered in chapter VI. The reader is referred to the introduction of chapter IV for a brief list of references on 3D modelling.

The next chapters deal with the determination of the earth response functions Z, ρ and φ from field measurements. The magnetic field which is measured is $\underline{B}$, the magnetic induction vector. This vector is related to the magnetic field strength by the second relation of (II.2). From now on the symbol $\underline{H}$ will designate a measured magnetic field in opposition to $\underline{E}$, a measured electric field. Therefore magnetic induction units are used for $\underline{H}$. The following practical units will be used for the remainder of this dissertation:

[H] (<-[B])=nT
[E]=mV/km
[ρ]= Ω.m
φ-> degrees.

CHAPTER III
Data Analysis

III.1. Introduction

Some aspects of data analysis in magnetotellurics are discussed in this chapter. All calculations are carried out in the frequency domain with the basic data set being generated through Fast Fourier Transformation. A linear model is assumed to represent the induction phenomenon by an incident electromagnetic plane wave on a flat earth. Model parameters are estimated through least-squares procedures. Data quality is monitored and selected prior to transformation to the frequency domain. This is achieved by manual data editing of the original data series. As a result of this process a cleaned data set as free as possible of unwanted features as, e.g., high energy spikes, is obtained.

The data used in this chapter is selected from a large data set collected in western Turkey, as part of the Turkish Dilatancy Project of 1984, TDP3. This data comprises one week of five components of the magnetotelluric field sampled at 5s intervals at two sites. The selected data is used as a test data set to demonstrate the techniques investigated in this chapter. TDP3 is a multidisciplinary experiment conducted on a cooperative basis by workers from Turkey and the British Geological Survey (BGS) in 1984. The main objective of the magnetotelluric contribution to TDP3 is to investigate, from the electrical point of view, the variations of rock properties induced by the dynamic processes associated with earthquakes (Beamish and Riddick, 1985a).

The North Anatolian Transformation Fault (NATF) cuts the TDP study area in the E-W direction dividing it into two sections. It is a right-lateral fault zone taking up most of the Anatolian scholle with a (of length) 1200km (Sengor et al., 1982). The crust in the region of TDP3 is undergoing active dislocation as evidenced by the existence of an earthquake swarm. Seismological observations indicate that the earthquakes occur at depths of 6-12km, and all shear wavetrains from these events indicate shear-wave splitting (Crampin et al., 1985). This splitting is compatible with an effective anisotropy of the rocks internal structure, such as that resulting from aligned cracks (Booth et al., 1985). This stress-cracking is characterized by oriented fluid filled cracks, consistent with the common direction of compression and tension in fault-plane mechanisms (Crampin and Booth, 1985) which permit sliding under low shear stresses. Subcritical crack-growth at the

stress concentrations, would open existing weakness parallel to the direction of maximum compressive stress (Crampin et al., 1985), eventually causing microcracks to connect. This allows fluids to flow into regions near the eventual fracture. The hypothesis of the existence of such extensive dilatancy anisotropy (EDA) provides a mechanism for electrical resistivity variations at low stress levels, and constitutes one of the main motivations behind the magnetotelluric contribution to the TDP3 experiment (Beamish and Riddick, 1985a).

The work described here covers data reduction, data analysis and presentation of results in the usual form of sounding parameters. A one-dimensional electrical model is produced at the end of the chapter. Data reduction is performed on data windows of 256 points for each component. Each window is obtained adding zeros to 192 determinations of the component considered. The data window is then transformed to the frequency domain using the Fast Fourier Transform (FFT). The whole frequency range is divided into 2 decades each of which, is subdivided into 10 non-overlapping bands. The spectral estimates are analysed using both single site (SS) and remote reference (RR) techniques. Results are compared using the same technique and using different techniques. The best set of results is chosen for the calculation of the usual sounding parameters, apparent resistivity and phase, presented in the form of sounding curves. These curves are then interpreted using a simple one-dimensional scheme.

Spectral estimates are selected on the basis of coherence functions, they are rejected if coherence functions fail a particular criterion. Accepted spectral estimates are stacked to produce one or two estimates of the impedance tensor, $\underline{\underline{Z}}$, at each band. The impedance tensor will also be referred to as a response function. Confidence intervals at the 68% level are attached to each impedance tensor component estimate. Both bias and random errors and their implications on the reliability of impedance estimates are discussed in detail.

This chapter is sub-divided into seven sections. Following this introductory section, section 2 gives an account of data acquisition. There the basic data set is described and exemplified. The relevant theory on estimation of spectral functions by Fourier transformation is given in section 3. Single site analysis is described in section 4. Five distinct coherence criteria are used to select data. Two extreme least-squares solutions for $\underline{\underline{Z}}$ are calculated, one upward biased and the other downward biased, this is

done in order to delineate a region where the unknown true value is confined. Noise is described and both bias and random errors are calculated and discussed. Remote reference analysis is described in section 5, where only one coherence criterion is used. Both magnetic and electric fields are used as a remote reference. The role of the predicted coherence function in RR analysis is described in detail. Data subsets selected using the predicted coherence function are compared and analysed. The dependence of the variance on the number of stacked spectral estimates is analysed in order to provide a qualitative assessment of the reliability of the impedance tensor estimates. In section 6 the best set of impedance estimates from the RR analysis is used to obtain sounding parameters. Those parameters are in turn used to produce a geoelectrical one-dimensional interpretation. Finally section 7 summarizes and presents the conclusions of this chapter.

III.2. Data Acquisition

The TDP3 area is shown in figure III.1. There are four magnetotelluric sites within or close to an earthquake swarm, shaded in the figure. Site 1 is a base site to which all other sites were radio-linked. Only data sets from site 2 and site 1 are analysed. These two sites are situated 29km apart on both sides of the NATF. EDA 105B tri-axial fluxgate magnetometers were used to record the three magnetic components. Four electrodes were laid in a cross arrangement with 100m distance between pairs. A fifth electrode provided a common ground. Eletrodes were non-polarizing copper-copper sulphate specially designed for the TDP3 project. The sensors were aligned along the N-S, E-W magnetic directions. All signals were band-pass filtered and amplified before conversion to digital form. All five signals passed through low-pass anti-aliasing filter, together with a long-period high-pass filtering stage. This later stage is optional and was switched out for the data considered here. All sites were radio-linked to site 1 by FM telemetry, the incoming signals being demodulated at the base. Data were collected using a DEC PDP 11/23 minicomputer system. A more detailed description of the system can be found elsewhere (Beamish and Riddick, 1985b).

Data were sampled at 5s during the 6 months of the TDP3 experiment. The 7 days of test data are numbered consecutively from 269 to 275. Five components were recorded at each site: Ex, Ey, Hx, Hy and Hz. Directions x and y are the magnetic north and east, respectively. Figure III.2 shows one hour of simultaneous measurements at both sites. Note that the natural scales of the

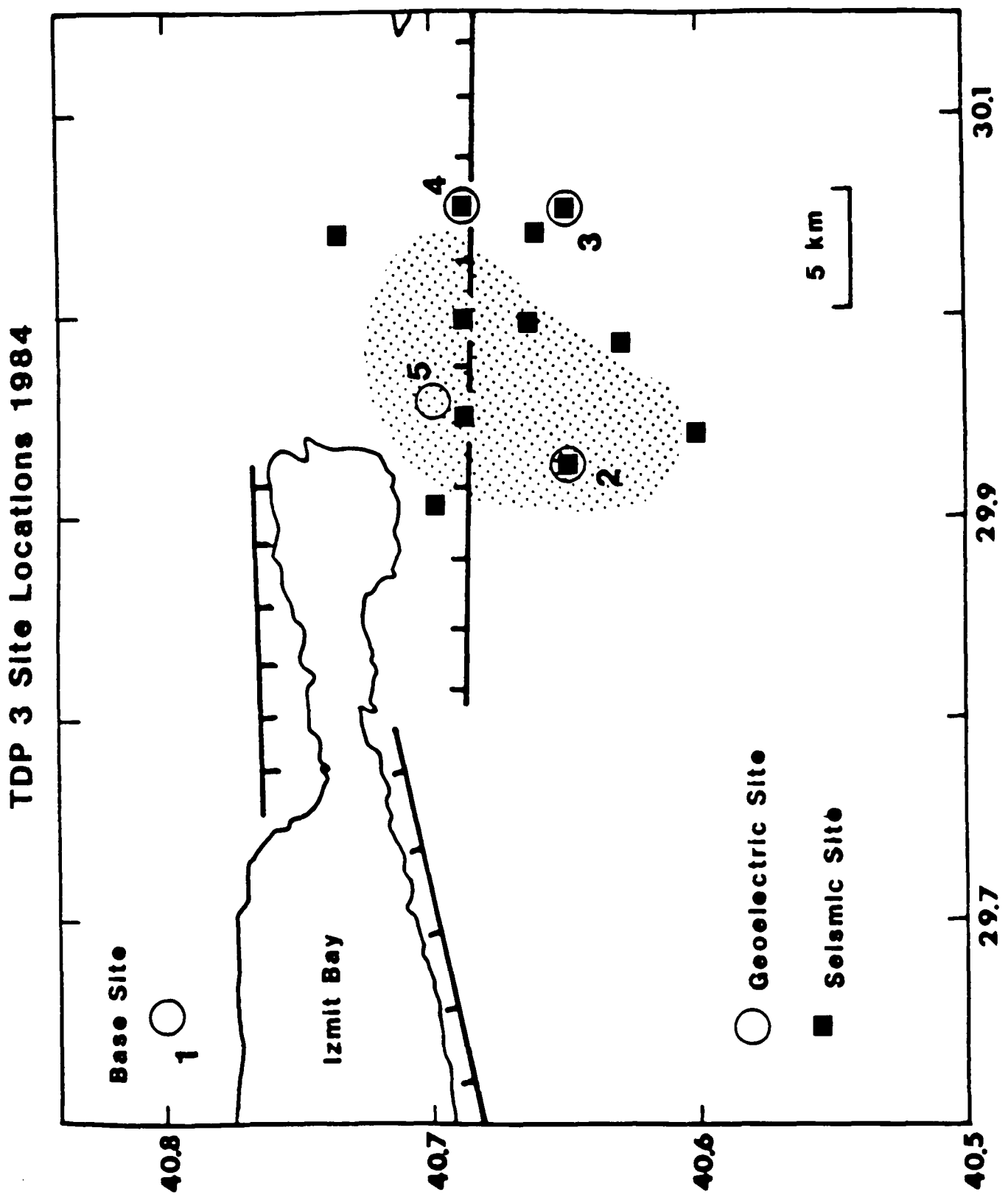
TDP 3 Site Locations 1984
Base Site
1
Izmit Bay
2
3
4
5
5 km
Geoelectric Site
Seismic Site
40.8
40.7
40.6
40.5
29.7
29.9
30.1

Figure III.1. Site locations within the TDP3 area. The shaded area shows the location of an earthquake swarm.

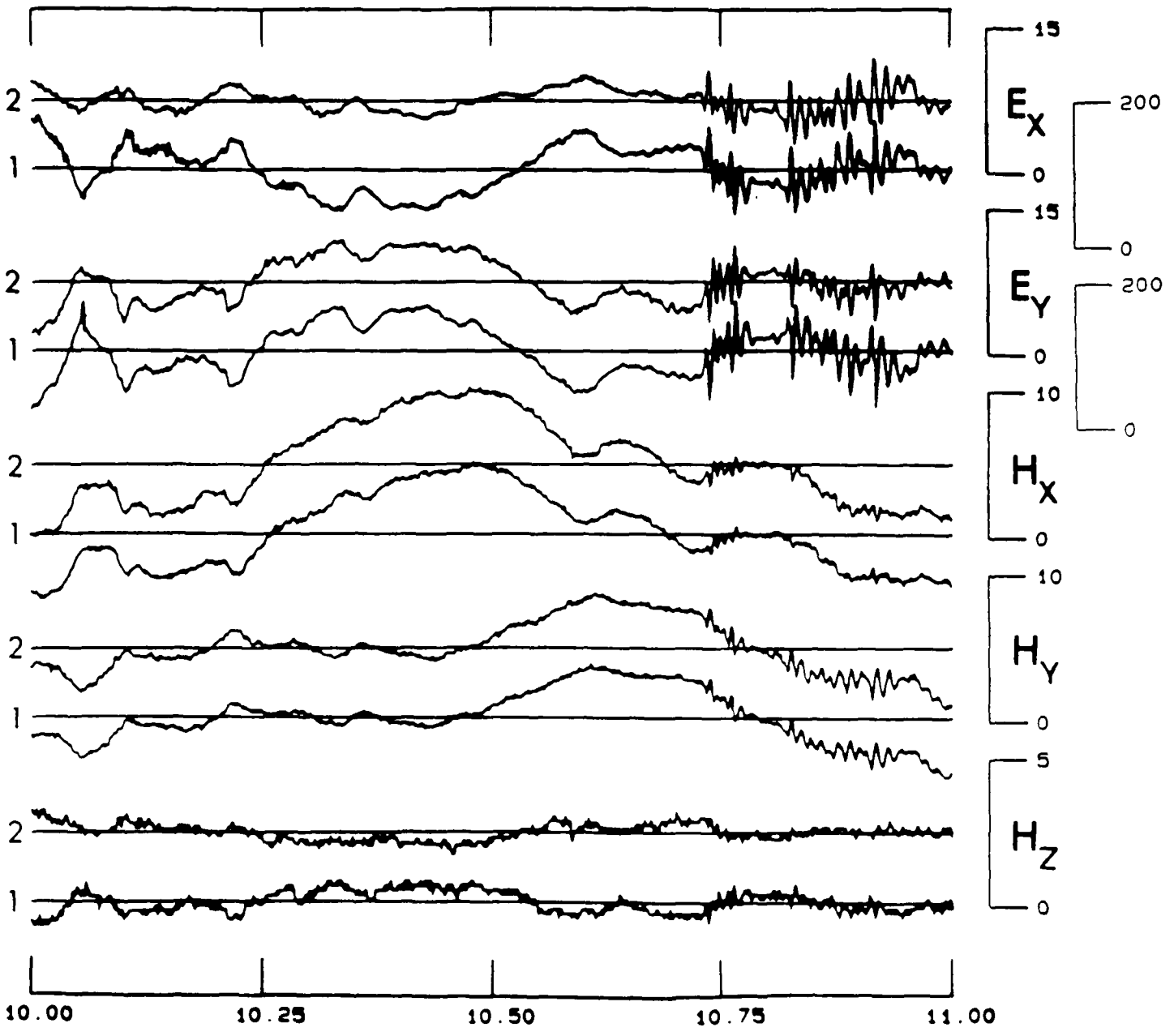
2
1
2
1
2
1
2
1
2
1
15
E_X
0
200
0
15
E_Y
0
200
0
10
H_X
0
10
H_Y
0
5
H_Z
0
10.00
10.25
10.50
10.75
11.00

Figure III.2. Example of 1 hour of simultaneous data from sites 1 and 2. Note the different scales for the telluric components, the scale for site 1 is more than 13 times that for site 2. E field is in mV/km and H field is in nT.

electric components at site 1 are more than 13x the corresponding components at site 2.

For spectral estimation purposes the data has been divided into two decades which are referred to as decades 4 and 5. The basic (raw) data series, sampled at $\Delta t=5s$, form decade 4 (10-100s). A data window consists of 192 points, or in other words has a length of 960s. The seven days provide 630 such data windows. Each window provides sufficient degrees of freedom for spectral estimation of the MT response functions across a decade. The data set for decade 5 (100-1000s) is produced by applying a low-pass filter to the basic data set and re-sampling at 50s. Again a data window consists of 192 points, having a length of 160min. The same seven days now provide 63 such data windows. It is important to point out that the data analysis scheme adopted here uses non-overlapping, i.e. independent, data windows.

III.3. Data Reduction and Conditioning

There are several procedures for estimating the spectral content, or simply the spectrum, of a time series (see, e.g., Hermance, 1973). A published FFT algorithm (Yfantis and Borgman, 1981) was used for estimating the Fourier transform of the time series. In this section the procedures for transforming data windows to the frequency domain are described.

Let x(t) represent a data window of a measured magnetotelluric field component. An estimate of its Fourier transform is given by

$$X(\omega,T)=\int_{-\infty}^{\infty} x(t)\cdot u(t;T)\exp(-i\omega t)\,dt \qquad \text{(III.1)}$$

where x(t) is defined in [-T/2,T/2], and T is the period. The function u(t;T) is a spectral window which reflects a limited knowledge on x(t) to the period of measurement, T. The Fourier transform of u(t;T) is designated by U(w;T).

The simplest spectral window is the rectangular window. Its time domain formulation is $u(t;T)=1$ along the data window $|t|\leq T/2$ and $u(t;T)=0$ otherwise. Despite its simplicity and "correctness" in the time domain, the shape of U(w;T) has large side lobes, both negative and positive. Power "leaks" through those lobes causing severe spectral distortion. As Fourier transformation assumes repetition of the data set beyond the window u(t;T), considerable power is present at the fundamental and lower frequencies. So

reduction of the spectral distortion may be achieved by both reducing lobe "leakage" and by reducing the power of frequencies whose periods are equal or longer than the record length. The first is achieved through window carpentry while the second is achieved by removing the mean or trends in the data (see, e.g., Bendat and Piersol, 1971, p.286ff).

Trend is defined as any frequency component with periods longer than the record length. Basically there are two methods of removing a trend from x(t). They are the average slope and least-squares, the former used only for linear trends. Removal of the mean was employed on the data set since it showed no apparent trend.

The rectangular window is clearly inadequate due to the distortion it introduces in the spectral representation of x(t). This can be minimized by choosing another window which tapers off gradually both ends of the data window. Most windows are real and even, yielding spectral representations that are also real and even. They fall in three main categories: trigonometric windows; power windows and exponential windows. A very good review on windows can be found elsewhere (Harris, 1978).

A window which is a combination of the rectangular and a Hanning window was used in this work. It is also known as a cosine tapered rectangular or Tukey window. This window is constant for 80% of its length and drops off during the extreme 10% at both ends. It may be expressed as

$$\mu(t;T) = \begin{cases} 0 & t < -T/2 \\ \frac{1}{2}\left(1+\cos 10\pi t/T\right) & -\frac{T}{2} < t < -\frac{2}{5}T \\ 1 & -\frac{2}{5}T < t < \frac{2}{5}T \\ \frac{1}{2}\left(1+\cos 10\pi t/T\right) & \frac{2}{5}T < t < \frac{T}{2} \\ 0 & t > T/2 \end{cases} \qquad \text{(III.2)}$$

(Båth, 1974, p.161). Note that changes are required in (III.2) when using the discrete Fourier transform (Harris, 1978).

The expected spectral value of a measurement is proportional to the input amplitude, the proportionally factor being a sum of the window terms which is in fact the DC signal gain of the window (Harris, 1978). For a rectangular window this factor is N, the length of the window. For all other windows, the gain is reduced

because at both extremities values go smoothly to zero. Therefore the resultant spectral amplitudes are biased. For the 80% tapered Tukey window, the coherent gain is 0.875 (Bendat and Piersol, 1971, p.323). To obtain a correct scale it is necessary to multiply the spectrum estimates by the reciprocal of the gain.

The basic data window length is N=192 data points. This is extended to N'=256 by adding zeros after application of the spectral window (III.2). Note that N' is the nearest whole power of 2 after 192. Before augmentation the discrete frequency values obtained through FFT are separated by $\Delta f=1/T=1/(N.\Delta t)$, where Δt is the sampling interval of x(t). As zeros were added to extend N->N', the spectral resolution becomes $\Delta f'=1/(N'.\Delta t)$. In other words there are N'/N more spectral estimates than without any extension. Each spectral estimate is complex, thus contributing 2 degrees of freedom. After the addition of zeros, the number of degrees of freedom for each estimate decreases to df=2.N/N'. Another interesting feature is that the variance of the spectral estimates is also reduced (Kanasewich, 1975, p.100). Variance can be reduced even further by overlapping data windows to a certain degree and choosing a suitable spectral window in order to minimize the correlation between successive transforms (Harris, 1978).

A power spectral density function of x(t) is given by

$$S_x(\omega) = \frac{2}{T} |X(\omega;T)|^2 \qquad \text{(III.3)}$$

The random portion of the error in the estimation of Sx(w) is given by the normalized error (Bendat and Piersol, 1971, p.191)

$$\varepsilon = \sqrt{2/df}$$

where df is the number of degrees of freedom. As df<2, $\varepsilon > 1$ implying that the standard deviation of the estimate Sx(w) is greater than the estimate itself. Furthermore the variance of each estimate does not depend on the record length T (Bendat and Piersol, 1971, p.189). This implies that the above power spectrum estimate is inconsistent.

The random error in the estimates Sx(w) is reduced by smoothing the estimates over a group of estimates. This can be done in two basic ways. First assume there are k independent sample records $x_i(t)$, i=1,...,k, of a single spectral component. The final estimate is the ensemble average of the k independent estimates at that frequency. The process is repeated for all frequencies in the

data window. For the second smoothing procedure the power spectrum of the data window x(t) is divided into k sub-intervals, or bands, composed of $l_1, l_2, \ldots, l_k$ contiguous spectral components. Bands may overlap to a certain degree. One ends up with k spectral estimates, each of them is an average of l_i, i=1,...,k, contiguous spectral estimates. Both schemes produce a smoothed spectral estimate with a reduced variance, as the number of degrees of freedom for each estimate increases n-fold, with n=k for the first scheme or n=1 for the second scheme.

The second scheme was chosen, i.e. band averaged estimates. Each decade is subdivided into 10 non-overlapping bands. Then each band yields an independent spectral estimate, which is located by the band centre frequency value. Those centre frequencies are equi-spaced on a log-frequency scale. The ratio of contiguous centre frequencies is given by (e.g., Vozoff, 1972)

$$\log \frac{f_{i+1}}{f_i} = \frac{1}{10} \qquad \text{(III.4)}$$

for each decade. The band scheme can be illustrated with the following table where band number, degrees of freedom, df, and centre periods, CP, for decade 4, are shown

Band :	10	9	8	7	6	5	4	3	2	1
df :	40.5	33.0	27.0	21.0	18.0	13.5	10.5	10.5	7.5	6.0
CP(s):	11.3	14.2	17.9	22.6	28.4	35.7	45.0	56.6	71.3	89.7

The scheme is the same for decade 5, it is only necessary to multiply the centre periods by 10. Although bands in this chapter are ordered by frequency all results are shown ordered by period, in other words, in decreasing order of band numbering.

Each frequency estimate Sx can be averaged over a number of raw spectral estimates inside each band of the type of (III.4). Note that requirement (III.4) is also equivalent to fixing the ratio centre frequency to bandwidth to a constant value, which is approximately 4.4. For a particular band the auto-spectrum estimate is obtained by band averaging spectral estimates (III.3) as

$$S_{xx} = \overline{S_x S_x^*} \qquad \text{(III.5)}$$

where (*) denotes complex conjugate, and the bar indicates a band averaged value. The frequency dependence is omitted from now on. If Sy is another spectral estimate, the cross-spectrum of Sx and Sy can be obtained as

$$S_{xy} = \overline{S_x S_y^*} = \left(\overline{S_y S_x^*} \right)^* \qquad \text{(III.6)}$$

for each band.

III.4. Single Site Analysis

III.4.1. Introduction

The estimation of the magnetotelluric impedance tensor is usually done using data collected at one particular site. This estimated tensor suffers from both random and bias errors. Bias errors arise since both the electric and the magnetic fields are degraded by noise.

Most workers estimate the impedance tensor at a single site (SS) using least-squares techniques (Sims et al., 1971), thus obtaining confidence intervals at a specified level where the, unknown, true value should lie (Reddy et al., 1976; Gundel, 1977). In another approach the impedance tensor elements are approximated by least-squares polynomials, attributing weights to each frequency band in accordance with data quality (Larsen, 1975). In principle random errors can be reduced to a desired level by increasing the number of data windows. A minimum variance estimator can be obtained using weights which are functions of the inverse of the variances (Gundel, 1977). Bias errors may be reduced in an unpredictable way by averaging stable least-squares estimates (Sims et al., 1971). Even total elimination of bias errors may be attempted if noise components are totally incoherent (Kao and Rankin, 1977).

Usually one estimates the impedance tensor $\underline{\underline{Z}}$ assuming that all the noises reside in either the electric or the magnetic field (Sims et al., 1971; Bentley, 1973). What is left to the analyst is a choice of averaging with suitable weights, which may be all equal to 1, which is the extreme solution (Larsen, 1980; Filloux, 1980; Hermance and Pedersen, 1980). With this approach it may be possible to estimate both random and bias errors (Reddy et al., 1976; Pedersen, 1982; Kroger et al., 1983). Another way of estimating $\underline{\underline{Z}}$ accounts for noise in both electric and magnetic fields simultaneously, using SVD (Jupp, 1978; Park and Chave, 1984).

The aim of this section is to estimate the bounds where the SS estimated $\underline{\underline{Z}}$ should lie using the test data set. Two stable estimates, one biased up and the other biased down, are used to

produce extreme bounds for $\underline{\underline{Z}}$. The discussion is restricted to the off-diagonal elements of $\underline{\underline{Z}}$.

III.4.2. Relationships for Two Input-Single Output Linear Systems

The magnetotelluric problem may be regarded as a two input-single output linear system. The inputs are either the magnetic or the telluric field components. A description of multiple input linear system theory based on multivariate spectral analysis, can be found elsewhere (Bendat and Piersol, 1971, p.147ff).

Assume $x_1(t)$, $x_2(t)$ are inputs sampled from stationary random process, and $x_3(t)$ is the output from the linear system $h_i(t)$, i=1,2. Both inputs and output are contaminated with noise $n_i(t)$, i=1,2,3, see figure (III.3). The system output $x_3(t)$ is given by the convolution

$$x_3(t) - m_3(t) = \sum_{i=1}^{2} \int_0^{\infty} h_i(\tau)\left(x_i(t-\tau) - m_i(t-\tau)\right) d\tau$$

where the weighting functions $h_i(\tau)$ are system outputs, at time t, of an unit pulse input applied at time $\tau < t$. Taking the Fourier transform one gets

$$X_3 - N_3 = H_1(X_1 - N_1) + H_2(X_2 - N_2) \qquad \text{(III.7)}$$

with a dependence on frequency assumed. The functions H_i are called response functions.

The response functions H_i may be expressed in terms of the signals auto- and cross-spectral density functions. The signal power is estimated by subtracting the noise power from the measured record power (see, e.g., Noponen and Nikkola, 1976; Kao and Rankin, 1977). To get expressions for both H_1 and H_2, cross spectra of the output signal (X_3-N_3) with the inputs (X_1-N_1) and (X_2-N_2) are evaluated as in (III.6). This results in a system of 2 equations in terms of the measured and noise auto and cross powers. Making the basic assumption that the noise series N_i are random and uncorrelated to each other and with the signals X_i, i=1,2,3 (Sims et al., 1971), one simplifies the system to

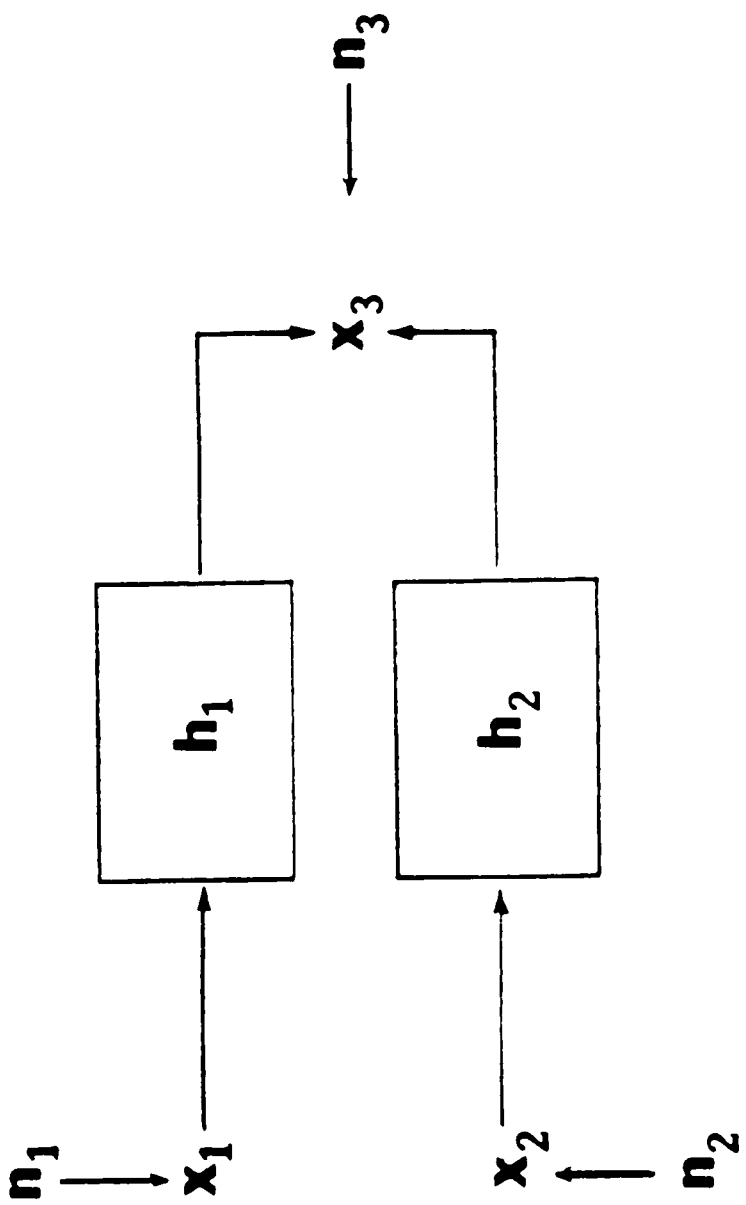
n3
x3
h1
h2
n1
x1
x2
n2

Figure III.3. A generic two input-single output linear system. Inputs $x_1(t)$ and $x_2(t)$ are contaminated by noise $n_1(t)$, $n_2(t)$. Output $x_3(t)$ is contaminated by noise $n_3(t)$.

$$S_{31} = H_1 (S_{11} - S_{N_1N_1}) + H_2 S_{12}^*$$
$$S_{32} = H_1 S_{12} + H_2 (S_{22} - S_{N_2N_2}) \qquad \text{(III.8)}$$

dependency on frequency assumed. The solution for, say, H_1, reads

$$H_1 = \frac{S_{31}\left[1 - \dfrac{S_{32}S_{12}^*}{S_{31}(S_{22} - S_{N_2N_2})}\right]}{(S_{11} - S_{N_1N_1})\left[1 - \dfrac{|S_{12}|^2}{(S_{11} - S_{N_1N_1})(S_{22} - S_{N_2N_2})}\right]} \qquad \text{(III.9)}$$

However the noise contribution is not known, so an estimate for H_1 is actually evaluated using the measured powers instead of the signal powers as

$$\hat{H}_1 = \frac{S_{31}\left(1 - \dfrac{S_{32}S_{12}^*}{S_{31}S_{22}}\right)}{S_{11}\left(1 - \dfrac{|S_{12}|^2}{S_{11}S_{22}}\right)} \qquad \text{(III.10)}$$

where the circumflex denotes an estimated quantity. In other words, $\hat{H}_1$ has a bias error due to the presence of noise in the auto-spectral density functions. The amount of bias is not known.

The quantity in the denominator of (III.10),

$$\gamma_{12}^2 = \frac{|S_{12}|^2}{S_{11}S_{22}} \qquad \text{(III.11)}$$

is real and satisfies $0 \leq \gamma_{12}^2 \leq 1$ (Bendat and Piersol, 1971, p.141) for all frequencies. The function γ_{12}^2 is called ordinary coherence. Note the distinction between coherence and coherency the latter being a complex function with modulus equal to $\sqrt{\sigma_{12}^2}$. When the series $x_1(t)$ and $x_2(t)$ are totally uncorrelated, $\sigma_{12}^2 = 0$ and conversely $\sigma_{12}^2 = 1$ if they are totally coherent. The definitions of

other ordinary coherence functions are obtained straightforwardly from (III.11).

The linear system shown in figure III.3 has two inputs. So the ordinary coherence cannot be used to measure how well the output is predicted by the two inputs combined. This is done by the predicted coherence function (Bendat and Piersol, 1971, pp.160-161)

$$\gamma^2_{3|12} = 1 - \frac{S_{N_3 N_3}}{S_{33}} \qquad \text{(III.12)}$$

which is real and also satisfies $0 \leq \gamma^2_{3|12} \leq 1$. The noise N is defined as the incoherent part of the measured output. From (III.7) it can estimated as

$$\hat{N}_3 = X_3 - \left(\hat{H}_1 X_1 + \hat{H}_2 X_2 \right) \qquad \text{(III.13)}$$

and then its auto power is estimated by $\hat{S}_{N_3 N_3} = \overline{N_3 N_3^*}$. As system responses are estimated in terms of auto- and cross-spectra, definition (III.12) may be expanded in terms of the measured powers. Some authors prefer to express the predicted coherence in this latter version. The quantity (III.12) is also known as the multiple coherence (see, e.g., Reddy and Rankin, 1974).

The coherence between one input and the output is not expressed correctly by the ordinary coherence. This is because, e.g., the input $x_2(t)$ appears as a noise component at the output when γ^2_{13} is estimated. Therefore the contribution of $x_2(t)$ must be removed. This is done using partial coherences like $\gamma^2_{31.2}$ or $\gamma^2_{32.1}$. The partial coherences are defined in terms of ordinary and predicted coherences as

$$\gamma^2_{31.2} = \frac{\gamma^2_{3|12} - \gamma^2_{32}}{1 - \gamma^2_{32}} \qquad \text{(III.14)}$$

or,

$$\gamma^2_{32.1} = \frac{\gamma^2_{3|12} - \gamma^2_{31}}{1 - \gamma^2_{31}} \qquad \text{(III.14')}$$

which also obey the usual inequality $0 \leq \gamma^2_{31.2}, \gamma^2_{32.1} \leq 1$.

Frequency response function estimates (III.10) involve random errors. Confidence limits may be evaluated from

$$\left(\hat{H}_i - H_i\right)^2 \leq \hat{r}_i^2 \qquad \text{(III.15)}$$

where $\hat{r}_i^2$ is given by (Pedersen, 1982)

$$\hat{r}_i^2 = \frac{1}{m'} F_{1;m';(1-\delta)} \frac{\left(1-\hat{\gamma}_{312}^2\right) S_{33}}{\left(1-\hat{\gamma}_{12}^2\right) S_{ii}} \qquad \text{(III.16)}$$

where n'=df-4, df is the number of degrees of freedom for the band considered and $F_{1;m';(1-\delta)}$ is a $100(1-\delta)\%$ point of an F distribution. This expression is exact under the assumption that the noise N_i is normally distributed and statistically independent and inputs are error free. Stationarity of the time series is not required.

Equation (III.16) gives an expression for the confidence limits attached to the random errors for both real and imaginary parts of H . These confidence limits are stated for a $(1-\delta)$ confidence level. Throughout this chapter $\delta=0.32$ is used, i.e. one standard error level. It is also important to note that expression (III.16) differs from similar expression used by some authors (Bendat and Piersol, 1971, p.205-206; Reddy et al., 1976; Gundel, 1977). This happens since $\hat{r}_i^2$, gives confidence limits for each H_i, while the above authors attach confidence limits to the set (H_1,H_2) (Pedersen, 1982).

III.4.3. The Magnetotelluric Impedance Tensor Estimation

The plane wave impedance for a one-dimensional earth has been defined in chapters I and II. For a two-dimensional or three-dimensional earth the impedance cannot be expressed as a scalar any longer, it must be expressed by a second rank tensor. It describes a linear system similar to the one in figure III.3, with two horizontal components of magnetic field acting as inputs and one horizontal component of the electric field as output. So the elements of $\underline{\underline{Z}}$ play a similar role as H_1 and H_2 in (III.7), the only difference is that two such equations are needed, one for each electric component. The impedance tensor is defined in matrix notation as

$$\underline{E} = \underline{\underline{Z}}\,\underline{H} + \underline{E}_n \qquad \text{(III.17)}$$

where $\underline{E}$ and $\underline{H}$ represent the measured fields while $\underline{E}n$ is the noise in

the output. In order to obtain an estimate of $\underline{\underline{Z}}$, cross spectral relationships between each output and the two inputs are calculated as in (III.8). The impedance tensor is estimated as a function of frequency. As frequency band-averaging is used it is assumed that each element of $\underline{\underline{Z}}$ changes slowly with respect to frequency within each band.

Let the pair (A,B) represent any two components of the horizontal fields (Ex,Ey,Hx,Hy). Least-squares estimates for $\underline{\underline{Z}}$ can be calculated, multiplying the equation (III.17) by (A^*,B^*) thus producing dyadic matrix products of the field vectors and then averaging over frequency bands (Sims et al., 1971). The average power spectral matrix is defined as

$$\left[\underline{T}\ \underline{W}\right] = \begin{bmatrix} \overline{T_x W_x^*} & \overline{T_x W_y^*} \\ \overline{T_y W_x^*} & \overline{T_y W_y^*} \end{bmatrix} \qquad \text{(III.18)}$$

where $\underline{T}$ and $\underline{W}$ are vectors and the bar indicates a spectral average. Estimates of $\underline{\underline{Z}}$ are obtained from

$$\left[\underline{E}\ \underline{F}\right] = \hat{\underline{\underline{Z}}}\ \left[\underline{H}\ \underline{F}\right] \qquad \text{(III.19)}$$

where $\underline{F}=(A,B)$, is a particular choice of horizontal field components. If $\underline{F}=\underline{H}$,

$$\hat{\underline{\underline{Z}}}^H = \left[\underline{E}\ \underline{H}\right]\left[\underline{H}\ \underline{H}\right]^{-1} \qquad \text{(III.20)}$$

which minimizes in a least-squares sense the error caused by noise in the output $\underline{E}$. In other words,

$$\frac{\partial}{\partial \hat{Z}_{ij}} \left| \underline{E} - \hat{\underline{\underline{Z}}}^H \underline{H} \right|^2 = 0 \qquad \text{(III.21)}$$

with i,j=x,y.

The admittance tensor is defined as

$$\underline{H} = \underline{\underline{Y}}\ \underline{E} + \underline{H}_M \qquad \text{(III.22)}$$

A least-squares solution for $\underline{\underline{Y}}$ can be found in a similar manner as before. Multiply this definition by the electric fields to get

$$\underline{\underline{\hat{Y}}} = [\underline{H}\ \underline{E}]\,[\underline{E}\ \underline{E}]^{-1} \qquad \text{(III.23)}$$

This estimate minimizes the error caused by noise in the output $\underline{H}$, that is

$$\frac{\partial}{\partial Y_{ij}} \left| \underline{H} - \underline{\underline{\hat{Y}}}\,\underline{E} \right|^2 = 0 \qquad \text{(III.24)}$$

Therefore one ends up with

$$\underline{\underline{\hat{Z}}}^{E} = \underline{\underline{\hat{Y}}}^{-1} \qquad \text{(III.25)}$$

which is an alternative estimate of $\underline{\underline{Z}}$.

There are six least-squares solutions of the impedance tensor

$$\underline{\underline{Z}} = \begin{bmatrix} Z_{xx} & Z_{xy} \\ Z_{yx} & Z_{yy} \end{bmatrix} \qquad \text{(III.26)}$$

which are evaluated from expressions like

$$\hat{Z}_{jx} = \frac{\overline{E_j A^*}\cdot\overline{H_j B^*} - \overline{E_j B^*}\cdot\overline{H_j A^*}}{\overline{H_x A^*}\cdot\overline{H_j B^*} - \overline{H_x B^*}\cdot\overline{H_j A^*}} \qquad \text{(III.27)}$$

From the six estimators, only four are stable, provided the incident fields are not highly polarized. All estimates suffer from bias errors since measured auto-powers are always biased estimates of the signal powers. Of the stable estimates, two are biased down due to random noise on $\underline{H}$ and not biased by random noise on $\underline{E}$. The other two are biased up due to random noise on $\underline{E}$, and are not affected by random noise on $\underline{H}$ (Sims et al., 1971). In this work two estimates $\underline{\underline{\hat{Z}}}^{H}$, (III.20), and $\underline{\underline{\hat{Z}}}^{E}$, (III.25), which are biased down and up respectively, are calculated in order to specify the bounds where the unknown $\underline{\underline{Z}}$ should lie.

Homogeneously induced fields are assumed in the course of magnetotelluric analysis. This ensures that the impedance tensor does not depend on the primary source field. Some authors find this requirement too restrictive. It is accepted that the existence of fields with sufficient slow horizontal variations (Price, 1962), or linear changing horizontal fields (Dmitriev and Berdichevsky, 1979)

are sufficient for practical purposes.

Noise is defined as the fraction of the measured fields which is not homogeneously induced. So signal and noise have different origins and are therefore incoherent. It is necessary to distinguish the coherency of the noise characteristics due to its influence on bias errors. This is paramount since the ability to reduce errors in estimates of the impedance tensor depends on the recognition of noisy data sections. Non-induced noise is observed in both magnetic and electric channels. Such noise often shows impulsive characteristics. Examples are the movement of vehicles, mechanical vibration of sensors, electric fences, agricultural machines, et cetera. For instance a moving vehicle may cause noise 500m away (Clarke et al., 1983). Man-made noise is characterized by inhomogeneously induced fields. The main sources are power networks. Impulses and jumps appear as result of abrupt changes in the demand for electricity. Elsewhere (Adam et al., 1986) an onset of noise following the abrupt load after a 3min standstill on the mining industry of a region is reported. Inhomogeneously induced noise can be highly coherent (Adam et al., 1986) and therefore undetectable by coherence-related winnowing techniques.

Noise effects

The effect of noise as bias errors on impedance tensor elements can be easily visualized. It can always be assumed that for a sufficient large number of samples, the variance on the elements of $\underline{\underline{Z}}$ becomes small when compared with the bias. Stationarity of signals and noise is assumed. Concentrate on one element of $\underline{\underline{Z}}$, namely Zyx. A downward biased estimate of Zyx is obtained substituting (A,B) by (Hx,Hy) in equation (III.27) (Sims et al., 1971),

$$Z_{jk} = \frac{\overline{E_j H_k^*}\cdot\overline{H_j H_j^*} - \overline{E_j H_j^*}\cdot\overline{H_j H_k^*}}{\overline{H_k H_k^*}\cdot\overline{H_j H_j^*} - \overline{H_k H_j^*}\cdot\overline{H_k H_k^*}} \qquad \text{(III.28)}$$

But the measured fields are contaminated by noise, i.e.

$$\underline{E} = \underline{E}_s + \underline{E}_n$$
$$\underline{H} = \underline{H}_s + \underline{H}_n \qquad \text{(III.29)}$$

where subscripts "s" and "n" indicate the signal and noise contribution. Equation (III.28) is composed of auto-spectral

estimates such as HxHx and cross-spectral estimates, such as HxHy or EyHx. Using (III.29),

$$\begin{aligned} \overline{H_x H_x^*} &= \overline{H_{x_s} H_{x_s}^*} + \overline{H_{x_n} H_{x_n}^*} \\ \overline{H_x H_y^*} &= \overline{H_{x_s} H_{y_s}^*} + \overline{H_{x_n} H_{y_n}^*} \\ \overline{E_y H_x^*} &= \overline{E_{y_s} H_{x_s}^*} + \overline{E_{y_n} H_{x_n}^*} \end{aligned} \qquad \text{(III.30)}$$

As signal and noise are assumed incoherent it remains to investigate three possible cases:

1- Noise exists in auto-powers only. This will be referred to as the incoherent noise case. In this fortunate case, noise components are incoherent and noise estimates as $\overline{Hx_n Hy_n^*}$ and $\overline{Ey_n Hx_n^*}$ vanish. Only noise auto-powers remain, like $\overline{Hx_n Hy_n^*}$. Therefore the impedance tensor estimate $\hat{Z}yx$ is biased by noise in the auto-powers. In this case a bias-reduced estimate could be calculated with an iterative scheme (Kao and Rankin, 1977).

2- Input noise components, Hx_n and Hy_n, are coherent. In this case estimates like $\overline{Hx_n Hy_n^*}$ do not vanish. The estimate $\hat{Z}yx$ is then biased by auto-powers and by input cross-powers.

3- En and Hn are coherent and so are the input noise components. Now none of the noise powers vanish. Therefore $\hat{Z}yx$ is biased not only by the auto-powers but also by all noise cross-powers.

Elsewhere (Kroger et al., 1983) bias errors were estimated using the signal-to-noise ratio and a noise impedance. Case 2, i.e. coherent input noise, may give rise to bias coupling effects (Pedersen and Svennekjaer, 1984). When this effect occurs, the least-squares analysis tend to magnify the diagonal elements of $\hat{\underline{\underline{Z}}}$. The more coherent the input channels are, the stronger this effect may be.

Coherence functions

An indication of the correlation between input and output is obtained using the predicted coherence function (III.12). It gives the cross-correlation between the electric field calculated through (III.17) and the measured field. Although this measure is widely used, levels of "acceptable coherence" vary widely among authors (Vozoff, 1972).

In section III.4.2 inputs and output were expressed by x_i=1,2,3. Such notation is convenient in a number of situations since it permits the auto- and cross-spectral functions to be expressed in a concise form as, e.g., S_{22} and S_{31}. Also coherence functions appear in a similar form as in (III.12). Accordingly the

magnetotelluric relations can also be expressed in a concise form if the field components are designated by numbers. The basic magnetotelluric relation (III.17) can expressed as

$$\langle 3 \rangle = Z_{3x} \langle 1 \rangle + Z_{3y} \langle 2 \rangle$$
$$\langle 4 \rangle = Z_{4x} \langle 1 \rangle + Z_{4y} \langle 2 \rangle \qquad \text{(III.31)}$$

Using this convention, spectral density functions may also be expressed in a concise form such as as, e.g., HxHx->S_{11} and ExHy->S_{32}. Also for the sake of simplifying the notation, $\hat{\underline{\underline{Z}}}$ will designate any of the two least-squares estimates, $\hat{\underline{\underline{Z}}}^{u}$ or $\hat{\underline{\underline{Z}}}^{t}$, while $\underline{\eta}$ will designate an output noise term.

In relation (III.17) there are two measured fields, $\underline{E}$ and $\underline{H}$, which are made of unknown proportions of signal and noise (III.29) and one, also unknown, output noise term. This last term conveys the information on the combined noise in all measurements. Therefore the predicted noise in all measurements is given by an expression similar to (III.13),

$$\hat{\underline{\eta}} = \underline{E} - \hat{\underline{\underline{Z}}}\,\underline{H} \qquad \text{(III.32)}$$

Its auto-spectrum is given by

$$|\overline{\hat{\eta}_l}|^2 = |\overline{E_l - \hat{Z}_{lu} H_u - \hat{Z}_{lj} H_j}|^2 \qquad \text{(III.33)}$$

with l=x,y. From the definition (III.12), the predicted coherence is expressed as

$$\hat{\gamma}^2_{i\,12} = 1 - \frac{|\overline{\hat{\eta}_l}|^2}{\hat{S}_{ii}} \qquad \text{(III.34)}$$

with l=x,y when i=3,4. Depending on the output, four predicted coherences can be estimated $\hat{\gamma}^2_{3\,12}$, $\hat{\gamma}^2_{4\,12}$, $\hat{\gamma}^2_{3\,34}$ and $\hat{\gamma}^2_{4\,34}$. Other relevant coherence functions follow from the definitions (III.11) and (III.14).

All coherence functions are biased estimators. The bias is more severe the lower the number of degrees of freedom. The following approximation can be used to calculate the bias in the ordinary coherence function (Carter et al., 1973),

$$B(\hat{\gamma}^2_{ij}) = \frac{1}{N}\left(1-\gamma^2_{ij}\right)\left(1+2\frac{\gamma^2_{ij}}{N}\right) \qquad \text{(III.35)}$$

where γ^2_{ij} is the theoretical value and N the number of degrees of freedom. The bias is estimated substituting the estimated ordinary coherence in place of the theoretical value in (III.35) (Nuttall and Carter, 1976). Therefore an unbiased estimate of the ordinary coherence is obtained making $\hat{\gamma}^2_{ij} \rightarrow \hat{\gamma}^2_{ij} - B(\hat{\gamma}^2_{ij})$.

A good approximation for the predicted coherence function is given by the maximum likelihood estimate (White, 1973)

$$\tilde{\gamma}^2_{ijk} = \frac{\hat{\gamma}^2_{ijk} - \frac{2}{N}}{1-\frac{2}{N}} \qquad \text{(III.36)}$$

The bias is obviously

$$B(\hat{\gamma}^2_{ijk}) = \hat{\gamma}^2_{ijk} - \gamma^2_{ijk}$$

or, substituting the true value by the maximum likelihood estimate,

$$B(\hat{\gamma}^2_{ijk}) = 2\left(1-\hat{\gamma}^2_{ijk}\right)/(N-2) \qquad \text{(III.37)}$$

The bias in the predicted coherence function estimated from (III.37) is illustrated in figure III.4 for the range of degrees of freedom and coherence values used in this section. This figure suggests that for $\hat{\gamma}^2_{ijk} \geq 0.85$ bias errors are always less than 10% for the entire range of degrees of freedom. Once estimates for both the ordinary and predicted coherences are bias corrected, the partial coherence estimates are also bias corrected by definition (III.14). All coherence function estimates used in this chapter are bias-corrected.

Estimation of $\underline{\underline{Z}}$

The estimation of $\underline{\underline{Z}}$ is done using expressions like (III.28) which are expressed in terms of measured quantities, which in turn are made of unknown proportions of signal and noise (III.29). The combined noise of all measurements is conveyed by $\underline{\eta}$ estimated through (III.32). The smaller is $\underline{\eta}$ the less biased the estimate $\underline{\underline{Z}}$ is expected to be. The predicted coherence $\hat{\gamma}^2_{ijk}$, (III.34), gives a measure of the noise power normalized to the output power, thus

BIAS ON PRED. COHER.

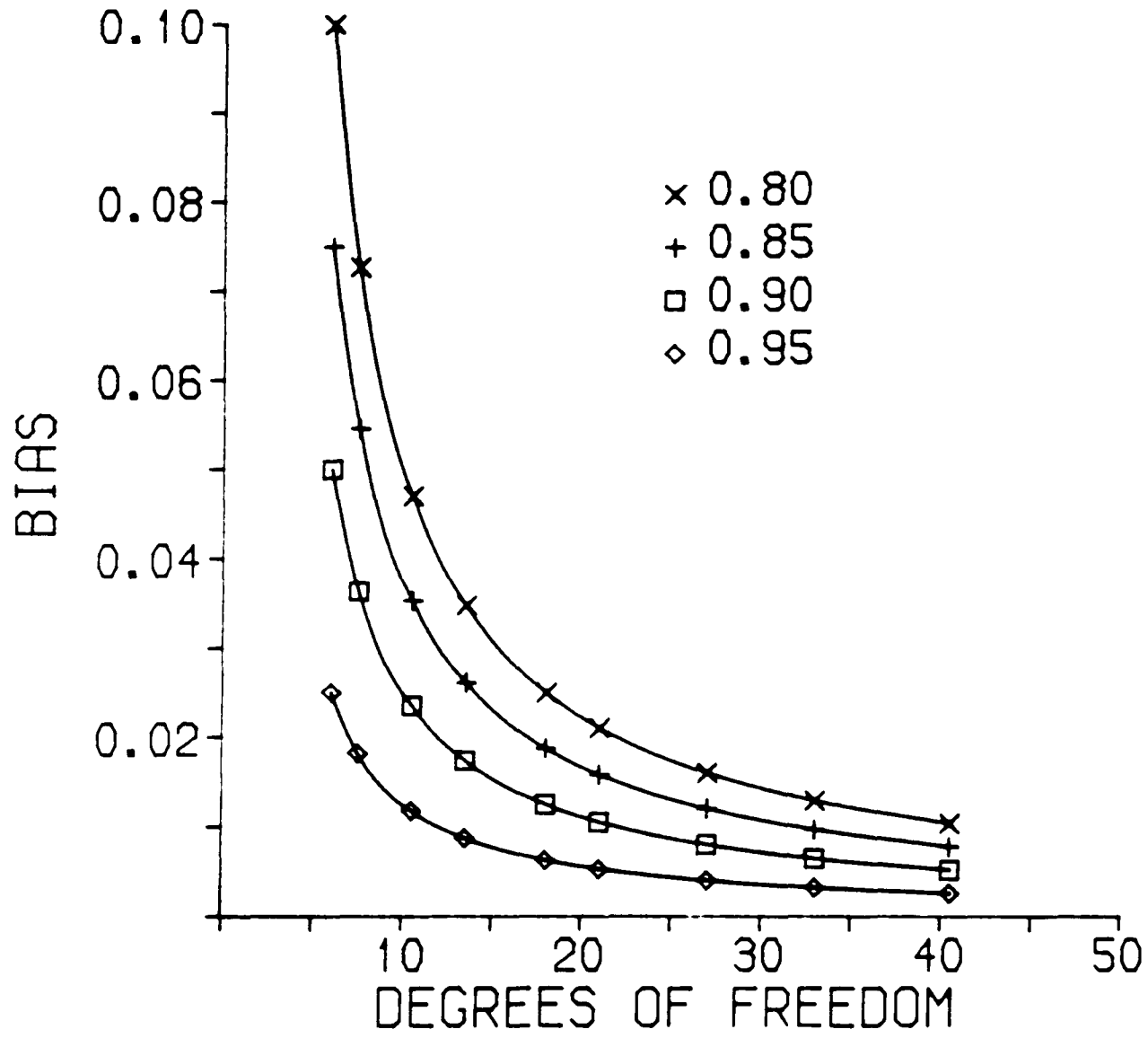

Figure III.4. Bias on estimates of multiple coherence function assuming $\tilde{\gamma}^2_{ijk}$ as an unbiased estimate of γ^2_{ijk}.

providing a quantitative measure which can be used to select band averaged values, or realizations for short. The selected realizations are expected to produce less biased estimates of $\underline{\underline{Z}}$. These estimates should provide accurate solutions since the variance can be made as small as desired by using increasingly longer data series.

Selection of data realizations is done either using predicted coherence estimates only, or in combination with other coherence functions. It is worthwhile examining the coherence characteristics of the whole data set. This can be done with aid of histograms of the predicted coherence. For each frequency band a histogram is produced, each one composed of 10 accumulators counting values of $\hat{\gamma}^2_{ijk}$, which fall in the intervals

[0.0,0.1), [0.1,0.2), [0.2,0.3), [0.3,0.4), [0.4,0.5),
[0.5,0.6), [0.6,0.7), [0.7,0.8), [0.8,0.9), [0.9,1.0] (III.38)

Figure III.5 shows the distribution of $\hat{\gamma}^2_{134}$, $\hat{\gamma}^2_{234}$, $\hat{\gamma}^2_{312}$ and $\hat{\gamma}^2_{412}$ clockwise from the top left corner, for the whole data set and decades 4 and 5. Decade 4 histograms show distributions skewed towards low values (->0.0) for the first few low period bands and, conversely, distributions skewed towards higher values (->1.0) for the last few bands. Decade 5 histograms show distributions more skewed towards higher values reflecting better signal-to-noise ratios. In figure III.5 the x-axis is divided into the 20 equally spaced frequency bands covering decades 4 and 5. All figures of this chapter follow this layout for the x-axis, unless otherwise specified. The bands are shown ordered by period, so the first band along the x-axis is band 10 of decade 4 while band 1 of decade 5 is the 20th. This convention for the x-axis can be illustrated using the 10 bands of decade 4:

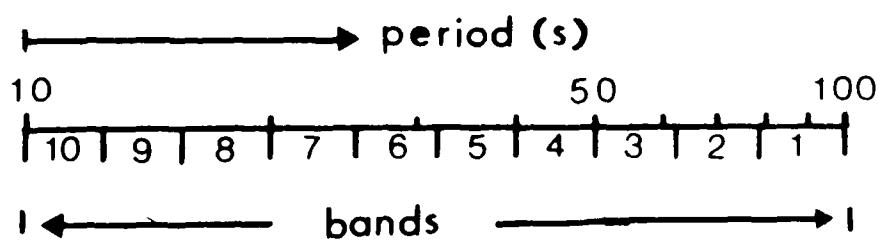

Decade 5 bands follow this same ordering.

The spectral quantities associated with the accepted realizations are treated independently. The spectral quantities derived from the accepted realizations from the data set are stacked. Estimates of $\underline{\underline{Z}}$ are then estimated from the stacked values. The obtained $\hat{\underline{\underline{Z}}}$ values are referred to as stacked estimates. The remainder of this section is devoted to a discussion on calculating stacked estimates of $\underline{\underline{Z}}$. Acceptance criteria based on coherence

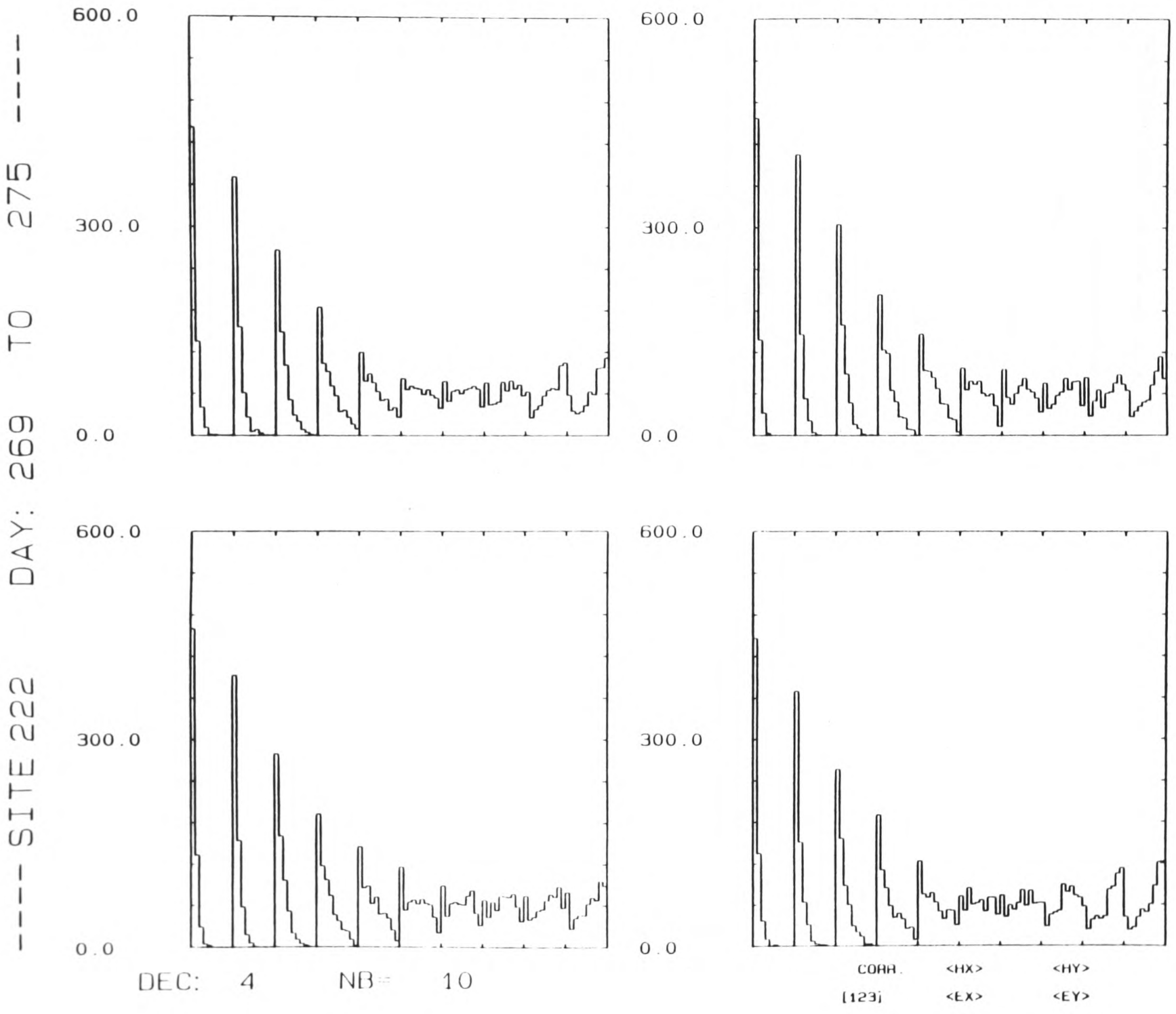
600.0
300.0
0.0
600.0
300.0
0.0
269 TO 275 ----
---- SITE 222 DAY
600.0
300.0
0.0
600.0
300.0
0.0
DEC: 4 NB= 10
CORR. <HX> <HY>
[123] <EX> <EY>

Figure III.5.a. Distribution of $\hat{\gamma}_{ijk}$ for each band, decade 4. Clockwise from the top left box one can see $\hat{\gamma}^2_{134}$, $\hat{\gamma}^2_{234}$, $\hat{\gamma}^2_{412}$, and $\hat{\gamma}^2_{312}$. There is one histogram at each band with 10 accumulators for values that are in the intervals [0.0,0.1), [0.1,0.2), ..., [0.9,1.0].

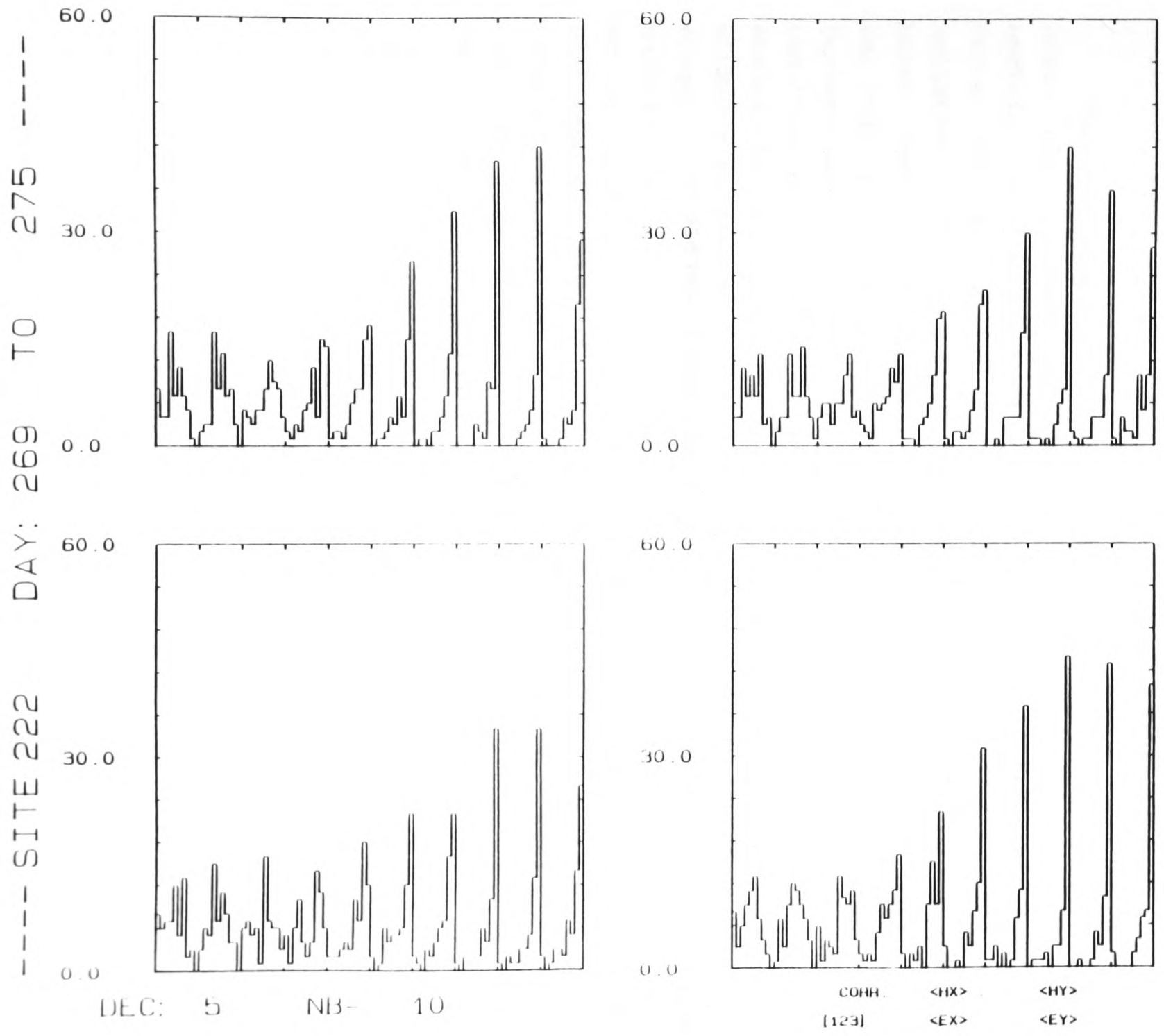
---- SITE 222 DAY 269 TO 275 ----
60.0
30.0
0.0
60.0
30.0
0.0
60.0
30.0
0.0
60.0
30.0
0.0
DEC: 5 NB- 10
COHR. <HX> <HY>
[123] <EX> <EY>

Figure III.5.b. Distribution of $\hat{\sigma}^2_{ijk}$ at each band, decade 5.

tests are employed and discussed in the light of their relative bias contributions. Coherence tests are based on a pre-set threshold, γ_t, either for the predicted coherence alone or in combination with other coherence functions. A realization is accepted if it has a predicted coherence, or a combination of coherence functions above the threshold. In order to have a relative assessment of bias errors within each coherence test two thresholds are used: $\gamma_t = 0.85, 0.95$. Only the off-diagonal elements of the impedance tensor, Zxy and Zyx, are chosen to illustrate all results.

Rejection tests for spectral stacking

The most widely used acceptance criterion in magnetotellurics uses only the predicted coherence and checks whether it is above a certain limit, as proposed 20 years ago (Swift, 1967). Since a high value for the predicted coherence does not necessarily lead to reliable estimates, one may expect to refine this criterion using other coherence functions. For instance, input-coherent noise data may require setting an upper threshold for the ordinary coherence between input channels, in order to limit coupling effects (Pedersen and Svennekjaer, 1984). Also partial coherences may be used to ensure that the amount of coherent signal in the off-diagonal tensor elements is greater than the corresponding signal in the diagonal elements. This may be done by ensuring that the off-diagonal partial coherence is greater than that of the diagonal derived one, or by some sort of geometrical mean of coherence functions. A USGS-type geometrical mean between predicted and off-diagonal coherence functions (Stanley and Frederick, 1979) and also a phasor criterion (Word et al., 1970), where two geometrical means, one for each output, are combined together are also considered.

Elsewhere (Pedersen and Svennekjaer, 1984) it is suggested that one could choose a rejection criterion based on the ratio

$$\left(1 - \hat{\gamma}^2_{ijk}\right) / \left(1 - \hat{\gamma}^2_{jk}\right)$$

This ratio is unstable for the data set considered. Values of this ratio range from 0.0027 to 55.0 for decade 4 and from 0.0017 to 6.03 for decade 5. As the behaviour of this ratio was found to be unsatisfactory, it was not used as a rejection criterion.

Assume i and j as outputs and o and d as the off-diagonal and diagonal inputs respectively. The five acceptance criteria, or tests, used are the following:

Test 1. $\hat{\gamma}^2_{io} \geq \gamma_t$

Test 2. $\hat{\gamma}^2_{ido} \geq \gamma_t$ and $\hat{\gamma}^2_{ied} > \hat{\gamma}^2_{ido}$
Test 3. $\hat{\gamma}^2_{ido} \geq \gamma_t$ and $\hat{\gamma}^2_{do} > \gamma_{t'}$
Test 4. $(\hat{\gamma}^2_{ido} \cdot \hat{\gamma}^2_{ie.d})^{1/2} \geq \gamma_t$
Test 5. $(\hat{\gamma}^2_{ido} \cdot \hat{\gamma}^2_{ie.d} \cdot \hat{\gamma}^2_{jdo} \cdot \hat{\gamma}^2_{je.d})^{1/4} \geq \gamma_t$
where γ_t and $\gamma_{t'}$ are thresholds for the predicted and ordinary coherences.

These tests are applied differently for the two bias cases. Assume test 1 and the downward biased case (III.31). If $\hat{\gamma}^2_{312} \geq \gamma_t$ the spectral density functions related to the first equation of (III.31) are stacked. This is done independently of $\hat{\gamma}^2_{412} \geq \gamma_t$ and, of course, the converse is also true. This is not so for the upward biased case. Since the admittance tensor is estimated it is necessary to invert it in order to get the impedance. Therefore in this case tests 1 to 4 have to be satisfied by both outputs simultaneously before the spectral density functions are stacked. This is not a problem for test 5 since the two outputs are tested simultaneously.

Results obtained when using the above tests are presented below. Both upward and downward biased estimates are shown together with their 68% level confidence intervals. So if $\hat{Z}^u_{xy}$ and $\hat{r}^u_{xy}$ are the upward biased estimate and its corresponding random error while $\hat{Z}^d_{xy}$ and $\hat{r}^d_{xy}$ correspond to the downward case, both $\hat{Z}^u_{xy}+\hat{r}^u_{xy}$ and $\hat{Z}^d_{xy}-\hat{r}^d_{xy}$ are used to provide the bounds where the unknown value of Z_{xy} should lie. In addition to the real and the imaginary parts of the off-diagonal tensor elements for both bias cases, the number of estimates of both auto- and cross-spectral functions stacked together with the final, i.e. calculated from the stacked values, predicted coherences are also presented. A single threshold is used for the ordinary coherence, $\gamma_{t'}=0.5$.

Test 1. Figure III.6 shows the results obtained using test 1. It is easy to see a reduction in bias at the higher threshold 0.95 when compared with 0.85. Since the number of estimates drop, some bands are missing or produce less stable results when the higher threshold is used. The resultant predicted coherence is lower for the longer periods of decade 4 although it is where the higher number of accepted estimates is found.

Test 2. In test 2 it is required not only that the predicted coherence is above a threshold, but also that the off-diagonal partial coherence is greater than the diagonal partial coherence. Figure III.7 shows the results for test 2. As in test 1 it is easy to see a reduction in bias when the higher threshold is used. Results from test 1 and 2 are similar, the latter showing slightly

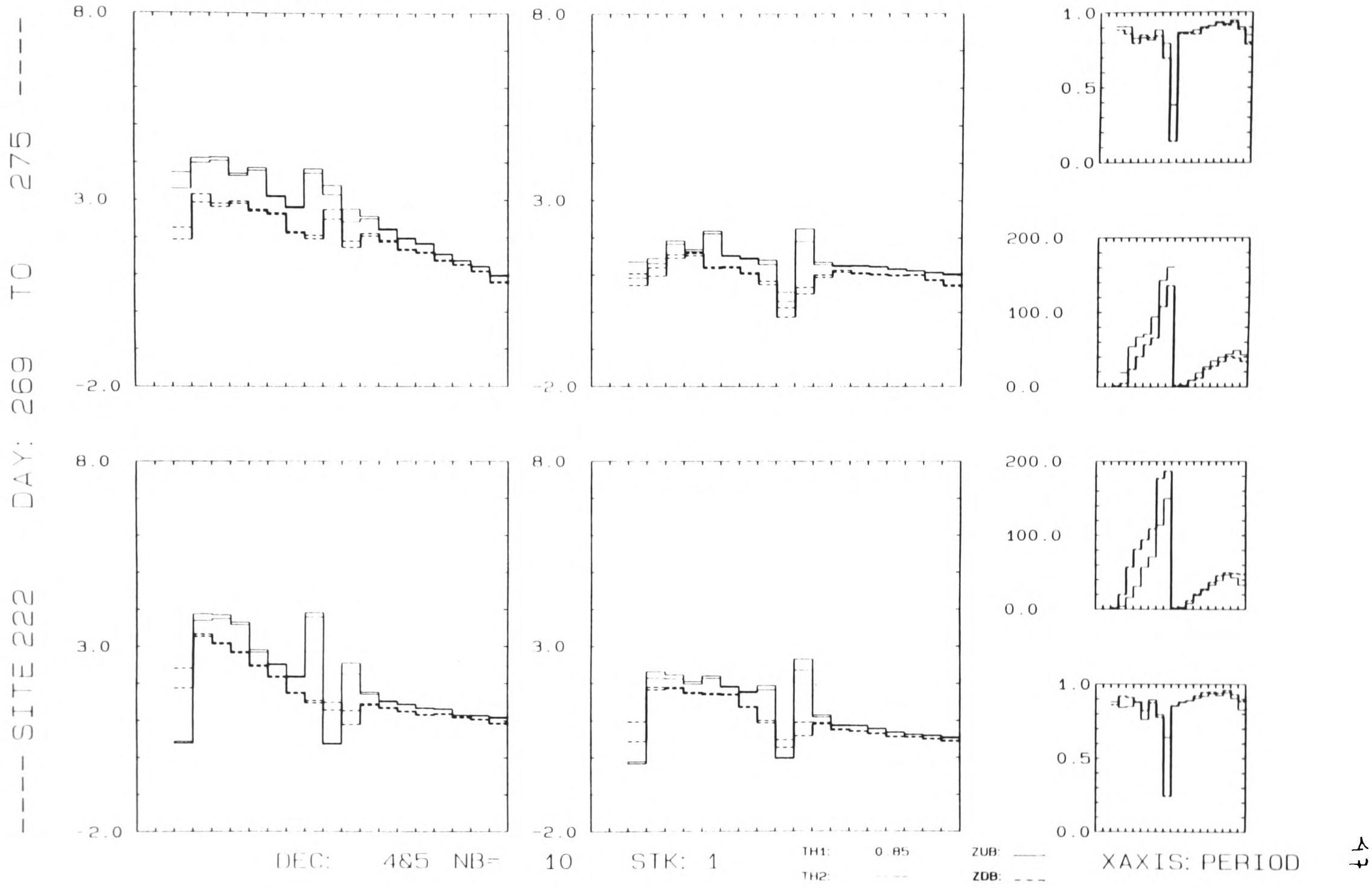
8.0
3.0
-2.0
8.0
3.0
-2.0
1.0
0.5
0.0
200.0
100.0
0.0
1.0
0.5
0.0
--- SITE 222 DAY 269 TO 275 ---
DEC: 4&5 NB= 10 STK: 1
TH1: 0.85
TH2:
ZUB:
ZDB:
XAXIS: PERIOD

Figure III.6.a. Estimates of Zxy and Zyx using test 1 for a threshold γ_t =0.85. Both upward (heavier lines) and downward (lighter lines) biased cases are shown together with the associated 68% random errors. Estimates are shown as defining the boundaries where the true values should lie. Thus boxes show the upward biased estimate plus its random error and the downward biased estimate less its random error. Top row, left to right there are Re(Zxy) and Im(Zyx), stacked predicted coherences (upper box) and number of estimates (lower box). Bottom row, left to right, there are Re(Zyx) and Im(Zyx), number of estimates (upper box) and stacked predicted coherences (lower box). Ordinates are linear and abscissae are divided into 20 equally log-spaced bands covering decades 4 and 5. Bands are ordered from left to right in increasing order of period. $\hat{\underline{\underline{Z}}}$ is expressed in mV/(nT.km). Unless specified otherwise, all figures of this chapter follow this same layout.

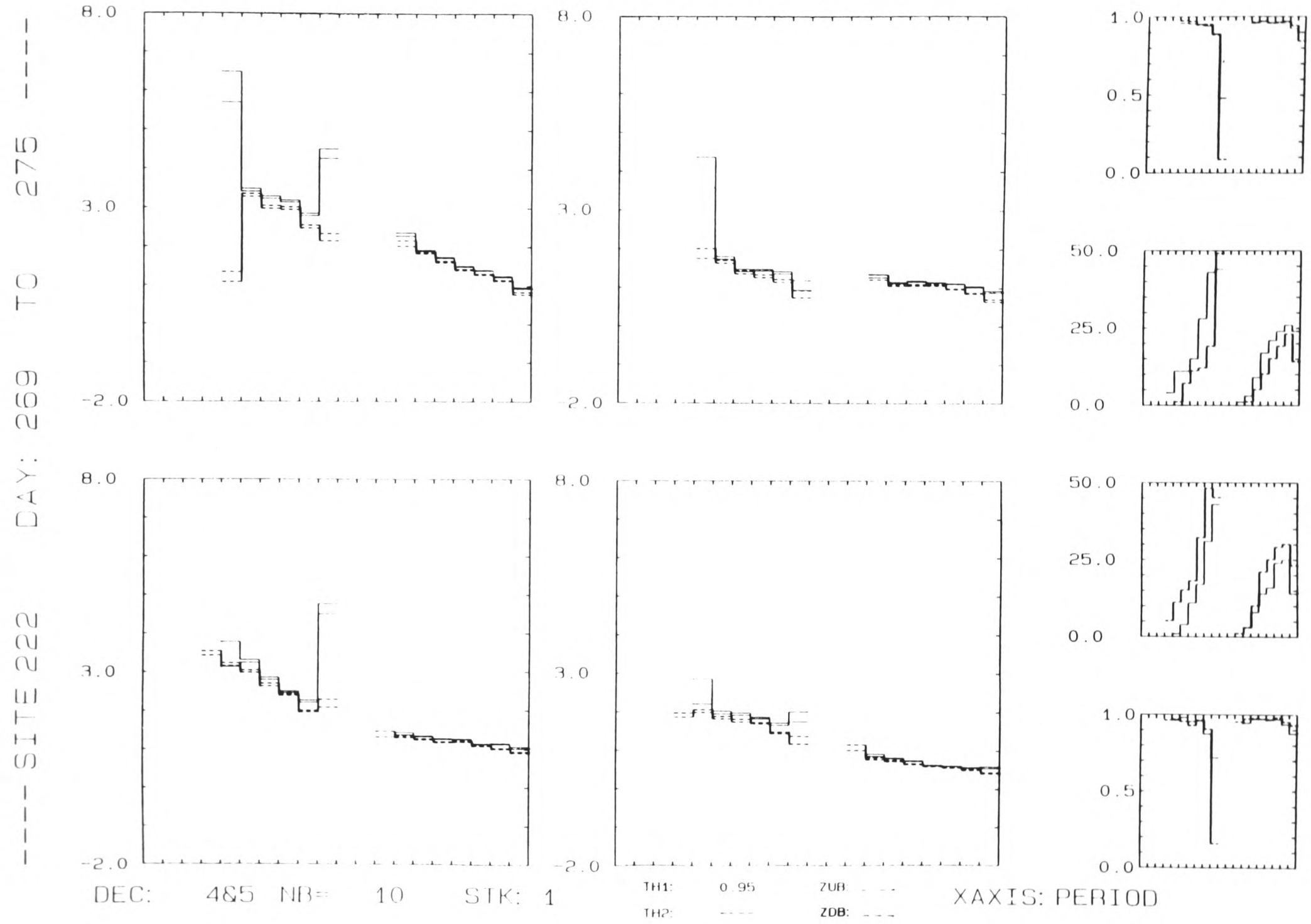
8.0
3.0
-2.0
8.0
3.0
-2.0
1.0
0.5
0.0
50.0
25.0
0.0
1.0
0.5
0.0
269 TO 275 ----
SITE 222 DAY
DEC: 4&5 NB= 10 STK: 1
TH1: 0.95 ZUB:
TH2: ZDB:
XAXIS: PERIOD

Figure III.6.b. Estimates of Zxy and Zyx, test 1 for a threshold of γ_t=0.95.

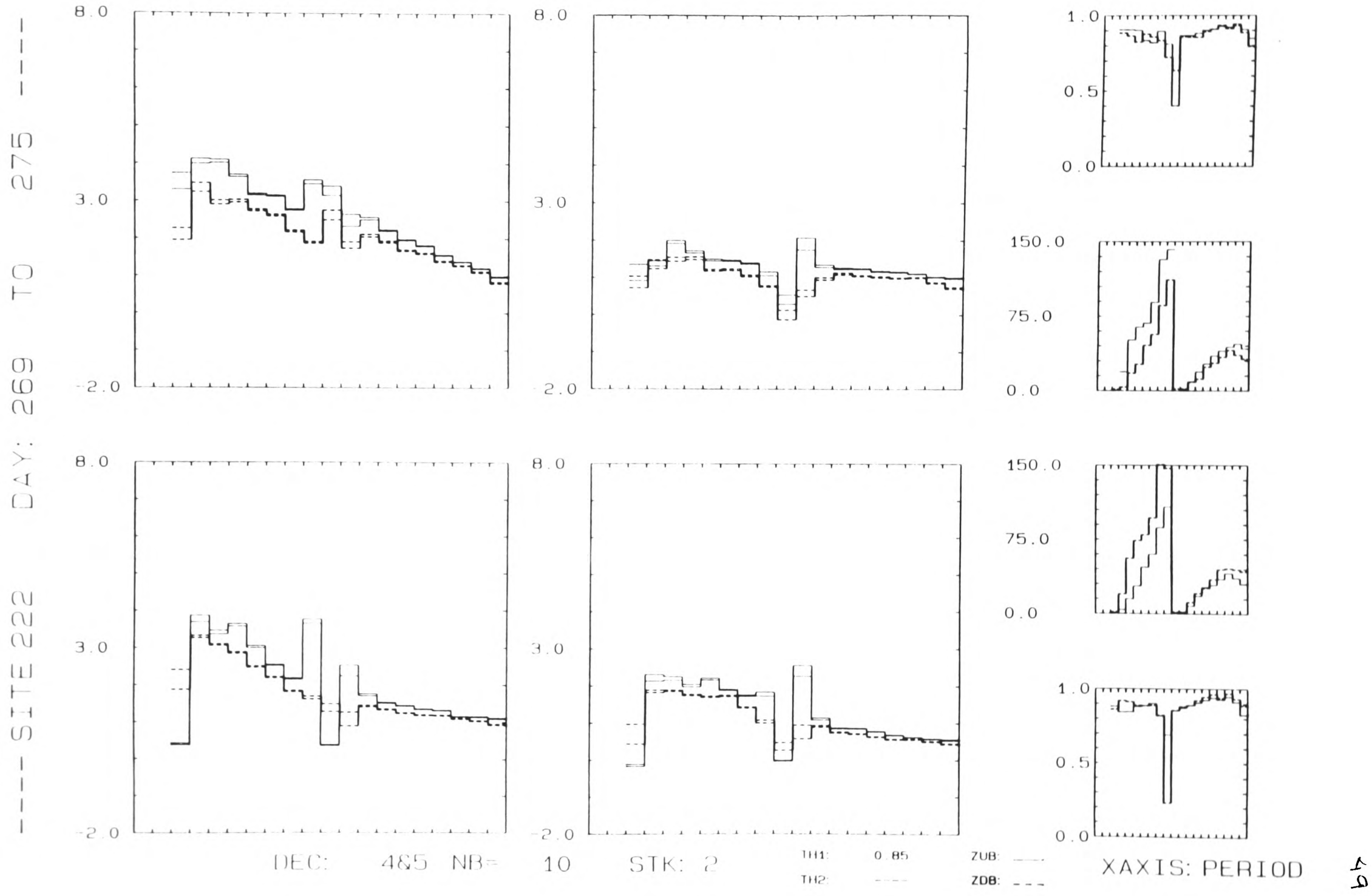
269 TO 275 ----
--- SITE 222 DAY
8.0
3.0
-2.0
8.0
3.0
-2.0
1.0
0.5
0.0
150.0
75.0
0.0
8.0
3.0
-2.0
8.0
3.0
-2.0
1.0
0.5
0.0
DEC: 485 NB= 10 STK: 2
TH1: 0.85
TH2:
ZUB:
ZDB:
XAXIS: PERIOD

Figure III.7.a. Estimates of Zxy and Zyx, test 2 for δ_t=0.85.

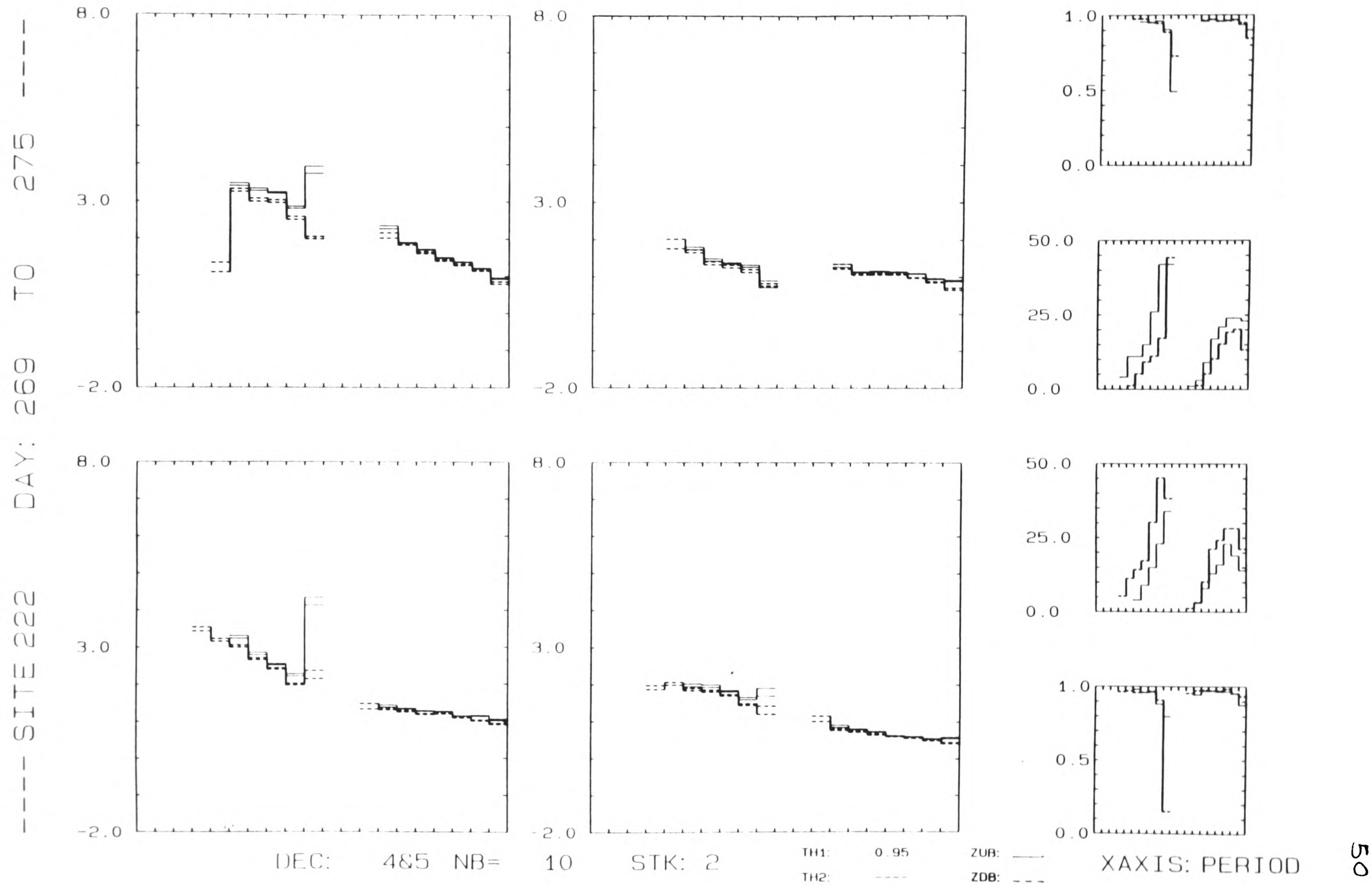
---- SITE 222 DAY 269 TO 275 ----
8.0
3.0
-2.0
8.0
3.0
-2.0
1.0
0.5
0.0
50.0
25.0
0.0
8.0
3.0
-2.0
8.0
3.0
-2.0
1.0
0.5
0.0
DEC: 4&5 NB= 10 STK: 2
TH1: 0.95
TH2:
ZUB:
ZDB:
XAXIS: PERIOD

Figure III.7.b. Estimates of Zxy and Zyx, test 2 for $\gamma_t = 0.95$.

less bias at some bands. In test 2, resultant predicted coherences tend to be higher than when using test 1.

Test 3. Two simultaneous thresholds are required for test 3. The threshold for the ordinary coherence is fixed at $\gamma_t=0.5$. As can be seen in figure III.8, test 3 does not improve results when compared with results from tests 1 and 2. Bias in test 3 tends to be greater than for those two tests. Since test 3 is more restrictive than tests 1 and 2, there are fewer estimates. It can be said that test 3 is not efficient in rejecting realizations which contribute significantly to bias errors.

Test 4. Results obtained when test 4 is applied are in figure III.9. When test 4 is used, bias is reduced in comparison to the previous tests. It appears that this test does reject some noisy estimates which tests 1, 2 and 3 fail to detect. Since there are fewer estimates, there are more bands with no results.

Test 5. The results obtained using test 5 are shown in figure III.10. The use of this test does not improve results when compared with tests 1, 2 and 4. Although it shows less bias than tests 1 and 2 for the lower threshold, the fewer number of estimates increase random errors and induce more scatter.

So far the bounds for the off-diagonal elements of the impedance tensor have been used for the comparative analysis of the performance of the rejection tests. It is evident that at some stage during the course of MT data analysis a single estimate must be obtained at each band. One such estimate can be derived by weighting the two biased estimates using the variances (Beamish, 1986a)

$$\hat{Z}_{\ell m} = \omega^{\mu}_{\ell m}\,\hat{Z}^{\mu}_{\ell m} + \omega^{d}_{\ell m}\,\hat{Z}^{d}_{\ell m} \qquad \text{(III.39)}$$

where

$$\omega^{(\mu;d)}_{\ell m} = \left(\hat{\pi}^{(\mu;d)}\right)^2 \Big/ \left[\left(\hat{\pi}^{\mu}_{\ell m}\right)^2 + \left(\hat{\pi}^{d}_{\ell m}\right)^2\right]$$

with a normalized error

$$\hat{\varepsilon}_{\ell m} = \left(\hat{Z}^{\mu}_{\ell m} + \hat{\pi}^{\mu}_{\ell m} + \hat{Z}^{d}_{\ell m} + \hat{\pi}^{d}_{\ell m}\right) \Big/ \left(2\,\hat{Z}_{\ell m}\right) \qquad \text{(III.40)}$$

at each band.

The performance of tests 1, 2 and 4 can be compared using the

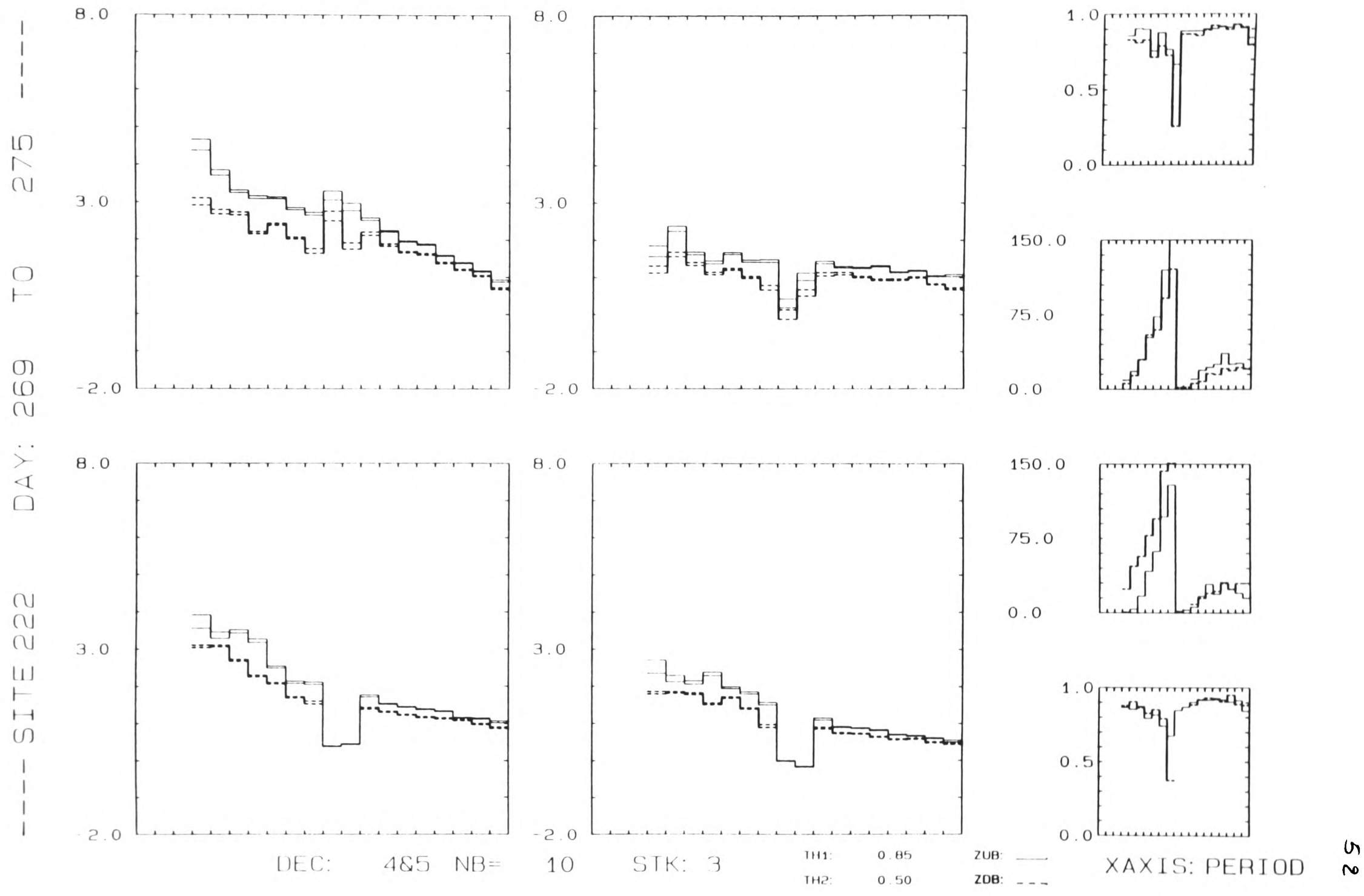
269 TO 275 ----
---- SITE 222 DAY
8.0
3.0
-2.0
8.0
3.0
-2.0
1.0
0.5
0.0
150.0
75.0
0.0
8.0
3.0
-2.0
8.0
3.0
-2.0
1.0
0.5
0.0
DEC: 4&5 NB= 10 STK: 3
TH1: 0.85
TH2: 0.50
ZUB:
ZDB:
XAXIS: PERIOD

Figure III.8.a. Estimates of Zxy and Zyx, test 3 for γ_t=0.85, $\gamma_{t'}$=0.5.

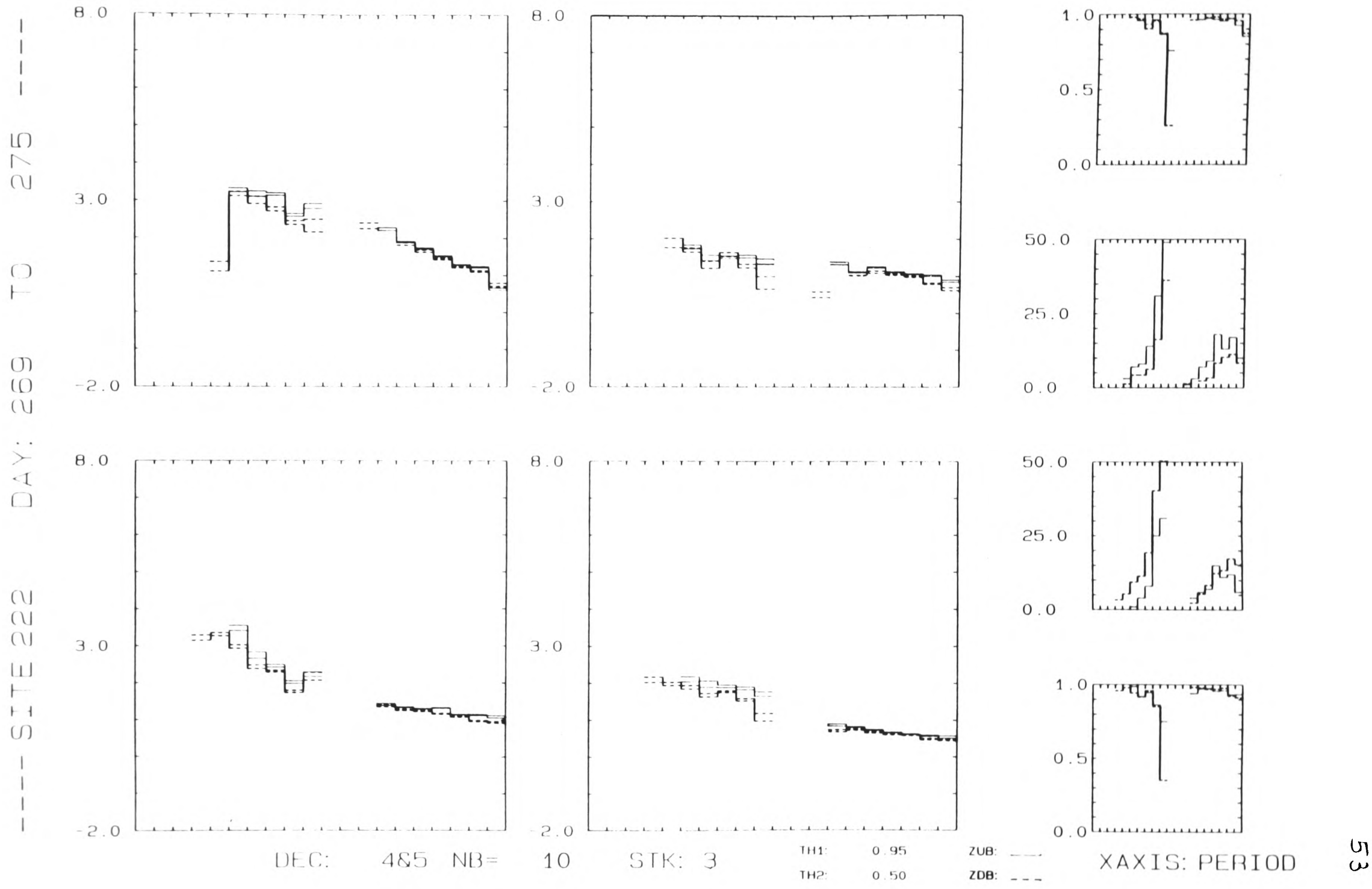
--- STE 222 DAY 269 TO 275 ---
8.0
3.0
-2.0
8.0
3.0
-2.0
1.0
0.5
0.0
50.0
25.0
0.0
1.0
0.5
0.0
DEC: 4&5 NB= 10 STK: 3
TH1: 0.95
TH2: 0.50
ZUB:
ZDB:
XAXIS: PERIOD

Figure III.8.b. Estimates of Zxy and Zyx, test 3 for σ_t=0.95, $\sigma_{t'}$=0.5.

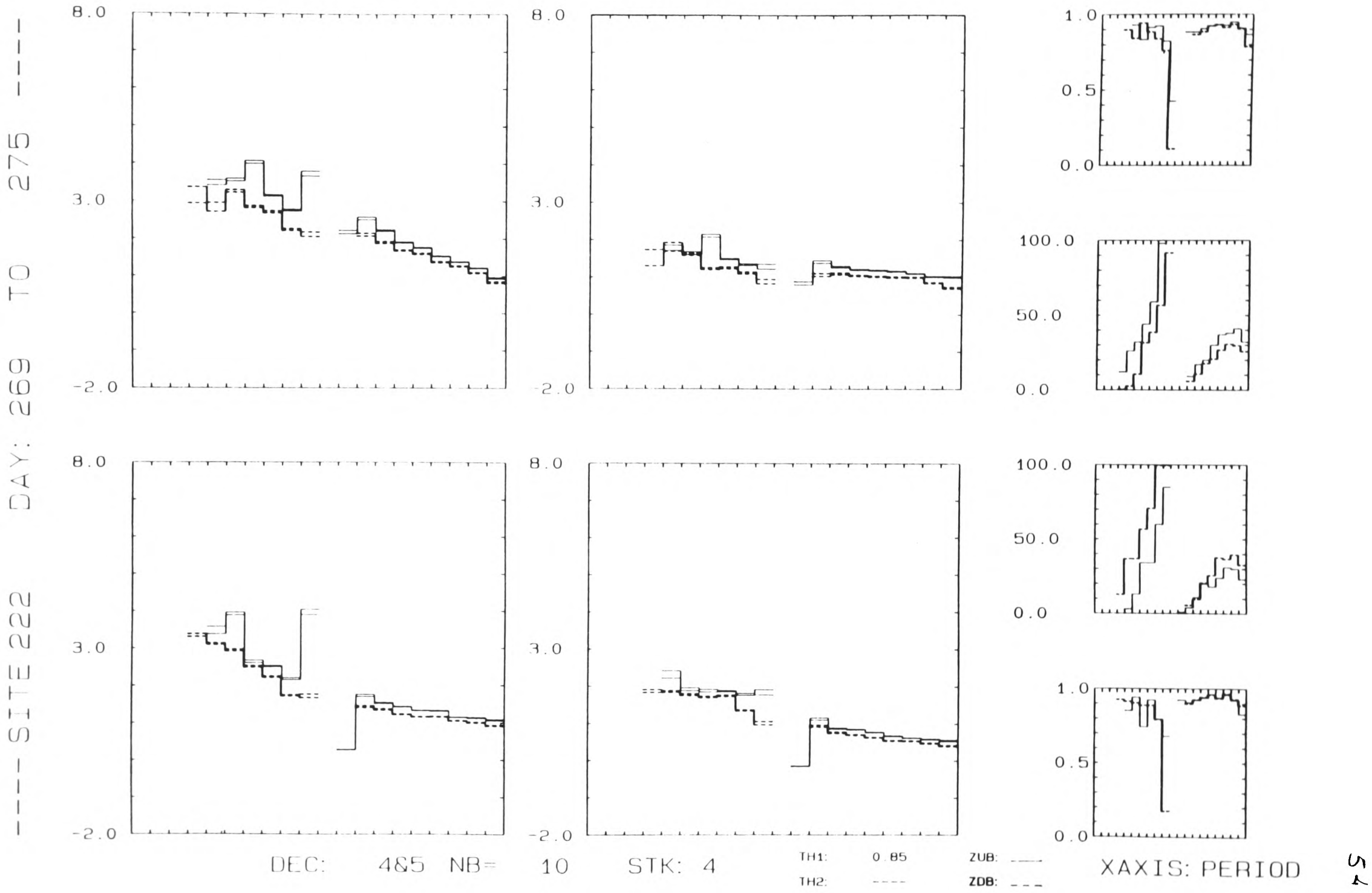
8.0
3.0
-2.0
8.0
3.0
-2.0
1.0
0.5
0.0
100.0
50.0
0.0
8.0
3.0
-2.0
8.0
3.0
-2.0
1.0
0.5
0.0
100.0
50.0
0.0
--- SITE 222 DAY 269 TO 275 ---
DEC: 4&5 NB= 10 STK: 4
TH1: 0.85
TH2:
ZUB:
ZDB:
XAXIS: PERIOD

Figure III.9.a. Estimates of Zxy and Zyx, test 4 for γ_t=0.85.

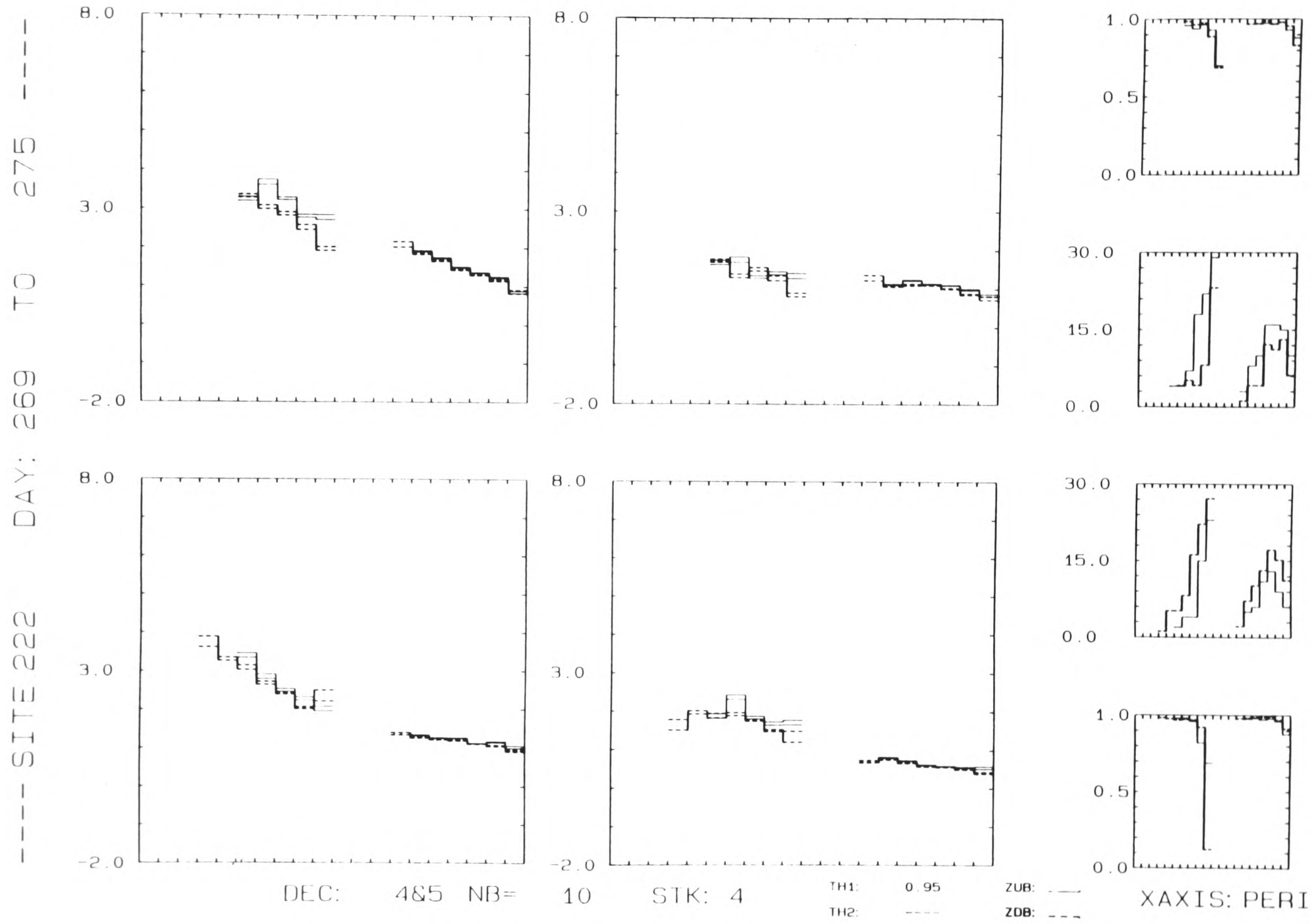
8.0
3.0
-2.0
8.0
3.0
-2.0
1.0
0.5
0.0
30.0
15.0
0.0
1.0
0.5
0.0
---- SITE 222 DAY 269 TO 275 ----
DEC: 4&5 NB= 10 STK: 4
TH1: 0.95
TH2:
ZUB:
ZDB:
XAXIS: PERIOD

Figure III.9.b. Estimates of Zxy and Zyx, test 4 for δ_t=0.95.

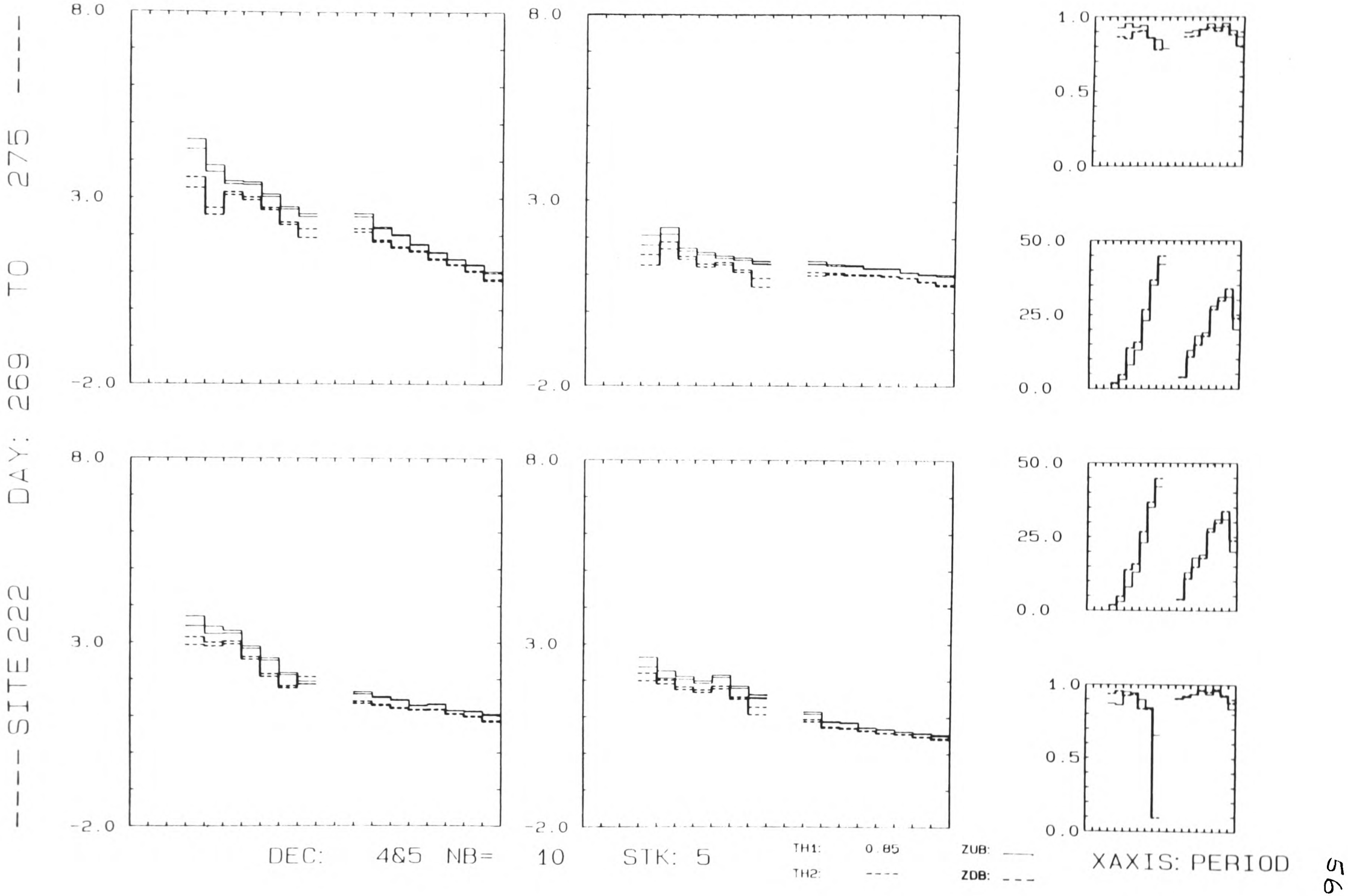
--- SITE 222 DAY 269 TO 275 ---
8.0
3.0
-2.0
8.0
3.0
-2.0
1.0
0.5
0.0
50.0
25.0
0.0
8.0
3.0
-2.0
1.0
0.5
0.0
DEC: 4&5 NB= 10 STK: 5
TH1: 0.85
TH2:
ZUB:
ZDB:
XAXIS: PERIOD

Figure III.10.a. Estimates of Zxy and Zyx, test 5 for γ_t=0.85.

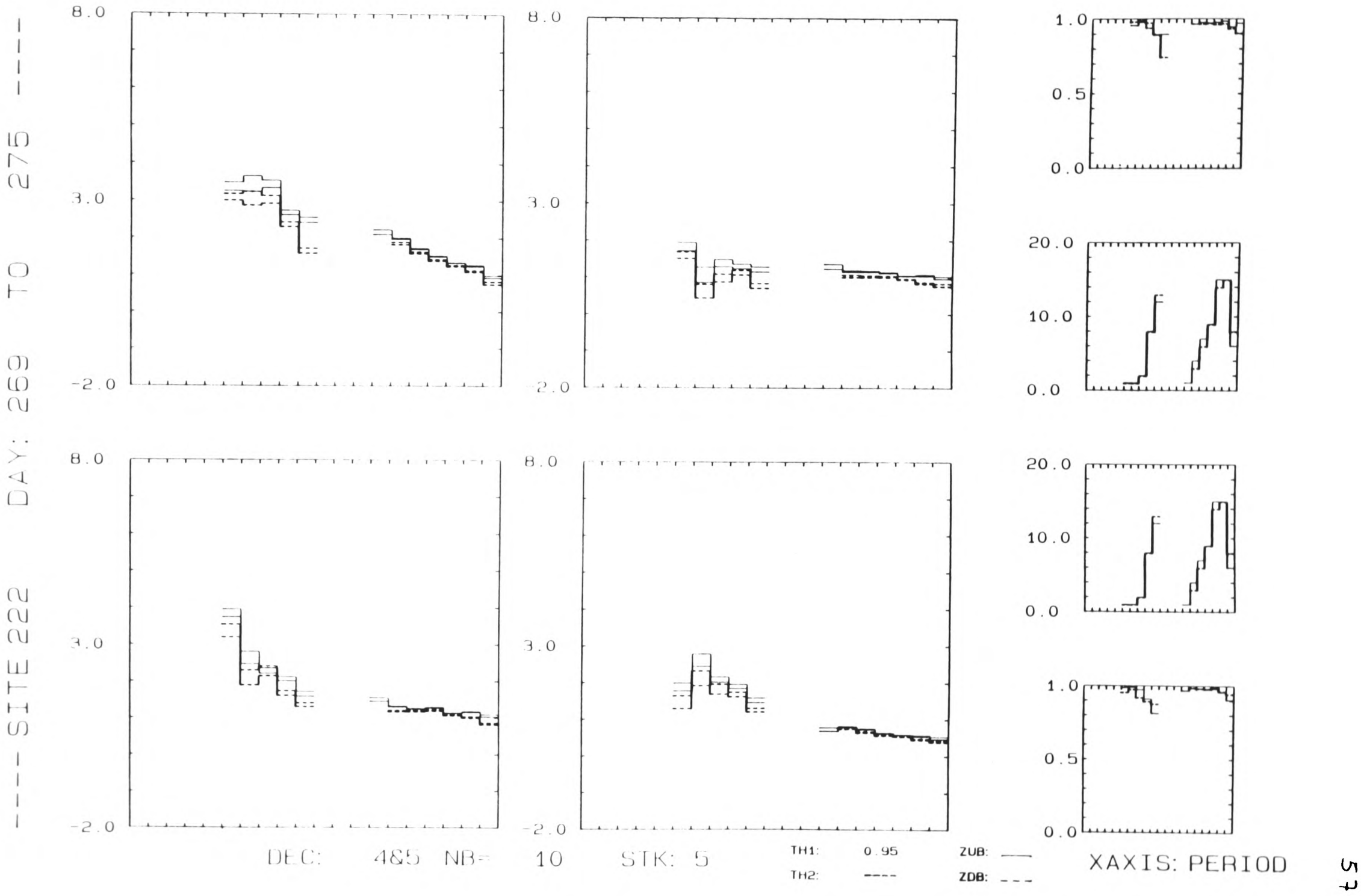
8.0
3.0
-2.0
8.0
3.0
-2.0
1.0
0.5
0.0
20.0
10.0
0.0
1.0
0.5
0.0
---- SITE 222 DAY 260 TO 275 ----
DEC: 4&5 NB= 10 STK: 5
TH1: 0.95
TH2:
ZUB:
ZDB:
XAXIS: PERIOD

Figure III.10.b. Estimates of Zxy and Zyx, test 5 for γ_t=0.95.

normalized error (III.40). As previously stated, test 4 is the test that gives the best results, although tests 1 and 2 also produce good results. Here best and good are used in the sense of: (1) reducing the bias by rejecting noisier data segments; and (2) stability in frequency, noting that the frequency bands are completely independent. Figure III.11 shows the values of $\hat{\varepsilon}_{\rho m}$ for the off-diagonal elements, using the lower threshold 0.85. In this figure the real and imaginary parts of the normalized errors are shown following the same layout of the previous figures of this section. Observe that test 4 provides error levels which are almost always below those of tests 1 and 2. Considering both real and imaginary parts, error levels amount to 10% on average for test 4. Differences in error levels between the three best tests are equal to or less than 5% for most of the bands. Only test 1 will be used for the remainder of this chapter due to its performance and simplicity.

III.5. Remote Reference Analysis

III.5.1. Introduction

Since random errors tend to reduce when a sufficiently large data set is provided, bias errors eventually become the main source of uncertainty in single site MT results. It is assumed here that bias arises predominantly from noise in the measured fields. An effective way of removing the bias errors in magnetotelluric data analysis is given by the remote reference method (Goubau et al., 1978a; Goubau et al., 1978b). The remote reference (RR) estimate produces a bias-free estimate provided noise at a reference (remote) site is incoherent with the noise at the base (local) site. In practice this is accomplished choosing a reference site at a sufficiently large distance from the base site. The degree of remoteness may vary from several kilometres to several meters (Goubau et al., 1984). Any precise definition of site separation would require a precise definition of noise sources.

The remote reference method requires measurement of two data channels at the remote site. Either the magnetic field or the electric field may be used as reference channels. It has been argued that since the electric field contains more noise and is prone to suffer from polarization effects due to the presence of geological inhomogeneities (Goubau et al., 1978a), one should usually use the magnetic field as a remote reference.

There are two important points worth mentioning. Firstly due

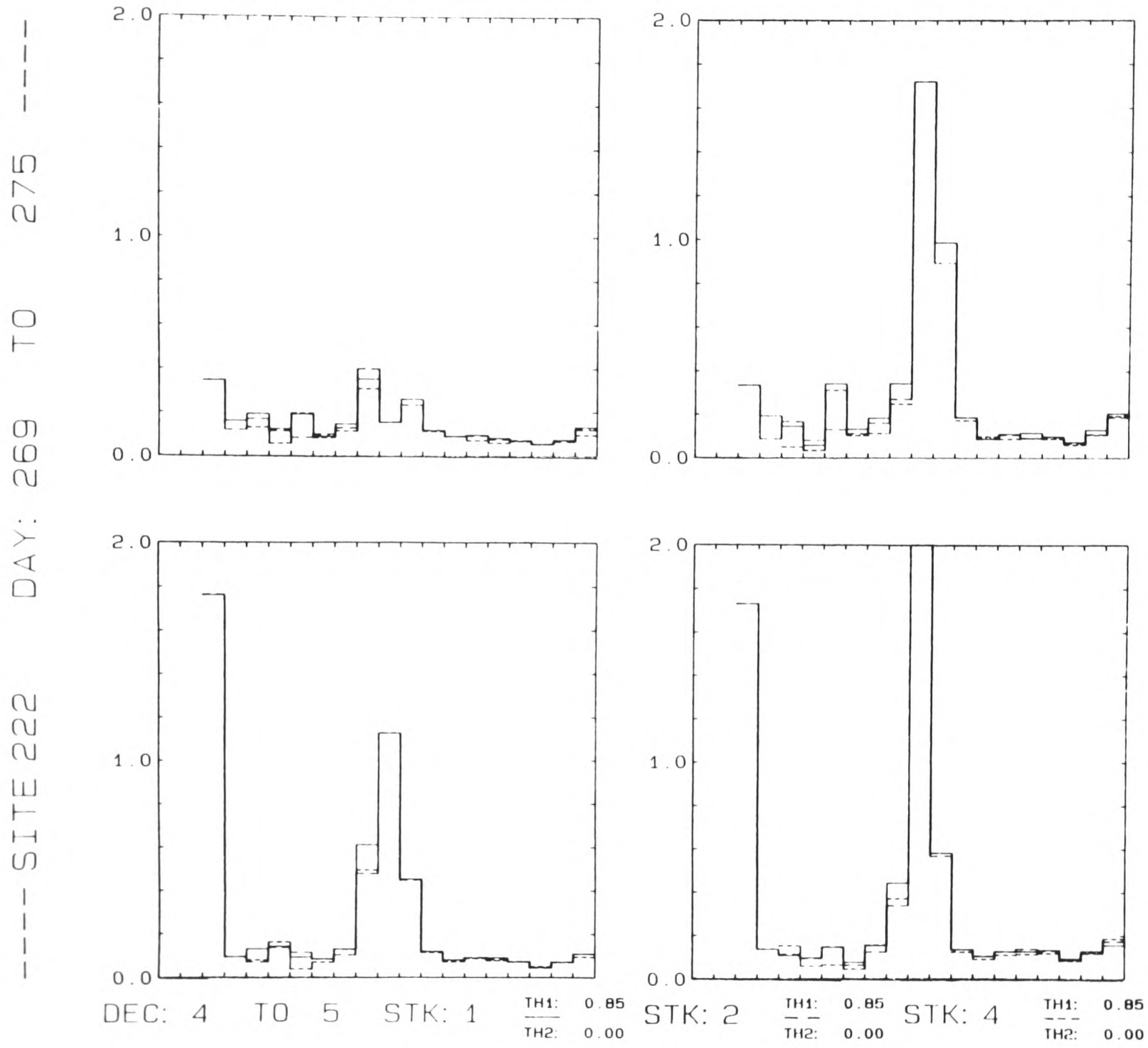
---- SITE 222 DAY 269 TO 275 ----
2.0
1.0
0.0
DEC: 4 TO 5 STK: 1
TH1: 0.85
TH2: 0.00
STK: 2
TH1: 0.85
TH2: 0.00
STK: 4
TH1: 0.85
TH2: 0.00

Figure III.11. Fractional errors $\hat{\varepsilon}_{\ell m}$ for Zxy and Zyx using tests 1 (solid line), 2 (longer dashes) and 4 (shorter dashes), for a threshold of 0.85. Top row, left to right, there are the normalized errors of Re(Zxy) and Im(Zyx). Bottom row, left to right, there are the normalized errors of Re(Zyx) and Im(Zyx).

to the fact that two additional channels are measured the variance of the remote reference estimates is expected to be larger than it would be if one had calculated them using SS analysis (Kroger et al., 1983). In other words it should be necessary to measure relatively more estimates for the RR case than it would be using a single site approach to attain the same variance level. Secondly, the RR method requires two sets of sensors for the magnetic components and very stable time bases and/or telemetry for synchronization.

Time synchronization

The distance between the local site, site 2, and the remote site, site 1, is about 30 km. Both sites were radio-linked and each site had its own time-base. Site 1 clock is assumed to give the reference time for site 2 as well as for the other sites. Site 2 clock was subject to a slow drift in relation to the site 1 clock. This gave rise to timing errors which could affect the phase estimates. During the time span of the test data set, days 269 to 275, the maximum time discrepancy between site 2 and 1 was 5s.

There are two kinds of timing errors between the sites. One is due to a slow drift of site 1 clock. This was very small and therefore neglected. The other is due the time difference between site 2 clock and site 1 clock. As data was transmitted digitally in 5s intervals, this last kind of timing error appears as 5s jumps. Such discrete time error could cause a maximum phase error of π for decade 4 and $\pi/10$ for decade 5.

Several workers have had to cope with timing errors. Even in a single site scheme it is possible to have timing errors. This is the case when the relative timing between magnetic and electric components is not accurate. The syncronization between the two fields may be done by maximizing the ordinary coherence and minimizing the frequency derivative of the phase cross-spectrum at the shortest periods (Chave et al., 1981) or by means of a linear regression of partial coherency phases with respect to frequency (Jones et al., 1983).

Let $x_1(t)$ and $x_2(t)$ be two time series, with spectral representations $X_1(w)$, $X_2(w)$. Their cross-spectrum is given by $S_{21}=\overline{X_2(w)\ X_1^*(w)}$. Assume that there is a clock for $x_1(t)$ and another for $x_2(t)$. The two clocks have a timing error $\Delta t=(t)_2-(t)_1$. Assuming the $x_1(t)$ clock has the correct time, one should write $x_2(t+\Delta t)$. In this case the cross-spectrum should read

$S'_{21}=\overline{X'_2(w)\ X^*_1(w)}$. The Fourier pair $x_2(t+\Delta t) <--> X_2(w).\exp(i.\Delta t.w)$ is a direct application of the time-shifting theorem (e.g., Båth, 1974, p.44). The timing correction is then straightforward,

$$S_{21} = S'_{21}\ \exp(-i\,\Delta t\,\omega) \qquad \text{(III.41)}$$

where Δt is a known time difference.

In the present case the timing error between site 2 and the remote reference, site 1, is known so the timing correction is a simple application of (III.41). This correction may be applied to either the raw or to the smoothed spectrum. In the present case it was applied to the smoothed spectral estimates. As a check, two pure sinusoidal time series of identical period T=55s were generated. Delays of $\Delta t=\pm 5s, \pm 10s$ were introduced in one of the series. Corrections were then applied to both raw and smoothed spectra. The two corrected phase values were always within 1.5 degrees from the true value.

III.5.2. Analysis of the Lock-in Signal Detection

Relationships and assumptions of the RR technique

The impedance tensor is defined by (III.17). Assume a remote site where a horizontal field $\underline{R}$ is chosen. This field may be either a magnetic or an electric field. Assume that the noises in $\underline{R}$ are uncorrelated with the noises in both $\underline{E}$ and $\underline{H}$ at the base site. This assumption stems from the fact the measured fields are noisy and the response functions are expressed in terms of cross-spectral density functions.

Analogously to the downward biased case of the single site estimate (III.20), a remote impedance tensor estimate is obtained forming dyadic products with $\underline{R}$, band-averaging and solving for $\underline{\underline{Z}}$

$$\hat{\underline{\underline{Z}}}^R = [\underline{E}\,\underline{R}]\,[\underline{H}\,\underline{R}]^{-1} \qquad \text{(III.42)}$$

where [ ] denotes an average power spectral matrix, (III.18). Expanding this expression one arrives at

$$\hat{Z}^{R}_{\ell m} = \frac{\overline{E_\ell R_m^*}\cdot\overline{H_n R_m^*} - \overline{E_\ell R_m^*}\cdot\overline{H_n R_m^*}}{\overline{H_y R_j^*}\cdot\overline{H_n R_n^*} - \overline{H_n R_j^*}\cdot\overline{H_y R_n^*}}$$

where l,m,n=x,y and n=m.

This problem may be decomposed into a double least-squares problem. A first regression is set up to obtain a predicted magnetic field as

$$\underline{\hat{H}} = \underline{\underline{T}}\,\underline{R} + \underline{H_n} \qquad \text{(III.43)}$$

where $\underline{H}$n is random noise at the local site and $\underline{R}$ is assumed to have a low noise level. The transfer tensor can be predicted in a similar way as in (III.20),

$$\underline{\underline{\hat{T}}} = [\underline{H}\,\underline{R}]\,[\underline{R}\,\underline{R}]^{-1}$$

With this estimate it is possible to predict a magnetic field, $\underline{\hat{H}}$, at the local site. This predicted field can be used to set up a second least-squares problem

$$\underline{E} = \underline{\underline{Z}}^{R}\,\underline{\hat{H}} + \underline{E_n} \qquad \text{(III.44)}$$

where $\underline{E}$n is the output random noise. By forming dyadics with $\underline{H}$n,

$$[\underline{E}\,\underline{\hat{H}}] = \underline{\underline{\hat{Z}}}^{R}\,[\underline{H}\,\underline{\hat{H}}]$$

and as $[\underline{F}\,\underline{\hat{H}}]=[\underline{F}\,\underline{R}]\,\underline{\underline{\hat{T}}}^{\dagger}$, where $\underline{\underline{\hat{T}}}^{\dagger}$ is the conjugate transpose of $\underline{\underline{T}}$, one ends up estimating the referenced impedance tensor as in (III.42).

The variance in $\underline{\underline{\hat{Z}}}^{R}$ can be estimated using an expression which resembles (III.16) for some restricted situations (Pedersen, 1982; Kroger et al., 1983). Here a more general expression for the variance is used. As its derivation can be found elsewhere (Gamble et al., 1979b), only an outline is given here. The expected variance of $\underline{\underline{\hat{Z}}}^{R}$ is evaluated by relating the error $\underline{\underline{\Delta}}=\underline{\underline{\hat{Z}}}^{R}-\underline{\underline{Z}}$ to the combined noise

$$\underline{\eta} = \underline{E} - \underline{\underline{Z}}\,\underline{H} \qquad \text{(III.45)}$$

The estimated combined noise, $\underline{\hat{\eta}}$, is found substituting $\underline{\underline{\hat{Z}}}^{R}$ in this

last relation, as in the SS case (III.32). Eliminating $\underline{E}$ in both (III.45) and its estimated counterpart one gets

$$\underline{\eta} + \underline{\underline{Z}}\ \underline{H} = \hat{\underline{\eta}} + \hat{\underline{\underline{Z}}}^{R}\ \underline{H}$$

or

$$\underline{\eta} = \hat{\underline{\eta}} + \underline{\underline{\Delta}}\ \underline{H} \qquad \text{(III.46)}$$

As in (III.42), form dyadic products with $\underline{R}$ and band-average to obtain

$$[\underline{\eta}\,\underline{R}] = [\hat{\underline{\eta}}\,\underline{R}] + \underline{\underline{\Delta}}\,[\underline{H}\,\underline{R}]$$

but as the first term on the right hand side of this relation vanishes due to (III.42), then

$$\underline{\underline{\Delta}} = [\underline{\eta}\,\underline{R}]\,[\underline{H}\,\underline{R}]^{-1}$$

Expanding this, each element will be of the form

$$\Delta_{ij} = \overline{\eta_i A_j^*} \,/\, D \qquad \text{(III.47)}$$

with

$$A_j = (-1)^{\delta_{jx}} R_x \cdot \overline{R_j H_k^*} + (-1)^{\delta_{jj}} R_y \cdot \overline{R_k H_h^*} \qquad \text{(III.48)}$$

where i,j,k=x,y; $k \neq j$, δ_{jx}, δ_{jj} are Kronecker delta functions and D=det[$\underline{H}$ $\underline{R}$].

Assume now there is an ensemble of N>>1 estimates for $\hat{\underline{\underline{Z}}}^{R}$. Each of these estimates is obtained from an independent data window. Define variance as

$$var\left(\hat{Z}_{ij}^{R}\right) = \langle |\Delta_{ij}| \rangle - |\langle \Delta_{ij} \rangle|^2$$

which is the sum of the variances of both real and imaginary parts of $\underline{\underline{Z}}^{R}$. The symbol $\langle\ \rangle$ represents an ensemble average. For the ensemble $\langle \Delta_{ij} \rangle = 0$ since the reference is uncorrelated with local noise. The variance can be approximated by

$$var\left(\hat{Z}_{ij}^{R}\right) = \frac{1}{N^2 |D|^2} \sum_{M=1}^{N} \langle |\eta_{i,M}|^2 |A_{j,M}|^2 \rangle$$

with an error of the order of 1/N. In this approximation it is assumed that $\eta_{i,m}$ and $A_{j,m}$ are statistically independent of $\eta_{i,n}$ and $A_{j,n}$ for $m \neq n$. Although this statistical independence does not hold true, the error in this approximation is still 1/N. If the following assumptions are valid: 1) local noises are uncorrelated with $\underline{R}$; 2) local noises are independent of signals, and 3) noises are stationary; the variance in $\hat{Z}_{ij}$ can be approximated by

$$\mathrm{var}\left(\hat{Z}^R_{ij}\right) = \frac{1}{N\,|D|^2}\,\left|\overline{\hat{\eta}_i}\right|^2\,\left|\overline{A_j}\right|^2 \qquad \text{(III.49)}$$

with an error of the order of 1/N (Gamble et al., 1979b), where N is the number of degrees of freedom. The expansion of this approximation is given by (III.33) and (III.48).

The above assumptions are likely to be satisfied in the case of a valid remote reference, i.e. the first assumption must be satisfied anyway. The second assumption is valid if noises are generated locally, note that if they are not, the first assumption would also fail. The stationarity of noise is required only in the sense that the ensemble average of the powers are equal to the measured time average (Gamble et al., 1979b). Since (III.49) is an approximation there is a lower limit for N on which the error in the variance estimate is kept at a reasonable level.

The predicted coherence function is given by an expression similar to the one employed to the SS downward biased case (III.34). Of course the RR value will be different from the SS estimate due to the explicit dependency on $\underline{\underline{\hat{Z}}}^R$. The RR predicted coherence function can be written as

$$\gamma^2_{i\,12} = 1 - \frac{\left|E_\ell - \left(\hat{Z}^R_{\ell x} H_x + \hat{Z}^R_{\ell y} H_y\right)\right|^2}{\hat{S}_{ii}} \qquad \text{(III.50)}$$

with ℓ=x,y when i=3,4. Other relevant coherence functions can also be expressed in terms of the RR impedance tensor. The predicted coherence given by (III.50) uses the local fields $\underline{E}$ and $\underline{H}$. As the RR problem can be decomposed into a double least-squares problem, one could choose to use coherence functions for each problem separately. For instance, one coherence would deal with a linear system where a predicted $\hat{H}x$ is the output and Rx and Ry are the inputs. A second coherence would then be estimated for another linear system where $\hat{E}x$ is the output and $\hat{H}x$ and $\hat{H}y$ are the inputs. The coherence between the remote field $\underline{R}$ and the predicted local electric field $\hat{\underline{E}}$ is another choice. In the present work the

predicted coherence given by (III.50) is used throughout. It not only gives the coherence between local fields but also is directly related to the combined local noise.

In calculating the RR estimates of the quantities described in this subsection it is necessary to compute 6 auto-powers and 14 cross-powers. They are:

$\overline{E_x E_x^*}$

---- $\overline{E_y E_y^*}$

$\overline{E_x H_x^*}$, $\overline{E_y H_x^*}$, $\overline{H_x H_x^*}$

$\overline{E_x H_y^*}$, $\overline{E_y H_y^*}$, $\overline{H_x H_y^*}$, $\overline{H_y H_y^*}$

$\overline{E_x R_x^*}$, $\overline{E_y R_x^*}$, $\overline{H_x R_x^*}$, $\overline{H_y R_x^*}$, $\overline{R_x R_x^*}$

$\overline{E_x R_y^*}$, $\overline{E_y R_y^*}$, $\overline{H_x R_y^*}$, $\overline{H_y R_y^*}$, $\overline{R_x R_y^*}$, $\overline{R_y R_y^*}$

Note that unlike the SS calculations the cross-power between the two electric components is not necessary.

Remote reference results with R=H

It has been suggested that even low thresholds of predicted coherence in remote reference analysis produce accurate impedance tensor estimates (e.g., Goubau et al., 1978a; Gamble et al., 1979a). If this is correct then coherence criteria such as the ones described in the last section are no longer important. The validity of this assertion is investigated here. Only test 1, i.e. the predicted coherence above a threshold, will be used as a selection criterion with two thresholds γ_t=0.1,0.5. Other tests are more restrictive leading to more bands without any estimates and a possible increase in the variance of the results. The relation between degrees of freedom and variance will be discussed later in this section.

The magnetic field components from site 1 are used as a remote reference. Figure III.12 shows the results using the two thresholds γ_t=0.1,0.5, on the complete data sets of sites 1 and 2. Results are comparable for both thresholds although they show more stability when using the higher threshold, but variances tend to be higher for γ_t=0.5. The resultant predicted coherences are well above the thresholds with the exception of only two bands. The suppression of bias is evident when SS and RR results are compared. Figure III.13 shows SS results for a threshold of γ_t=0.5. This result is the SS equivalent of the γ_t=0.5 RR results. Comparing these results with those of figure III.12.b , it is easy to see how bias degrades the accuracy of the SS estimates at all bands but a few of decade 5, where coherences are high. This comparison shows strikingly how powerful the RR technique is. A more instructive

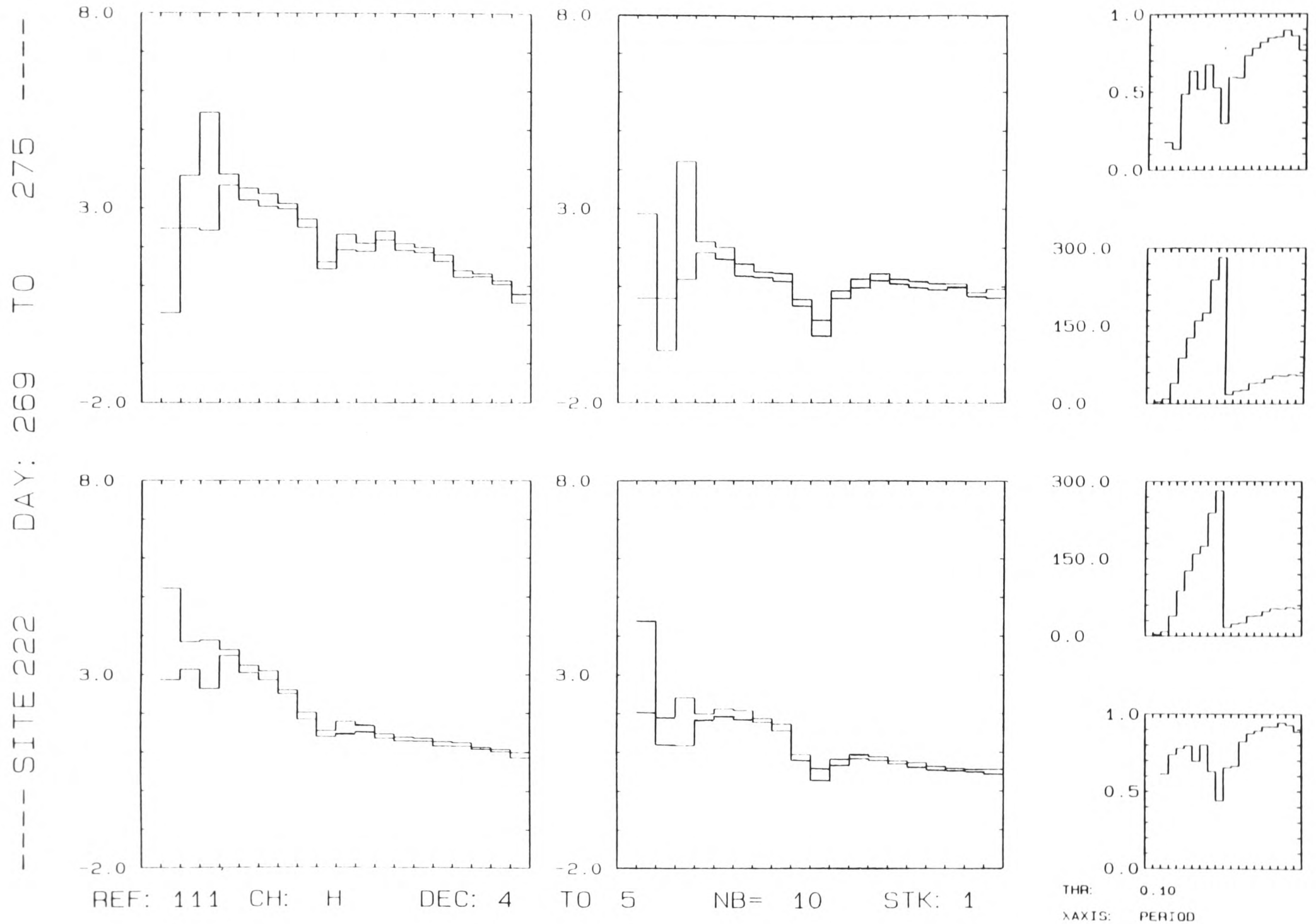
--- SITE 222 DAY 269 TO 275 ---
8.0
3.0
-2.0
8.0
3.0
-2.0
1.0
0.5
0.0
300.0
150.0
0.0
8.0
3.0
-2.0
8.0
3.0
-2.0
1.0
0.5
0.0
REF: 111 CH: H DEC: 4 TO 5 NB= 10 STK: 1
THR: 0.10
XAXIS: PERIOD

Figure III.12.a. Estimates of Zxy and Zyx using $\underline{H}$ as remote reference for a threshold γ_t=0.1.

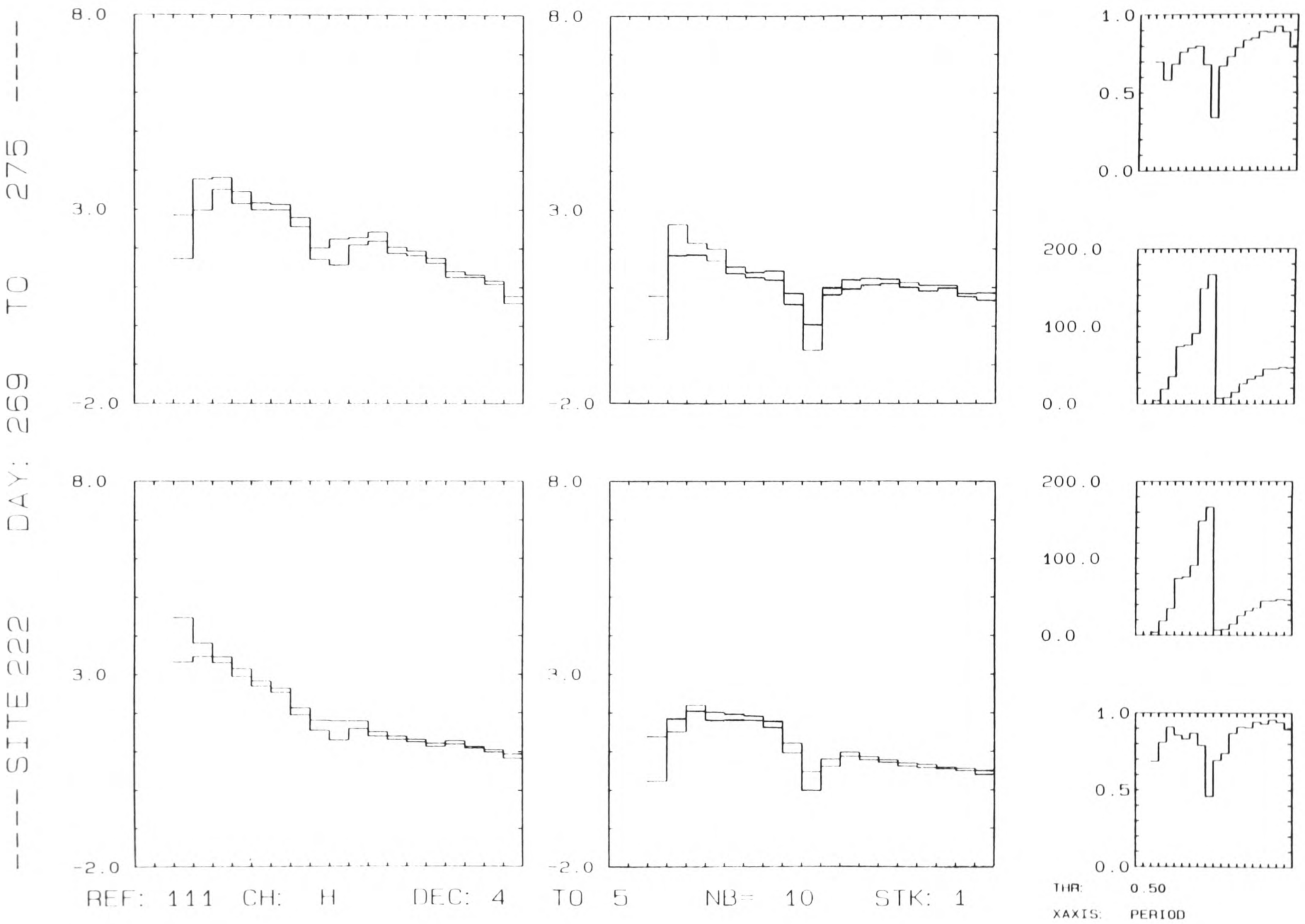
---- SITE 222 DAY 269 TO 275 ----
8.0
3.0
-2.0
8.0
3.0
-2.0
1.0
0.5
0.0
200.0
100.0
0.0
1.0
0.5
0.0
REF: 111 CH: H DEC: 4 TO 5 NB= 10 STK: 1
THR: 0.50
XAXIS: PERIOD

Figure III.12.b. Estimates of Zxy and Zyx using $\underline{H}$ as remote reference for a threshold δ_t=0.5.

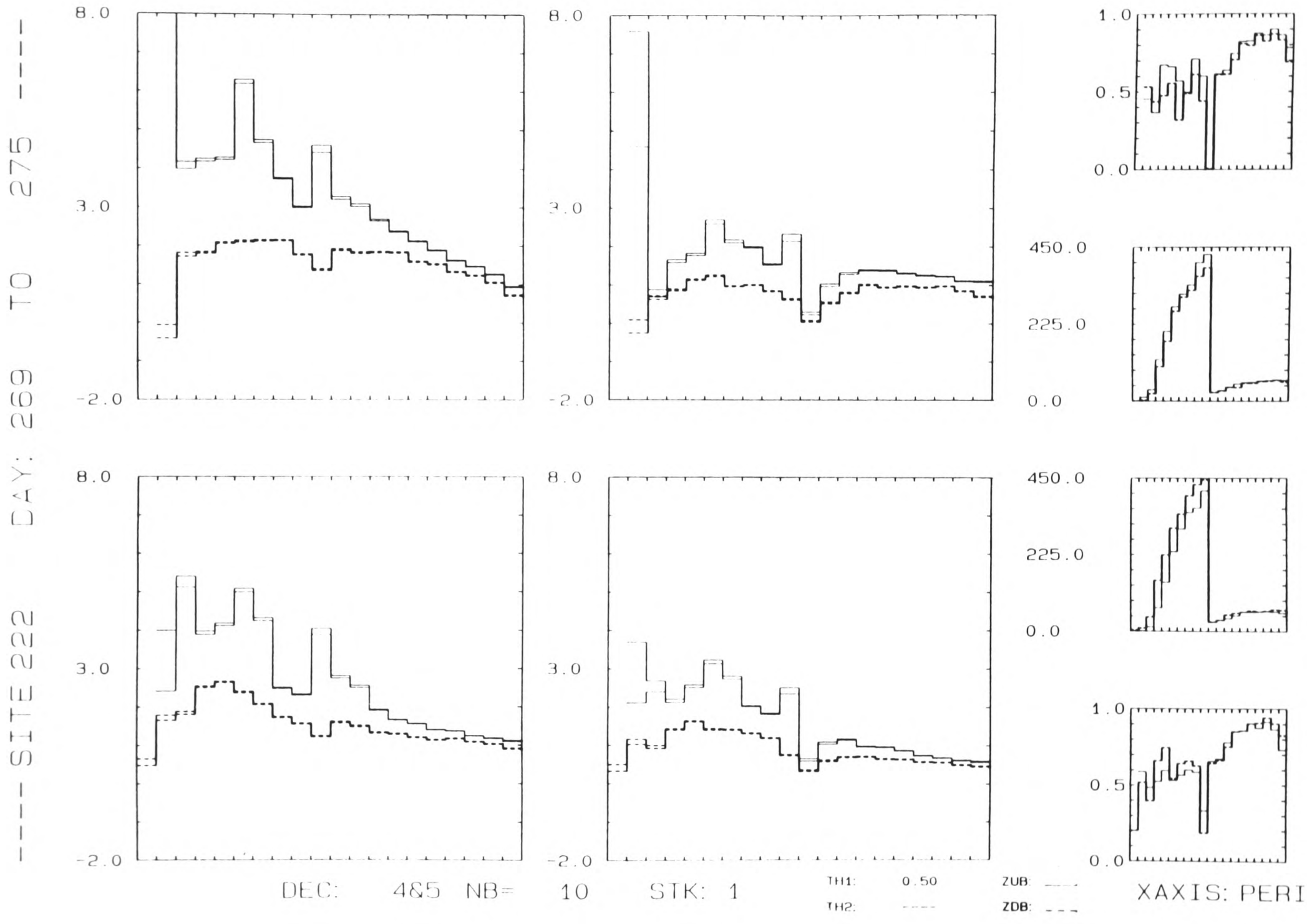
8.0
3.0
-2.0
8.0
3.0
-2.0
1.0
0.5
0.0
450.0
225.0
0.0
8.0
3.0
-2.0
8.0
3.0
-2.0
1.0
0.5
0.0
DEC: 4&5 NB= 10 STK: 1
TH1: 0.50
TH2:
ZUB:
ZDB:
XAXIS: PERIOD

Figure III.13. Estimates of Zxy and Zyx using single site analysis for a threshold of ζ_t=0.5.

comparison between RR and SS techniques is done using higher thresholds for the SS predicted coherence functions, since it is well known that a threshold as low as $\gamma_t=0.5$ cannot produce SS results of acceptable accuracy.

In order to compare SS and RR estimates it is better to choose what could be called the best sets of estimates from both techniques. The SS results for a threshold $\gamma_t=0.85$ can be considered good in terms of bias errors, number of estimates available and variance levels. The RR results for a threshold $\gamma_t=0.5$ is chosen as the best set of RR estimates. They can be considered as a suitable choice since both the predicted coherences, the number of stacked realizations and non-null bands are compatible. Both SS and RR results are shown in figures III.6.a and III.12.b, respectively. The comparison becomes easier if the two sets of results are overlaid as is shown in figure III.14, where the RR results appear hatched. There are a few conclusions which can be drawn from this figure. RR results are within the SS bounds for most of the bands, showing a smoother behaviour. It can also be seen that RR estimates do not tend necessarily towards an arithmetic nor a variance weighted SS average of both bias cases. The two sets of results can also be compared with regard to the levels of SS combined bias and random errors and RR random errors. This can be done using the SS fractional errors defined in (III.40) and their RR counterparts,

$$\hat{\varepsilon}^{R}_{ij} = \left[var\left(\hat{Z}^{R}_{ij} \right) \right]^{1/2} / \hat{Z}^{R}_{ij}$$

with i,j=x,y. Figure III.15 shows the real and imaginary parts of the fractional errors for the off-diagonal elements of $\underline{Z}$, estimated by the SS (dashed line) and RR (solid line) techniques. The RR error levels amount to 5% for most bands and are always below the SS levels.

Figure III.14 brings forward another interesting point. The SS derived random errors are smaller than their RR counterpart. Higher variance levels on RR estimates are explained in terms of the presence of remote noises brought into the calculations from the remote site, while only local noises contribute to the variance in SS estimates. That is why low noise levels are required at the remote site. Usually it is the bias errors that degrade the SS estimates of $\underline{\underline{Z}}$, not the variance. Nevertheless some facts are overlooked in this comparison of variance levels. In fact the two sets of impedance tensor estimates and their associated random errors displayed in figure III.14 are not straightfowardly

---- SITE 222 DAY: 269 TO 275 ----

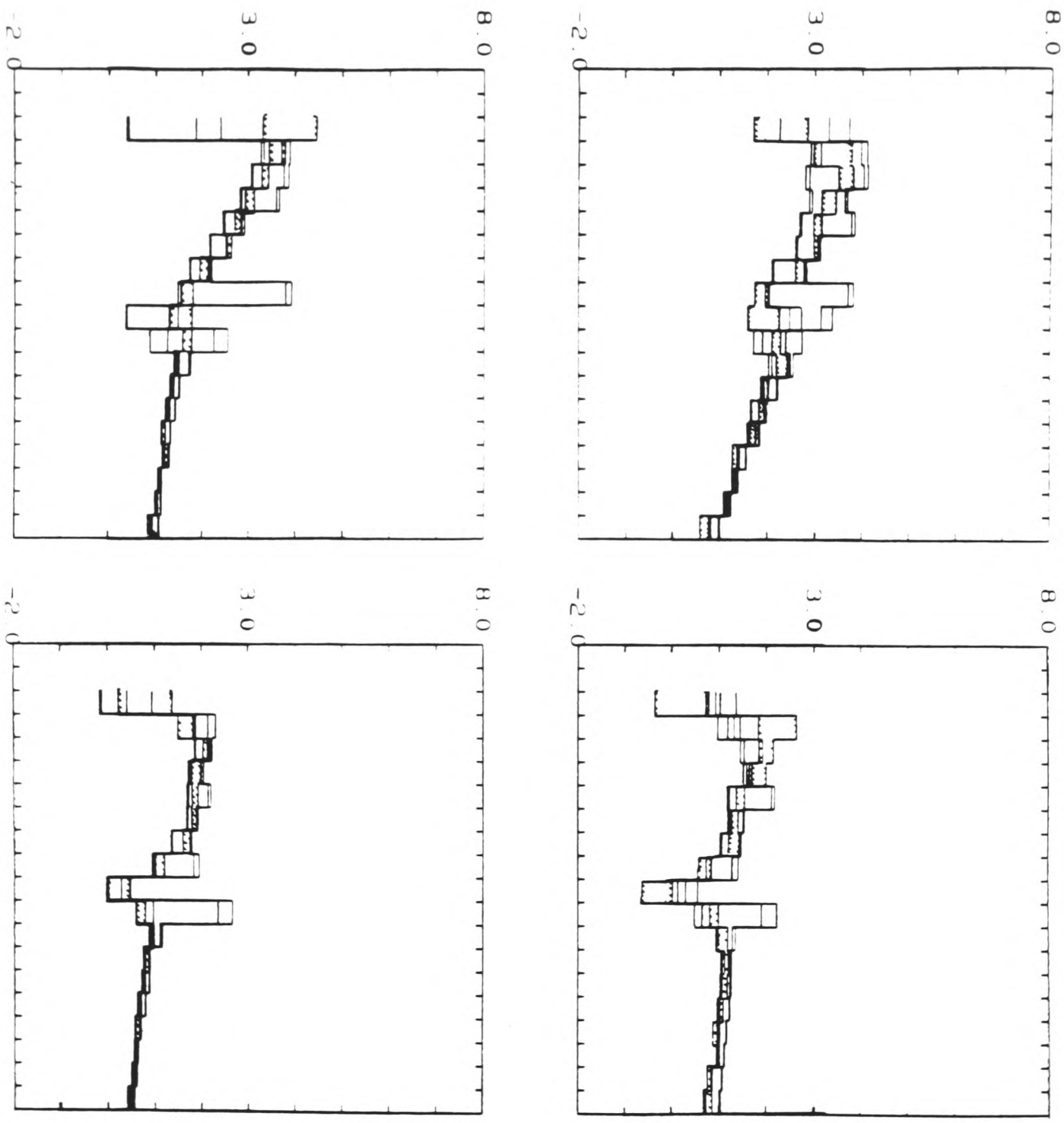

Figure III.14. Remote reference (hatched) and single site estimates (lines) of Zxy and Zyx. The thresholds are γ_t=0.5 for the remote reference and γ_t=0.85 for the single site analysis.

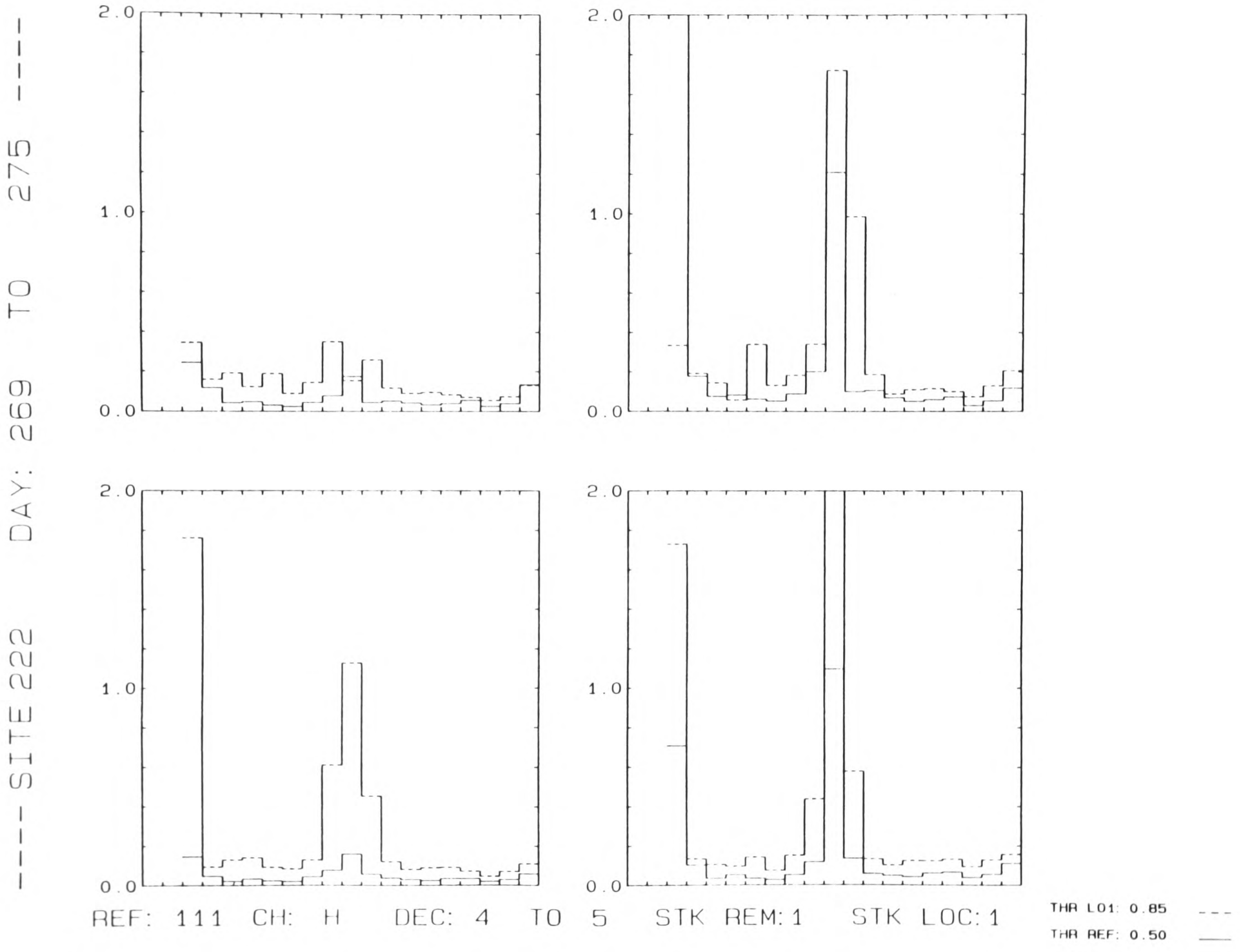
---- SITE 222 DAY 269 TO 275 ----
2.0
1.0
0.0
2.0
1.0
0.0
2.0
1.0
0.0
2.0
1.0
0.0
REF: 111 CH: H DEC: 4 TO 5 STK REM: 1 STK LOC: 1
THR L01: 0.85 ---
THR REF: 0.50 ——

Figure III.15. Fractional errors $\hat{\varepsilon}_{ij}$ for both single site (dashed line) and remote reference (solid line) estimates of Zxy and Zyx using test 1. Single site threshold is 0.85 and remote reference threshold is 0.5, remote channel H. This figure follows the same layout as figure III.11.

comparable. Although the number of accepted realizations shown in figures III.6.a and III.12.b are more or less of similar values, the SS technique selects realizations which are not necessarily the same as selected by the RR technique, resulting in two subsets with an unspecified degree of overlap. This is not caused only by the two different coherence thresholds, even if they were equal the two subsets would not necessarily be the same. This will be subject of further investigation later in this chapter. With these facts in mind, the comparison between the two sets of estimates together with their associated errors, is valid in the sense that they represent a choice of the best of results from both SS and RR techniques.

Obviously the choice of a particular threshold depends on the characteristics of the data set considered. The test data sets have so far been used to provide RR estimates using predicted coherence thresholds of γ_t=0.1,0.5, figure III.12. It is in fact possible to use all the available data, i.e. with no coherence rejection, and still obtain reliable RR estimates for most of the bands. The RR results for this case are shown in figure III.16. In this figure the location of bands 3 and 5 of decade 4 are indicated for future reference. Estimates for the leftmost bands are not reliable and show large variances. Apart from these few frequency bands, the comparisons reveal that all available data set can be used to provide RR estimates. This fact will be subject to further investigation later in this chapter. At the moment it is more instructive to concentrate on the RR variance.

On the variance in the RR technique

The variance defined in (III.49) provides a quantitative way of assessing the quality of the impedance tensor estimates, in comparison to a qualitative criterion as given by the "smoothness" of the estimates against a chosen function of period or frequency. From expression (III.49) one can see that the variance depends on the inverse of N, the number of degrees of freedom. Moreover that definition is only approximate and carries an error of the order of 1/N (Gamble et al., 1979b). In other words the variance is better approximated by (III.49) for N>>1, i.e. above a minimum value. Although the dependence on 1/N is not very strong, one may assume also that the variance can be progressively reduced by increasing the number of degrees of freedom N. The more data that are collected and analysed, the smaller the variance should become. Although this idea is shared by several workers (e.g., Pedersen, 1982; Kroger et al., 1983), it is not so straightforward since the the variance is also a function of the error power, which in turn is

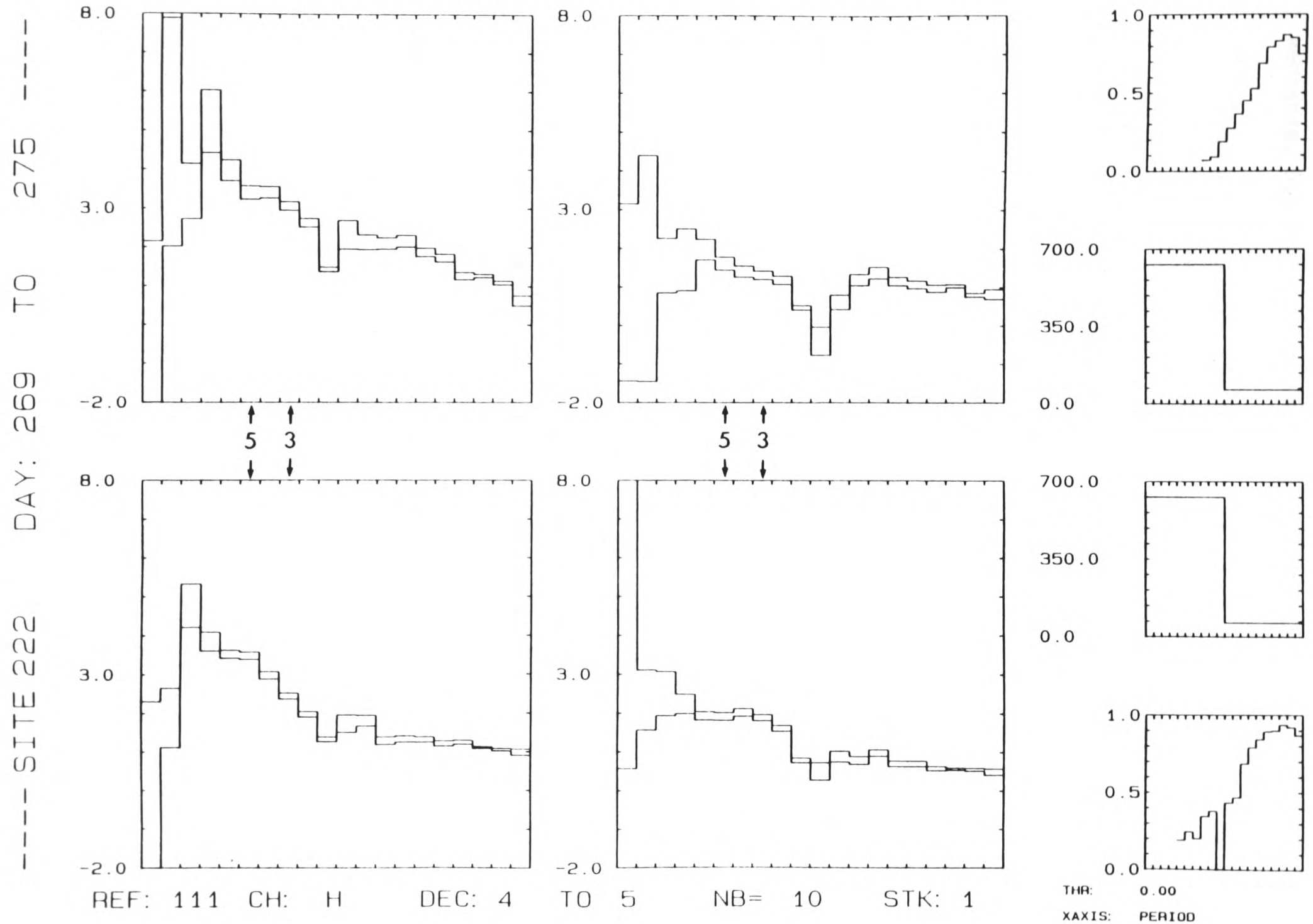
269 TO 275 ----
---- SITE 222 DAY:
8.0
3.0
-2.0
5 3
1.0
0.5
0.0
700.0
350.0
0.0
REF: 111 CH: H DEC: 4
TO 5 NB= 10 STK: 1
THR: 0.00
XAXIS: PERIOD

Figure III.16. Estimates of Zxy and Zyx using $\underline{H}$ as a remote reference without any coherence rejection. Location of bands 3 and 5 of decade 4 appear indicated with arrows.

simply related to the predicted coherence. There are still two other quantities in (III.49), Aj and D, which also contribute to the variance, but they do not depend on the local noises.

The investigation of how var(Zij) depends on the coherence and on N, can be done using coherence sub-intervals, fixing the number of degrees of freedom, and then comparing against the estimates obtained using the whole data set from figure III.16. Divide the obtained coherence estimates into 6 distinct groups:

$$=0. \quad , (0.0,0.25], \quad (0.25,0.5],$$
$$(0.5,0.75], (0.75,0.9] \text{ and } (0.9,1.0] \qquad \text{(III.51)}$$

Note that these sub-intervals are disjoint. Choose N as the maximum available number of realizations it is possible to select at all sub-intervals. Due to the signal-to-noise characteristics of the test data set, this investigation is restricted to a few bands of decade 4.

It is possible to stack N=10 realizations at all sub-intervals (III.51) for band 3 of decade 4. This is the maximum N that the test data set allows. Figure III.17 shows the estimates of Zxy and Zyx for each of the coherence sub-intervals. The estimates obtained using the whole data set for band 3 which is shown in figure III.16, are indicated by the heavy broken lines. Observe that the estimates for the last sub-interval ranging (0.9,1.0], with N=10 realizations, are essentially identical at a 68% confidence level to the ones obtained using the whole data set with N=630 realizations. Raising the confidence level to 95% makes most of the six sub-intervals consistent with the estimates from the whole data set.

A similar picture emerges when this last analysis is repeated for other bands. Band 4, decade 4, with N=7 degrees of freedom leads us to the same conclusions, i.e. estimates from the last of the sub-intervals (III.51) agree with those computed using all data set with no data selection. Coherence selected estimates begin to differ from unselected estimates for N=4. As before those conclusions are obtained at a 68% confidence interval. For a confidence interval of 95%, N=3 degrees of freedom is sufficient to ensure consistent estimates. Figure III.18 shows the estimates for band 5, decade 4, giving another example where coherence selected estimates match, within one standard deviation, unselected results. In this case there are N=5 degrees of freedom. Band 5 location is also indicated in figure III.16.

Results from the last two figures show that the remote reference technique provides an inherent weighting which enhances

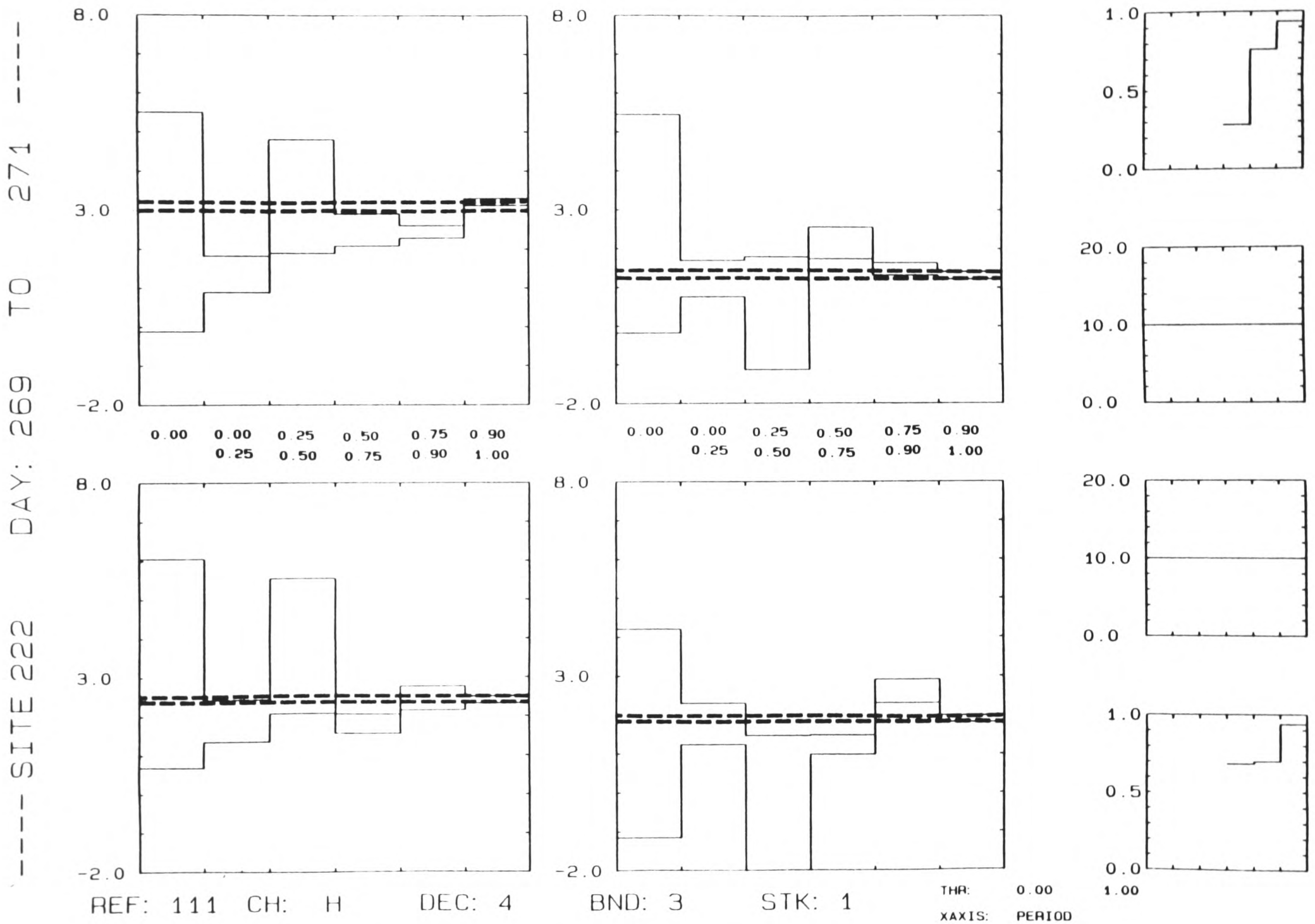
DAY 269 TO 271 ----
SITE 222 ----
8.0
3.0
-2.0
0.00 0.00 0.25 0.50 0.75 0.90
0.25 0.50 0.75 0.90 1.00
1.0
0.5
0.0
20.0
10.0
REF: 111 CH: H DEC: 4
BND: 3 STK: 1
THR: 0.00
XAXIS: PERIOD
1.00

st

Figure III.17. Estimates of Zxy and Zyx for band 3 of decade 4 by sub-intervals of predicted coherence (solid lines). The 6 sub-intervals are ordered from left to right as: =0., (0.,0.25], (0.25,0.5], (0.5,0.75], (0.75,0.9], and (0.9,1.]. The number of degrees of freedom is fixed at N=10. The heavy broken lines show the estimates obtained for the same band setting no coherence criterion, i.e. N=630 degrees of freedom.

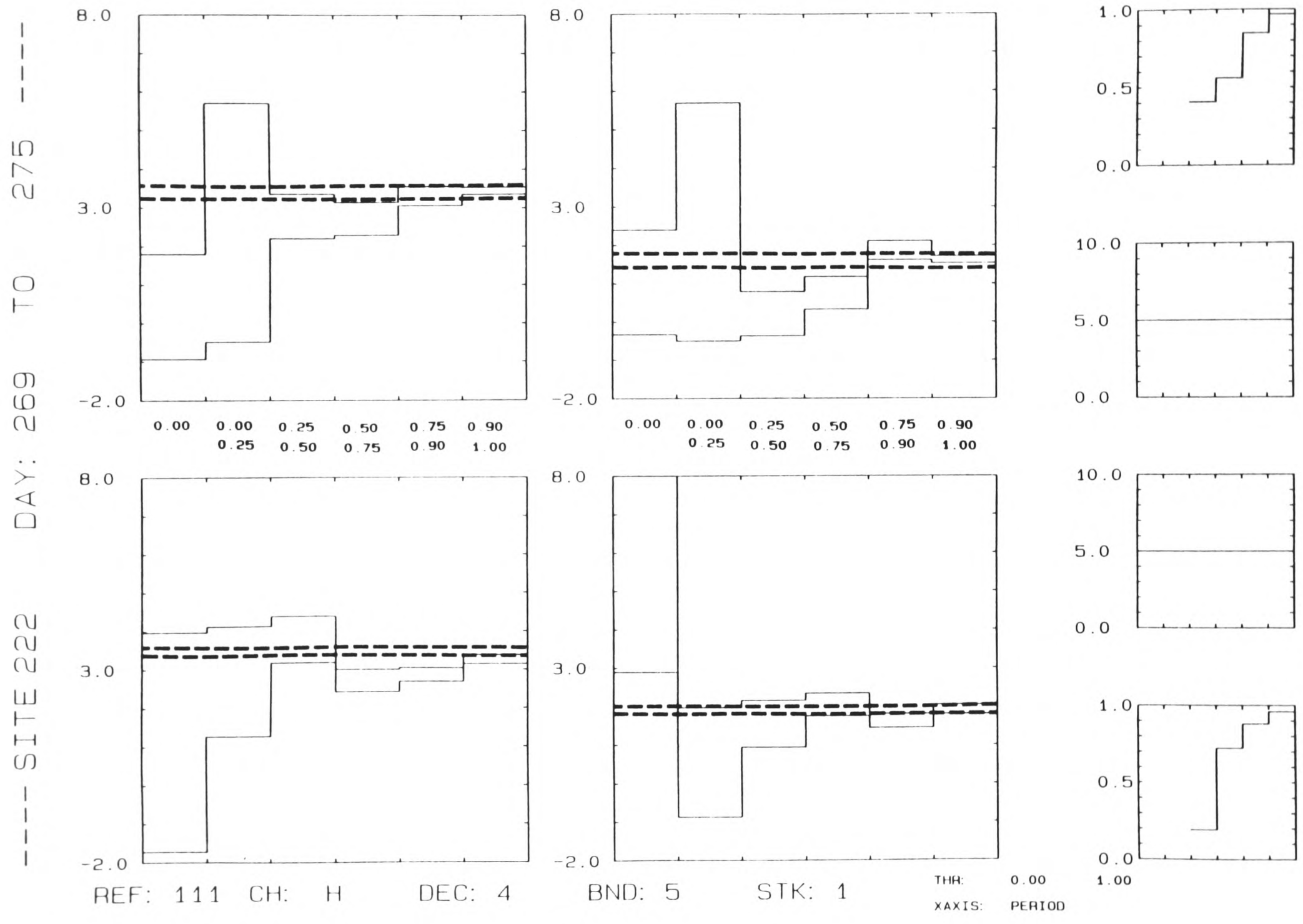
DAY 269 TO 275 ----
---- SITE 222
8.0
3.0
-2.0
0.00 0.00 0.25 0.50 0.75 0.90
0.25 0.50 0.75 0.90 1.00
1.0
0.5
0.0
10.0
5.0
REF: 111 CH: H DEC: 4
BND: 5 STK: 1
THR: 0.00 1.00
XAXIS: PERIOD

Figure III.18. Estimates of Zxy and Zyx for band 5, decade 4, by sub-intervals of predicted coherence (solid lines). The sub-intervals are the same as in the previous figure. The number of degrees of freedom is fixed at N=5. The heavy broken lines show the estimates obtained at the same band setting no coherence criterion, i.e. N=630 degrees of freedom.

the contribution of the higher quality data. The accumulation of more data windows will not automatically reduce the variance significantly. Accurate estimates are obtained using only data windows with low associated predicted error powers even for low N values. In particular only 5 realizations are sufficient to ensure results with better than 5% accuracy. This indicates that the accuracy of remote reference estimates depends very little on data set length but depends strongly on its inherent noise content.

The last two terms in the approximate definition of the variance (III.49) are $|Aj|^2$ and $|D|^2$, with Aj given by (III.48) and

$$\mathcal{D} = \overline{H_u R_u^*} \cdot \overline{H_y R_y^*} - \overline{H_u R_y^*} \cdot \overline{H_y R_u^*} \qquad \text{(III.52)}$$

which depend only on the signals. Indeed extracting the signal and noise terms in $\underline{H}$ and $\underline{R}$ as in (III.29),

$$\begin{aligned} D &= det\left\{ [\underline{H}_s \underline{R}_s] + [\underline{H}_s \underline{R}_n] + [\underline{H}_n \underline{R}_s] + [\underline{H}_n \underline{R}_n] \right\} \\ &= det\left\{ [\underline{H}_s \underline{R}_s] \right\} \\ &= det\left\{ [\underline{H}_s \underline{H}_s] \right\} \end{aligned}$$

in other words, D depends only on the signals since: remote noises are uncorrelated with local noises; and noises are independent of the signals. Moreover assuming that $\underline{R}$ is a magnetic field, D is the determinant of the coherence matrix of the magnetic field signals $[\underline{H}s\underline{H}s]$. Polarization parameters can be obtained in terms of this matrix (Fowler et al., 1967). In particular D->0 as the polarization of the signal $\underline{H}s$ increases. Then at a certain noise level $|\hat{\eta}_i|^2$ the variance of $\hat{\underline{\underline{Z}}}^R$ diverges as the polarization of the signal increases. Obviously the same conclusion applies to the estimate of the referenced impedance tensor (III.42), as the polarization increases the estimate also diverges. It is also easy to see that noise contributions to $|Aj|^2$ result in an additive term that, as long as noise powers in $\underline{R}$ can be considered sufficient small, may be neglected. So $|Aj|^2$ can be approximated by its noise-free value.

Remote reference results with $\underline{R}=\underline{E}$

In principle the electric fields can be used as a remote reference. However as electric channels are usually noisier than the magnetic ones, the variance should increase. Moreover the amplitude of the electric components depends primarily on the local

geoelectric structure (Goubau et al., 1978a), making them unsuitable as a remote reference. Figure III.19 shows the results obtained using $\underline{E}$ as a remote reference with a threshold of $\gamma_t=0.5$. It is clear that the estimate of $\hat{\underline{\underline{Z}}}$ is now subject to large uncertainties. A comparison between results using either the electric field or the magnetic field as a remote reference can be done by looking back to figure III.12.b and referring to figure III.19. The two results are not inconsistent, the estimates obtained using $\underline{R}=\underline{E}$ are merely inaccurate. Note that the predicted error powers as monitored by the predicted coherences are not very dissimilar from the corresponding coherences estimated using $\underline{R}=\underline{H}$, indicating that the local electric field is not particularly noisy.

The probable cause of the observed inaccuracy is the type of noise experienced by the reference $\underline{E}$ field used. A typical example of the noise affecting a large number of $\underline{E}$ data windows at both sites is shown in figure III.20. Both data and data first differences are shown in this figure. First differences from a data series $x(t)$ are formed as $x_i'=x_i-x_{i-1}$, where the sub-indexes indicate a value at a particular time t_i. The application of a straightforward first-difference formula is therefore an effective high-pass filter with a gain of $2\sin(\pi f/f_N)$ at the Nyquist frequency, f_N. The first differences shown monitor the level shifts that occur within the sampling period. The $\underline{E}$ fields observed at both sites experienced severe level shifts. In the above example the shifts are not simultaneous, i.e. coherent, at the two sites. However it is observed that the magnitude of a typical level shift is far greater than the natural signal level. In such circumstances, an adequate spectral representation of the data cannot be achieved since the power level at the Nyquist frequency is artificially large. In the case when this effect appears in both channels and is cross-correlated, the results become unpredictable. Note that the power spectrum for $f>f_N$ is folded back such that for $0\leq f\leq f_N$, there is a contribution at f from powers at frequencies $(2nf_N-f)$ and $(2nf_N+f)$, n is an integer. In the example of figure III.20, the contribution of level shifts will vary as the squares of their amplitudes. It is apparent for this type of noise that the aliased contributions dominate those from the signals. When two data channels suffer this effect and are cross-correlated the results obtained will become unpredictable since both spectra are inadequate. Noise of the type shown in figure III.20 was not experienced in the magnetic fields at either of the two sites. In conclusion it can be said that when noise of the type considered here persists within a data set, strong limitations are imposed on the RR technique. Those limitations are due to an inadequate

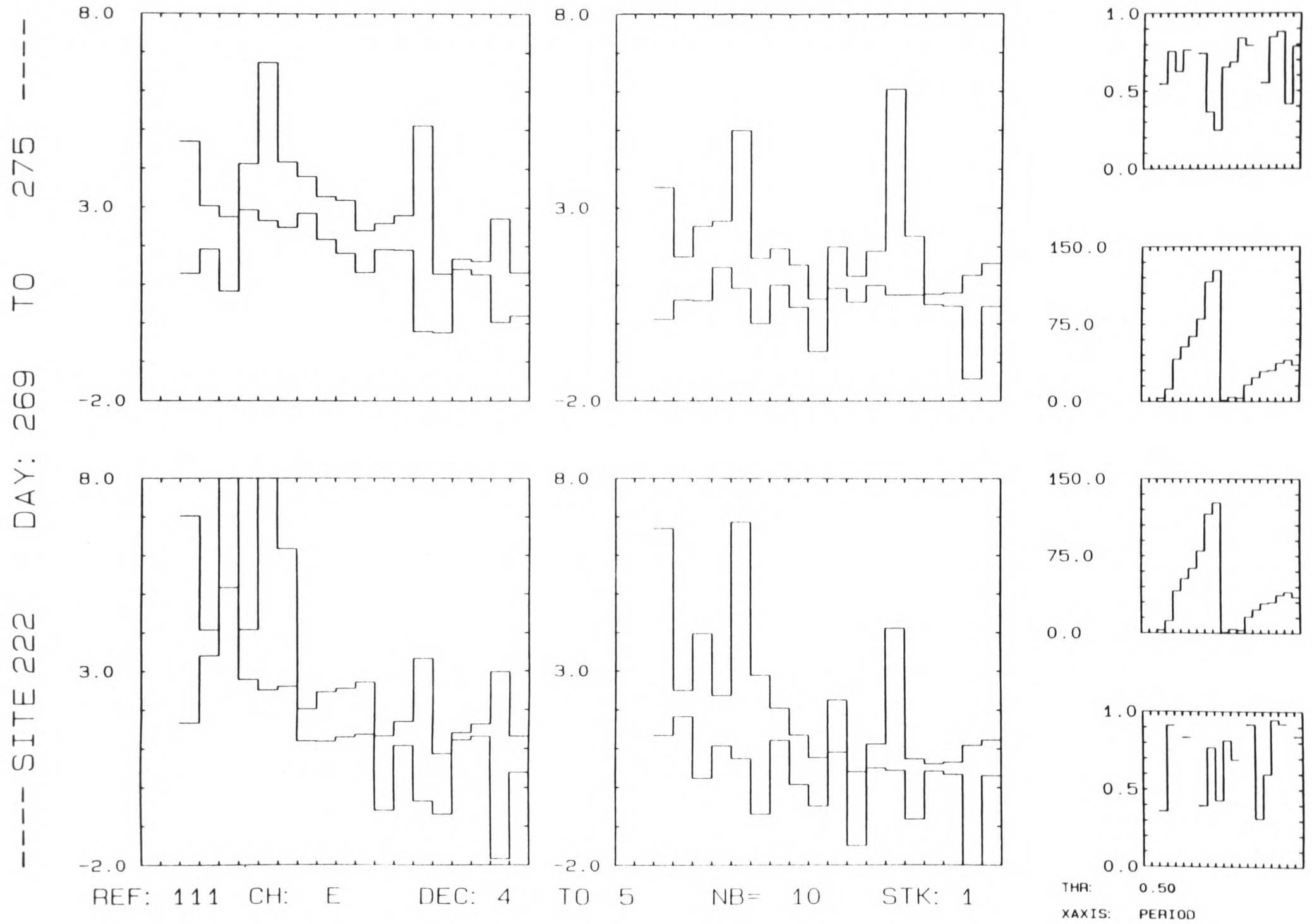
DAY 269 TO 275 ----
--- SITE 222
8.0
3.0
-2.0
8.0
3.0
-2.0
1.0
0.5
0.0
150.0
75.0
0.0
1.0
0.5
0.0
REF: 111 CH: E DEC: 4
TO 5 NB= 10 STK: 1
THR: 0.50
XAXIS: PERIOD

Figure III.19. Estimates of Zxy and Zyx using $\underline{E}$ as a remote reference for a threshold γ_t=0.5.

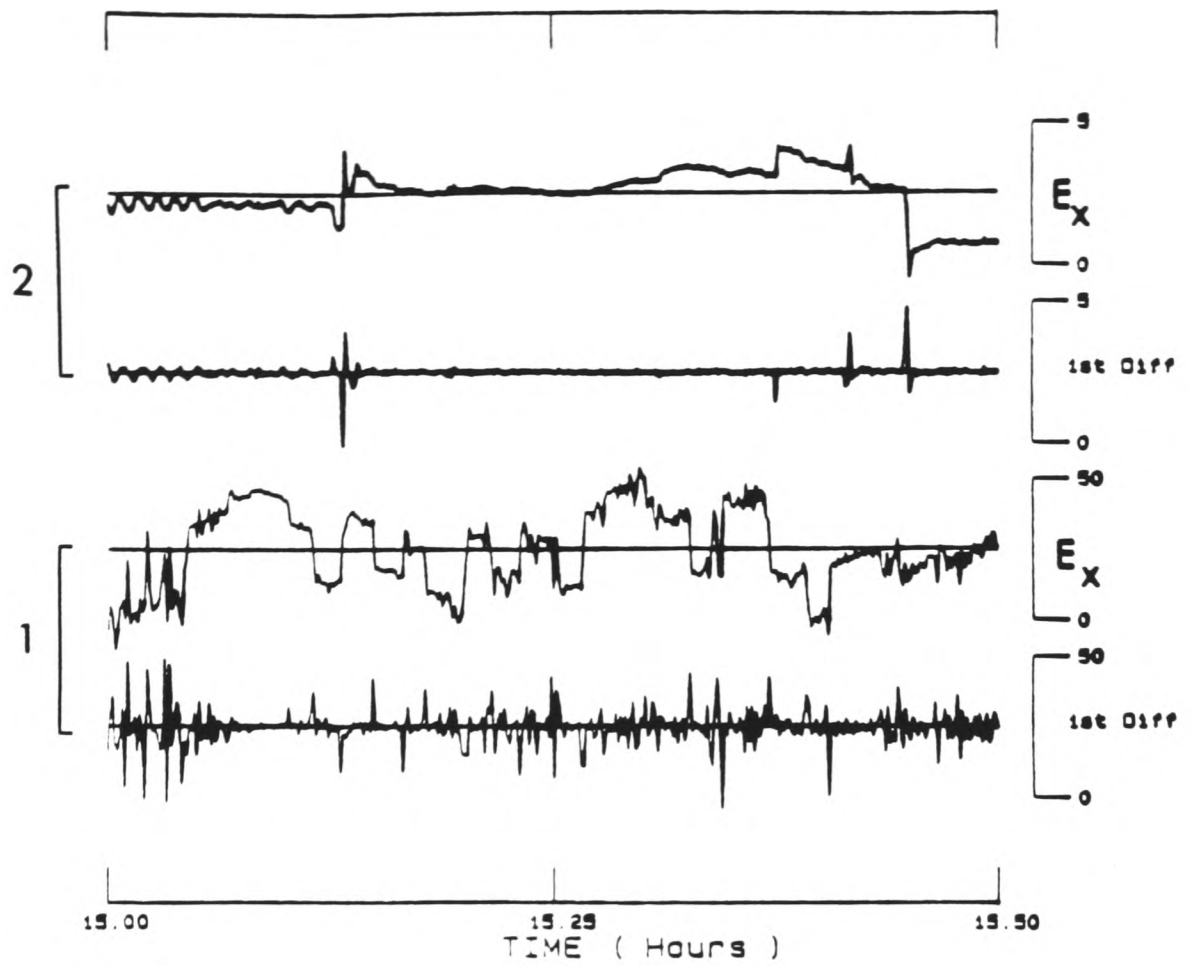
2
1
5
E_x
0
5
1st Diff
0
50
E_x
0
50
1st Diff
0
15.00
15.25
15.50
TIME (Hours)

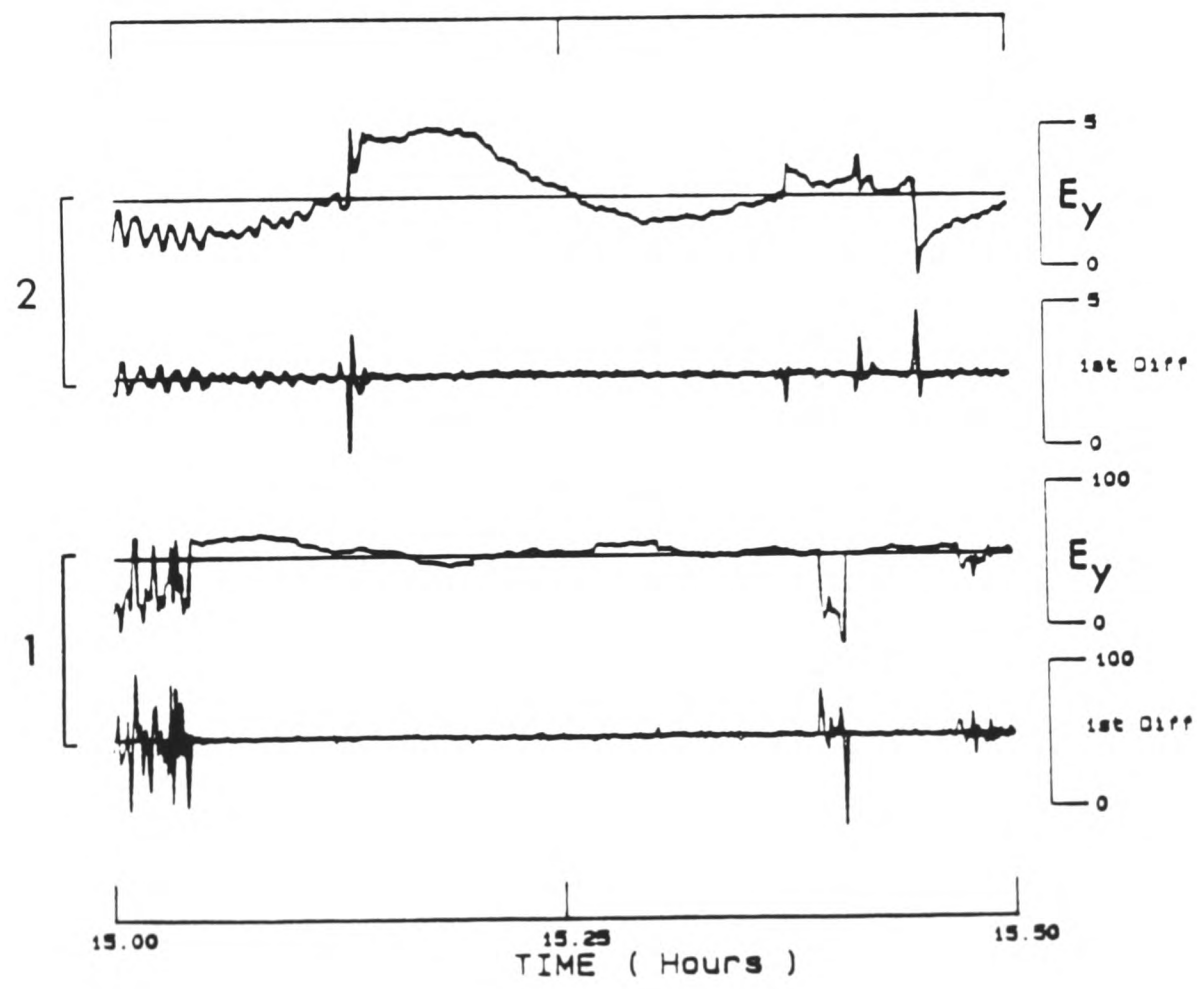
2
1
5
E_y
0
5
1st Diff
0
100
E_y
0
100
1st Diff
0
15.00
15.25
15.50
TIME (Hours)

Figure III.20. An electrical field data section recorded simultaneously at sites 1 and 2. Field units are in mV/km.

spectral representation caused by aliasing. It is generally true that such limitations are restricted to the $\underline{E}$ field (Adam et al., 1986).

III.5.3. The Role of the Predicted Coherence

It has been shown that it is possible to get reliable RR estimates for most bands using very low thresholds for the predicted coherences or even no selection at all. Nevertheless the accuracy of such estimates depends on their noise content. Since the RR technique provides an inherent weighting of the stacked realizations, it seems that just a few good signal-to-noise data windows are sufficient to produce good estimates. Obviously if too few or no such data windows are available, estimates will be inaccurate. The role of a selection criterion such as test 1, i.e. the predicted coherence, is to select the best among all data windows. Although the predicted coherence was used with this objective in the SS analysis, its reliability is now greatly improved as a result of the robustness of the RR analysis. Good data windows are recognized and lower thresholds can be used, resulting in a more efficient use of the data set. These points are important since high thresholds in SS calculations do not necessarily imply that only the best, in the sense of noise content, realizations are considered in the estimation of the impedance tensor. On the other hand the literature treats the RR function of the predicted coherence with reticence, implying that arbitrarily low thresholds may be used in the course of analysis (Goubau et al., 1978a; Gamble et al., 1979a; Dekker and Hastie, 1981; Fischer, 1982; Kroger et al., 1983). Those facts are going to be considered in the remainder of this section.

The first point to be considered is why RR estimates can be refined using a moderate threshold, $\gamma_t=0.5$. An answer can be provided by investigating how realizations with distinct coherence values contribute towards the final estimates. This may be done by grouping windows into the 6 disjoint groups of (III.51). Figure III.21.a to III.21.f show the estimates of the off-diagonal elements of $\underline{\underline{Z}}$ for each of those groups. It is easy to see why remote reference estimates using a moderate threshold of $\gamma_t=0.5$ are better; results start to appear clearly delineated from the (0.5,0.75] group onwards. This same figure together with figure III.12, suggests that higher thresholds are not desirable since they tend to reject useful information. So, although it is possible to estimate $\underline{\underline{Z}}$ simply stacking all realizations, the refinement provided by setting a moderate threshold for the predicted coherence is highly

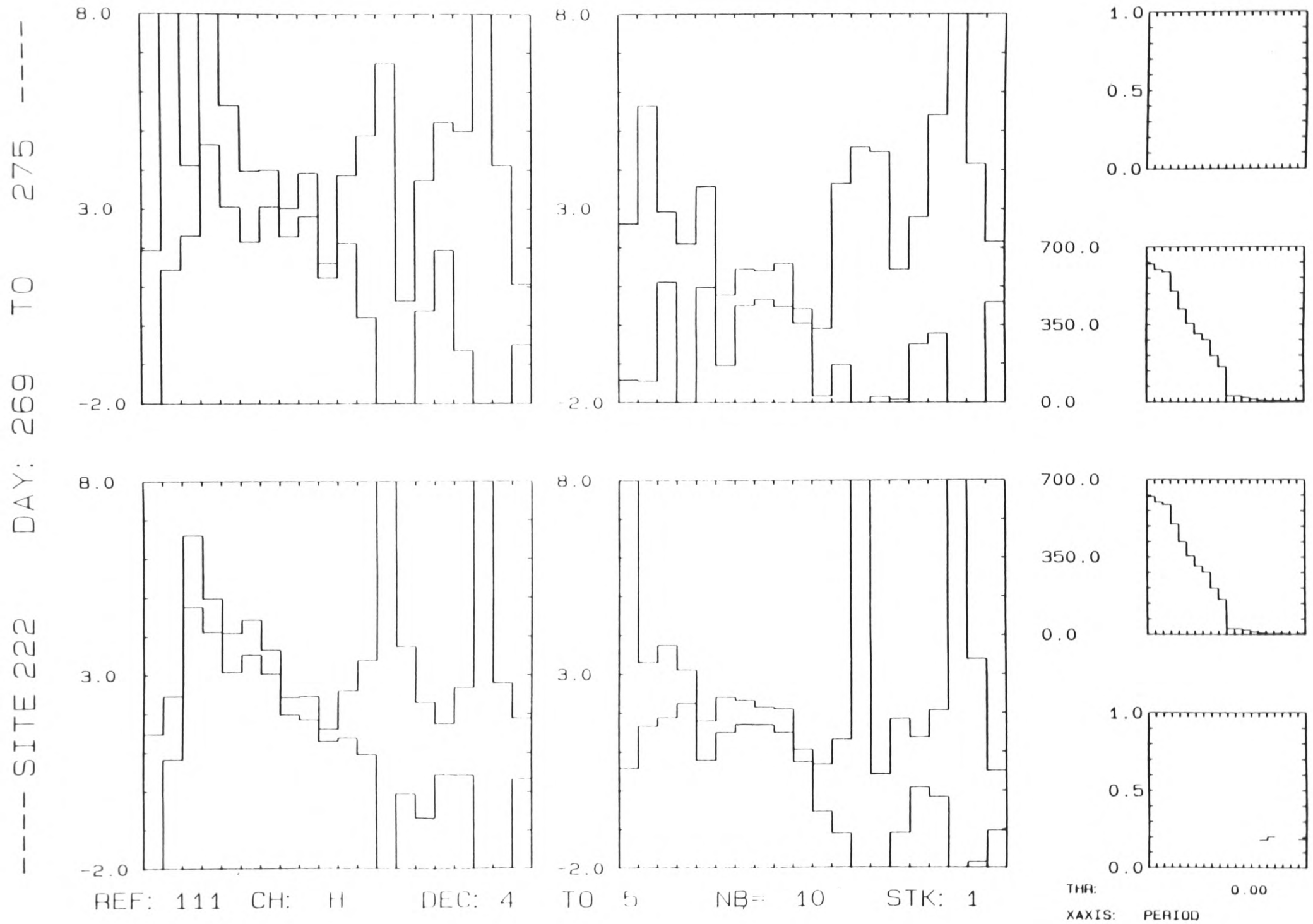
8.0
3.0
-2.0
8.0
3.0
-2.0
1.0
0.5
0.0
700.0
350.0
0.0
1.0
0.5
0.0
THR: 0.00
XAXIS: PERIOD
---- SITE 222 DAY 269 TO 275 ----
REF: 111 CH: H DEC: 4 TO 5 NB= 10 STK: 1

Figure III.21.a. Remote reference estimates of Zxy and Zyx, using $\underline{H}$ as reference with predicted coherence estimates equal to 0.0.

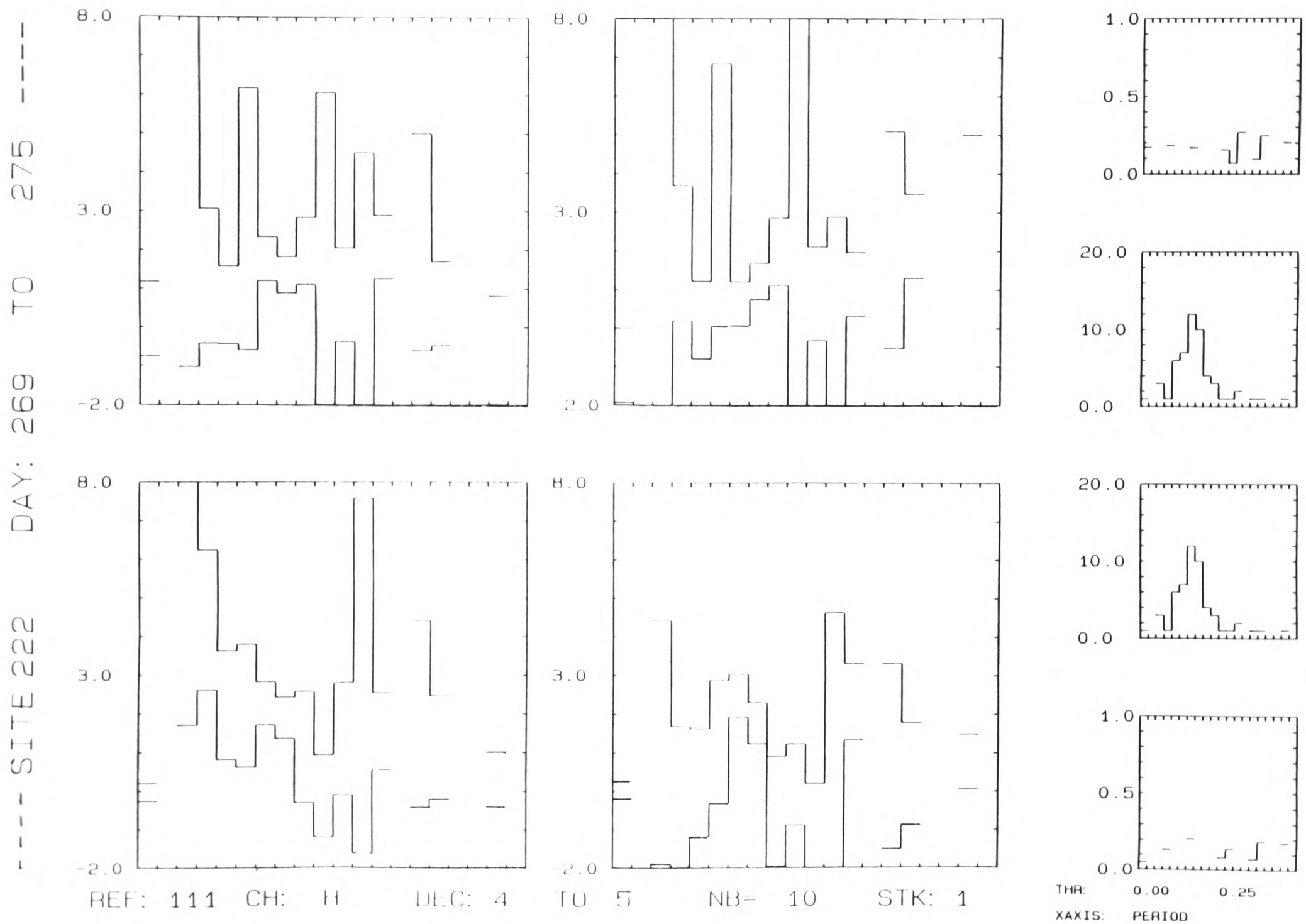
---- SITE 222 DAYS 269 TO 275 ----
8.0
3.0
-2.0
8.0
3.0
-2.0
1.0
0.5
0.0
20.0
10.0
0.0
20.0
10.0
0.0
1.0
0.5
0.0
REF: 111 CH: H DEC: 4
TO 5 NB= 10 STK: 1
THR: 0.00 0.25
XAXIS: PERIOD

Figure III.21.b. As before with predicted coherence estimates in the interval (0.0,0.25].

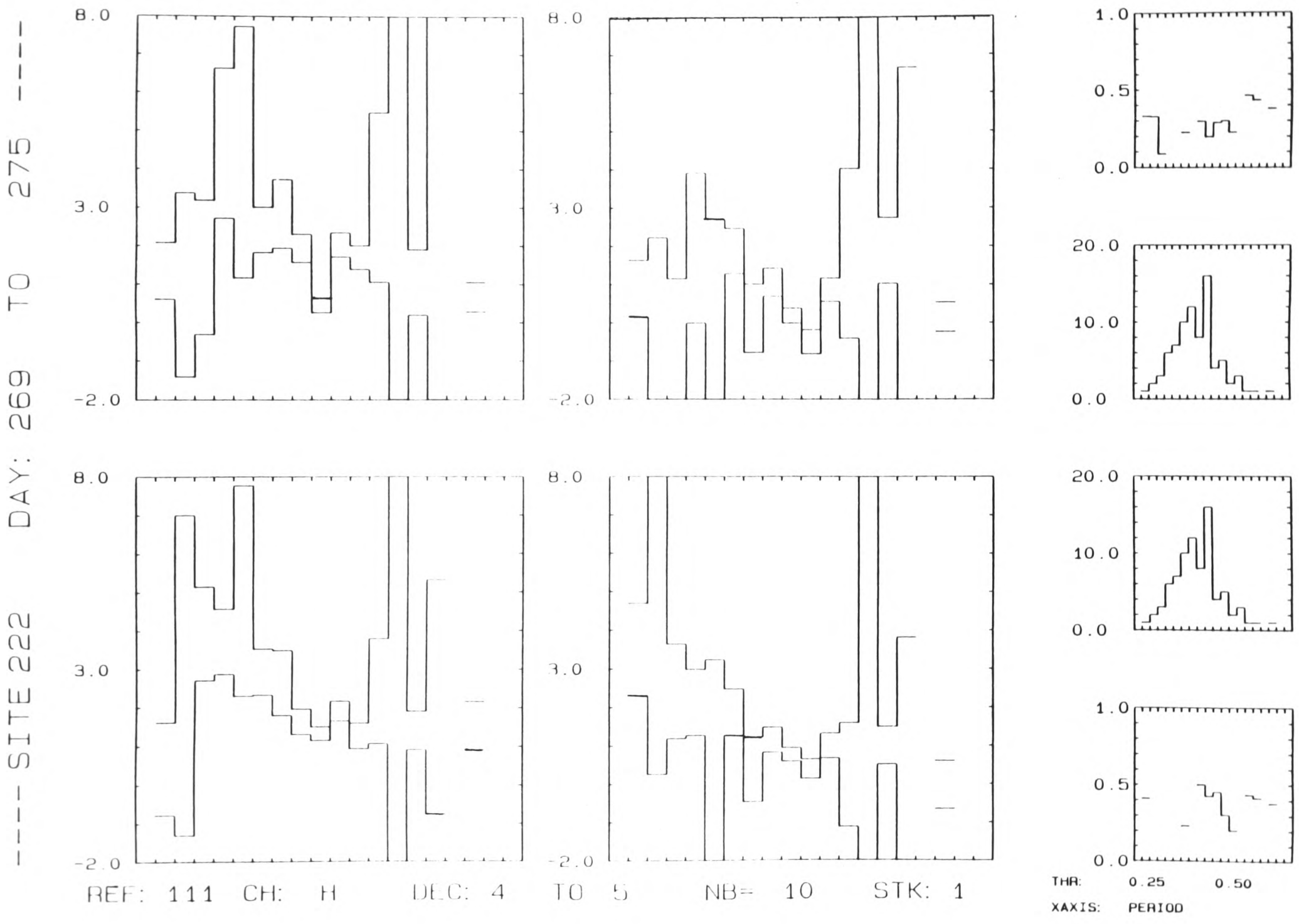
DAY 269 TO 275 ----
---- SITE 222
8.0
3.0
-2.0
8.0
3.0
-2.0
1.0
0.5
0.0
20.0
10.0
0.0
1.0
0.5
0.0
REF: 111 CH: H DEC: 4 TO 5 NB= 10 STK: 1
THR: 0.25 0.50
XAXIS: PERIOD

Figure III.21.c. As before with predicted coherence estimates in the interval (0.25,0.5].

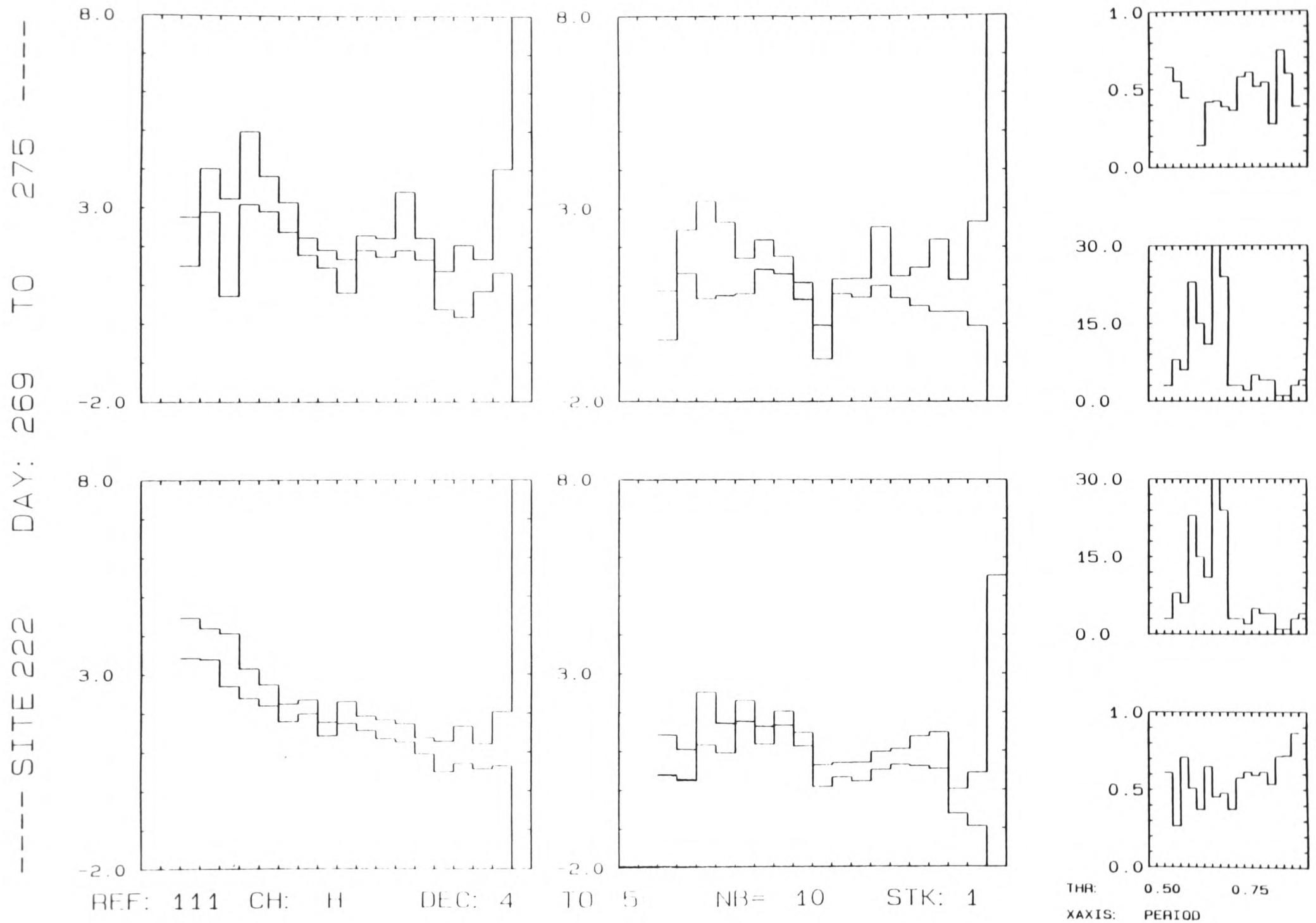
8.0
3.0
-2.0
8.0
3.0
-2.0
1.0
0.5
0.0
30.0
15.0
0.0
1.0
0.5
0.0
---- SITE 222 DAY 269 TO 275 ----
REF: 111 CH: H DEC: 4 TO 5 NB= 10 STK: 1
THR: 0.50 0.75
XAXIS: PERIOD

Figure III.21.d. As before with predicted coherence estimates in the interval (0.5,0.75].

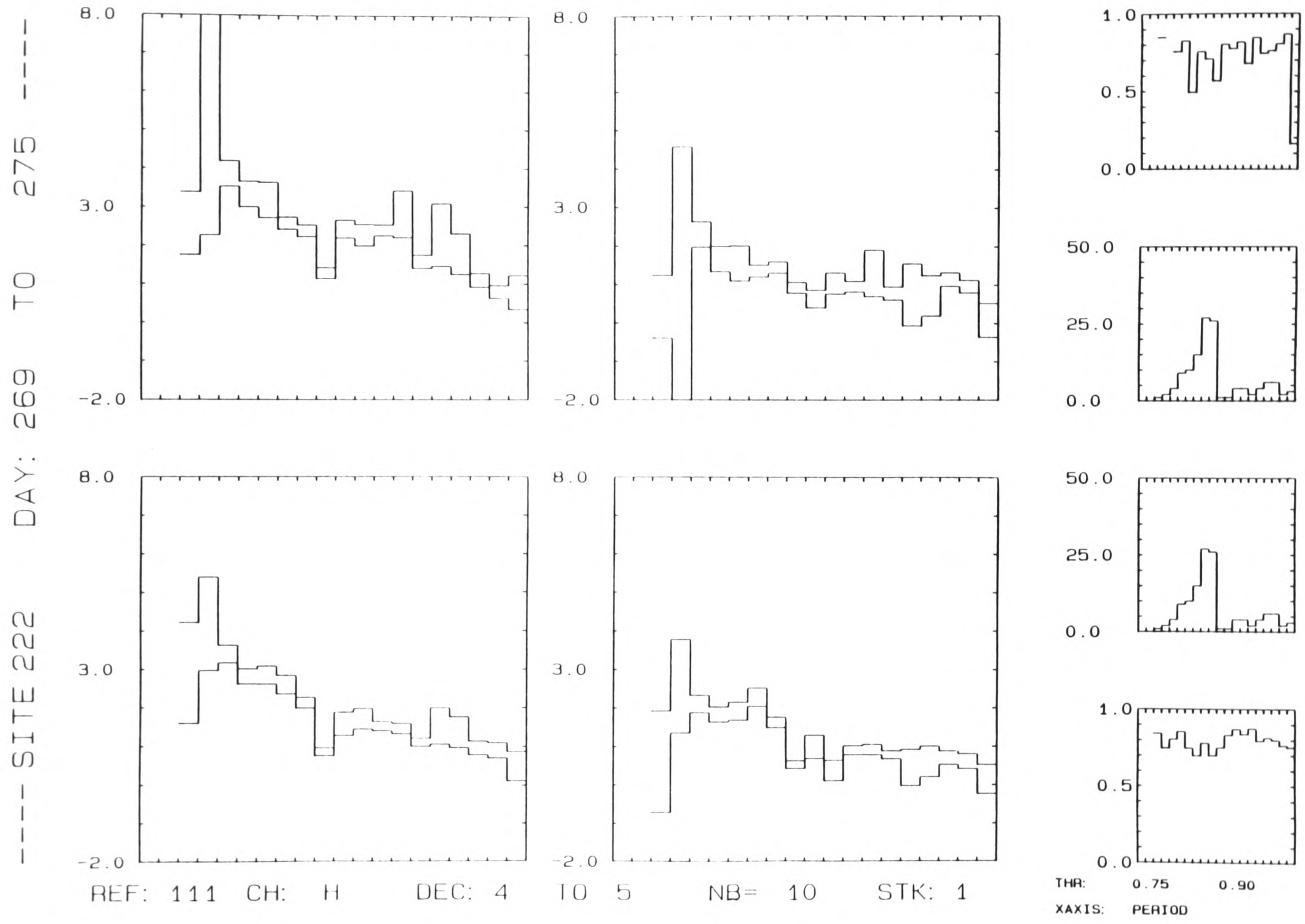
DAY 269 TO 275 ----
---- SITE 222
8.0
3.0
-2.0
8.0
3.0
-2.0
1.0
0.5
0.0
50.0
25.0
0.0
8.0
3.0
-2.0
8.0
3.0
-2.0
1.0
0.5
0.0
REF: 111 CH: H DEC: 4 TO 5 NB= 10 STK: 1
THR: 0.75 0.90
XAXIS: PERIOD

Figure III.21.e. As before with predicted coherence estimates in the interval (0.75,0.9].

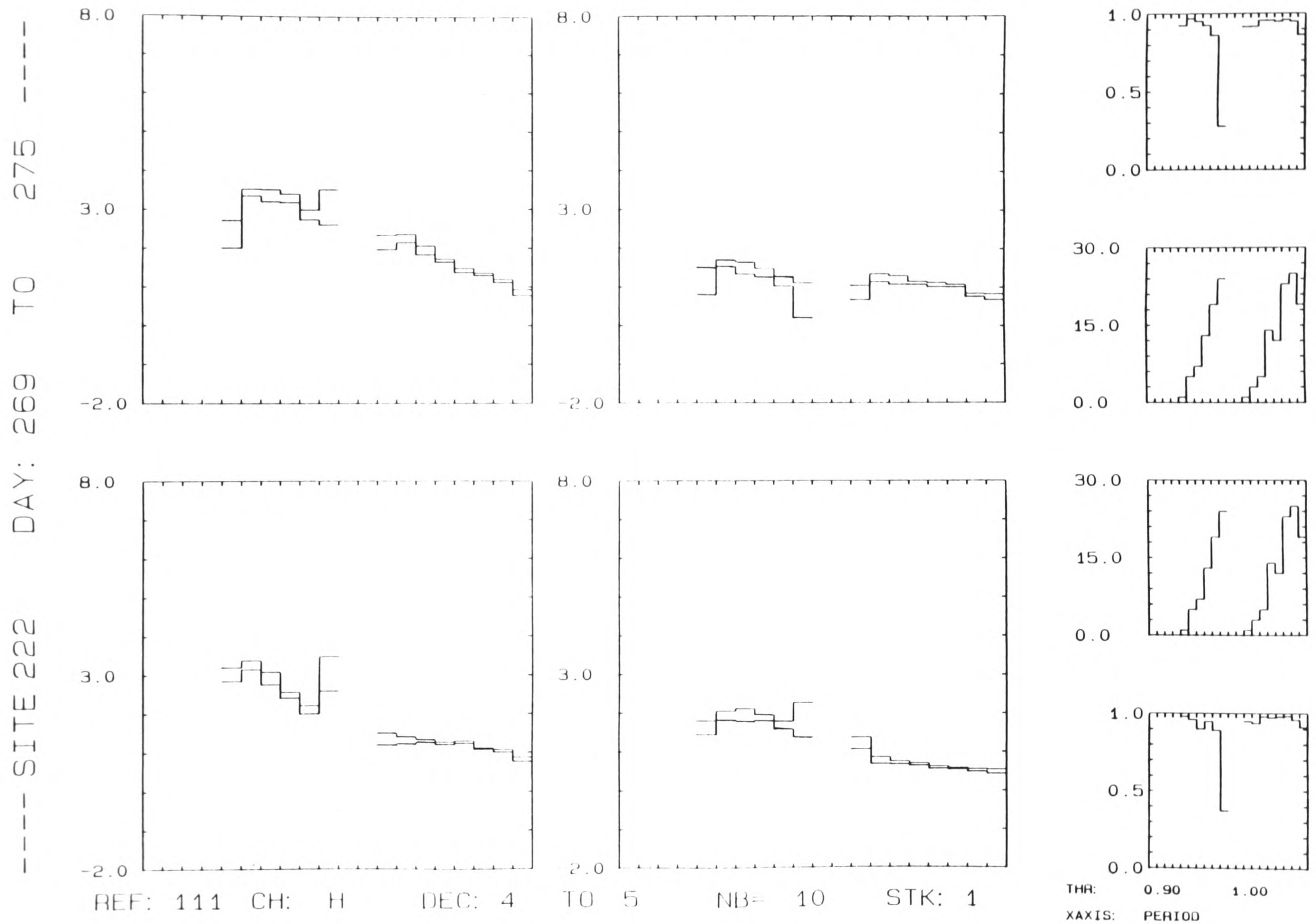
---- SITE 222 DAY 269 TO 275 ----
8.0
3.0
-2.0
8.0
3.0
-2.0
1.0
0.5
0.0
30.0
15.0
0.0
1.0
0.5
0.0
REF: 111 CH: H DEC: 4
TO 5 NB= 10 STK: 1
THR: 0.90 1.00
XAXIS: PERIOD

Figure III.21.f. As before with predicted coherence estimates in the interval (0.9,1.0].

desirable. In this way one can be sure of getting the best estimates, in the sense of signal-to-noise ratios, that the data set can provide.

Comparisons between predicted coherences

The effectiveness of the RR predicted coherence can be better understood by comparing it with its SS counterpart. It is necessary to change the notation in order to make the distinction between SS and RR coherences, as well as between impedance and admittance related coherence values. Drop the sub-indexes of γ^2_{ijk} and substitute for the symbol of the tensor followed by either L, when dealing with SS (III.34), or by either R or S (III.50), in accordance with the remote reference field. From now on R will be used for the remote magnetic field while S will be used for the remote electric field. Under this notation, $\gamma^2_{3,2}$ and $\gamma^2_{4,2}$ will be written as $\gamma^2_{z,L}$ for the SS case, or as either $\gamma^2_{z,R}$ or $\gamma^2_{z,S}$ when R or S is used as a remote reference, respectively.

It was observed that the impedance-related SS estimate of the predicted coherence is always equal to or greater than its RR estimate coherence, irrespective of the remote channel, i.e.

$$\hat{\gamma}^2_{z,L} \geq \hat{\gamma}^2_{z,(R,S)} \qquad \text{(III.53)}$$

As this empirical result holds true for all bands, band 1 of decade 4, centred at 89.7s, can be chosen to illustrate this relation. In figure III.22 estimates of $\hat{\gamma}^2_{z,R}$ are plotted against $\hat{\gamma}^2_{z,L}$, with both Ex and Ey as outputs, using all data windows of the test data set, i.e. 630 realizations.

In figure III.22 there are several points where one or both coherences are zero. It is worth having a closer look at those points because they shed more light on the question of how effective RR and SS predicted coherences are in rejecting noisier realizations. Effectiveness is used here in the sense of recognizing and rejecting only the noisier realizations. This investigation can be done in terms of histograms, accumulating coherence estimates which fall in one of the 6 intervals (III.38) as was done in figure III.5. Figure III.23 shows the distribution of points $\hat{\gamma}^2_{z,R}$ against $\hat{\gamma}^2_{z,L}=0$ on the top row and $\hat{\gamma}^2_{z,L}$ against $\hat{\gamma}^2_{z,R}=0$ on the bottom row. Both Ex and Ey output cases are shown together for the whole data set, i.e. 1260 estimates are analysed. The left boxes in the figure correspond to decade 4 while the right ones correspond to decade 5. Apart from the obvious fact that if $\hat{\gamma}^2_{z,L}=0$

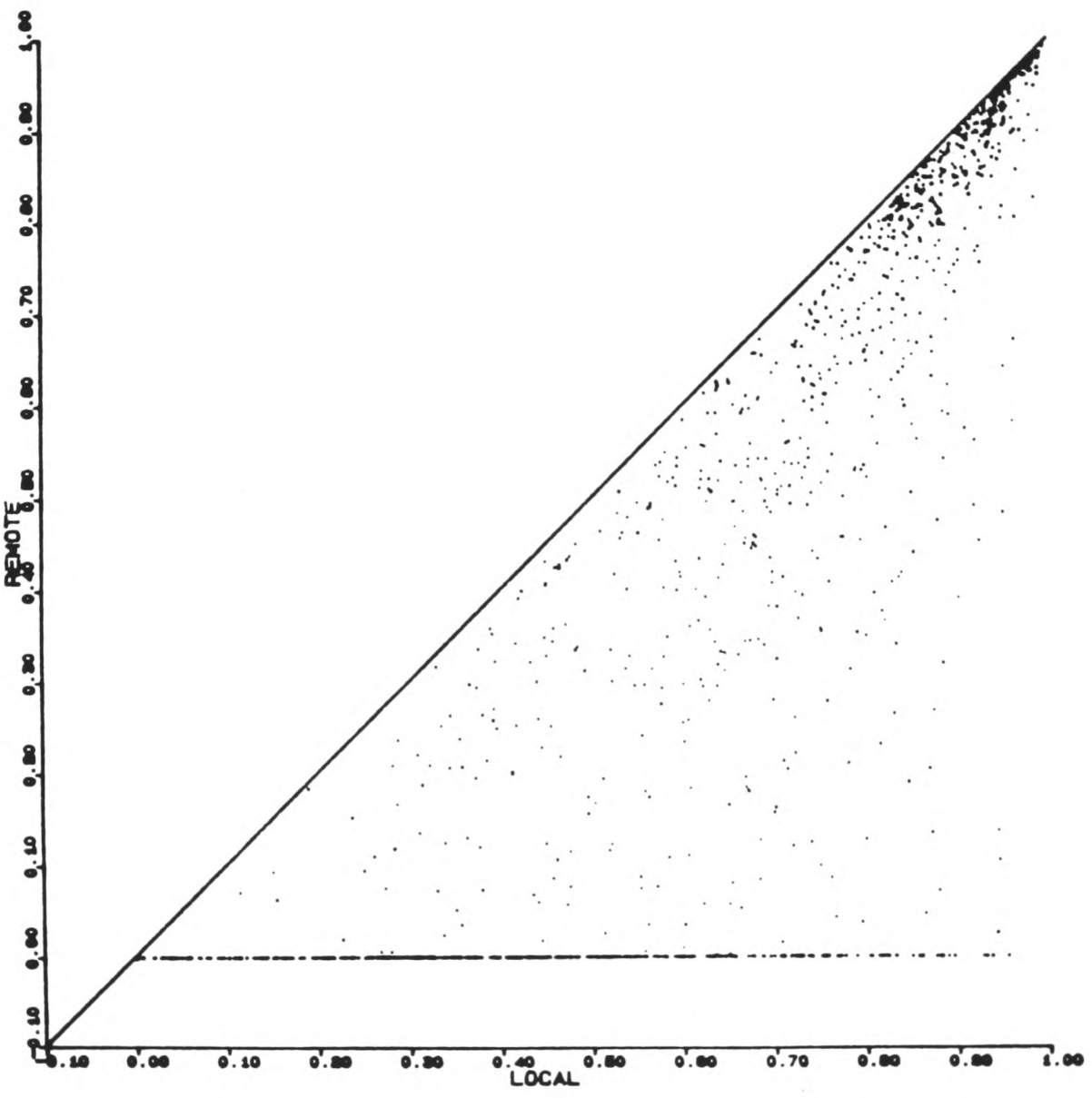

SIT: 222 Z REF: 111 Z H

DAY: 269 TO 275 DEC: 4 BAND 1

Figure III.22. Plot of $\hat{\gamma}^2_{\ell,R}$ against $\hat{\gamma}^2_{\ell,L}$ for band 1, decade 4 with Ex and Ey as outputs. The equivalence line $\hat{\gamma}^2_{\ell,R} = \hat{\gamma}^2_{\ell,L}$ is also shown.

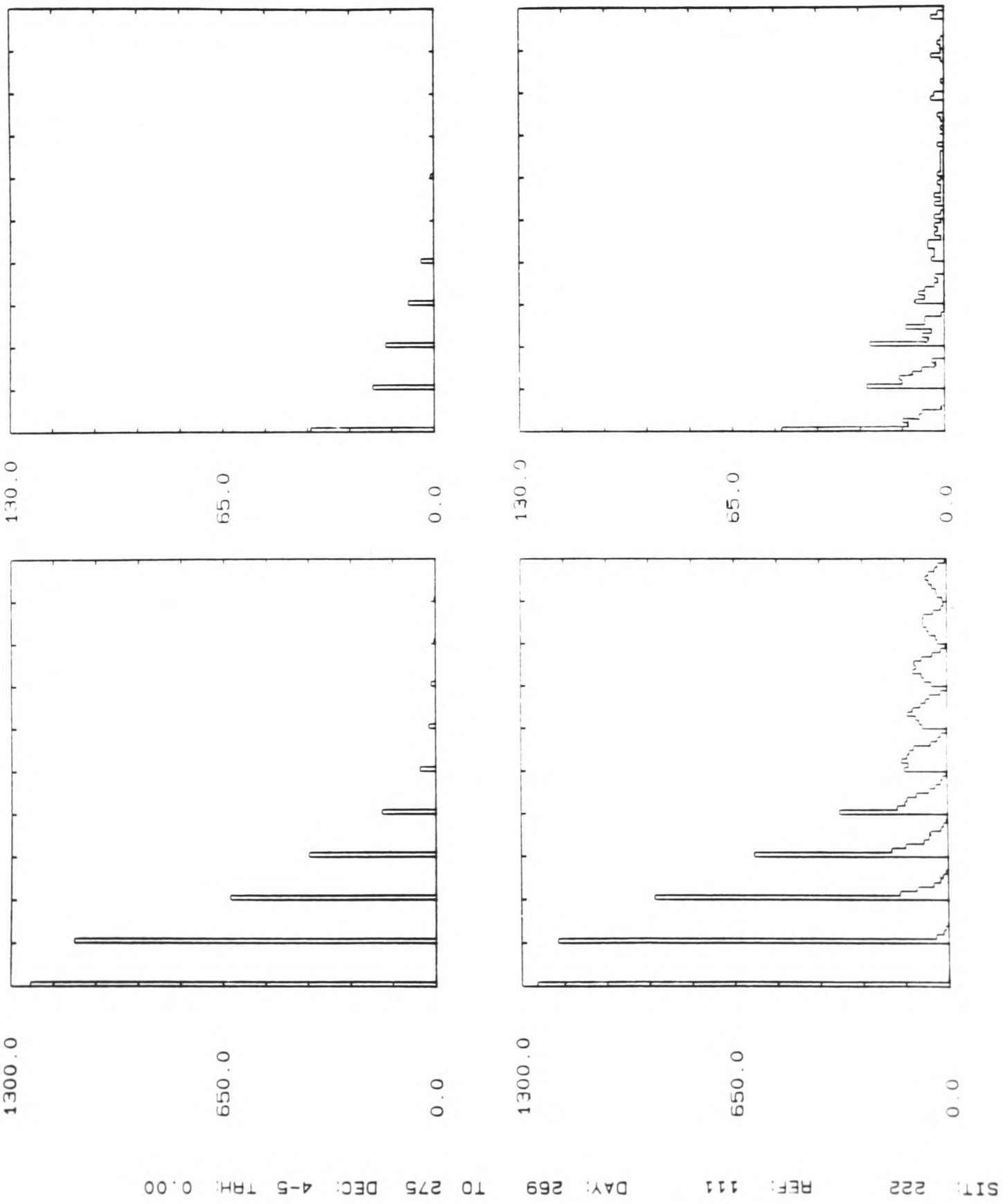
130.0
65.0
0.0
1300.0
650.0
0.0
130.0
65.0
0.0
1300.0
650.0
0.0
SIT: 252 REF: 111 DAY: 269 TO 275 DEC: 4-5 TRK: 0.00

Figure III.23. Histograms showing the distribution of points $\hat{\gamma}^2_{2,R}$ against $\hat{\gamma}^2_{2,L}=0$ on the top row, and of $\hat{\gamma}^2_{2,L}$ against $\hat{\gamma}^2_{2,R}=0$ on the bottom row. Decade 4 histograms are in the first column while decade 5 ones are in the second.

then $\hat{\gamma}^2_{\epsilon,R}=0$, it is also possible to see that at longer periods the probability that $\hat{\gamma}^2_{\epsilon,L}\to 1$ for $\hat{\gamma}^2_{\epsilon,R}=0$ increases. And more important, this happens at bands where the signal-to-noise ratios are higher. It is observed that SS predicted coherences can be as high as 1.00 but have a null RR counterpart. Therefore SS coherences can be misleading even at high values, as can be seen in figures III.22 and III.23. The picture that emerges when the electric field is used as a remote reference is very similar. This together with (III.53) indicate that the predicted coherence estimate obtained using the electric field as a remote reference, is a reliable measure of the noise content of a data window.

This comparative investigation can be extended to the predicted coherences estimated using the admittance tensor, $\underline{\underline{Y}}$. This extension is justified since the upward biased SS estimate of the impedance tensor is calculated by inverting the admittance, (III.25). Relation (III.53) does not hold any longer as it can be seen when plotting $\hat{\gamma}^2_{Y,(R,S)}$ against $\hat{\gamma}^2_{Y,L}$ as estimates now lie on both sides of the equivalence diagonal, irrespective of the choice of the remote channels, R or S. Figure III.24 shows a plot of $\hat{\gamma}^2_{Y,R}$ against $\hat{\gamma}^2_{Y,L}$ for band 1, decade 4.

Coherence selection of data subsets

It is worth stressing that relation (III.53) holds irrespective of the choice of the remote fields. This suggests that $\hat{\gamma}^2_{\epsilon,R}$ and $\hat{\gamma}^2_{\epsilon,S}$ are both of comparable efficiency in selecting adequate data sets, with respect to their noise content. The composition of data subsets selected by using either R or S and setting several thresholds for the predicted coherences in the range [0,1] is investigated. The comparison of impedance tensor estimates using R- and S-derived data subsets brings new facts to light. Test 1 with thresholds 0.1 and 0.5 is still used as an acceptance criterion. Only the magnetic field is used as a remote reference for the final estimate of $\underline{\underline{Z}}$, but both $\hat{\gamma}^2_{\epsilon,R}$ and $\hat{\gamma}^2_{\epsilon,S}$ are calculated and then used in the selection of data subsets. Three data subsets are selected: an R-derived, an S-derived and an X-derived data subset, which contains the realizations belonging to both previous subsets. It is worth remembering that $\hat{\gamma}^2_{\epsilon,R}$ is used to select the first data subset, while $\hat{\gamma}^2_{\epsilon,S}$ is used to select the second one. In all cases the R-derived set is larger than the S-derived one, the difference between them being relatively greater for decade 5. Data belonging to the intercession of the two data sets represent most of the accepted realizations. The realizations in the intercession of the R- and S-derived data sets contribute 71%, or more, of all the accepted

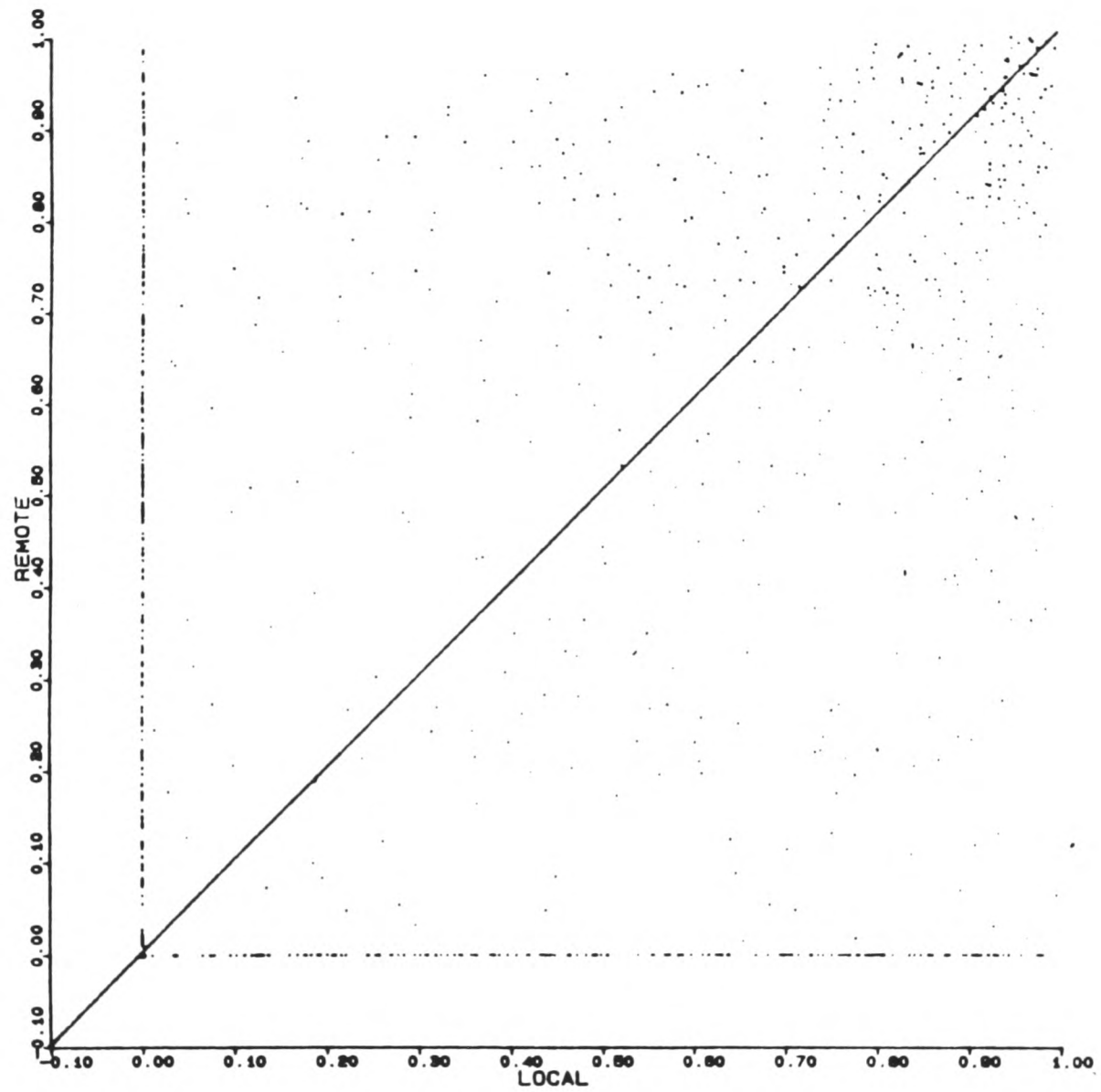

SIT: 222 Y REF: 111 Y H

DAY: 269 TO 275 DEC: 4 BAND 1

Figure III.24. Plot of $\hat{\gamma}^2_{z,R}$ against $\hat{\gamma}^2_{y,L}$ for band 1, decade 4, with Ex and Ey as outputs. The equivalence line $\hat{\gamma}^2_{y,R} = \hat{\gamma}^2_{y,L}$ is also shown.

realizations.

The R-derived results are used as a basis for comparison. Start with R- and S-derived data subsets. Figure III.25 shows the estimates for the off-diagonal elements of $\hat{\underline{\underline{Z}}}$, using R- (solid lines) and S-derived (dashed lines) data subsets. Call them $\hat{\underline{\underline{Z}}}^{R}$ and $\hat{\underline{\underline{Z}}}^{S}$, respectively. Both estimates show similar values and, apart from bands where there are fewer realizations, both estimates agree well. This becomes more evident for the higher threshold γ_t=0.5; in this case the two group of estimates are comparable using criteria like smoothness, lower variances and high predicted coherences. Similar results are obtained when comparing R- and X-derived subsets. Figure III.26 shows $\hat{\underline{\underline{Z}}}^{R}$ (solid lines) and $\hat{\underline{\underline{Z}}}^{X}$ (dashed lines) estimates for both thresholds 0.1 and 0.5. As can be seen for the lower threshold the $\underline{\underline{Z}}^{X}$estimates appear smoother, have lower variances and show higher predicted coherences than the corresponding $\hat{\underline{\underline{Z}}}^{R}$estimates. For the higher acceptance threshold both estimates become again comparable although $\hat{\underline{\underline{Z}}}^{X}$predicted coherences are still higher than their counterparts.

Although remote reference estimates are poor when a remote electric field is used, the predicted coherence is still effective in detecting noise present in the measured powers. Its utility lies in data winnowing or rejection, yielding cleaner data sets. This can be shown using the single site least-squares framework on these RR selected data subsets. The motivation behind it is the expectation of a significant bias-error reduction, as a result of lower noise levels on the selected subsets. As this reduction should be achieved irrespective of the remote channels, it is more interesting to restrict this investigation to the S-selected data subsets. Estimates of $\underline{\underline{Z}}$ are obtained through the SS analysis described in this chapter.

Start imposing $(\gamma_t)_{z,s}$=0.1 as a threshold for the RR derived predicted coherence $\gamma_{z,s}$. Relation (III.53) shows that any threshold $(\gamma_t)_{z,L} \geq 0.1$ may be chosen for the SS derived predicted coherences. Figure III.27 shows the SS estimates of the off-diagonal elements of $\underline{\underline{Z}}$ using thresholds $(\gamma_t)_{z,L}$=0.1,0.5,0.85. A reduction in the bias error is evident for the two lower thresholds, viz. compare with figure III.13. The use of the highest threshold produces similar results as the SS analysis shown in figure III.6.a. Further reduction of bias errors is achieved at lower SS predicted coherences thresholds if RR coherence threshold is raised to 0.5. Now estimates are comparable to SS results selected at much higher thresholds. This can be seen comparing figure III.28 with figure

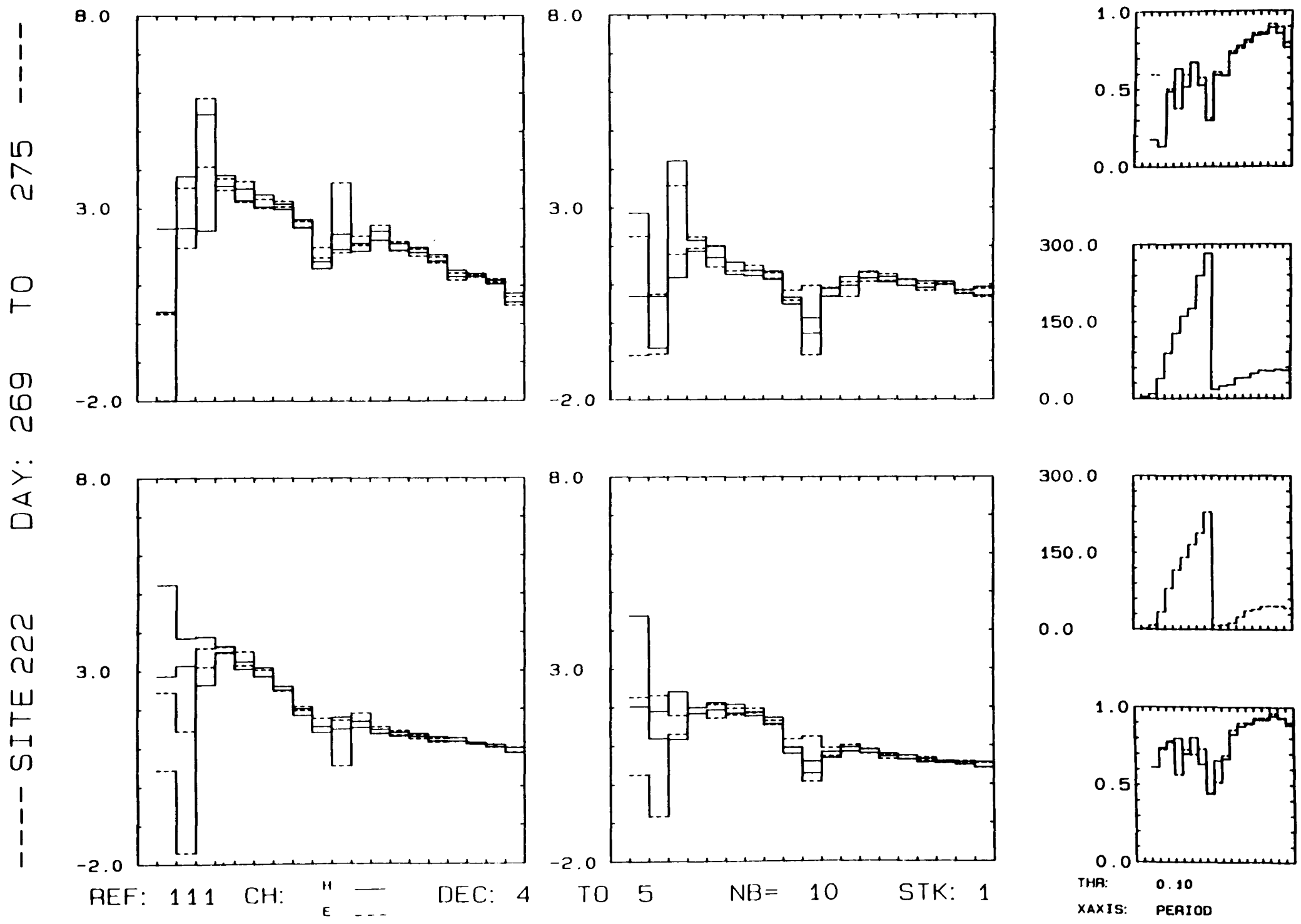
269 TO 275 ----
DAY
--- SITE 222
8.0
3.0
-2.0
8.0
3.0
-2.0
1.0
0.5
0.0
300.0
150.0
0.0
8.0
3.0
-2.0
8.0
3.0
-2.0
1.0
0.5
0.0
REF: 111 CH:
H
E
DEC: 4
TO 5
NB= 10
STK: 1
THR: 0.10
XAXIS: PERIOD

Figure III.25.a. Remote reference estimates of Z^{R}_{xy}, Z^{S}_{xy}, Z^{R}_{yx}, and Z^{S}_{yx} using R-selected (solid lines) and S-selected (dashed lines) data subsets. Remote reference threshold γ_t=0.1.

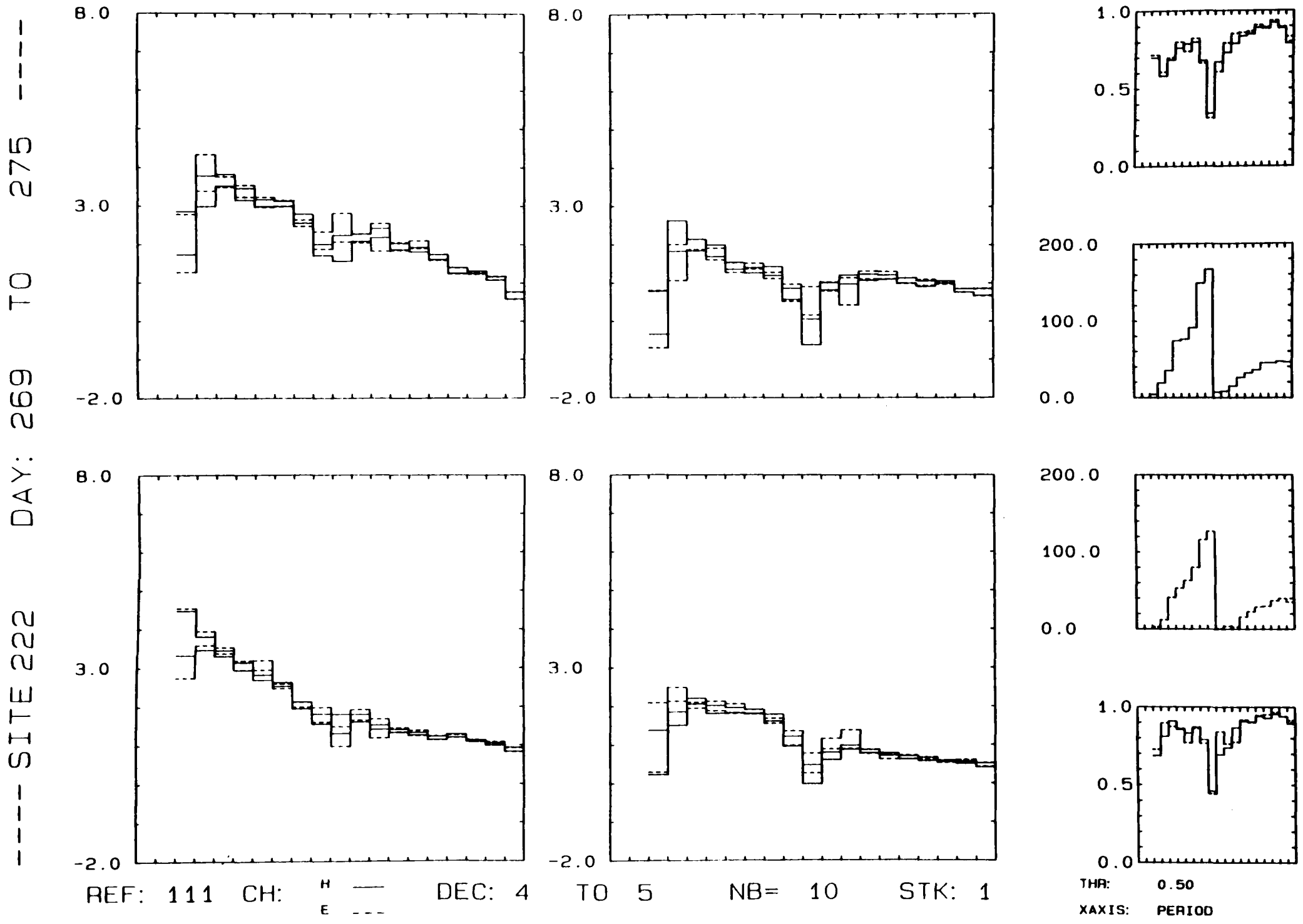
8.0
3.0
-2.0
8.0
3.0
-2.0
1.0
0.5
0.0
200.0
100.0
0.0
1.0
0.5
0.0
THR: 0.50
XAXIS: PERIOD
---- SITE 222 DAY 269 TO 275 ----
REF: 111 CH: H —— E --- DEC: 4 TO 5 NB= 10 STK: 1

Figure III.25.b. Same quantities for a remote reference threshold γ_t=0.5.

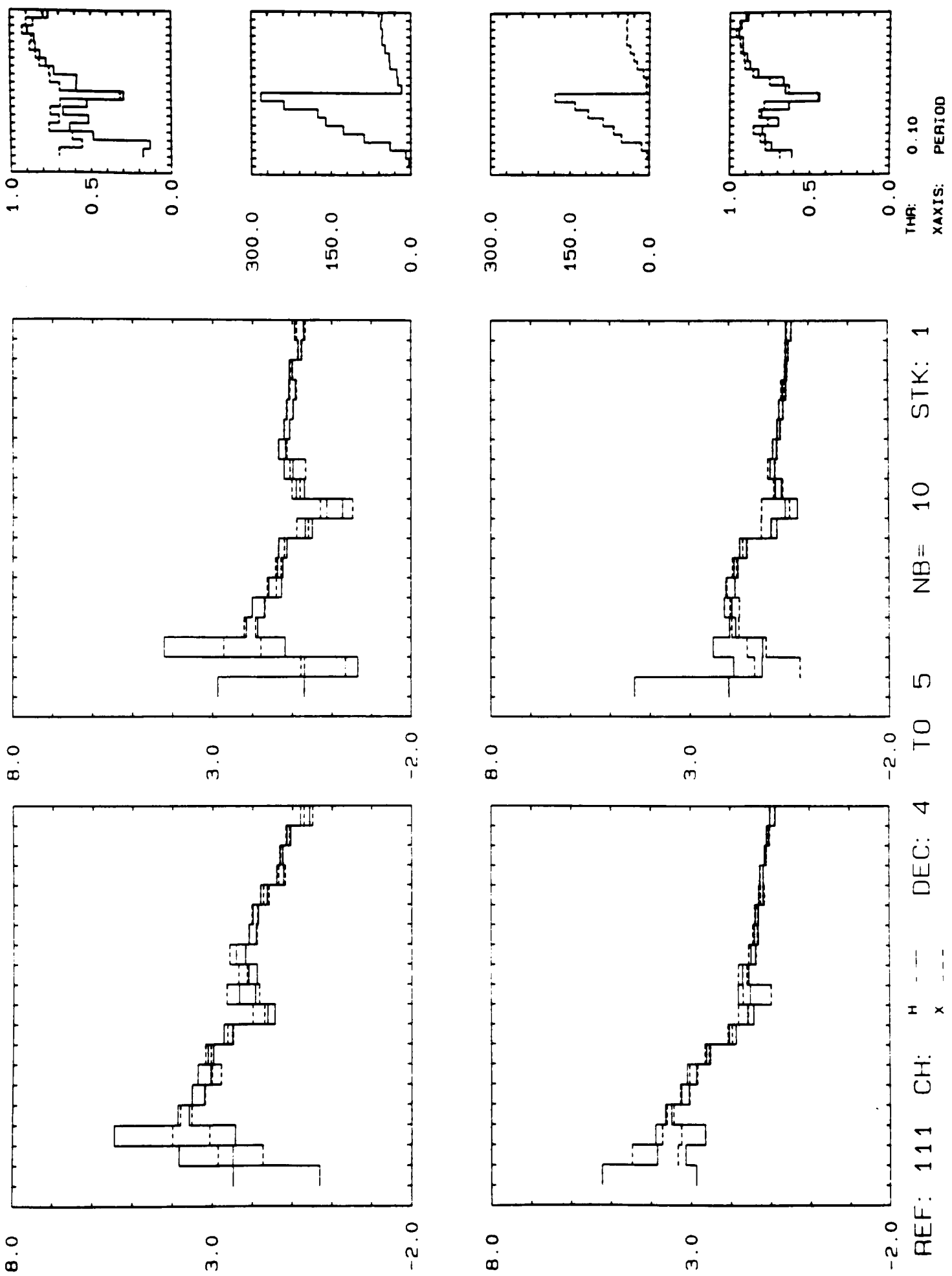
---- SITE 222 DAY: 269 TO 275 ----
REF: 111 CH: H — DEC: 4 TO 5 NB= 10 STK: 1
THR: 0.10
XAXIS: PERIOD
8.0
3.0
-2.0
1.0
0.5
0.0
300.0
150.0
0.0

Figure III.26.a. Remote reference estimates of Z_{xy}^{R}, Z_{xy}^{x}, Z_{yx}^{R}, and Z_{yx}^{x} using R-selected (solid lines) and X-selected (dashed lines) data subsets. Remote reference threshold $\sigma_t = 0.1$.

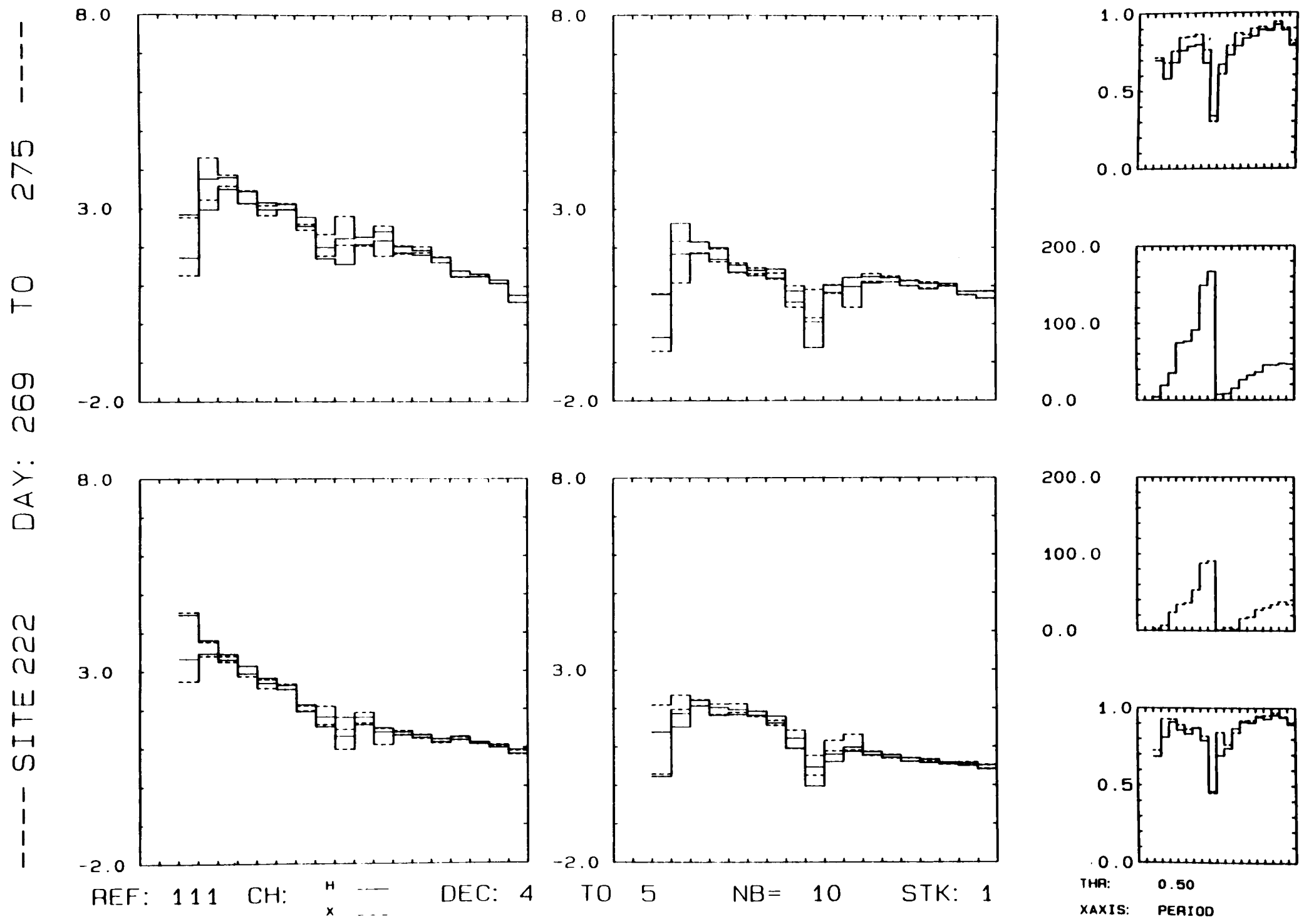
--- SITE 222 DAY 269 TO 275 ---
8.0
3.0
-2.0
8.0
3.0
-2.0
1.0
0.5
0.0
200.0
100.0
0.0
200.0
100.0
0.0
1.0
0.5
0.0
REF: 111 CH: H X
DEC: 4
TO 5
NB= 10
STK: 1
THR: 0.50
XAXIS: PERIOD

Figure III.26.b. Same quantities for a remote reference threshold $\gamma_t = 0.5$.

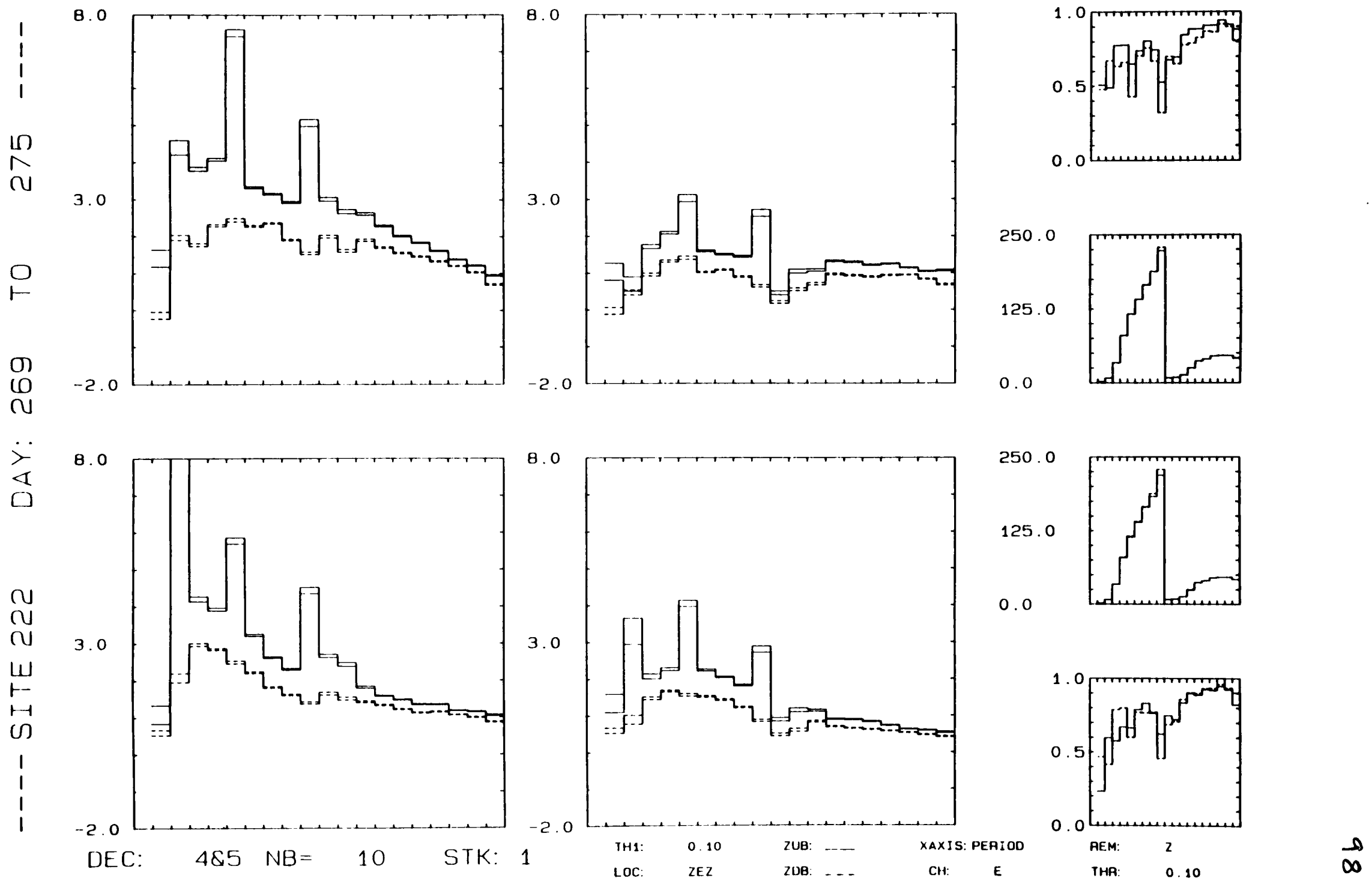
269 TO 275 ----
---- SITE 222 DAY:
8.0
3.0
-2.0
8.0
3.0
-2.0
1.0
0.5
0.0
250.0
125.0
0.0
8.0
3.0
-2.0
8.0
3.0
-2.0
1.0
0.5
0.0
DEC: 4&5 NB= 10 STK: 1
TH1: 0.10 ZUB: ___ XAXIS: PERIOD REM: Z
LOC: ZEZ ZDB: - - - CH: E THR: 0.10

Figure III.27.a. Estimates of Zxy and Zyx using SS technique on S-derived data sets for $(\gamma_t)_{z,s}$ =0.1. Both upward biased (solid lines) and downward biased (dashed lines) are shown together with their associated random errors. Local threshold: $(\gamma_t)_{z,L}$ =0.1.

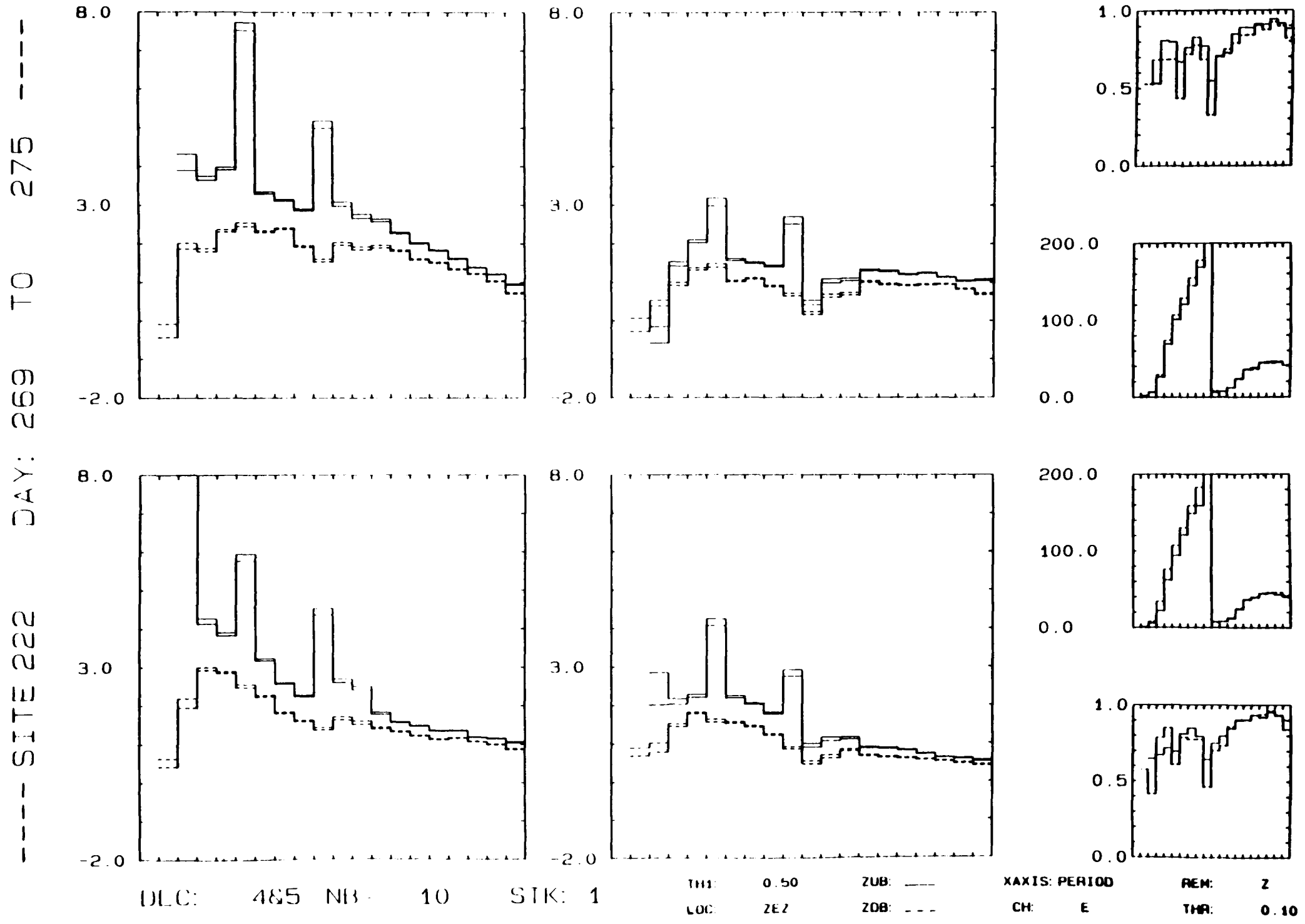
269 TO 275 ----
---- SITE 222 DAY
8.0
3.0
-2.0
8.0
3.0
-2.0
1.0
0.5
0.0
200.0
100.0
0.0
8.0
3.0
-2.0
1.0
0.5
0.0
DLC: 485 NB: 10 STK: 1
TH1: 0.50 ZUB: ___
LOC: ZEZ ZOB: - - -
XAXIS: PERIOD REM: Z
CH: E THR: 0.10

Figure III.27.b. Same quantities using a local threshold of $(\zeta_t)_{2,L} = 0.5$.

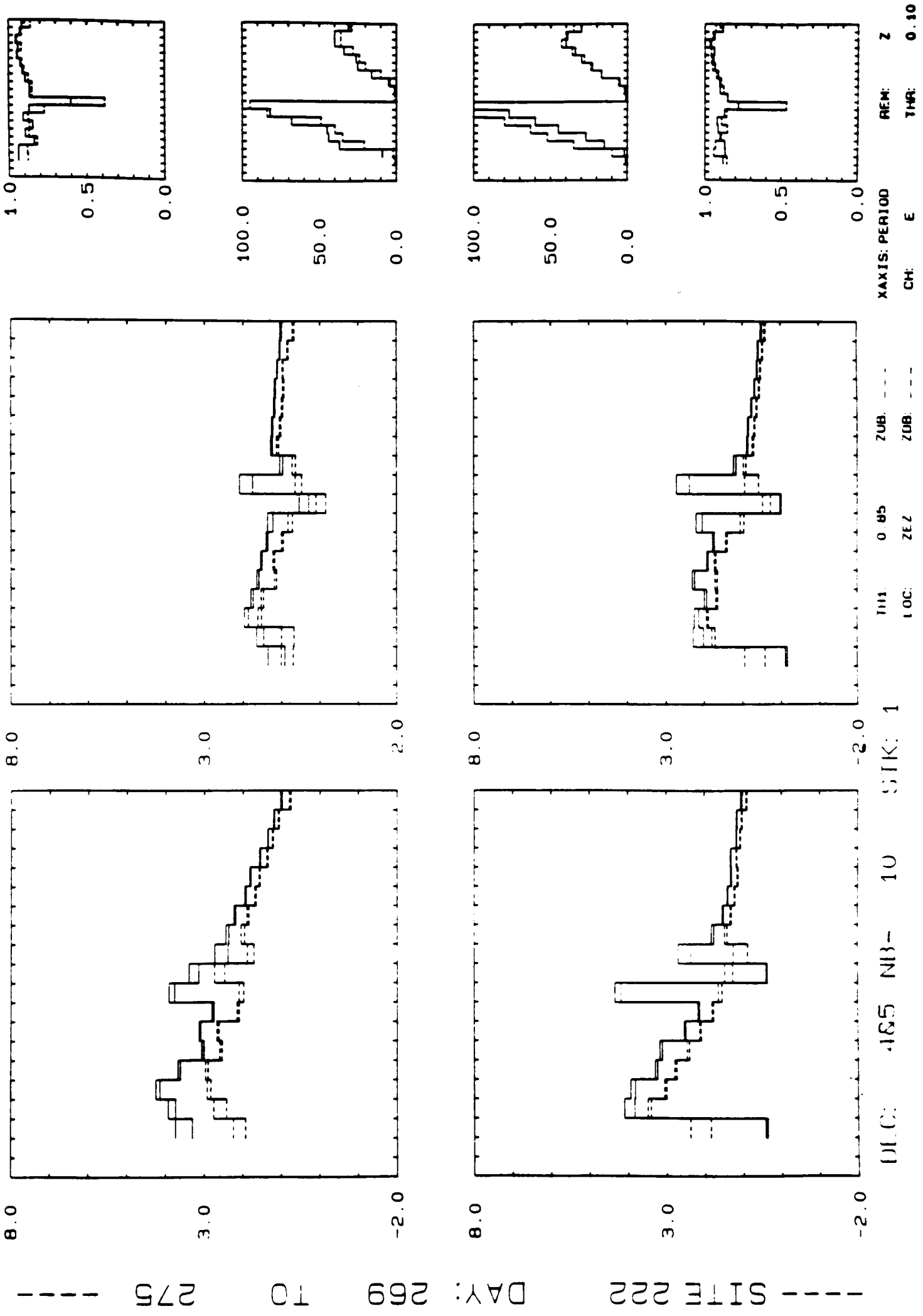
1.0
0.5
0.0
100.0
50.0
0.0
8.0
3.0
-2.0
XAXIS: PERIOD
CH: E
REM: Z
THR: 0.10
---- SITE 222
DAY: 269 TO 275 ----
DEC: 485 NB- 10 SIK:

Figure III.27.c. Same quantities using a local threshold of $(\delta_t)_{z,L} = 0.85$.

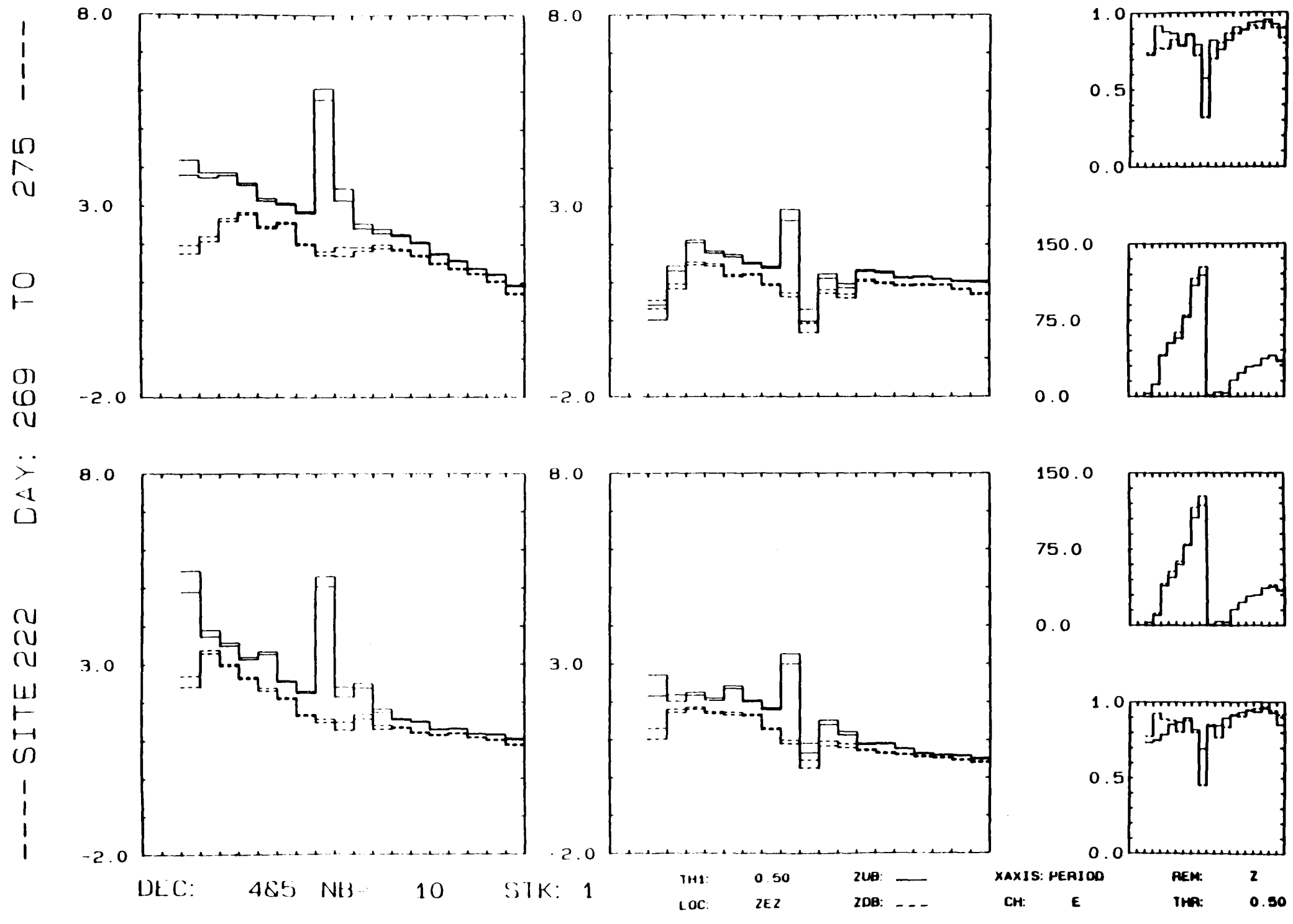
8.0
3.0
-2.0
8.0
3.0
-2.0
1.0
0.5
0.0
150.0
75.0
0.0
1.0
0.5
0.0
269 TO 275 ----
--- SITE 222 DAY
DEC: 4&5 NB= 10 STK: 1
TH1: 0.50
LOC: ZEZ
ZUB: ——
ZDB: - - -
XAXIS: PERIOD
CH: E
REM: Z
THR: 0.50

Figure III.28.a. Estimates of Zxy and Zyx using SS technique on S-derived data sets for $(\gamma_t)_{z,S}$ =0.5. Local threshold: $(\gamma_t)_{z,L}$ =0.5.

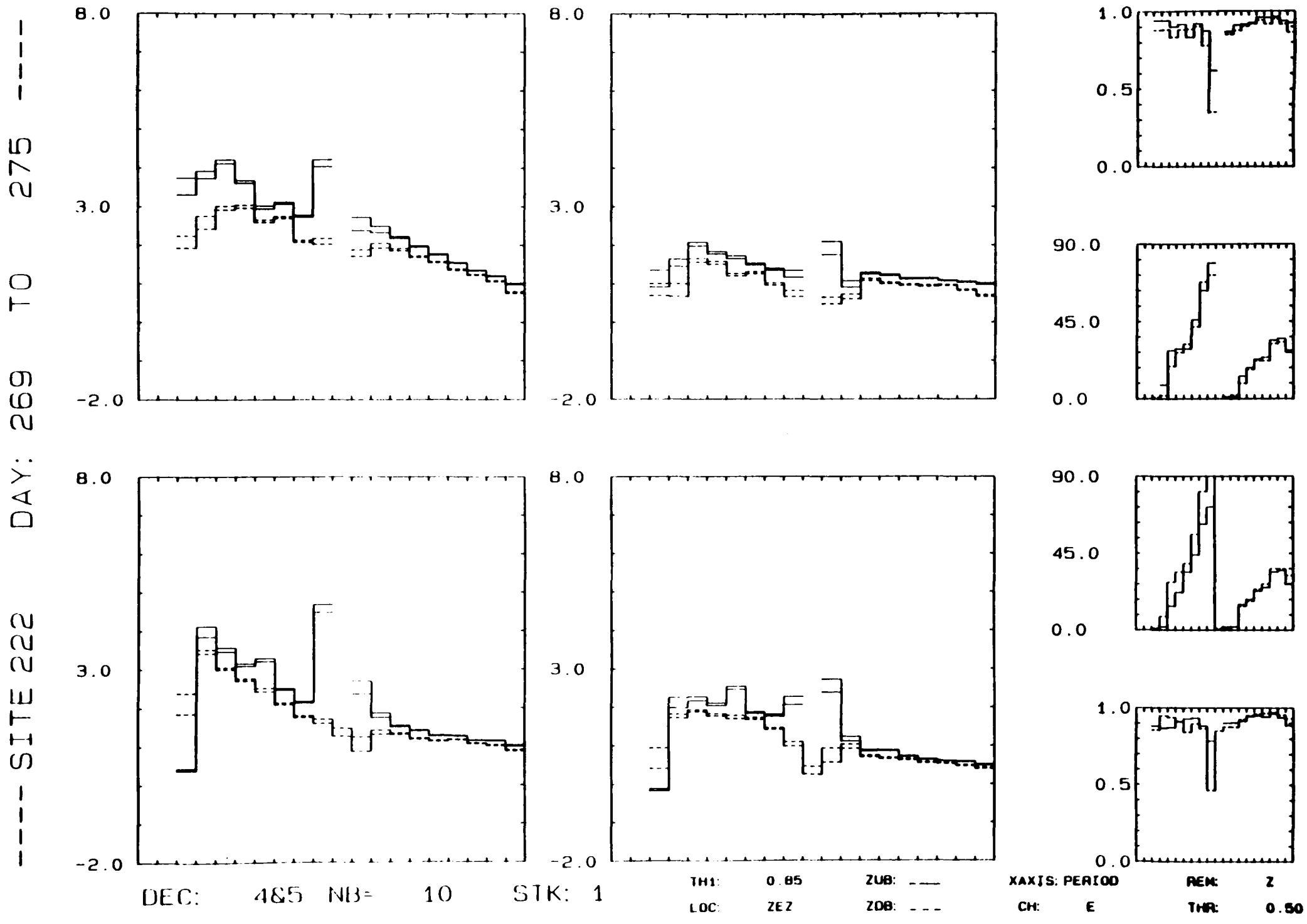
--- SITE 222 DAY 269 TO 275 ---
8.0
3.0
-2.0
8.0
3.0
-2.0
1.0
0.5
0.0
90.0
45.0
0.0
1.0
0.5
0.0
DEC: 485 NB= 10 STK: 1
TH1: 0.85 ZUB: ___
LOC: ZEZ ZDB: - - -
XAXIS: PERIOD REM: Z
CH: E THR: 0.50

Figure III.28.b. Same quantities using a local threshold of $(\gamma_c)_{z,L}=0.85$.

III.6.a. The difference resides in the fact that data windows come from data subsets already selected in terms of signal content using the RR technique. It is important to remember that it is not advisable to set a higher threshold for $\hat{\gamma}^{\ell}_{i,s}$ since the number of the accepted realizations drops significantly. The same conclusions are obtained from R-selected data subsets. In fact S- and R-selected data subsets produce similar SS results.

One may ask the usefulness of using a remote electric reference for selecting data sets since in the end, SS framework is used to estimate $\underline{\underline{Z}}$. This hybrid technique might prove be useful in situations where for any reason, e.g., economic, it is not possible to have remote magnetic channels, but remote electric channels are feasible. Reliable RR estimates of $\underline{\underline{Z}}$ are usually impossible to obtain using a remote electric field. A data subset obtained using this hybrid technique contains only low noise level realizations, so one can be sure to end up with the less biased SS estimates of $\underline{\underline{Z}}$ that is possible from the available data. In addition it should be possible to use the electric information from the remote telluric site as well (Hermance and Thayer, 1975). Another possibility is to use a bias reduction iterative technique (Kao and Rankin, 1977) on the S-selected data subset more effectively than would otherwise be possible. Results obtained from the selected data subsets sets may be located somewhere between the usual SS results and RR results using a remote magnetic field. This can be further illustrated using fractional errors, definition (III.40). Figure III.29 shows the fractional errors for the usual SS results (1), the selected SS results (2) and the RR results (3), using the same threshold $\gamma_t=0.5$.

III.5.4. Signal and Noise Estimation

The predicted coherence (III.50) is directly related to the local noise power normalized with respect to the measured power. It has proved to be an efficient quantity in detecting noisy data windows. Nevertheless signal and noise content in the measured powers give a clearer picture of the quality of the whole data set. In this section signal and noise content in the local fields are estimated using the remote fields. This procedure can be found in the literature (Gamble et al., 1979b). The estimation of the signal and noise fractions in the measured powers is particularly useful in assessing RR result quality since this technique allows the production of estimates irrespective of their noise content.

Assume the RR impedance tensor estimated as in (III.42). The measured local fields $\underline{E}$ and $\underline{H}$ are composed of signal and additive

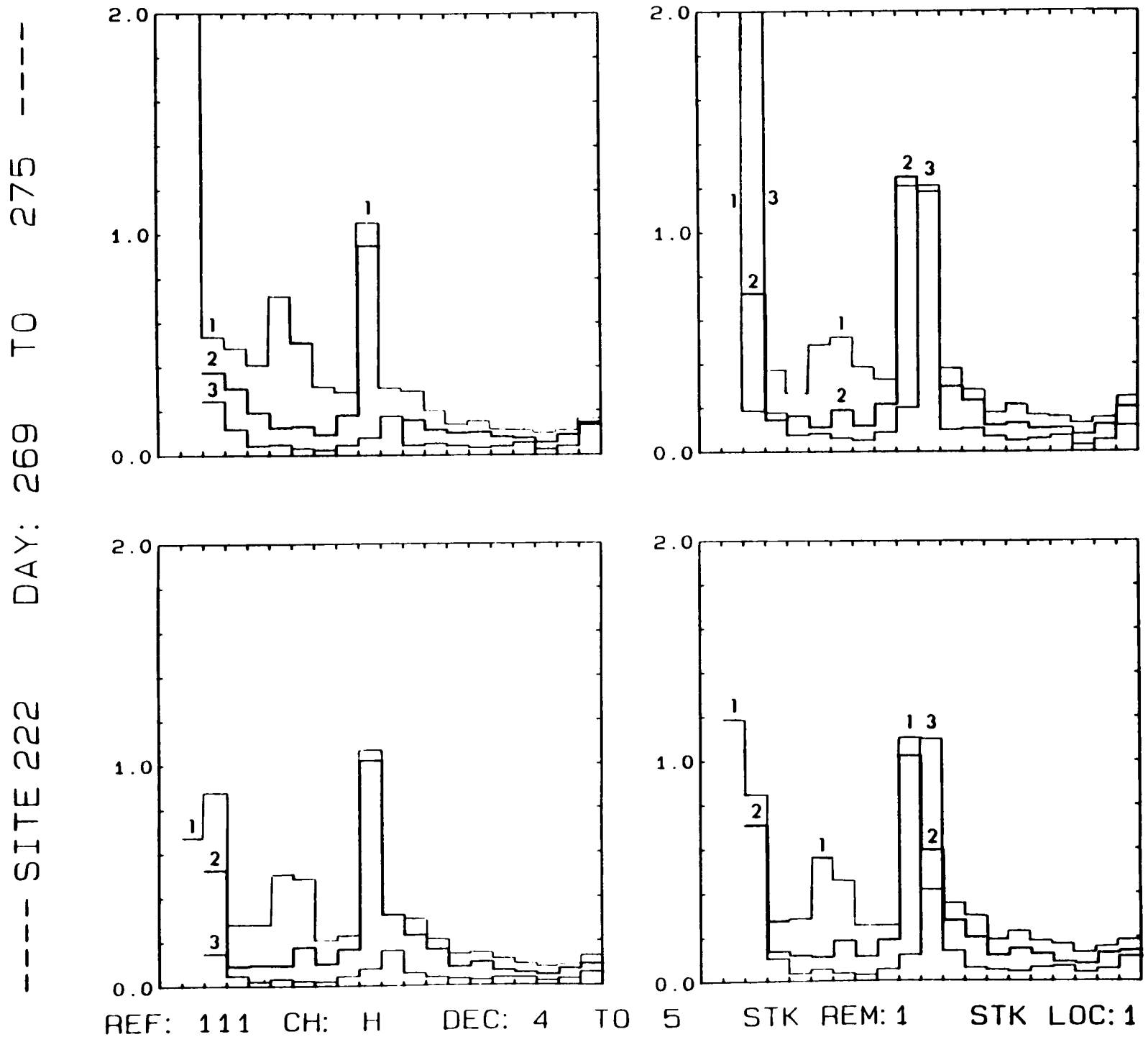

THR LO1: 0.50 ZEZ
THR REF: 0.50

Figure III.29. Fractional errors for Zxy and Zyx using SS technique on the original data set (line 1) and on the S-derived data subset (line 2), and using remote reference technique (line 3). The threshold for all computations is 0.5.

noise as in (III.29). Start with the local electric field. The electric field signal power is given by the hermitian spectral matrix [EsEs], while the noise power is given by

$$[E_n E_n] = [E\ E] - [E_s E_s] \qquad \text{(III.54)}$$

Therefore it is necessary to estimate only the signal power since the noise power is derived directly from it and the measured power. An estimate of the electric field is given by

$$\hat{E} = \hat{Z}^R H \qquad \text{(III.55)}$$

which has contributions from both signal and noise present in the measured fields. Using the basic assumption that noises are uncorrelated with the signals and with each other, dyadics can be constructed with (III.55) to get an estimate like

$$[\hat{E}\ E] = \hat{Z}^R [H\ E] \qquad \text{(III.56)}$$

or [E $\hat{E}$], as there is no reason to prefer one particular order. In particular it is easy to see that [E $\hat{E}$]=[$\hat{E}$ E]†. Moreover unlike [EsEs], [$\hat{E}$ E] is not hermitian. It is therefore reasonable to estimate the signal power by

$$\widehat{[E_s E_s]} = \frac{1}{2}\left\{[\hat{E}\ E] + [E\ \hat{E}]\right\} \qquad \text{(III.57)}$$

which is hermitian. The noise power is estimated using (III.54)

$$\widehat{[E_n E_n]} = [E\ E] - \widehat{[E_s E_s]} \qquad \text{(III.58)}$$

since noise is additive.

The magnetic signal and noise powers are derived in the same way. Start with an estimated magnetic field

$$\hat{H} = (\hat{Z}^R)^{-1} E \qquad \text{(III.59)}$$

to get

$$[\hat{H}\ H] = (\hat{Z}^R)^{-1} [E\ H] \qquad \text{(III.60)}$$

where $(\hat{Z}^R)^{-1}=([E\ R]\ [H\ R]^{-1})^{-1}=[H\ R]\ [E\ R]^{-1}=\hat{Y}$, is the admittance. The estimated signal power is given by

$$[\widehat{\underline{H}_s\,\underline{H}_s}] = \frac{1}{2}\left\{[\hat{\underline{H}}\,\underline{H}] + [\hat{\underline{H}}\,\underline{H}]^{\dagger}\right\} \qquad \text{(III.61)}$$

while the noise power is

$$[\widehat{\underline{H}_m\,\underline{H}_m}] = [\underline{H}\,\underline{H}] - [\widehat{\underline{H}_s\,\underline{H}_s}] \qquad \text{(III.62)}$$

since noise is additive.

Signal and noise powers are investigated in both x and y directions, i.e. the off-diagonal (real) elements of the spectral matrices (III.57), (III.58), (III.61), (III.62). Figure III.30 shows the accumulated signal (solid lines) and noise (dashed lines) powers in the local fields in both x and y directions on the left and right boxes respectively. In this figure the electric field signal and noise contents are displayed on the top row and the magnetics on the bottom row. The estimates have been calculated from the complete data set with no selection. It is easy to see how the signal content increases sharply towards longer periods. The figure shows that signal content of the first three bands of decade 4 can be one or more orders of magnitude below the noise. This indicates that even when it is possible to obtain estimates at those bands, their reliability should be carefully assessed. This is the case when RR estimates are calculated using no rejection criterion as shown in figure III.16. The use of coherence based rejection criteria with relatively low thresholds avoids this problem.

The signal and noise powers can also provide additional information with regard to the previous discussion on S-selected data subsets. It was concluded that the RR predicted coherence is a more powerful parameter in selecting data sets than its SS counterpart irrespective of the choice of the reference channels. The dimensionless signal-to-noise ratios in both x and y directions can be used to compare the three selected data subsets. A lower threshold, 0.1, is chosen to illustrate this point. Figure III.31 shows that the signal-to-noise ratios are almost always lower for the SS selected data set (solid lines) than for both R- (longer dashes) and S-selected (shorter dashes). Both R- and S-selected signal-to-noise ratios tend to follow each other closely.

III.6. Sounding Parameters

Up to this point the earth's response functions have been expressed in terms of the impedance tensor. In this section the results for site 2 will be presented in terms of the usual sounding

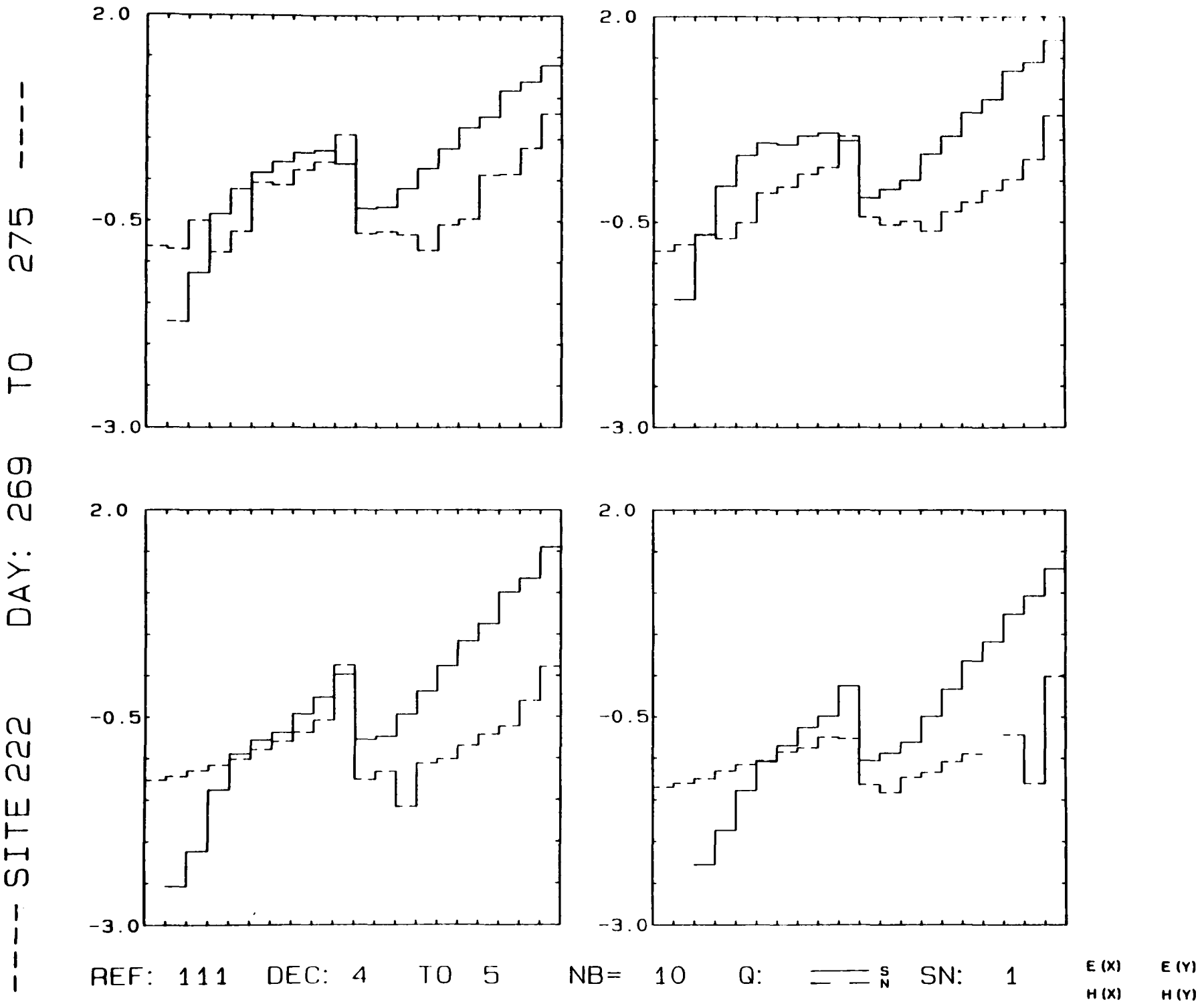
2.0
-0.5
-3.0
2.0
-0.5
-3.0
--- SITE 222 DAY: 269 TO 275 ---
2.0
-0.5
-3.0
2.0
-0.5
-3.0
REF: 111 DEC: 4 TO 5 NB= 10 Q: SN: 1
E (X) E (Y)
H (X) H (Y)

Figure III.30. Estimates for the signal (solid lines) and noise (dashed lines) powers for the local fields $\underline{E}$ and $\underline{H}$. The two top boxes show the correspondent estimates for $\underline{E}$ in the x-direction (left) and y-direction (right). The two bottom boxes show the corresponding estimates for $\underline{H}$, also in the x and y directions. The ordinates are in log(mV/km) for E and log(nT) for H.

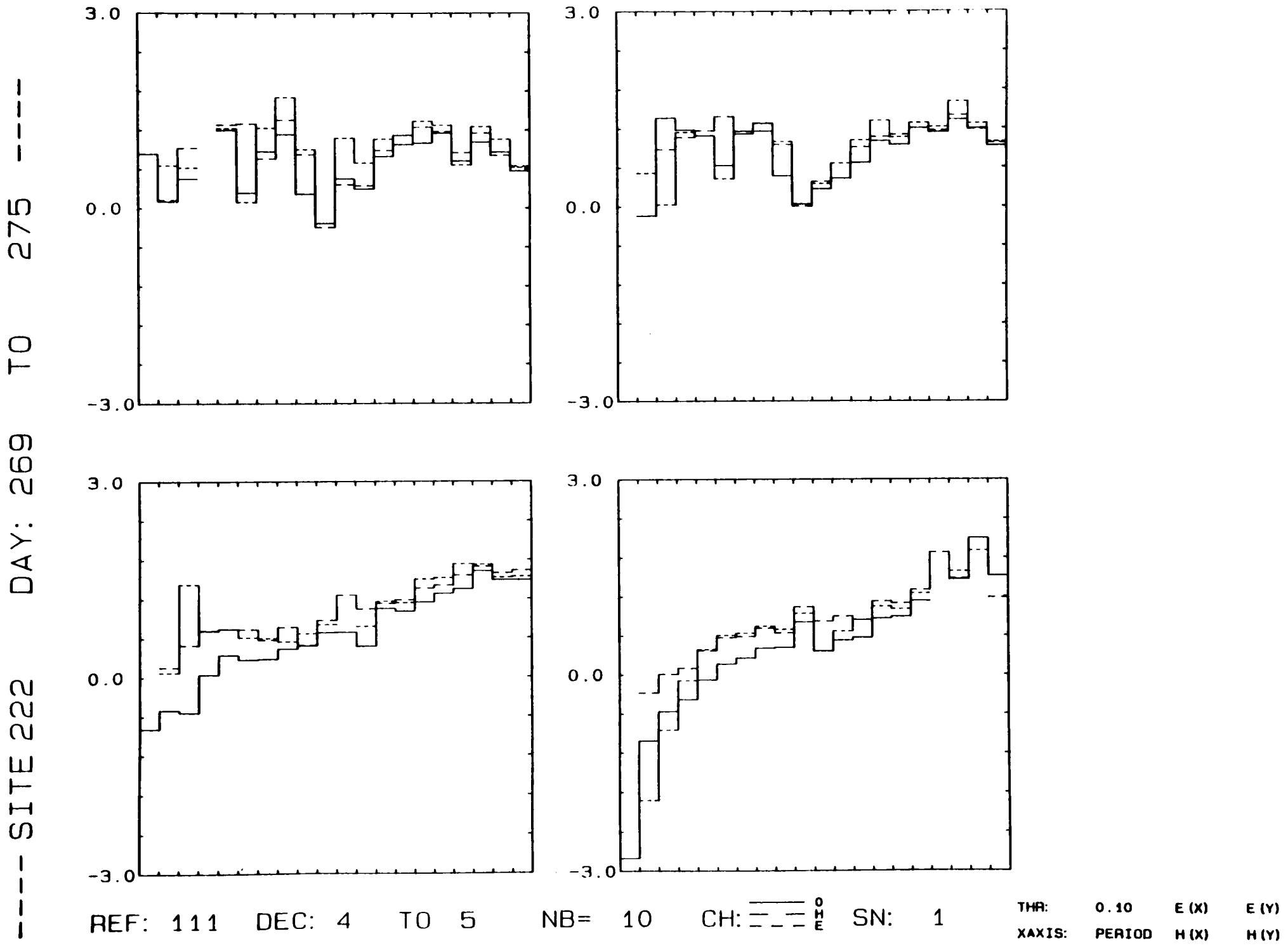
3.0
0.0
-3.0
3.0
0.0
-3.0
---- SITE 222 DAY: 269 TO 275 ----
3.0
0.0
-3.0
3.0
0.0
-3.0
REF: 111 DEC: 4 TO 5 NB= 10 CH: H E SN: 1
THR: 0.10 E(X) E(Y)
XAXIS: PERIOD H(X) H(Y)

Figure III.31. Signal-to-noise ratios for the local fields $\underline{E}$ and $\underline{H}$, using predicted coherence selection with a threshold of 0.1. Single site selected estimates are shown with solid lines. Remote reference selected estimates are shown with dashed lines, longer dashes for R-selection and shorter dashes for S-selection.

parameters, apparent resistivity and phase. Only the best set of RR estimates, i.e. the one obtained with a threshold of 0.5 for the predicted coherence, will be used. This set is shown in figure III.12.b.

Once the impedance tensor has been estimated in the original coordinate system it is necessary to rotate it to the direction of the structural strike. The motivation behind the procedure is to rotate $\underline{\underline{Z}}$ in order to make the off-diagonal elements reach a minimum value. In this procedure it is assumed that the earth has a quasi-two dimensional structure with the x-axis aligned with the strike direction. Along this direction the electrical conductivity does not change and Maxwell's equations split into two modes. Nevertheless the earth is in general 3D and such a rotation may be artificial. The geoelectric structural dimensionality is indicated by certain parameters called dimensionality indicators. These indicators in turn are based on the horizontal rotation properties of $\underline{\underline{Z}}$.

The rotation of $\underline{\underline{Z}}$ is given by

$$\underline{\underline{Z}}'(\Theta) = \underline{\underline{U}}\,\underline{\underline{Z}}\,\underline{\underline{U}}^{-1} \qquad \text{(III.63)}$$

where Θ is measured clockwise and $\underline{\underline{Z}}'(\Theta)$ is the rotated tensor. The rotation matrix is

$$\underline{\underline{U}} = \begin{bmatrix} \cos\Theta & \sin\Theta \\ -\sin\Theta & \cos\Theta \end{bmatrix}$$

The loci of the elements of $\underline{\underline{Z}}'(\Theta)$ describe ellipses or their degenerations in the complex plane. These ellipses are described by the centroids (see, e.g., Beamish, 1986b)

$$\begin{aligned} Z_1 &= \left(Z'_{xy}(\Theta) - Z'_{yx}(\Theta) \right)/2 = \left(Z_{xy} - Z_{yx} \right)/2 \\ Z_2 &= \left(Z'_{xx}(\Theta) + Z'_{yy}(\Theta) \right)/2 = \left(Z_{xx} + Z_{yy} \right)/2 \end{aligned} \qquad \text{(III.64)}$$

and the axes

$$\begin{aligned} Z_3(\Theta) &= \left(Z'_{xy}(\Theta) + Z'_{yx}(\Theta) \right)/2 \\ Z_4(\Theta) &= \left(Z'_{xx}(\Theta) - Z'_{yy}(\Theta) \right)/2 \end{aligned} \qquad \text{(III.65)}$$

In definitions (III.64) and (III.65), $\pm Z_1$ are the two centroids of

rotation of the off-diagonal elements Zxy and Zyx, and Z_2 is the centroid of the ellipse described by the two diagonal elements, Zxx and Zyy. All three ellipses have $Z_3(\theta_0)$ as the major and $Z_4(\theta_0)$ as the minor axes.

There are several methods for estimating the structural strike, θ_0. One can combine the $\underline{\underline{Z}}$ elements to find θ_0 (Sims and Bostick, 1969; Vozoff, 1972; Dekker and Hastie, 1981; Eggers, 1982), or analyse them in connection with the tipper in order to get an unambiguous strike direction (Gamble et al., 1982; Pedersen and Svennekjaer, 1984). Other methods favour minimization or maximization of coherence functions (Reddy and Rankin, 1974; Jones, 1977). Nevertheless in 3D situations the calculated value of θ_0 depends on the relative position of the measurements (Ting and Hohmann, 1981). In a recent study two new analytical rotation angles were proposed (Spitz, 1985) based on a previous eigenstate formulation (Eggers, 1982). Here the azimuth is given by (Swift, 1967)

$$\theta_0 = \frac{1}{4} \frac{Z_4(0)\,Z_3^*(0) + Z_2^*\,Z_1}{|Z_4(0)|^2 - |Z_3(0)|^2} \qquad \text{(III.66)}$$

which in the general three-dimensional case maximizes $|Z_3(\theta)|$ (Sims and Bostick, 1969).

Expanding equation (III.63) one can show that Z_1 and Z_2 are rotationally invariant. In particular, Z_1 and

$$Z_{eff}^2 = \left(Z_2^2 - Z_4^2(0)\right) + \left(Z_1^2 - Z_3^2(0)\right) = Z_{xx}Z_{yy} - Z_{xy}Z_{yx} \qquad \text{(III.67)}$$

which was first introduced by Berdichevsky, are often used in one-dimensional modelling of actual inhomogeneous structures (Rokityansky, 1982, p.192).

The main lineament direction within the study area is approximately E-W, expressed by the North Anatolian Fault and several minor faults. The measuring axes were oriented with respect to this direction with the x-direction perpendicularly to the strike; the declination is approximately 3° degrees east. The rotation angle θ_0 which makes Zxy reach its largest value reflects the strike direction. As it can be seen in figure III.32, the azimuth determinations are all between 5 and 9 degrees west but for

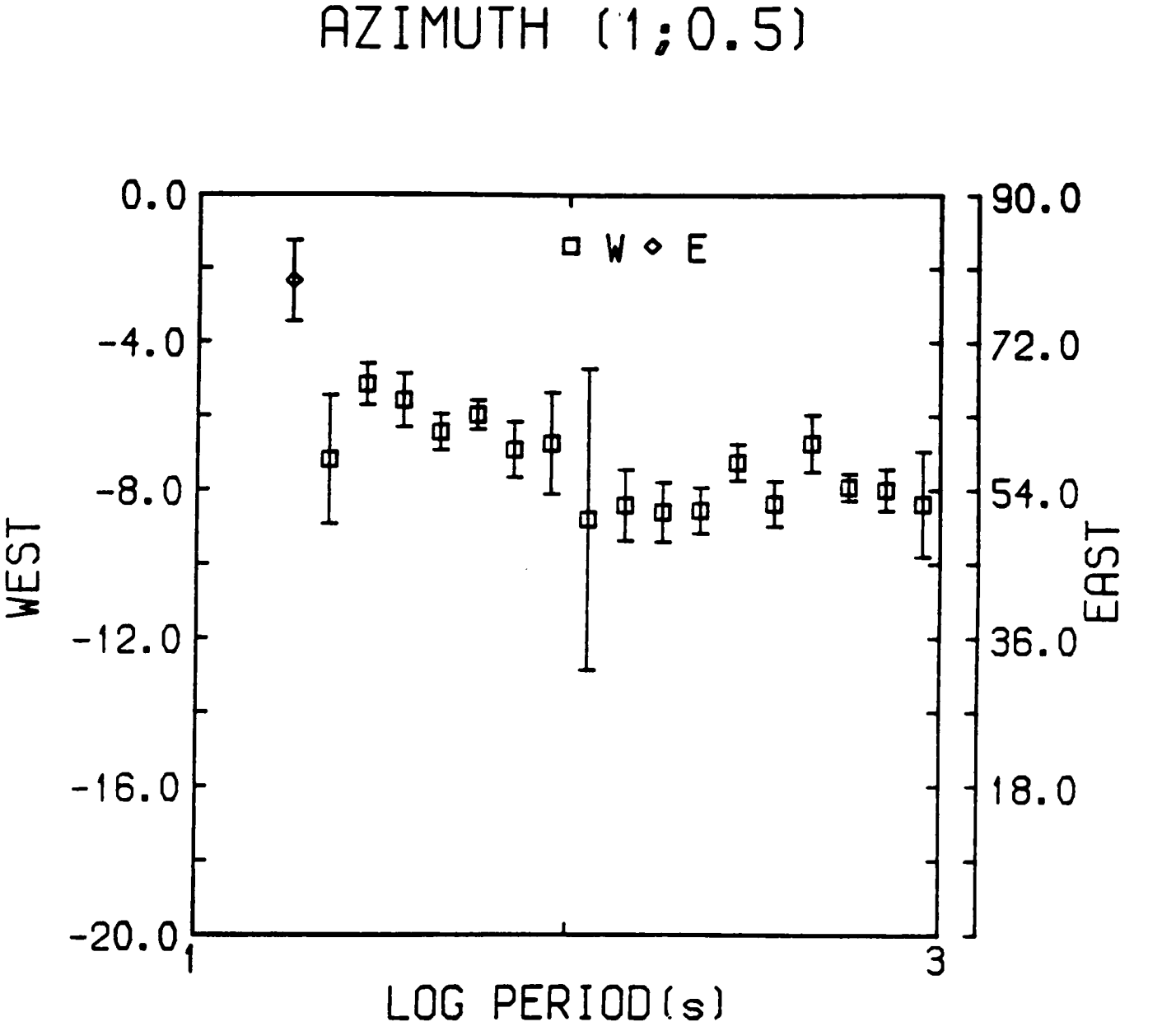
AZIMUTH (1;0.5)
0.0
-4.0
-8.0
-12.0
-16.0
-20.0
WEST
W ◇ E
90.0
72.0
54.0
36.0
18.0
EAST
1
3
LOG PERIOD(s)

Figure III.32. Azimuthal angles for site 2. Note that all but the first determination indicate westerly rotation.

a single short period determination which may be affected by a shallower structure. Since errors are introduced when the impedance tensor is rotated and because the azimuths of rotation are small, no rotation was performed. The resistivity and phase values in the measured directions are retained throughout this section. If the structure were 2D the x-direction would represent the H-polarization mode.

A number of dimensionality indicators have been derived from the quantities (III.65). A tutorial on the performance of such indicators and of other one-dimensionality tests based on inverse theory can be found elsewhere (Beamish, 1986b). The commonest dimensionality indicator is the skew

$$s = \left| Z_2 / Z_1 \right| \qquad \text{(III.68)}$$

which provides an indicator of three-dimensionality. Nevertheless forward 3D models indicate that skew is an unreliable indicator of three-dimensionality; it can attain low values in a three dimensional environment, even s=0 along the symmetry axis of a 3D structure (Reddy et al, 1976; Ting and Hohmann, 1981). Another indicator is the eccentricity of the rotation ellipse defined by

$$\beta(\theta) = \left| Z_4(\theta) \right| / \left| Z_3(\theta) \right| \qquad \text{(III.69)}$$

which although not invariant under rotation, vanishes for two-dimensional structures when θ is the strike direction. More interesting are the normalized dimensional weights which assess the relative importance of the 1D, 2D and 3D contributions (Kao and Orr, 1982)

$$\begin{aligned} D_1 &= |Z_1| / D_0 \\ D_2 &= |Z_3(\theta_0)| / D_0 \\ D_3 &= \left(|Z_2| + |Z_4(\theta_0)| \right) / (2 D_0) \\ D_0 &= |Z_1| + |Z_3(\theta_0)| + \tfrac{1}{2}\left(|Z_2| + |Z_4(\theta_0)| \right) \end{aligned} \qquad \text{(III.70)}$$

Other dimensionality indicators involve vertical field transfer functions (Vozoff, 1972).

Here skew, eccentricity and the dimensional weights are used to estimate the geoelectrical dimensionality of site 2. Skew values are high, usually greater than 1, and show large error bars as seen

in figure III.33. The eccentricity displays low values and small error bars as can also be seen in figure III.33. Those low values reflect a considerable two-dimensional contribution along the measurement directions. It is easy to show that since the rotational part of the eccentricity is written in terms of sin 2θ and cos 2θ, $\beta(\theta)$ is a minimum along and perpendicular to the strike direction of a two-dimensional structure. The dimensional weights (III.70), shown in figure III.34, suggest that the two-dimensional contribution is relatively small and that site 2 is probably more three-dimensional than anything else. Their error bars, not shown for clarity, are large and if considered together, span a range of values of the order of 0.8.

Results are usually presented as sounding curves where the impedance tensor elements are converted to apparent resistivity

$$\rho_{ij} = \frac{1}{5f} \left| Z_{ij} \right|^2 \qquad \text{(III.71)}$$

and phase of Zij, i,j=x,y. Figures III.35 and III.36 show the apparent resistivities and phase, respectively, in both major (Zxy) and minor (Zyx) directions. It is worth remembering that these are unrotated values. If the measuring frame is rotated, errors are increased, with the phase showing a relatively larger increase. The apparent resistivity curves in both major and minor directions differ very little for decade 4 and appear to separate at longer periods. Phase is rather flat, around 30 degrees, showing little differences between major and minor values. Values tend to split towards the end of each decade but with major and minor changing relative position.

Although site 2 does not appear to be 1D, it is still possible to have at least some indication of the resistivity distribution using a 1D inversion scheme. In situations like this is common to use an invariant-derived apparent resistivity such as III.67. Here both major and minor are inverted using the Schmucker transformation (Schmucker, 1970) in order to derive a resistivity profile. It is worth mentioning that it has been suggested elsewhere (Spies and Eggers, 1986) that one should use the Schmucker tranformed resistivity and depth as sounding parameters instead of the usual apparent resistivity and phase because they are less prone to suffer undesirable fluctuations.

Figure III.37 shows the Schmucker transformations along the major and minor directions. The two inversions produce similar 1D conductivity profiles, which basically go from a conductive region,

SKEW & ECCENT. (1;0.5)

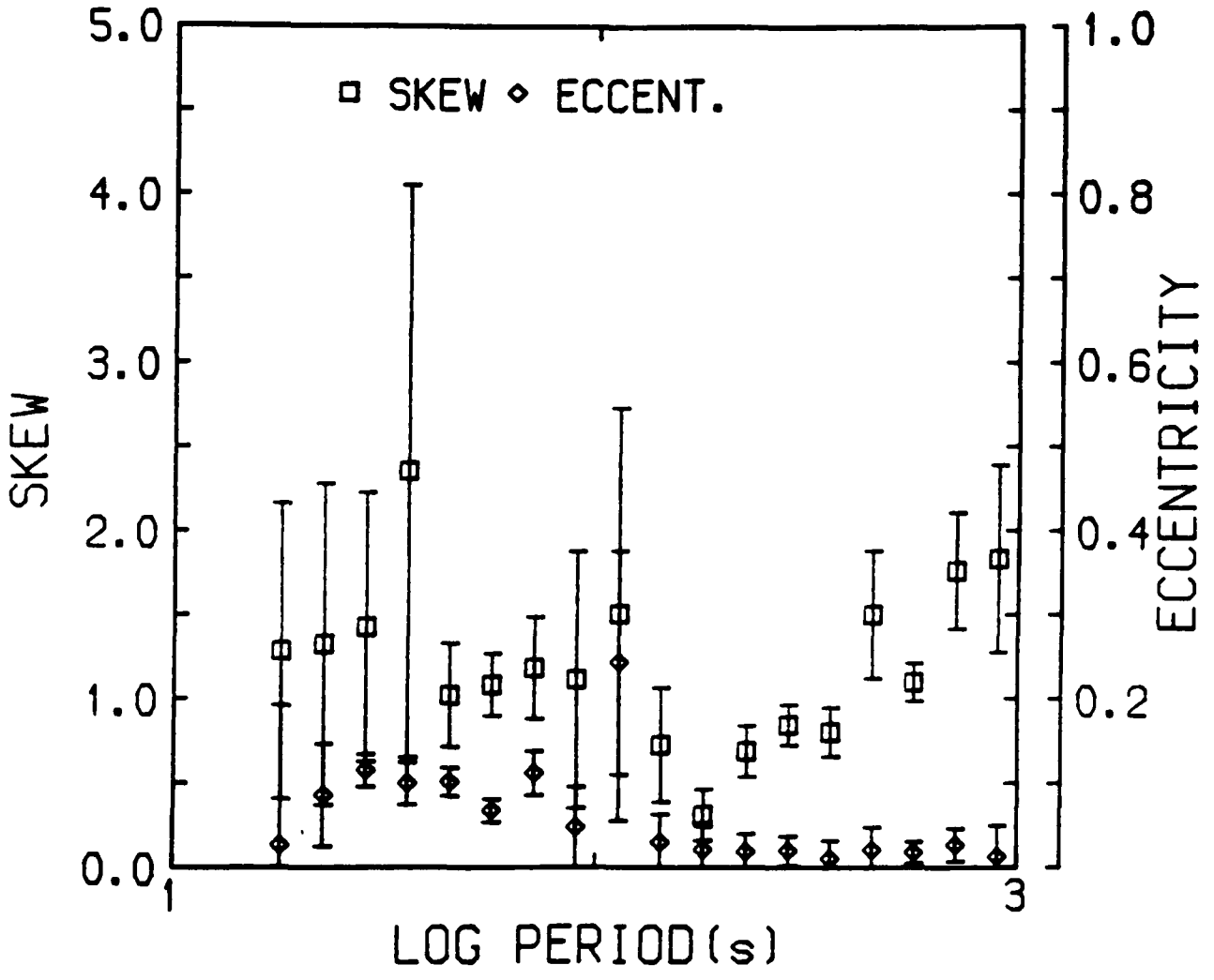

Figure III.33. Skew and eccentricity for site 2. Note on the different scales used in this figure.

DIM. WEIGHTS (1;0.5)

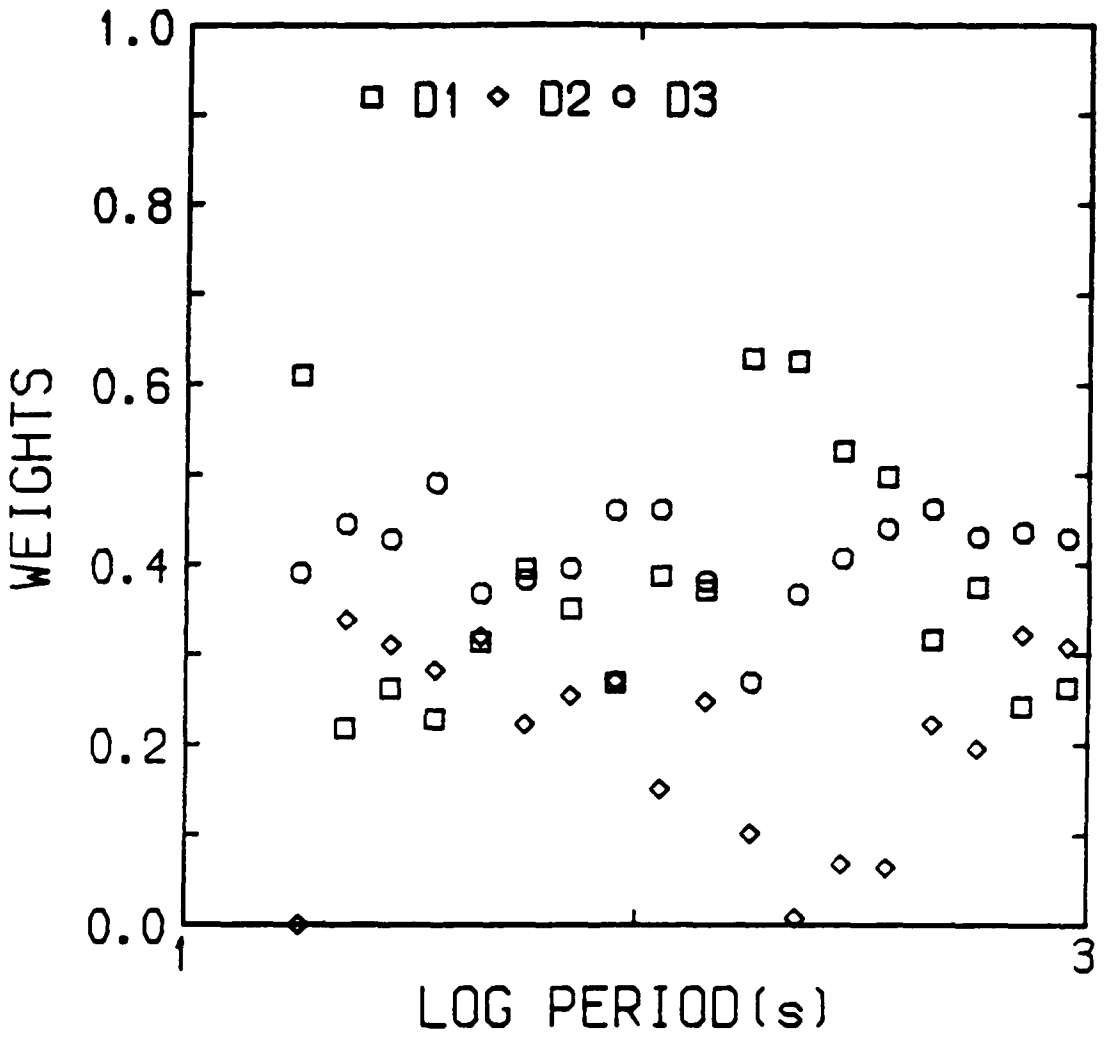

Figure III.34. Normalized dimensional weights D1, D2 and D3, for site 2.

UNROTATED (1;0.5)

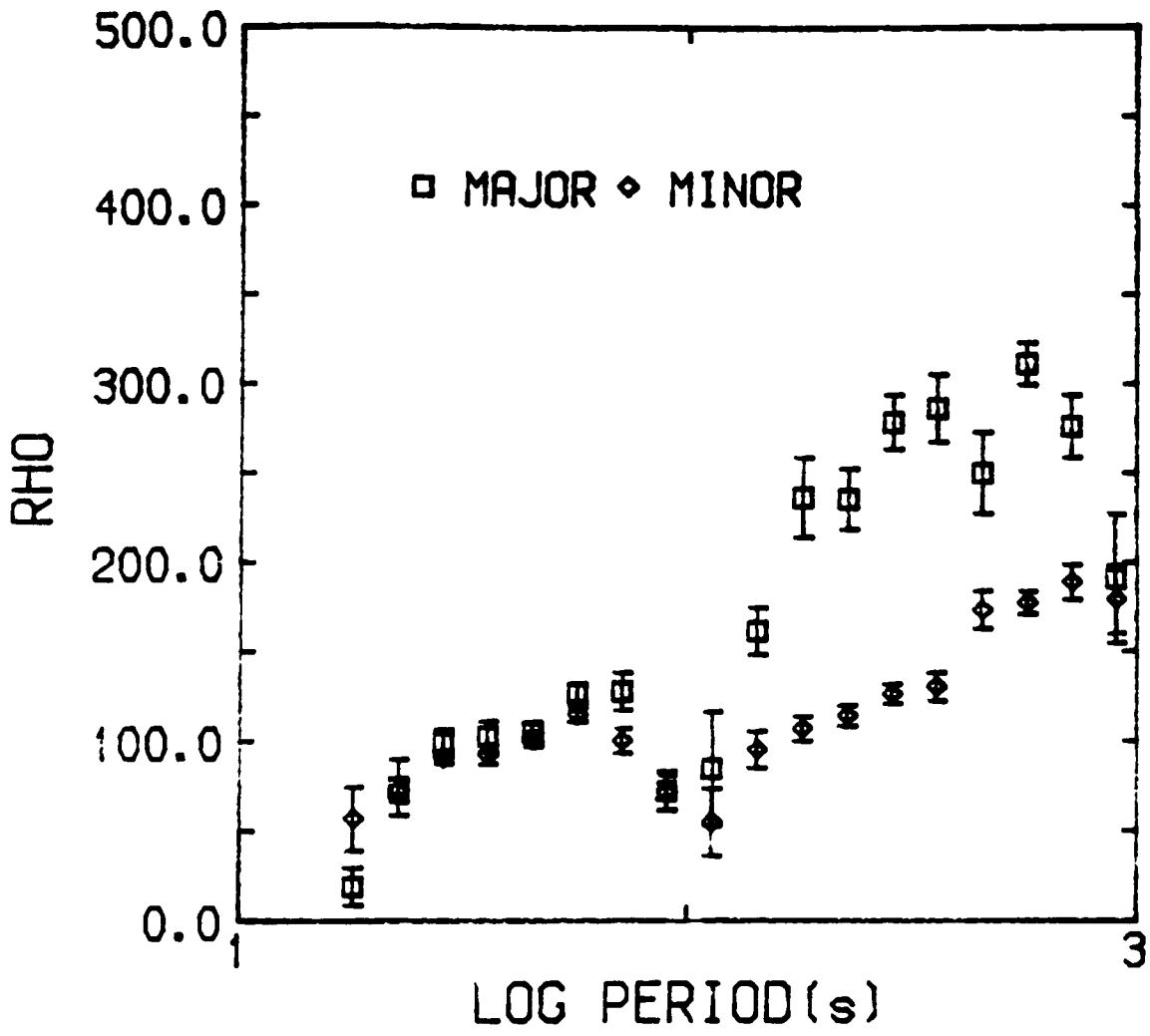

Figure III.35. Major and minor unrotated apparent resistivities for site 2. The vertical scale is linear.

UNROTATED (1;0.5)

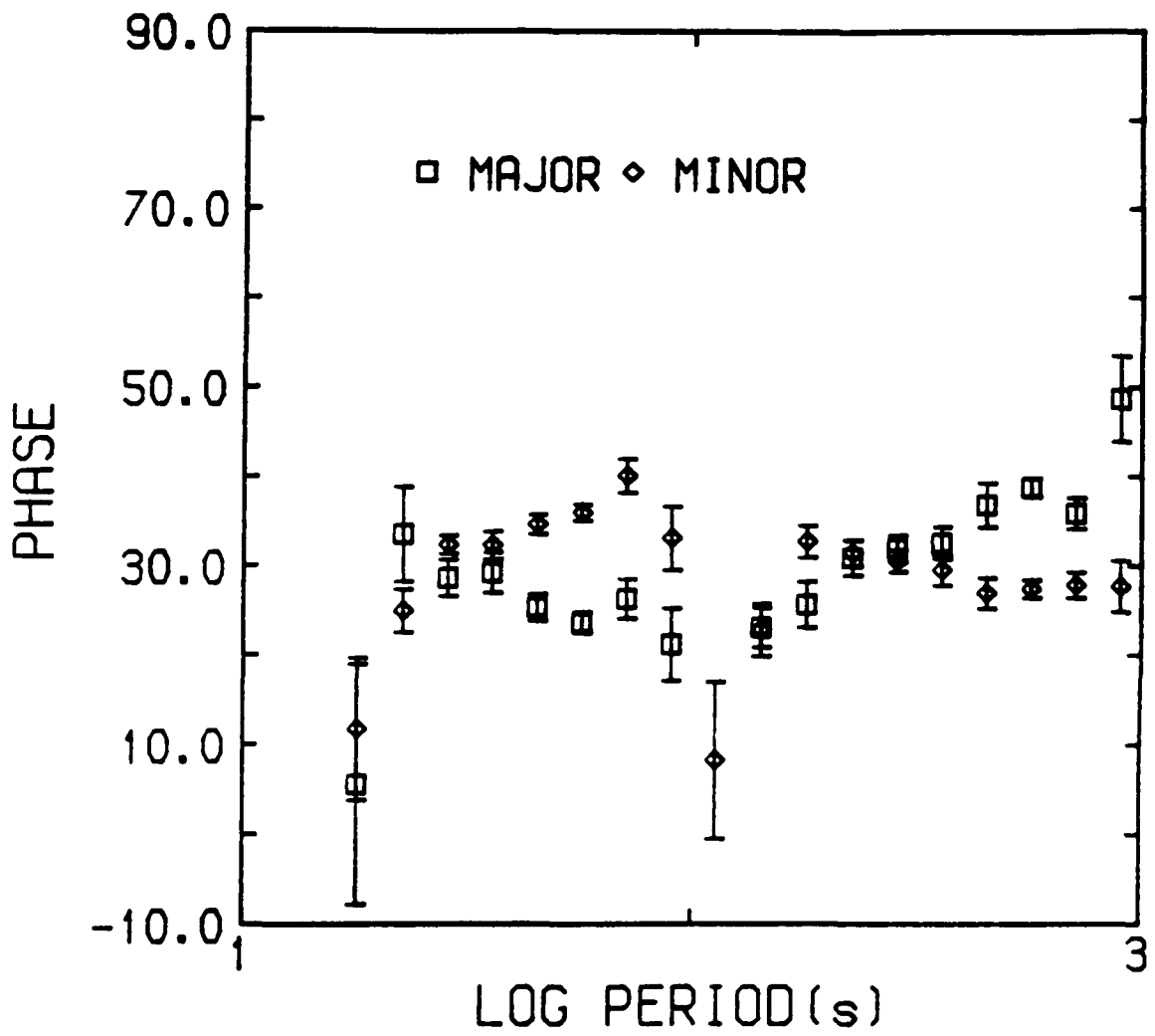

Figure III.36. Major and minor unrotated phases for site 2.

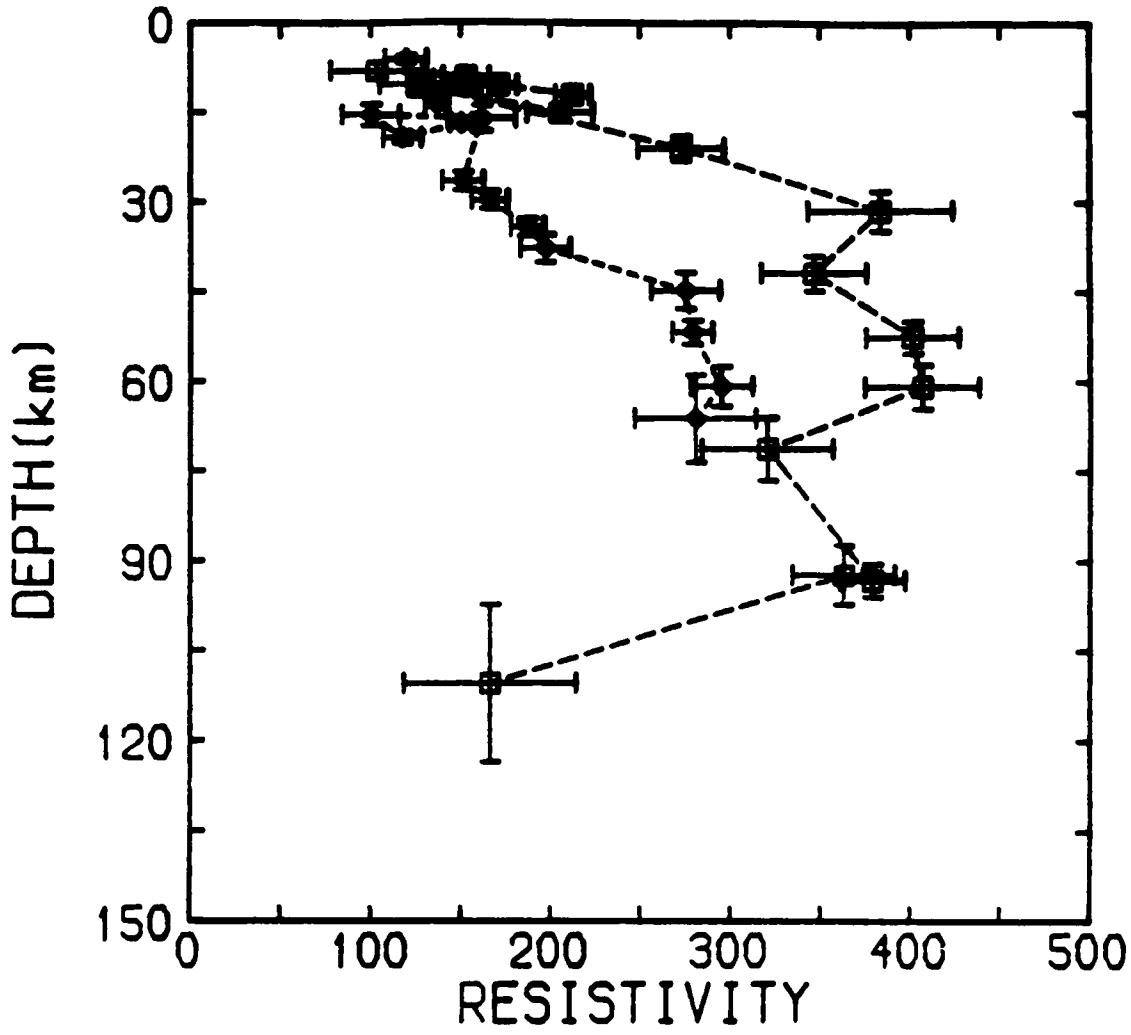
SCHMUCKER (1;0.5)
□ MAJOR ◇ MINOR
DEPTH(km)
0
30
60
90
120
150
0
100
200
300
400
500
RESISTIVITY

Figure III.37. Schmucker transformation in both major and minor directions.

100Ω.m at depths 10-20 km, to a more resistive region, ≥300Ω.m. There is a hint of a more conductive region lying deeper, but that occurs at the limit of penetration of the curves. Although the two curves appear clustered at shallower depths there is an indication of a lower crustal conductivity zone with the same order of magnitude as observed in other active regions (Shankland and Ander, 1983; Gough, 1986c).

III.7. Summary and Conclusions

In this chapter some aspects of data analysis in MT are discussed. The original time series consists of 7 days of MT data sampled at 5s intervals at two sites 29km apart. The four horizontal components of magnetotelluric field at both sites are used in the analysis. The original time series is transformed to the frequency domain via FFT producing a basic data set, or test data set which was used throughout this chapter. The spectral estimates obtained from the test data set are analysed through both single site and remote reference techniques in order to produce estimates of the impedance tensor elements. Only the off-diagonal elements of $\underline{\underline{Z}}$ are used in the analysis of this chapter.

The objective of this chapter is to produce accurate estimates for the impedance tensor. This is achieved by either estimating two biased estimates using the SS technique in order to outline a region where the unknown true value is or by estimating a single estimate using the RR technique. Coherence functions are used extensively in the selection of data windows with the best signal-to-noise ratios. Partial and ordinary coherences are used in combination with the predicted coherence in the SS analysis. Only the predicted coherence of the local fields was used in the RR technique, as it proved to be a reliable estimator of the noise content of a data window.

All coherence function estimates are upward biased quantities and so need to be corrected. The higher the coherence estimate is, the smaller the bias will be; for only 5 degrees of freedom a coherence level of 0.85 is sufficient to ensure the bias is less than 10%. If not corrected the bias of coherence functions has implications on both SS and RR techniques. Usually one chooses high coherence levels when applying SS technique. For instance a 6% bias for a coherence level of 0.85, allow realizations with coherence of 0.80 to be accepted. This is particularly undesirable since usually there are fewer high predicted coherence realizations as the relative probability of obtaining a realization at the [0.80,0.85)

level is greater than obtaining one at [0.85,0.9). It is well known that just a few lower coherence estimates can cause spectral instability which reflects on the final stacked results. On the other hand it has been shown in this chapter that lower levels of predicted coherence are highly desirable when employing the RR technique. In this case bias in the coherence functions are greater making more likely the stacking of lower predicted coherences which will contribute only to the variance of the final estimate.

The SS technique allows the computation of 6 least-squares estimators, although 2 are unstable for a 1D earth. All four are biased estimators, two being downward biased by noise on the magnetic components while the other two are upward biased by noise on the telluric components. In order to delimitate a region where the unknown true value of impedance tensor lies, two estimates, one downward biased and other upward biased, are calculated together with their associated random errors. Only the off-diagonal elements of the impedance tensor are used to demonstrate the results.

Single site results are obtained from realizations selected using 5 coherence acceptance criteria. All tests involve the predicted coherence functions either alone or combined with the partial coherences or the ordinary coherence between the input channels. Results obtained using the 5 tests are compared against each other using two coherence thresholds, 0.85 and 0.95. It has been found that the higher threshold is too restrictive, resulting in several bands with few or no estimates at all. Nevertheless with respect to bias content only, the higher threshold yields better estimates in those bands where there are sufficient degrees of freedom to permit the computation of statistically valid results. Three tests produced results which can be considered the best ones among the 5 sets of results. The so-called USGS coherence test, test 4 in the text, where a geometric mean of the predicted with the off-diagonal partial coherences is calculated and checked if above a selected coherence threshold, produces the best set of results. The two other tests require that the predicted coherence is above a selected coherence threshold. In one of them, test 2, there is an additional requirement that the off-diagonal partial coherence is greater than the partial coherence for the diagonal elements of the impedance tensor. The other test, test 1 in the text, requires only that the predicted coherence is above the selection threshold.

The RR technique allows the computation of unbiased estimates of the impedance tensor. The estimate is unbiased as long as local noises are uncorrelated to remote noises. Test 1 was used on the RR

calculations due to its simplicity and because it is not as restrictive as tests 2 and 4 since it allows the stacking of more realizations and consequently better statistics. Unlike the SS technique where 4 stable biased estimates can be calculated, the RR technique provides a unique stable estimate of $\underline{\underline{Z}}$. The RR problem can be decomposed in two least-squares problems. First a local magnetic field is predicted using the remote field and, second a local electric field is predicted using the predicted magnetic field. Because of this there is a number of possibilities for choosing predicted coherences for data selection. In this work it is shown that the predicted coherence between the local fields, estimated using the RR derived impedance tensor is an efficient parameter in data selection. Such a coherence function not only gives the coherence between the local fields but also is directly related to the local noise. The predicted coherence between the local fields is used throughout this work for both SS and RR techniques.

Elsewhere it has been suggested that the RR technique is capable of producing accurate results even for arbitrarily low predicted coherences thresholds or even complete data sets with no selection at all. In this work it is shown that data selection based on the predicted coherence is necessary in the RR data analysis, although coherence thresholds are much lower than the corresponding SS thresholds. By using only a coherence based data selection one can be confident about the reliability of RR estimates. Moreover lower thresholds imply a more efficient use of the available data as less realizations are discarded. The RR technique provides an inherent weighting of the accepted realizations with the best signal-to-noise characteristics.

Two coherence thresholds were chosen to demonstrate how the accuracy of RR results improve with data selection; these thresholds are 0.1 and 0.5, well below their SS counterparts. It was found that results are more stable although with variances slightly higher for the higher threshold. The estimates for the 0.5 threshold are considered as the best RR set of results. Higher thresholds are not advisable since they tend to reject useful information. The best RR results are within the bounds given by the SS results obtained using a threshold of 0.85, which is considered the best set of SS results. Nevertheless the RR results cannot be predicted either by arithmetic averaging or by a variance-weighted average of the two extreme SS biased estimates. The RR fractional error levels amount to about 5% and are always below the corresponding SS levels, which have contributions from both random

and bias errors.

The comparison between the best RR and SS sets of results shows that the random errors tend to be larger in the first case. It is usually accepted that this is due to the remote noise contribution when using the RR technique; in the SS case only local noises contribute to the random errors. It has been suggested that to obtain RR random errors at a level comparable to the SS random errors it is necessary to stack relatively more RR realizations, thus reducing the variance. It is shown here that the RR variance is not straightforwardly linked to the number of realizations, or degrees of freedom. The variance does depend strongly on the local noise content. Not considering degrees of freedom and local noise content the variance will be kept at low levels if: the reference field has a low noise level and if the magnetic field is not polarized. The first condition gives an additional criterion which a remote site has to comply with. The second is one of the reasons why the electric field usually is not a suitable remote reference. Moreover since the expression used to estimate the variance is approximate and carries an error of the order of 1/N, where N is the number of degrees of freedom, there is also a lower limit for N in order to keep the error in the variance at a reasonable level.

Contrary to accepted wisdom, the RR variance does not automatically reduce by simply increasing N. It is shown here that it depends heavily on local noise content which in turn is monitored by the RR predicted coherence as used in this chapter. The dependence of the variance on the local noises and on the degrees of freedom is demonstrated by grouping realizations with respect to coherence intervals. A set of RR results obtained for the whole data set with no acceptance criterion is used in the comparisons. Results are compared for a 68% confidence interval, i.e. one standard deviation. Comparisons show that results, i.e. an estimate together with associated random errors, obtained by stacking only realizations from the highest coherence group, (0.9,1.0], are essentially the same as the ones obtained from the unselected data set with many more degrees of freedom. Results obtained with only N=5 degrees of freedom agree to better than 5% accuracy with the ones obtained from the unselected data set with N=630 degrees of freedom. It seems that N=5 may be considered as a lower limit since results obtained with N=4 degrees of freedom start to disagree with the corresponding N=630 results.

Several conclusions can be drawn from the comparisons using

coherence groups. Firstly the expectation of reducing variance levels by simply collecting more data is not straightfowardly achieved. Data must be selected in terms of coherence in order to produce reliable RR estimates. This selection should be done using moderately low coherence thresholds as, say 0.5, avoiding loss of useful data windows. Secondly the RR predicted coherence estimated using the local fields is a reliable measure of the noise power levels. This in turn provides a way of accessing the reliability of an RR result. Indeed as shown for the unselected RR results, bands 1 and 2 of decade 4 are not reliable as all realizations stacked have very low (->0) predicted coherences values, indicating very low signal-to-noise ratios. Finally the RR technique provides an inherent weighting of the best signal-to-noise realizations, as is demonstrated by the comparison of similar results obtained from N=630 and from N=10, 7 and 5 degrees of freedom. Probably this weighting is one of the reasons why several authors are reticent on the subject of selecting data; it is possible to obtain RR results without any selection on coherence grounds, although their accuracy will depend on the signal-to-noise ratios.

Remote reference results obtained using a remote electric field are subject to large uncertainties. A comparison with the corresponding results obtained using the remote magnetic reference suggests that results are not inconsistent but are grossly inaccurate. Probably the causes for the observed inaccuracy are related to the type of noise the telluric channels are prone to suffer. Firstly the electric field response tends to be polarized in the direction of highest resistivity thus causing the impedance tensor estimates to diverge. Secondly severe level shifts are observed in the electric records which, if correlated hinder an adequate spectral representation of the data. In particular the local telluric noise levels as monitored by the predicted coherence are not especially high, since coherence levels are comparable to the ones obtained for a magnetic remote reference.

It has been indicated in this chapter that a few good signal-to-noise realizations are probably sufficient to produce accurate results. Since the RR technique favors the best quality data, low thresholds can be used as signal information is not degraded by the presence of data of lesser quality. This can be shown by dividing the results obtained for the whole data set into groups of coherence levels. It is easy then to see why a moderate threshold of 0.5 is desirable, from the 6 disjoint coherence intervals covering the range [0,1], results start to appear clearly defined from the group (0.5,0.75] onwards. This again gives more

weight to the affirmation that is necessary to use a selection criterion with moderate thresholds in RR calculations. This illustrates how efficient in detecting noise powers the RR predicted coherence can be since a high level of SS coherence does not imply that only the best realizations are stacked. It is shown here that the RR coherence estimate is always lower or equal to the SS estimate, and this remains true regardless the remote field, magnetic or electric. Single site coherence estimates as high as 1.00 may correspond to a null RR estimate. The two RR-derived coherences, E- and H-derived, do not show any particular relative behaviour and have more or less the same levels. This suggests that both RR derived coherences are of comparable efficiency in detecting noisier realizations.

The usefulness of both RR derived predicted coherence is demonstrated using SS techniques on RR selected data subsets. The same two RR thresholds are used to select subsets: 0.1 and 0.5. Three subsets are selected, one R-selected subset containing only data windows selected using coherence values estimated using a remote magnetic field, an S-selected subset selected using a remote electric field and an X-selected subset selected containing remote data windows that are in both R- and S-selected subsets. It was found that 71% or more of the data windows of the R and S subsets belong to the X subset suggesting that both RR predicted coherence estimates tend to select the same number of data windows, for the two thresholds used. Single site techniques applied on both R- and S- selected subsets produce similar results. Moreover results obtained from the S-selected subsets at the 0.5 threshold are comparable to the best set of strict SS results, i.e. SS selected, at 0.85 threshold. This shows that although RR results for a remote telluric site are grossly inaccurate the RR predicted coherence estimated using a remote telluric site is still reliable measure of the local noise powers. Single site results from S-selected subsets may be located somewhere between the RR reference results at the same coherence level and the conventional SS results at much higher coherence levels. Such a hybrid technique which uses the SS technique on S-selected subsets may prove to be useful in situations where for any reason is not possible to have a remote magnetic site but a remote telluric site is still feasible. Hybrid results will be of better quality than strict SS results at any coherence level. Signal-to-noise ratios confirm that the relative signal content of both R- and S-selected subsets are comparable.

An interpretation of site 2 was done with the best RR set of results, i.e. using a coherence threshold of 0.5. The azimuth of

rotation and eccentricity of the rotation ellipse confirmed the geological strike. As the measuring directions were referred to the geological strike, results and interpretation are presented unrotated. One dimensional resistivity profiles along major and minor directions are given in terms of the Schmucker transformation. The 1-D conductivity profiles indicate the existence of a lower crustal high conductive layer (HCL) of the same order of magnitude and at similar depths as found in other active regions. There is an indication that this HCL overlays a more resistive layer which extends down to the extreme penetration depth the period range allows.

CHAPTER IV
Data Inversion and Modelling

IV.I. Introduction

The objective of this chapter is to examine the techniques which were used in this work for inverting (1D) and modeling (2D) magnetotelluric data. The approximate Schmucker transformation together with two more complex algorithms for 1D inversion and a finite difference algorithm for forward 2D modelling are considered. These techniques are briefly described below.

The final goal in measuring the behaviour of the electromagnetic field, either natural or artificially created, is to obtain information on the earth's electrical parameters and their distribution. Apart from the 1D case where inversion schemes are well established it is common procedure to interpret data by means of a geoelectric model. For this interpretation one either proceeds using analogue model experiments or performs theoretical calculations. Analogue model experiments are performed in the laboratory with a reduced copy of the real structure. Analogue models have been used in several cases to model different features such as topography (Faradzhev et al., 1972) and subducting plates (Dosso and Nienaber, 1986). There are several ways of modeling using theoretical calculations. Analytical solutions exist for simple geometric shapes with some sort of symmetry or for some special cases where there is a perfect insulator or conductor (Rankin, 1962; d'Erceville and Kunetz, 1962; Berdichevsky and Dmitriev, 1976). Numerical modeling can be carried out using differential or integral equations. The former result in large, but sparse and banded matrices as the anomalous field has to be calculated at every grid point of a mesh covering the whole earth or a realistic sub-region of it. Although the mathematics are more involved in the case of integral equations, the unknown fields need to be evaluated only in the inhomogeneity or on its surface.

Differential equation methods are generally preferred when simulating complex structures. In the finite difference method, Maxwell's equations and boundary conditions are written down in the form of finite differences for a chosen net of points (Jones, 1973; Brewitt-Taylor and Weaver, 1976). In the finite element method the earth is sub-divided into an assemblage of small elements (Reddy and Rankin, 1975; Kaikkonen, 1977). The energy of the electromagnetic field is considered within each element to meet the condition that the integrated field energy is minimal. Another approach to the

solution of the induction problem is to use an equivalent electrical network (Swift, 1971; Ku et al., 1973) which can be solved efficiently by using the method of diakoptics (Brewitt-Taylor and Johns, 1980). The integral equation method uses surface and volume integral techniques based on Green's tensor (Parry and Ward, 1971; Weidelt, 1975). Due to its small demand on computer resources it may be the best numerical technique when solving three-dimensional problems, as long as the inhomogeneities are not too large or numerous (Ting and Hohmann, 1981).

IV.2. One-Dimensional Inversion

The field relationships governing the 1D case have been described in section II.3. In this section the 1D inversion of MT field data is considered. In a layered earth where conductivity varies only with depth, sounding curves can be inverted directly. In order to perform a meaningful 1D inversion, the sounding curve must display prescribed rotational characteristics such as the ones discussed at the end of chapter II. Necessary and sufficient conditions for the existence of a one-dimensional model can be found in the literature (Weidelt, 1972; Parker, 1980; Weidelt, 1986). In addition, when a 1D situation exists, the exponential attenuation of the electromagnetic fields limits the information on the conductivity distribution at greater depths (Parker, 1982).

Most of the work on the inversion of magnetotelluric data uses a parametrization of the earth in terms of a finite series of discrete layers (Wu, 1968; Jupp and Vozoff, 1975; Larsen, 1981). In another approach the earth is assumed to have a continuous resistivity profile (Oldenburg, 1979). The assessment of the degree of nonuniqueness of a conductivity model is of paramount importance in the inversion problem. The Backus and Gilbert method (Parker, 1977) considers the space of unknowns on the inverse problem to be infinite-dimensional. So when for computational simplicity one reduces the infinite model space to a finite dimension, the true number of degrees of freedom cannot be adequately described (Parker, 1977). Moreover the linearization of the inverse problem cannot provide systematic inference on the real conductivity structure, and even methods which avoid linearization such as the Monte Carlo method (Jones, 1977), fail to produce a sufficiently large set of solutions (Parker, 1983). Fully non-linear solutions have been used to assess the range of model variability for a given data set (Parker, 1983). Such solutions measure the acceptability of a given particular model through a chi-square (χ^2) measure of misfit and provide three classes of models; D+, H+ and C^2+. The D+ optimum

solution is a delta-function model made of a finite number of delta-functions (zero thickness but finite conductance), the H+ solution is made of uniform layers with constant product of the conductivity times thickness squared and the C^2+ solution constitutes a class of models where the conductivity varies smoothly with depth.

Approximate inversion

The first method of inversion used is referred to as Schmucker's transformation (Schmucker,1970). In this heuristic method the imaginary part of Zij is used to define the depth to a perfect substitute conductor

$$h^* = \frac{T}{2\pi} \, Im(Z_{ij}) \qquad \text{(IV.1)}$$

where i,j=x,y and h^* is expressed in km. The transformed apparent resistivity is in turn given by the real part of Zij,

$$\rho^* = 0.4 \, Re^2(Z_{ij}) \qquad \text{(IV.2)}$$

where ρ^* is expressed in Ω.m. Plots of ρ^* against h^* give an approximation of the true conductivity distribution for 1D situations. This technique is used in chapter III.

Linearized inversion

The second method of inversion used in this work is based on local linearization. There are many MT inversion schemes based on linearization and least-squares minimization. A particular formulation which can be found in the literature (Jupp and Vozoff, 1975) is used in this work, therefore only an overview of it is given here.

Assume M data values represented by the vector

$$\underline{d}^t = (d_1, \ldots, d_M) \qquad \text{(IV.3)}$$

while the earth is represented by the model

$$\underline{x}^t = (x_1, \ldots, x_N) \qquad \text{(IV.4)}$$

with N degrees of freedom. Model data generated by the direct problem are represented by the vector function

$$\underline{f}^t(\underline{x}) = \left(f_1(\underline{x}), \ldots, f_M(\underline{x}) \right) \qquad \text{(IV.5)}$$

The selection criterion for the best fit is given by the minimum of

$$F(\underline{x}) = \left[\frac{1}{M} \sum_{i=1}^{M} \frac{(d_i - f_i(\underline{x}))^2}{d_i^2} \right]^{1/2} \qquad \text{(IV.6)}$$

,i.e. the root mean square relative error. The Taylor expansion of the vector $\underline{f}(\underline{x})$ around a starting model, say $\underline{x}$, is

$$\underline{f}(\underline{x}+\underline{\Delta x}) = \underline{f}(\underline{x}) + \underline{\underline{J}}\,\underline{\Delta x} + \underline{R}(\underline{x}+\underline{\Delta x}) \qquad \text{(IV.7)}$$

where $\underline{\underline{J}}=|\partial f_i/\partial x_j|$ with i=1,...,M and j=1,...,N, is the Jacobian matrix of the vector $\underline{f}(\underline{x})$ and usually M>N. The remainder $\underline{R}(\underline{x},\underline{\Delta x})$ accounts for the higher order derivatives of $\underline{f}(\underline{x})$. Each element of the Jacobian Jij measures the variation of the model value f_i with respect to variations in x_j. Thus the matrix $\underline{\underline{J}}$ is called the sensitivity matrix. Suppose the p-th column of $\underline{\underline{J}}$ is very small, this indicates that the parameter x_p has little influence on the model data. This parameter may be then considered as irrelevant.

Assuming that the vector function $\underline{f}(\underline{x})$ is linear, $\underline{R}(\underline{x},\underline{\Delta x})$ may be neglected. This is the method's limitation since now the search in the model space is confined to a region in the vicinity of the starting model (Parker, 1977). From a starting model $\underline{x}^t=(x_1,\ldots,x_N)$ the technique proceeds in an iterative manner in order to find a modification $\underline{\Delta x}$ which minimizes:

i) $||\underline{\varepsilon} - \underline{\underline{J}}\,\underline{\Delta x}||$

ii) $||\underline{\Delta x}||$ among solutions of i),

where $\underline{\varepsilon}=\underline{d}-\underline{f}$ is a known vector. These conditions give a unique solution to the linearized inverse problem, i.e.,

$$\underline{\underline{J}}\;\underline{\Delta x} = \underline{\varepsilon} \qquad \text{(IV.8)}$$

When some of its vector-columns are not linearly independent the rank of $\underline{\underline{J}}$ is always $p \leq \min(M,N)$. A deficient rank makes the problem undeterminated with respect to certain parameters. Under these conditions it is useful to decompose the Jacobian as

$$\underline{\underline{J}} = \underline{\underline{U}}\;\underline{\underline{\Lambda}}\;\underline{\underline{V}}^t \qquad \text{(IV.9)}$$

(e.g. Golub and Van Loan, 1983, p.16-20), where $\underline{\underline{U}}$ and $\underline{\underline{V}}$ are orthogonal. This decomposition is particularly useful because it

permits the quantification of rank deficiency. The diagonal matrix $\underline{\Lambda}$ contains the singular values $\alpha_1 \geq \alpha_2 \geq \ldots \geq \alpha_p$, where p is the rank of $\underline{\underline{J}}$, implying that (N-p) parameters are irrelevant, i.e. cannot be inferred from the data. The inverse problem (IV.5) has the solution

$$\underline{\Delta u} = \underline{\underline{V}}\,\underline{\underline{\Lambda}}^{-1}\,\underline{\underline{U}}^{t}\,\underline{\varepsilon} \qquad \text{(IV.10)}$$

obtained from (IV.8) and (IV.9). The stability of this solution is achieved through truncation of unimportant parameters and Marquardt's correction step (Marquardt, 1963). The above scheme of linearized inversion is used in chapters V and VI.

The Monte Carlo method

The third method of inversion uses the Monte Carlo method. A full description can be found elsewhere (Jones, 1977). Only an overview of the algorithm is given here.

A model $\underline{x}$, (IV.4), is chosen at random in the model space. Such a model is initially constructed from the sounding curves by empirical curve matching. Its response function $\underline{f}(\underline{x})$, (IV.5), is then calculated and compared with the data $\underline{d}$, (IV.3). The logarithm of the apparent resistivities and phase, in radians, are used in this comparison. The use of logarithms follows from arguments of log-normal resistivity distribution (Bentley, 1973). The discrepancy between $\underline{f}(\underline{x})$ and $\underline{d}$ is given by

$$\Psi = \sum \left[(\log \hat{\rho} - \log \rho)^2 + (\hat{\varphi} - \varphi)^2 \right] \qquad \text{(IV.11)}$$

where the summation is carried out over all frequencies and $\hat{\rho}$ and $\hat{\varphi}$ are model responses. New models are generated by perturbing the initial model with a series of random numbers, $r_1, r_2, \ldots$ as $h_i' = h_i 2^{r_k}$ and $\rho_i' = \rho_i . 10^{r_k}$, where h_i and ρ_i are the thicknesses and resistivities of the initial model, while the primed quantities refer to the new model. The random sequence, $r_1, r_2, \ldots$ is normally distributed with zero mean and unit variance. Hence 68% of the h_i' and ρ_i' are respectively between $h_i/2$ and $2h_i$, and $\rho_i/10$ and $10\,\rho_i$. The response of a new model is calculated and if it is within a 95% confidence interval, or two standard deviations, for a number of data points it is accepted. The quantity (IV.11) is calculated and if $\Psi' < \Psi$, the new model replaces the initial one.

The random search in the model space is conditioned by bounds on the parameters imposed by the user. Those bounds are set in the light of the sounding curves. The search for new models continues

until a specified number is reached. At the end of each iteration the information from the previous best five models is used to re-adjust the bounds and an average model is used to start a new iteration process. This feedback mechanism speeds up the computational process but on the other hand restricts the random search to a neighbourhood of the starting model. This may be illustrated by monitoring the model parameters together with their bounds after each iteration during an inversion. As an example consider the inversion of apparent resistivity and phase at the Canadian site 72 along the measured x-direction (refer to chapter VI). The initial model consists of 2 layers above a half-space, i.e. two thicknesses and three resistivities characterize the model. The logarithms of both resistivity values (R) and the three thicknesses (h) from the best models after each iteration are shown in figure IV.1. In this figure the results with their adjusted upper and lower bounds are shown after each one of a total of six iterations. As can be seen, all results converge quickly to a local minimum in the parameter space situated in the vicinity of the initial model. This scheme of inversion is used in chapter VI.

IV.3. Two-Dimensional Modelling

The field relationships obeyed in the 2D case have been outlined in chapter II. In this section some general comments on the two-dimensional modeling using the finite difference scheme will be given. In particular the comments are directed to a particular finite difference algorithm (Brewitt-Taylor and Weaver, 1976), which is used in this work. The finite difference scheme has been widely used in two-dimensional modeling. The classical finite difference method was first used to study electromagnetic induction in 2D structures in the late 50's (Neves, 1957). It has also been used in 2D inversion algorithms (Jupp and Vozoff, 1977). The so-called transmission-line analogy also uses the finite difference formulation (Ku et al., 1973; Brewitt-Taylor and Johns, 1980).

The finite difference formulation used here is extensively described elsewhere (Brewitt-Taylor and Weaver, 1976; Weaver and Brewitt-Taylor, 1978). In this formulation the sharp boundaries and consequent introduction of "fictitious" field values from an earlier formulation (Jones and Pascoe, 1971) is substituted by the concept of "transition zones". Under this interpretation the conductivity changes from one region to another in a smooth linear manner. The electromagnetic field equations are calculated at each point on a grid which describes the model. These differential equations are reduced to an algebraic linear system for the unknown field values

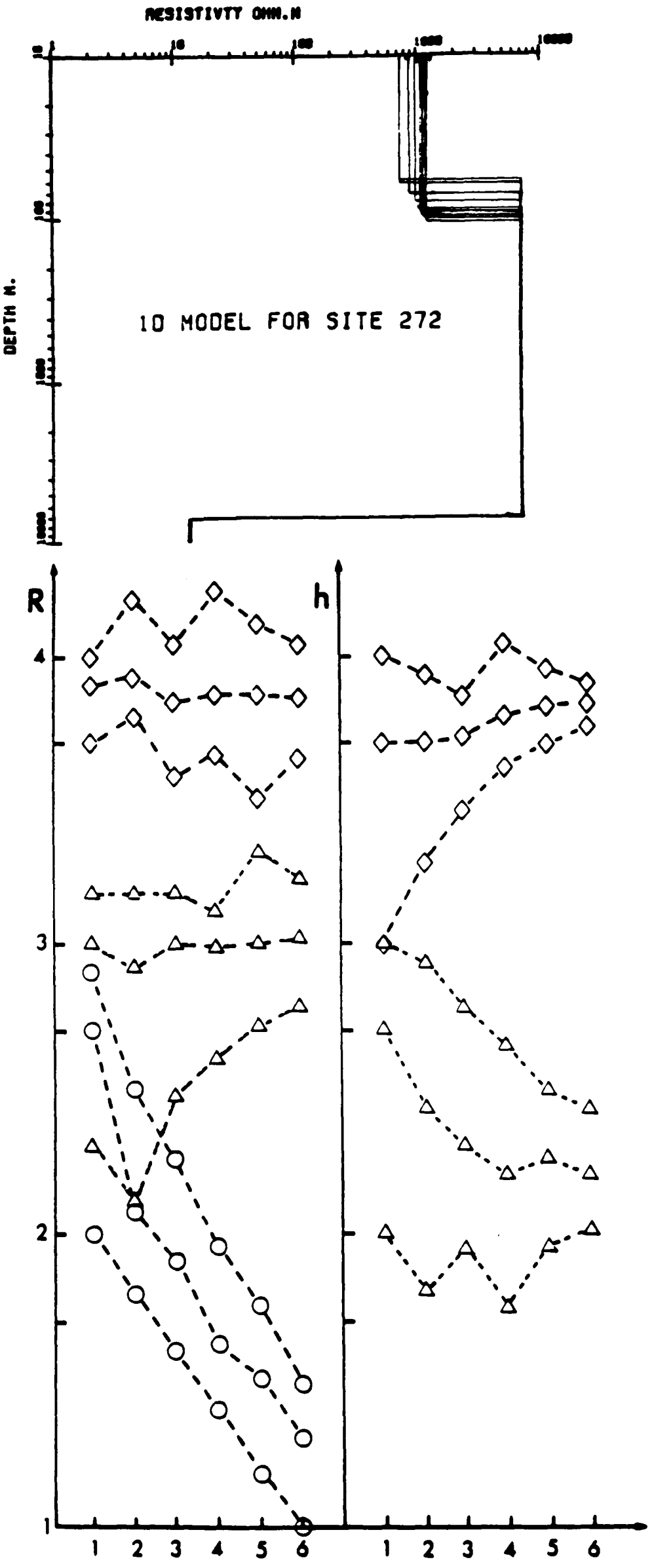
RESISTIVTY OHM.M
DEPTH M.
1D MODEL FOR SITE 272
R
h
1
2
3
4
1 2 3 4 5 6
1 2 3 4 5 6

Figure IV.1. Logarithms of resistivity and thicknesses obtained after each of 6 iterations using Monte Carlo inversion of apparent resistivity and phase along the measuring x-direction at site 72 (refer to chapter VI). On the top the best final three-layer models are shown. Resistivities (R) are shown on the left side and thicknesses (h) are on the right side. Triangles refer to the first layer, diamonds refer to the second layer and circles refer to the third layer. Each parameter grouping consists of the actual parameter value and its upper and lower bounds.

inside the grid. The matrix of this system is large but sparse and banded. Boundary conditions, expressed as finite difference conditions, are also included in this system. The grid design comes as a compromise between demand on computational resources and expected accuracy. Some guidelines on grid design can be found elsewhere (Doucet and Van Ngoc, 1984).

The derived fields, Ex and Hx for the E- and H-polarization cases respectively, are calculated by central differences at the centres of cells rather than at the nodes. The other components of the electromagnetic field are calculated at the nodes, so nodal derived fields are obtained by interpolation when needed. To overcome loss of accuracy caused by this interpolation, a new formulation for the derived fields at nodes is available and can be found elsewhere (Weaver et al., 1985; Weaver et al., 1986). A new version of the finite differences program incorporating those modifications became available recently (Brewitt-Taylor and Weaver, 1986). The version used here with the necessary modifications was compared against a published analytical calculation for a two-dimensional model (Weaver et al., 1985). The results are for the H-polarization case only. The model is composed of 3 resistive segments 50km thick overlying a basement of infinite resistivity. The resistivities are 10, 1 and 2 Ω.m, with the central segment 20km long. A 35x16 node grid is used with lateral dimensions y=-130km to 60km and z=0km to 50km. Figure IV.2 shows the amplitude and phase of Ey/Hx along the surface for a period of 300s. Results agree reasonably well with the greater discrepancies occurring above the left block. The discrepancies between the finite difference algorithm values were greater for the version which has been used here (FD1) than for the corresponding published finite difference values (FD2) (Brewitt-Taylor and Weaver, 1986). The FD1 version shows numerical-analytical discrepancies in amplitude and phase of 3% on average while the FD2 version shows smaller discrepancies which are 1% on average. The FD1 version of the finite difference algorithm is used in chapters V and VI.

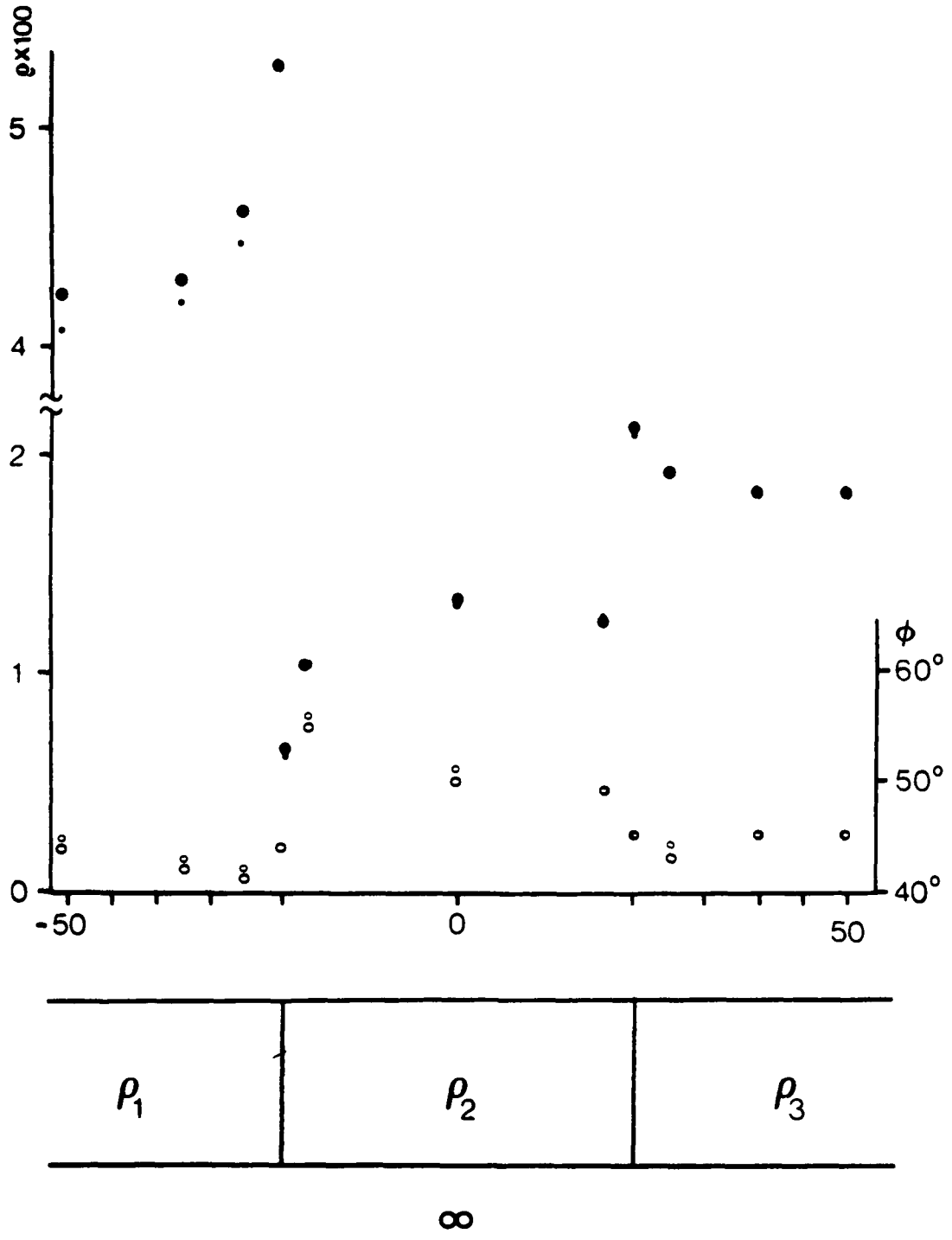
ρx100
5
4
2
1
0
-50
0
50
φ
60°
50°
40°

ρ_1
ρ_2
ρ_3

∞

Figure IV.2. Comparison between analytical results (Weaver et al., 1985) for the four resistivity model shown and finite difference calculations along the surface z=0 at 300s. The resistivities of the segments are ρ_1=10, ρ_2=1, and ρ_3=2 Ω m over a resistive basement at 50km. The heavy circles represent the amplitude and the open circles the phase of Ey/Hx. The larger symbols are the published analytical results and the smaller ones represent results obtained with the version of the finite difference algorithm used in this dissertation. Vertical units are V/nT and degrees and horizontal distances along the Y-axis are shown in km.

CHAPTER V
An Evaluation of the Topographic Effect of a Slope

V.1. Introduction

The presence of topography represents a complicating factor in the interpretation of magnetotelluric data. It belongs to the class of surface inhomogeneities. In general the problem is three-dimensional and frequency dependent, and in some particular cases it can be approximated by a two-dimensional structure. A recent review on topographical distortions of electromagnetic fields can be found elsewhere (Menvielle and Szarka, 1986). The objective of this chapter is to analyse the frequency dependent effect of a slope on an otherwise uniform half-space. This problem can be approximated by a two-dimensional model. The motivation behind this study arose when considering the data from the Canadian traverse considered in chapter VI. In order to isolate the effect of the slope, the problem is kept as simple as possible assigning a uniform conductivity to the earth.

The distortions induced by topographic features on land surveys have been studied for more than two decades. A number of different techniques have been used to model local topography. Plexiglass ridges have been used in analogue models (Faradzhev et al., 1972). Two-dimensional approximations were carried out using transmission system and network analogies (Ku et al., 1973, Mozley, 1982), finite elements (Wannamaker et al., 1986) and a modification of Rayleigh scattering theory (Jiracek, 1973) for modeling single topographic features (Reddig and Jiracek, 1984). The simpler telluric case has been analysed with the aid of conformal transformation (Thayer, 1975; Harinarayana and Sarma, 1982). Distortions on sounding curves are available in album format (Berdichevsky and Dmitriev, 1976). In principle any numerical technique in which field values are calculated across a model can be used in evaluating the distortions due to a topographic feature. In addition it may also be possible to normalize impedance tensor elements to compensate for the topographic distortions (Mozley, 1982).

V.2. Modelling Procedure

For the modeling of the topography a finite difference algorithm (Brewitt-Taylor and Weaver, 1976) was used in calculating surface responses, refer to chapter IV for an introduction to the algorithm. A single basic grid was used for all the models considered. The y-axis is perpendicular to the strike direction and

the z-axis points downwards. The grid is made of 51 nodes along the y-direction and 31 nodes along the z-direction. Since grid elements are rectangular, slopes are approximated by a series of steps. The height difference between lower and higher (horizontal) sides is kept constant at 1km, while allowing slope angles to vary from 10 to 90 degrees. The half-space below the slope is assumed to be of uniform resistivity, $\rho = 100 \Omega.m$.

Both overall grid size and the smallest distance between two grid points depend on the skin depths considered. The skin depth is given by expression (II.16) which can be re-written as

$$\delta = \frac{5}{\pi}\sqrt{10T} \qquad (V.1)$$

with the period T in seconds. Eight period values are considered here covering the range from 0.005s to 100s. These provide skin depths varying from 356m to 50.3km. Distances between grid points will depend on their proximity to the slope. The nearer to the slope a grid point is, the smaller its distance to neighbouring grid points. The smallest distance between two grid points was chosen to be 0.2km. This value is slightly larger than the skin depth corresponding to 0.001s. The whole grid is a square of dimensions 800x800km. This is sufficient to ensure that any slope model is about 8 skin depths from the edges at 100s. Grid geometry was inspired by published guidelines (Doucet and Ngoc, 1984). The air is simulated by assigning a high resistivity value $\rho_{air} = 10^{20} \Omega.m$. The horizontal electromagnetic field is calculated for both polarizations through the grid. Apparent resistivity and phase are calculated along the surface. The finite difference program produces stable results only outside the slope, thus the investigation reported here is restricted to points situated outside the slope. Distances are then measured from the left of the slope $y<0$ or from the right of it, $y>0$. Therefore when referring to results of a particular model in the text below, it is assumed that the distance is measured from the nearest edge of the slope. Models are referred to by the angle of inclination α. Six models are considered here, $\alpha = 10$, 20, 45, 60, 80, and 90 degrees. Figure V.1 illustrates in grid scale the 45° slope model used in the calculations, note that the distances in this figure are grid distances and not distances from the slope.

Since the same grid was used for all periods, it is necessary to assess the quality of the results throughout the whole period range. For this purpose a half-space model with the surface at $z=0$ is used. Consider all grid points on the surface with grid

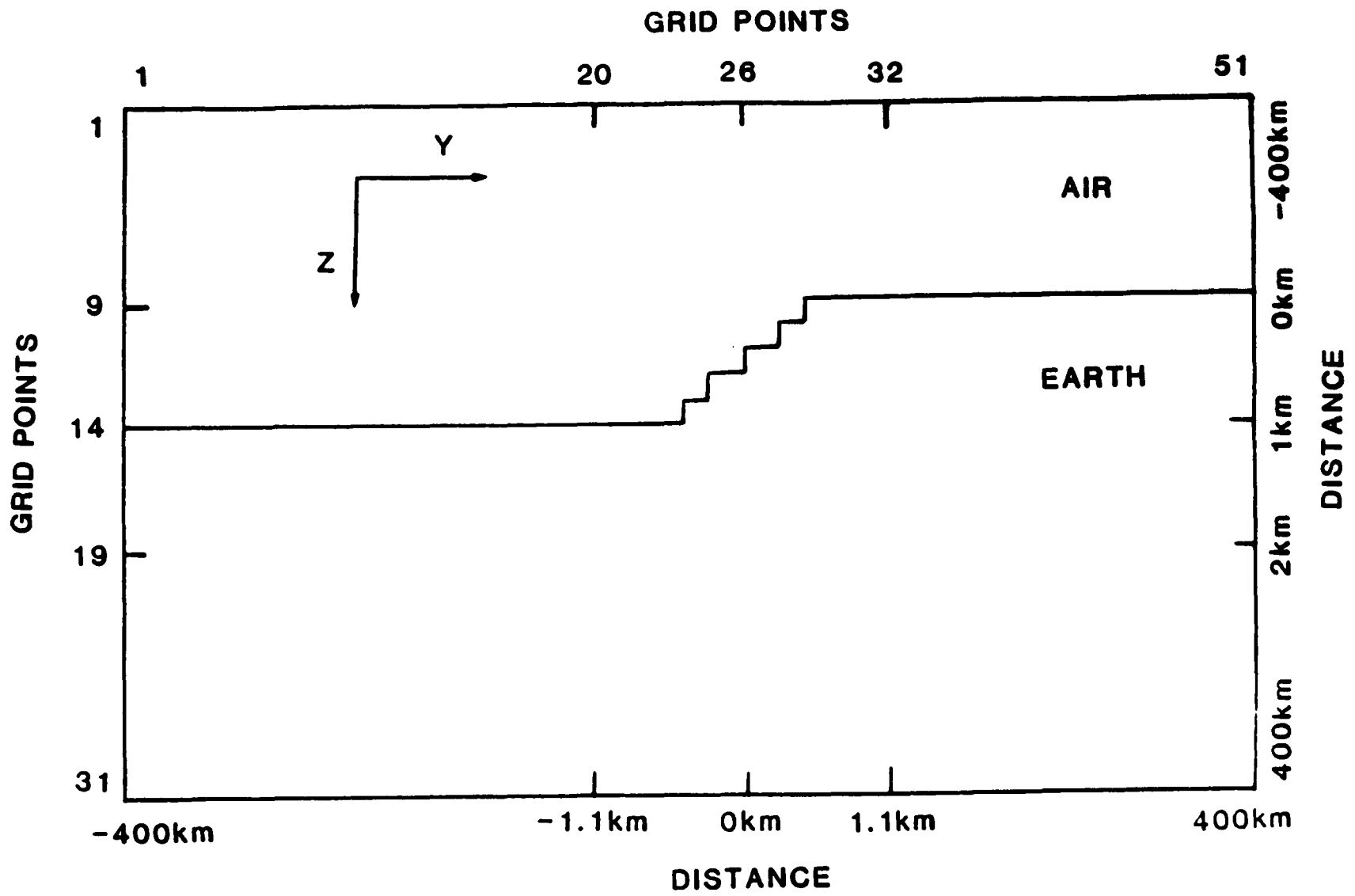
GRID POINTS
1
20
26
32
51
1
9
14
19
31
GRID POINTS
Y
Z
AIR
EARTH
-400km
0km
1km
2km
DISTANCE
400km
-400km
-1.1km
0km
1.1km
400km
DISTANCE

Figure V.1. Model, in grid scale, of a 45° slope showing the thickness of the air layer required by E-polarization calculations.

distances $|y| \leq 100$km. At each period the mean and standard deviation values are calculated for the apparent resistivity and phase. Both polarization results are considered together, giving a total of 90 values used in the calculation of each quantity. Figure V.2 shows the mean values and standard deviations for points $|y| \leq 100$km (grid distance). The half-space results show good numerical stability. The mean values for both apparent resistivity and phase agree with the theoretical values, the biggest discrepancy is 0.3% for the apparent resistivity at T=100s. The standard deviations are always less than 10%. Restricting the calculation to points $|y| \leq 10$km makes the standard deviation values drop to $\leq 7\%$. Note that a slope model is always less than 6km in length.

V.3. Results

Begin by analysing the distortions on the apparent resistivity and phase against distance for both E-polarization, ρ_E and φ_E, and H-polarization, ρ_H and φ_H. This analysis is restricted to points $|y| \leq 8$km from the slope as distortions are not significant at a 10% level beyond this distance. For model calculations the degree of distortion is simply measured by the departure from the theoretical values, in other words of ρ from 100Ω.m and of φ from 45°.

Spatial distortions due to a slope

Spatial distortions for the E-polarization case are presented in figure V.3 for a few selected periods. As can be seen both ρ_E and φ_E are more affected the shorter the period is. For periods $T \geq 5$s distortions are less than 10% and therefore are not shown in this figure. As the period increases the distortion amplitudes decrease but the distance where the effect can be detected increases. Also the distortions are stronger for points on the right of the slope, $y>0$. At such points distortions can reach 70%, although the effect is very localized. At points $y<0$ distortions are limited to about 10%. Phase distortions are small and follow the same pattern as the apparent resistivity, i.e. both follow the topography in the sense that slope distortion produces lower values on the lower side and higher values on the higher side. The E-polarization results shown in figure V.3 are clearly frequency dependent in character. This reflects the inductive nature of the distortion experienced in this mode. The maximum distortions occur when the skin depth in the medium is of the same order as the electromagnetic scale length of the topographic feature. Skin depths for the periods considered in figure V.3 range from 0.35km for T=0.005s to 11.2km for T=5s.

FLAT SURFACE

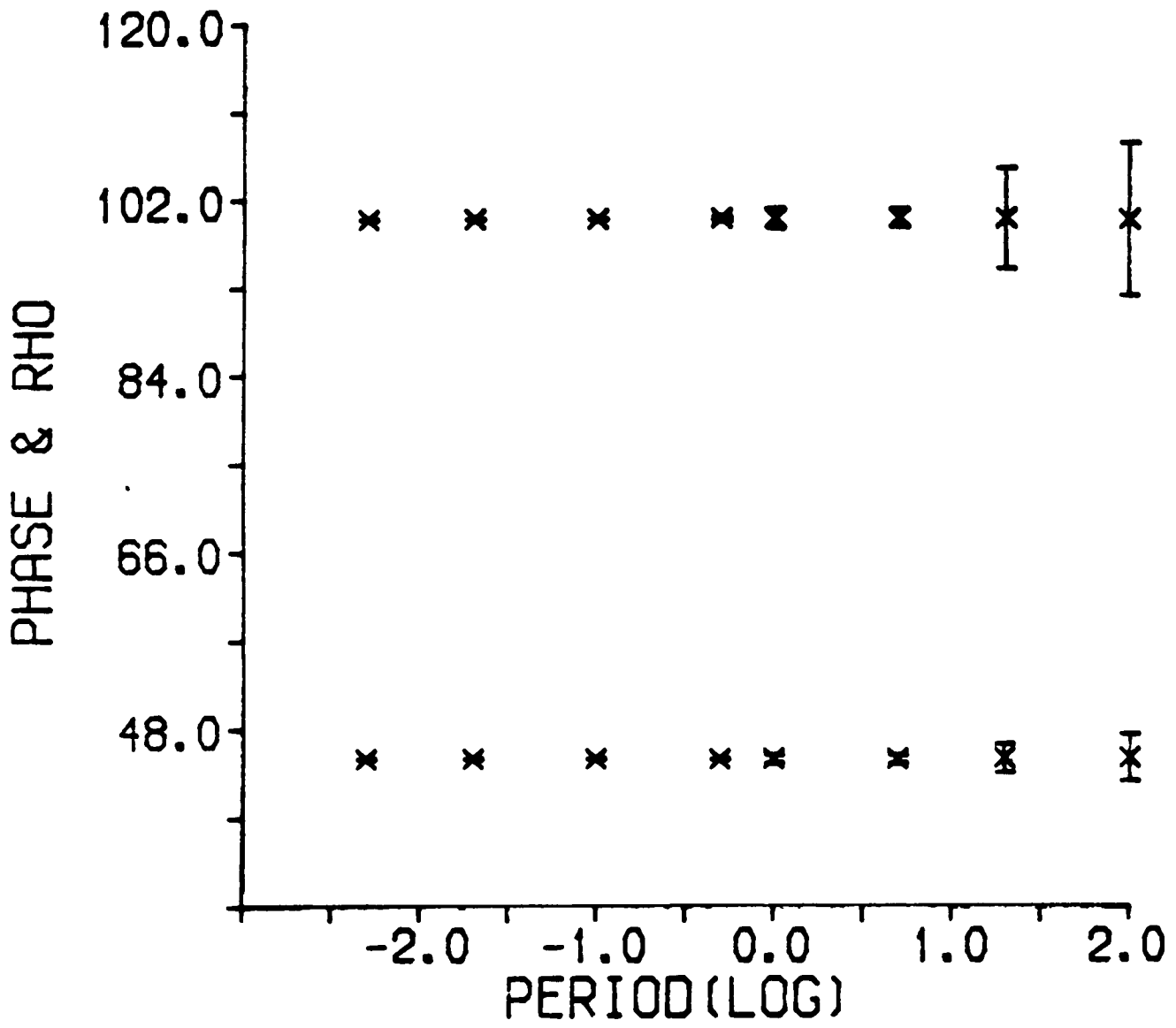

Figure V.2. Mean values and standard deviations for apparent resistivity and phase for points along the surface $|y| \leq 100$km. Both polarizations are considered. Apparent resistivity is in Ω.m and phase is in degrees.

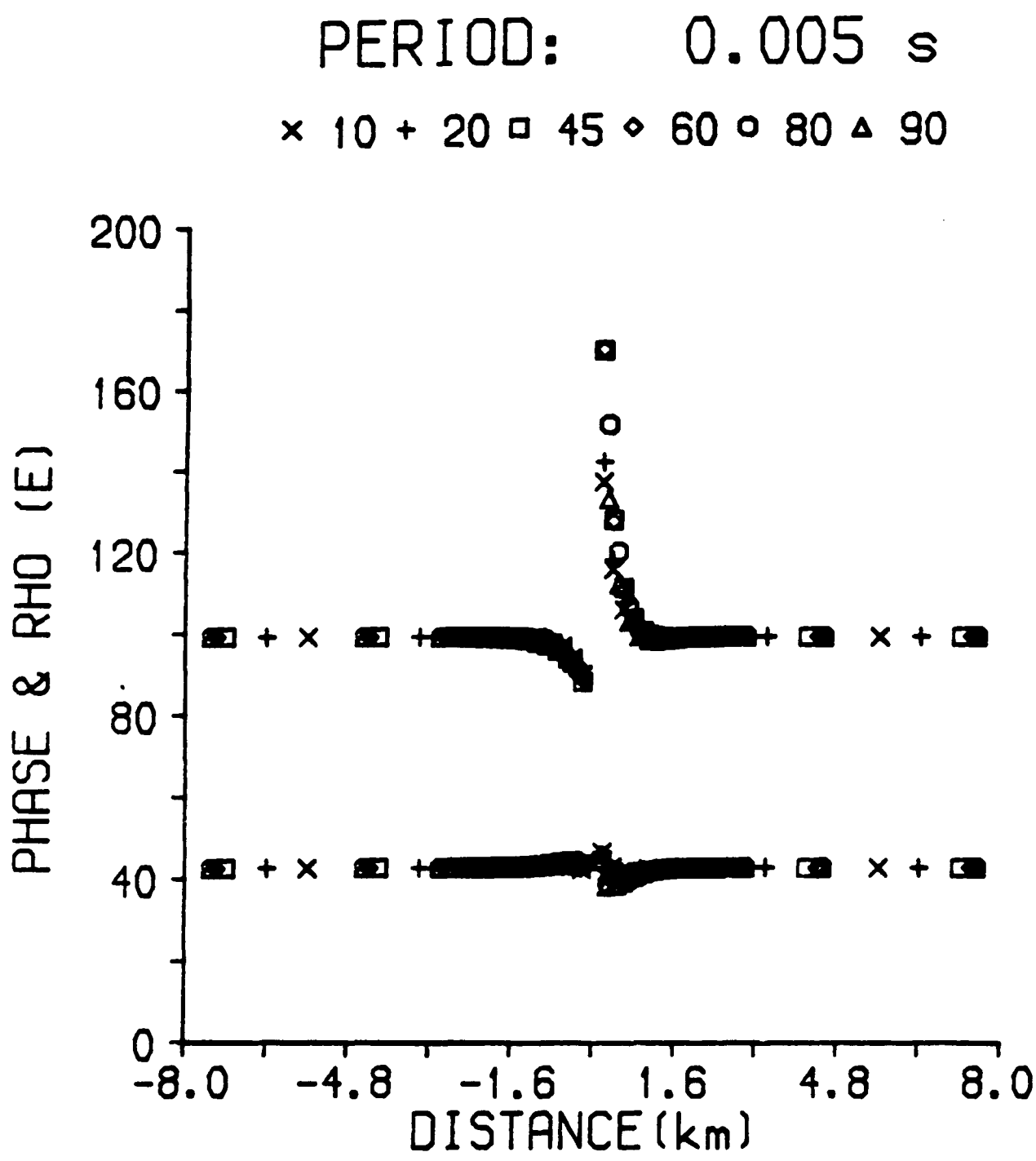
PERIOD: 0.005 s
× 10 + 20 □ 45 ◇ 60 ○ 80 △ 90
PHASE & RHO (E)
200
160
120
80
40
0
-8.0
-4.8
-1.6
1.6
4.8
8.0
DISTANCE(km)

Figure V.3.a. Apparent resistivity and phase for the E-polarization case against distance for T=0.005s. In this and in the following figures each model response is represented by a particular symbol. The grid geometry makes the relative distances from the slope differ for each model. As a consequence the maximum distortions appear to occur at angles less than 90 degrees as can be seen in this and in the next figures. This effect is simply pictorial as the small differences in the relative distances are not apparent. At a given distance the distortions are more drastic the greater the angle.

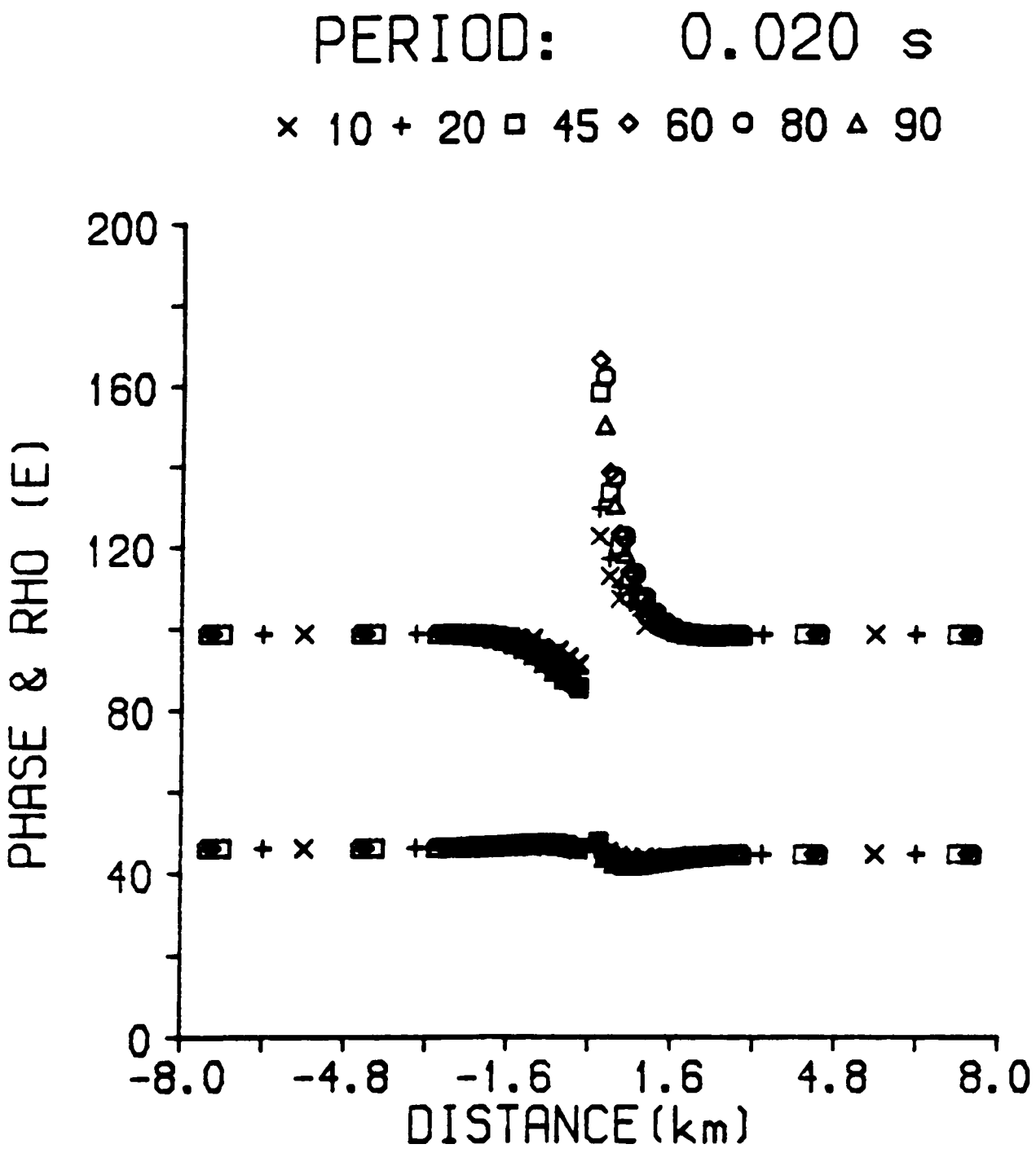
PERIOD: 0.020 s
× 10 + 20 □ 45 ◇ 60 ○ 80 △ 90
200
160
120
80
40
0
PHASE & RHO (E)
-8.0
-4.8
-1.6
1.6
4.8
8.0
DISTANCE(km)

Figure V.3.b. Apparent resistivity and phase for the E-polarization case against distance for T=0.02s.

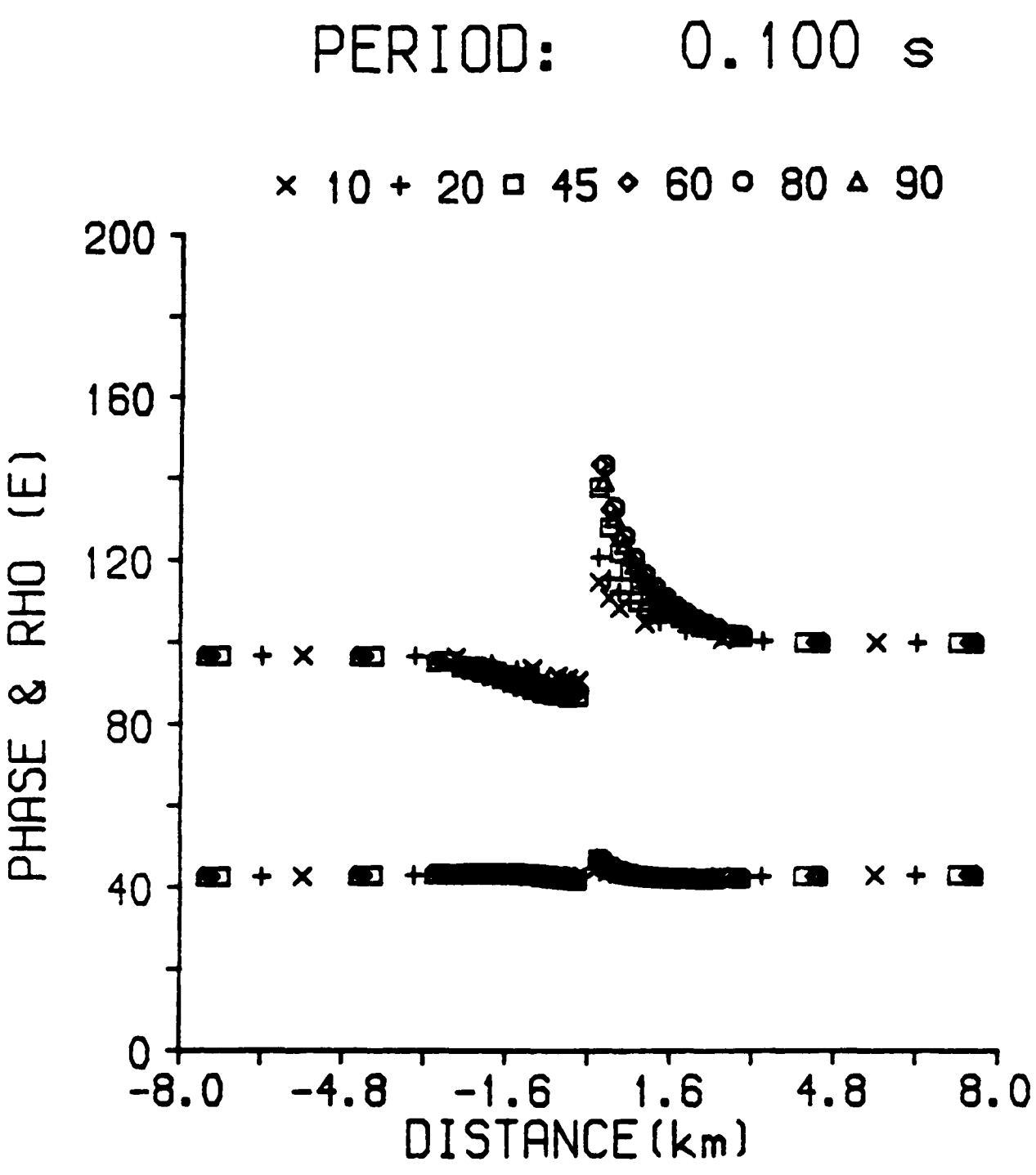
PERIOD: 0.100 s
× 10 + 20 □ 45 ◇ 60 ○ 80 △ 90
PHASE & RHO (E)
200
160
120
80
40
0
-8.0
-4.8
-1.6
1.6
4.8
8.0
DISTANCE(km)

Figure V.3.c. Apparent resistivity and phase for the E-polarization case against distance for T=0.1s.

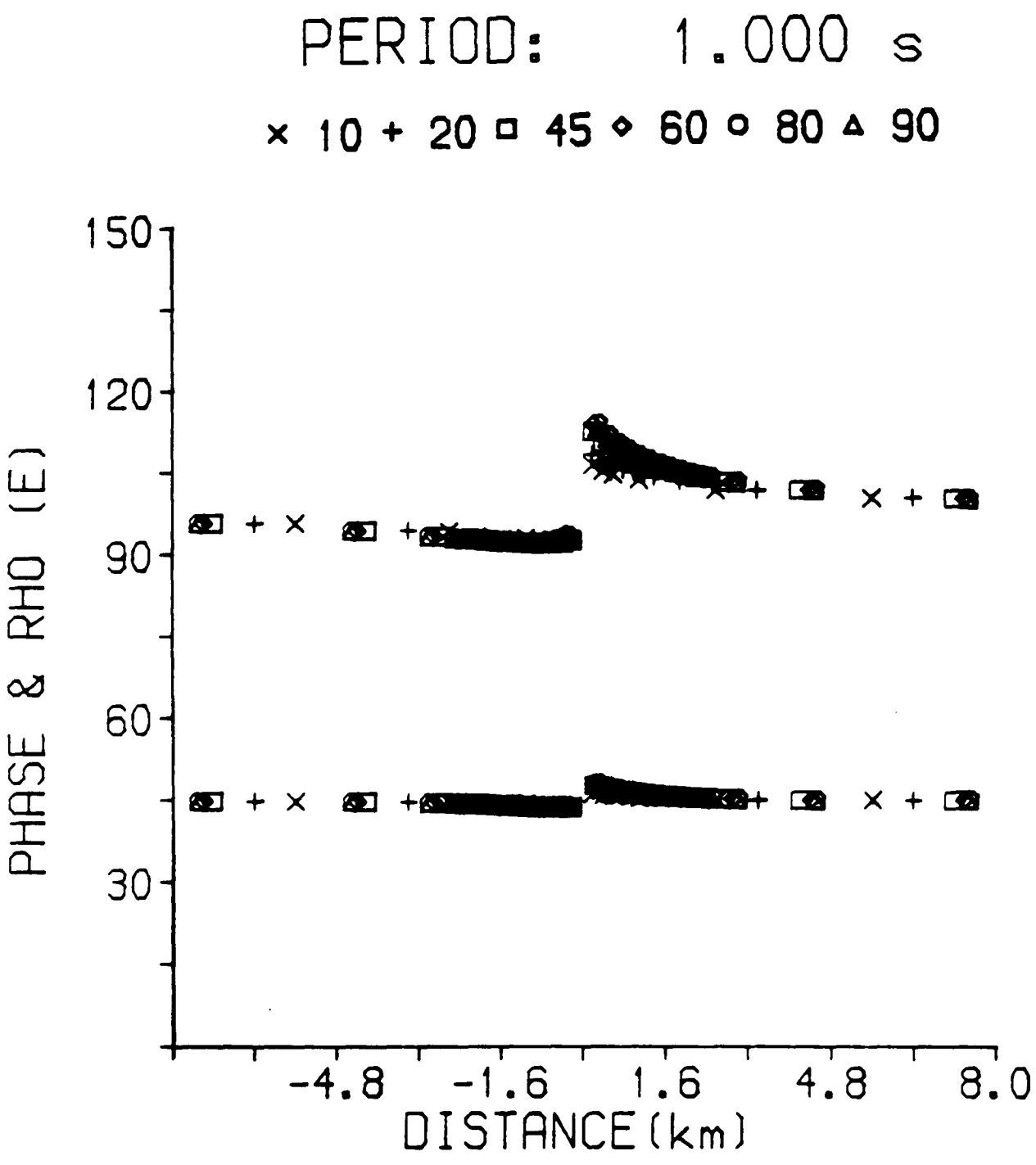
PERIOD: 1.000 s
× 10 + 20 □ 45 ◇ 60 ○ 80 △ 90
150
120
90
60
30
PHASE & RHO (E)
-4.8
-1.6
1.6
4.8
8.0
DISTANCE(km)

Figure V.3.d. Apparent resistivity and phase for the E-polarization case against distance for T=1s.

It is well known that the H-polarization case, when induced currents are perpendicular to the slope, is more affected than the E-polarization case. Figure V.4 shows both ρ_H and φ_H for a few selected periods. The longer the period, the more affected the apparent resistivity ρ_H is, while the phase φ_H is distorted above 10% only at points $y>0$ for periods $T\leq 1s$. Moreover the phase is more affected at shorter periods, as occurs for the E-polarization case, while ρ_H displays the reverse behaviour. Values of ρ_H can be distorted in excess of 100% on both sides of the slope.

Distortions of sounding curves at particular sites

Another interesting point is how sounding curves are distorted at one particular site. Six sites are selected: $|y|=0.4,1$, and 2km. Begin with the least distorted E-polarization case. As it is already known from figure V.3, only sites near the slope are significantly affected, so the analysis may be restricted to distances $|y|\leq 1km$. Figure V.5 shows the sounding curves for the four nearer sites. The two extreme sites $|y|=2km$ show distortions which are below 10% and thus may be neglected. For the remaining four sites distortions can reach 15% on the lower side and 50% on the higher side. H-polarization derived sounding curves for ρ_H are strongly distorted at all 6 sites as shown in figure V.6. Unlike the E-polarization case, the phase is also very distorted at points $y>0$. On the lower side phases are very little distorted but apparent resistivities suffer distortions which are of the same order as the ones experienced on the higher side reaching 100%. On the higher side phase distortions reach 58% at similar periods where maximum distortions on the apparent resistivities occur for the E-polarization case.

As can be inferred from the last two figures the effect of the slope is essentially to produce an artificial two-layer sounding curve at the most distorted locations. In order to investigate such effects, the sounding curves are inverted at two sites, $|y|=1km$. For this inversion a 1D linearized inversion scheme (Jupp and Vozoff, 1975) is employed. This algorithm is described in chapter IV. Both apparent resistivity and phase are inverted jointly, and all inversions have the same two-layer starting model with $\rho_1=\rho_2=100\Omega.m$ and h=10km for the thickness of the first layer.

Inversions of the E-polarization data show very little deviation from the true structure. For $|y|=1km$ inversions are virtually unaffected by the presence of the slope. However inversions of the H-polarization data are affected by the slope.

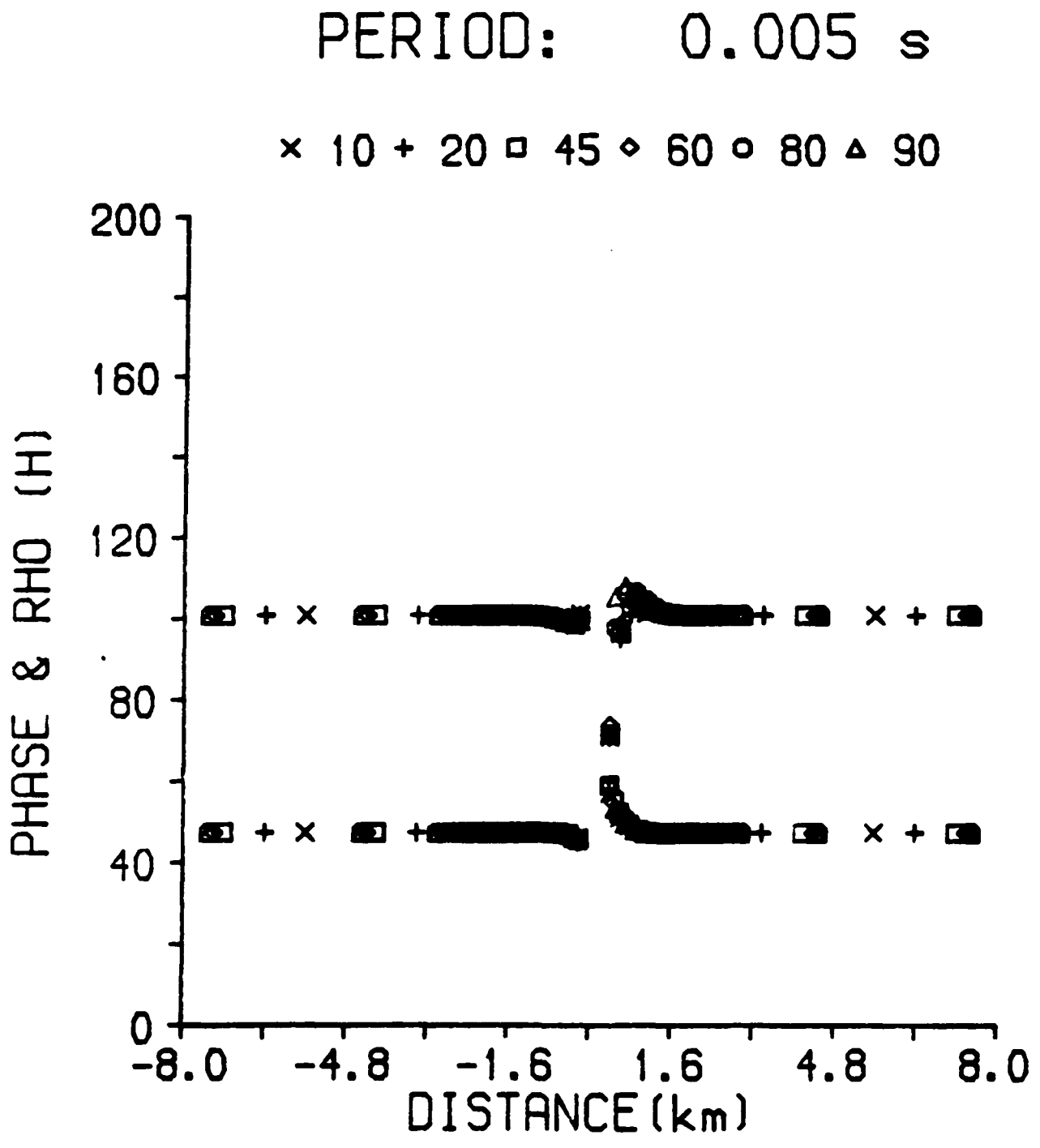
PERIOD: 0.005 s
× 10 + 20 □ 45 ◇ 60 ○ 80 △ 90
200
160
120
80
40
0
PHASE & RHO (H)
-8.0
-4.8
-1.6
1.6
4.8
8.0
DISTANCE(km)

Figure V.4.a. Apparent resistivity and phase for the H-polarization case against distance for T=0.005s.

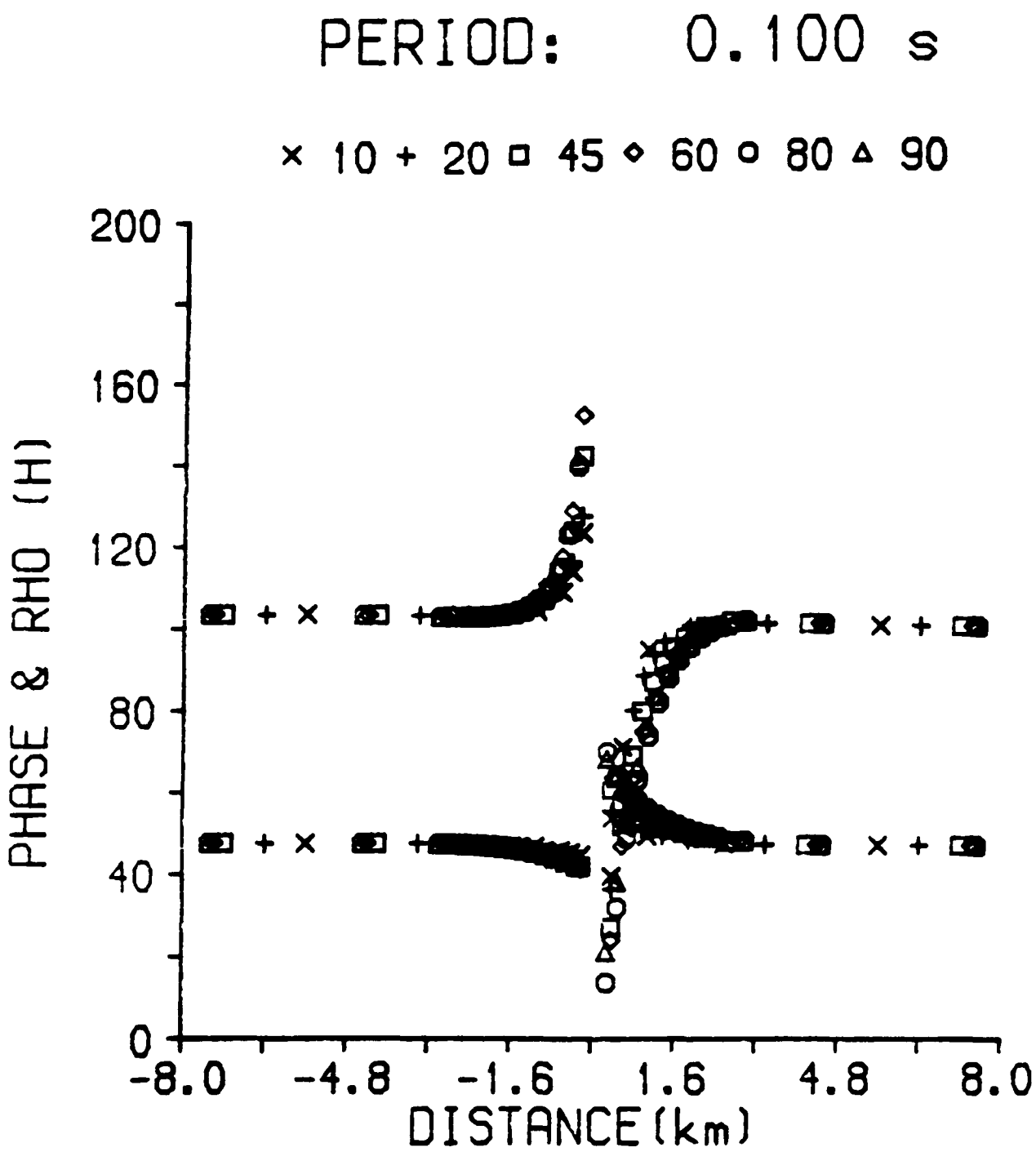
PERIOD: 0.100 s
× 10 + 20 □ 45 ◇ 60 ○ 80 △ 90
200
160
120
80
40
0
PHASE & RHO (H
-8.0
-4.8
-1.6
1.6
4.8
8.0
DISTANCE(km)

Figure V.4.b. Apparent resistivity and phase for the H-polarization case against distance for T=0.1s.

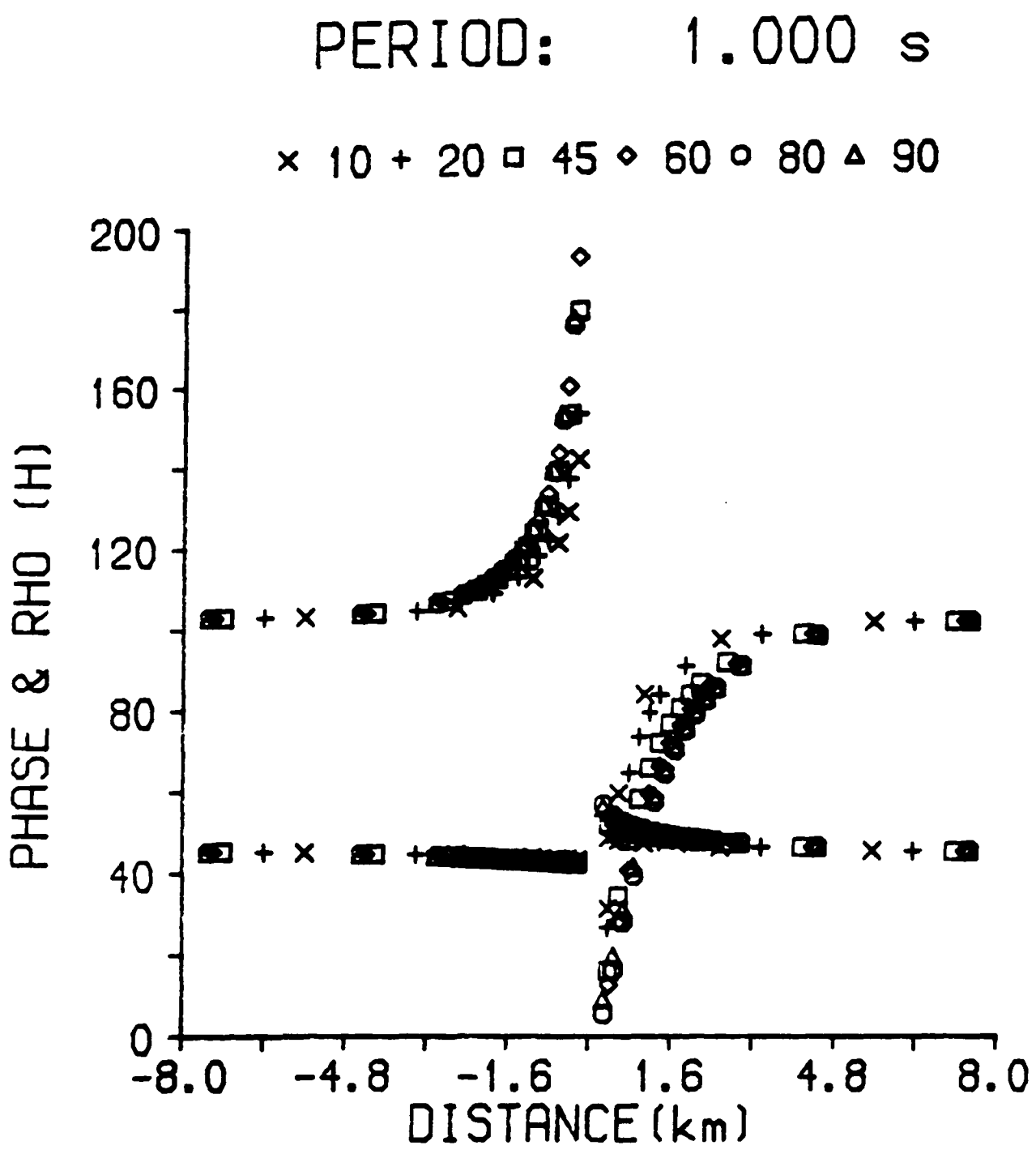
PERIOD: 1.000 s
× 10 + 20 □ 45 ◇ 60 ○ 80 △ 90
PHASE & RHO (H)
200
160
120
80
40
0
-8.0
-4.8
-1.6
1.6
4.8
8.0
DISTANCE(km)

Figure V.4.c. Apparent resistivity and phase for the H-polarization case against distance for T=1s.

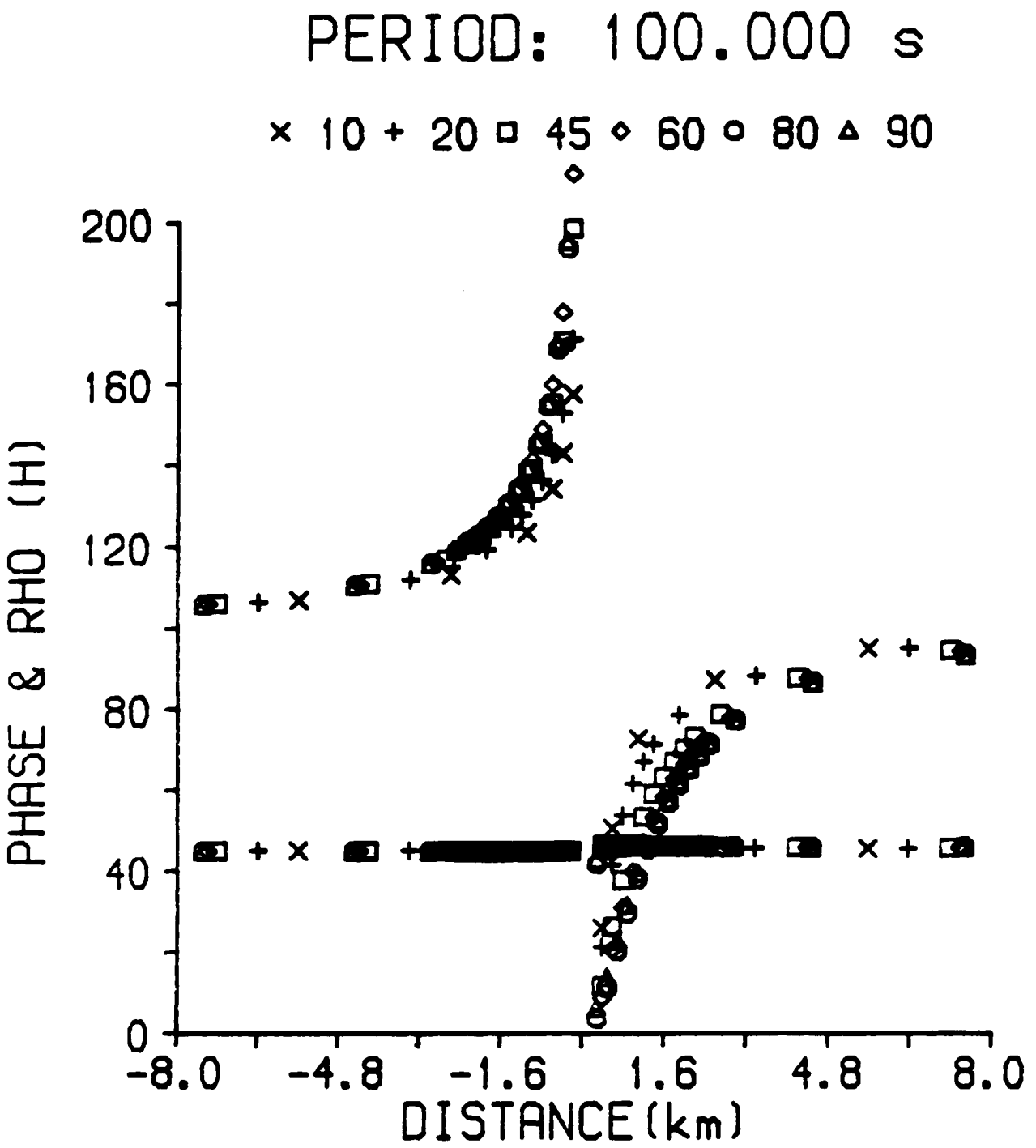
PERIOD: 100.000 s
× 10 + 20 □ 45 ◇ 60 ○ 80 △ 90
200
160
120
80
40
0
PHASE & RHO (H)
-8.0
-4.8
-1.6
1.6
4.8
8.0
DISTANCE(km)

Figure V.4.d. Apparent resistivity and phase for the H-polarization case against distance for T=100s.

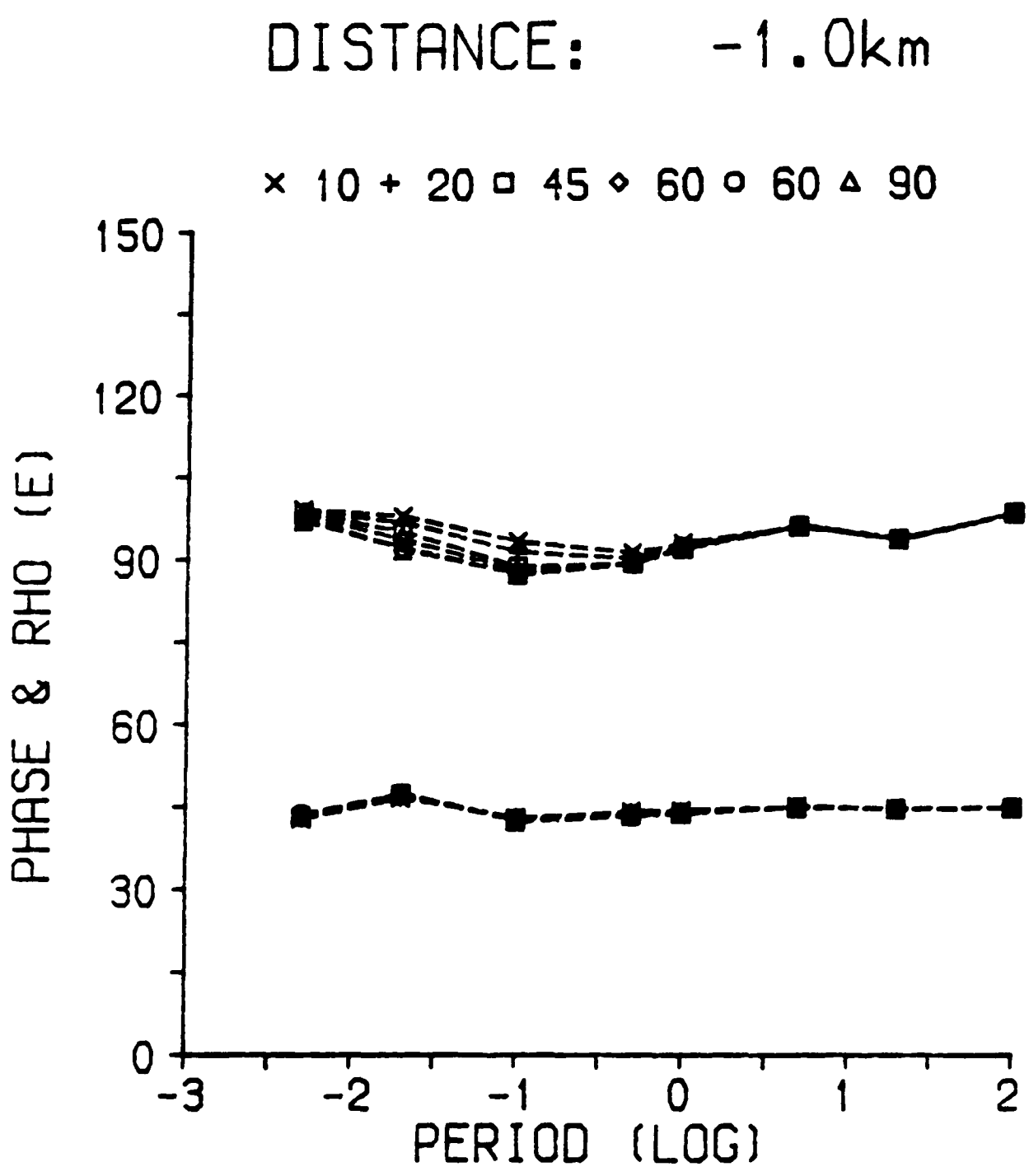
DISTANCE: -1.0km
× 10 + 20 □ 45 ◇ 60 ○ 60 △ 90
PHASE & RHO (E)
150
120
90
60
30
0
-3
-2
-1
0
1
2
PERIOD (LOG)

Figure V.5.a. Sounding curves for the E-polarization case at Y=-1km.

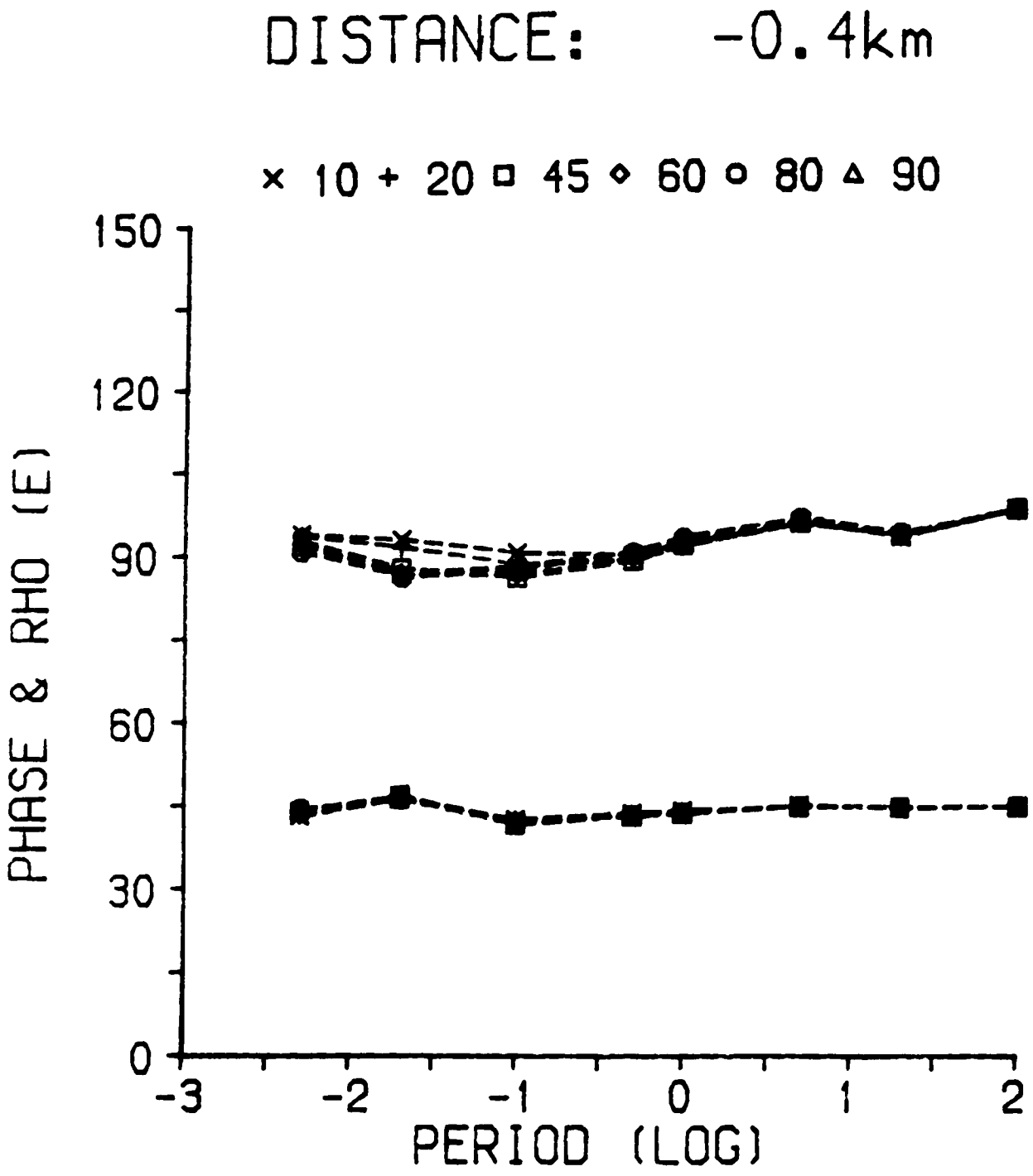
DISTANCE: -0.4km
× 10 + 20 □ 45 ◇ 60 ○ 80 △ 90
150
120
90
60
30
0
PHASE & RHO (E)
-3
-2
-1
0
1
2
PERIOD (LOG)

Figure V.5.b. Sounding curves for the E-polarization case at Y=-400m.

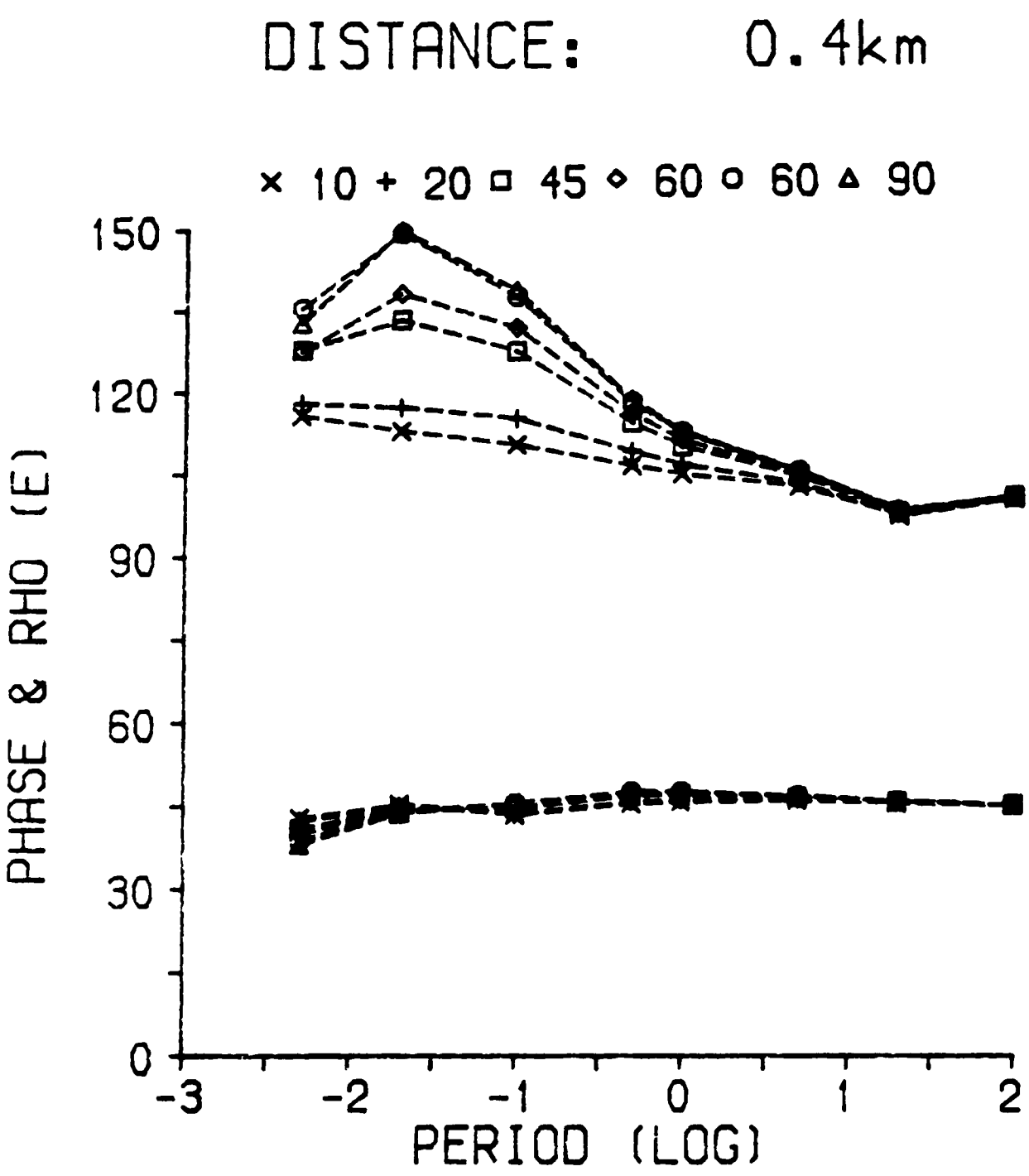
DISTANCE: 0.4km
× 10 + 20 □ 45 ◇ 60 ○ 60 △ 90
150
120
90
60
30
0
PHASE & RHO (E)
-3
-2
-1
0
1
2
PERIOD (LOG)

Figure V.5.c. Sounding curves for the E-polarization case at Y=400m.

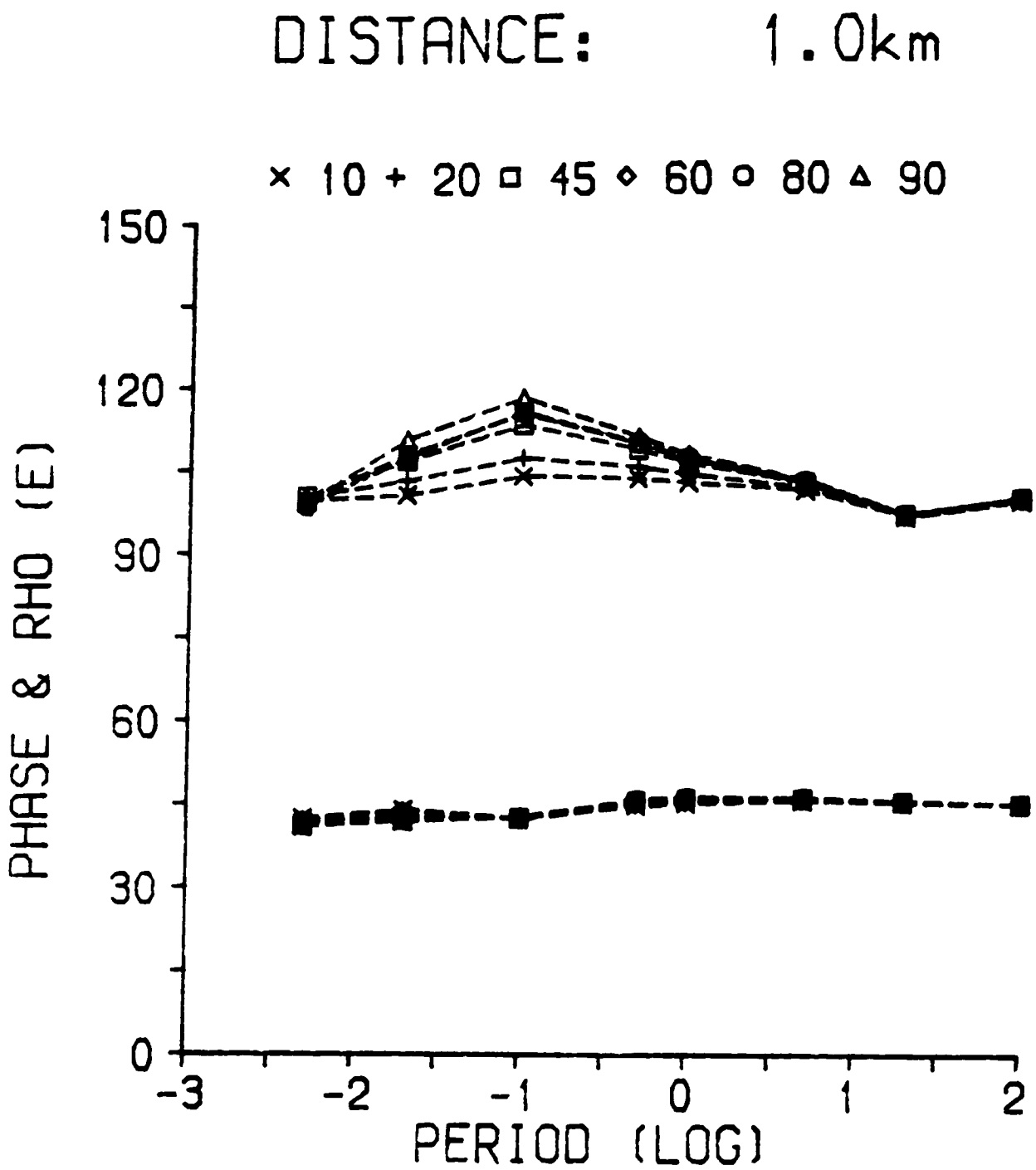
DISTANCE: 1.0km
× 10 + 20 □ 45 ◇ 60 ○ 80 △ 90
150
120
90
60
30
0
PHASE & RHO (E)
-3
-2
-1
0
1
2
PERIOD (LOG)

Figure V.5.d. Sounding curves for the E-polarization case at Y=1km.

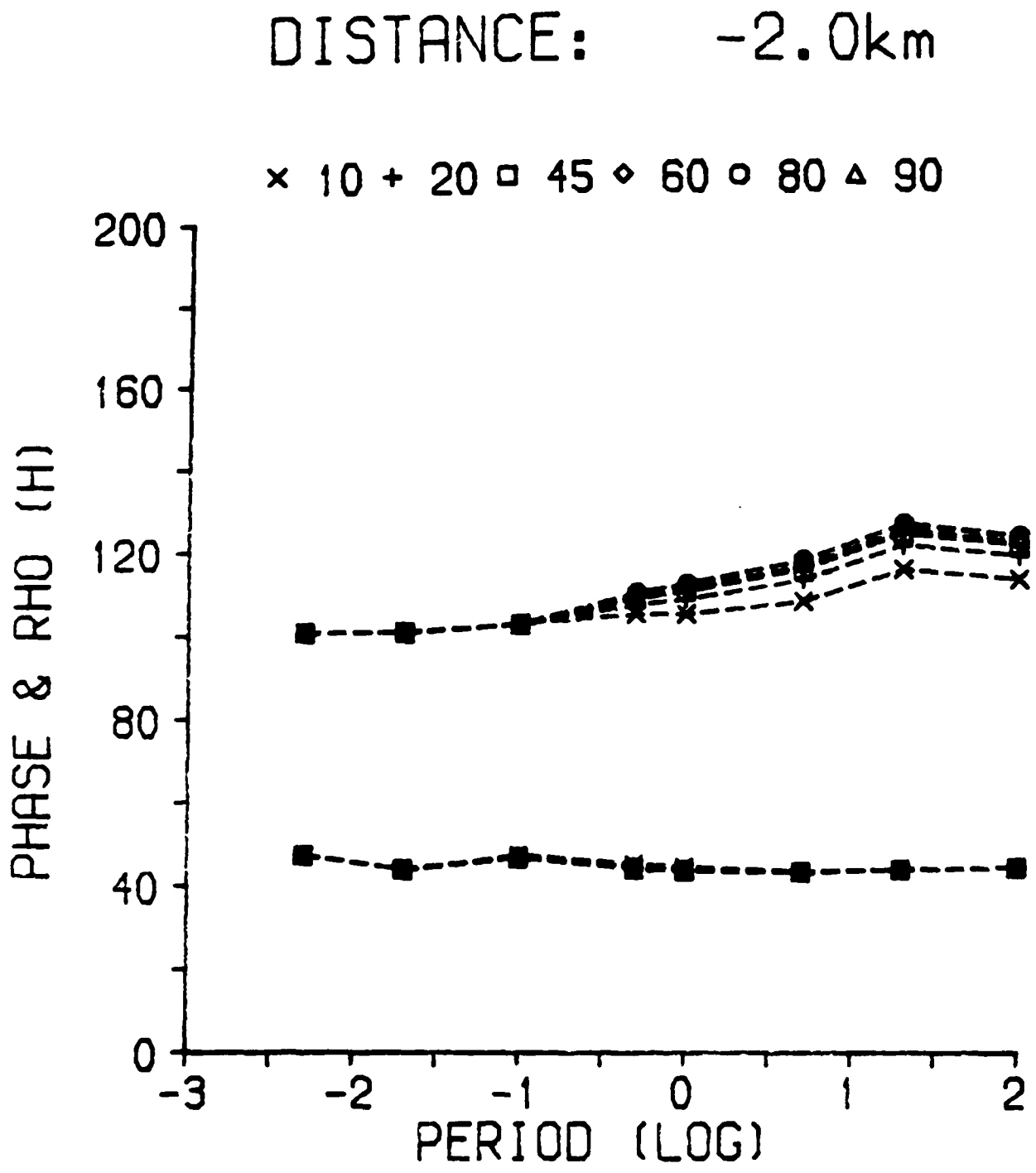
DISTANCE: -2.0km
× 10 + 20 □ 45 ◇ 60 ○ 80 △ 90
200
160
120
80
40
0
PHASE & RHO (H)
-3
-2
-1
0
1
2
PERIOD (LOG)

Figure V.6.a. Sounding curves for the H-polarization case at Y=-2km.

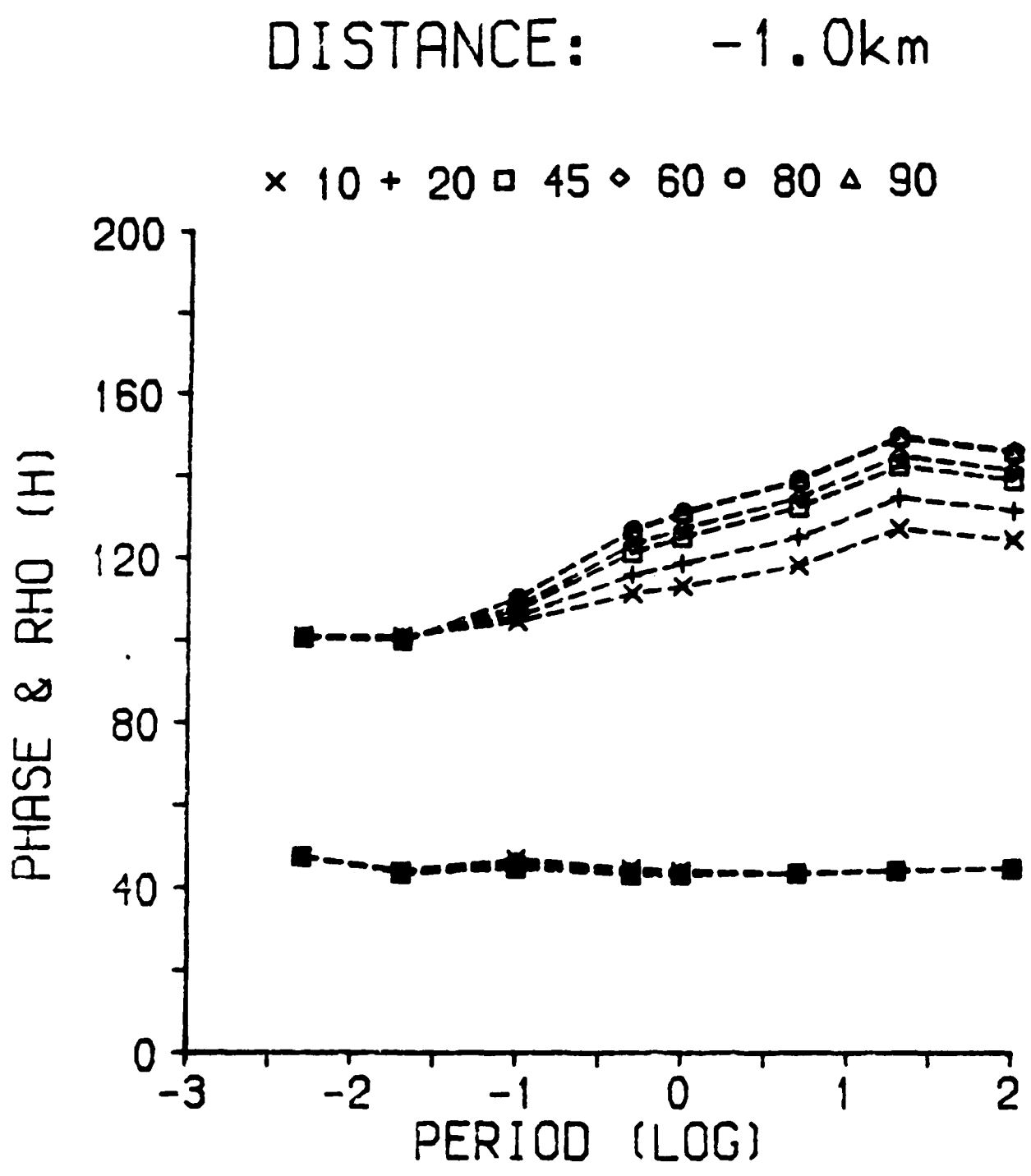
DISTANCE: -1.0km
× 10 + 20 □ 45 ◇ 60 ○ 80 △ 90
200
160
120
80
40
0
PHASE & RHO (H)
-3
-2
-1
0
1
2
PERIOD (LOG)

Figure V.6.b. Sounding curves for the H-polarization case at Y=-1km.

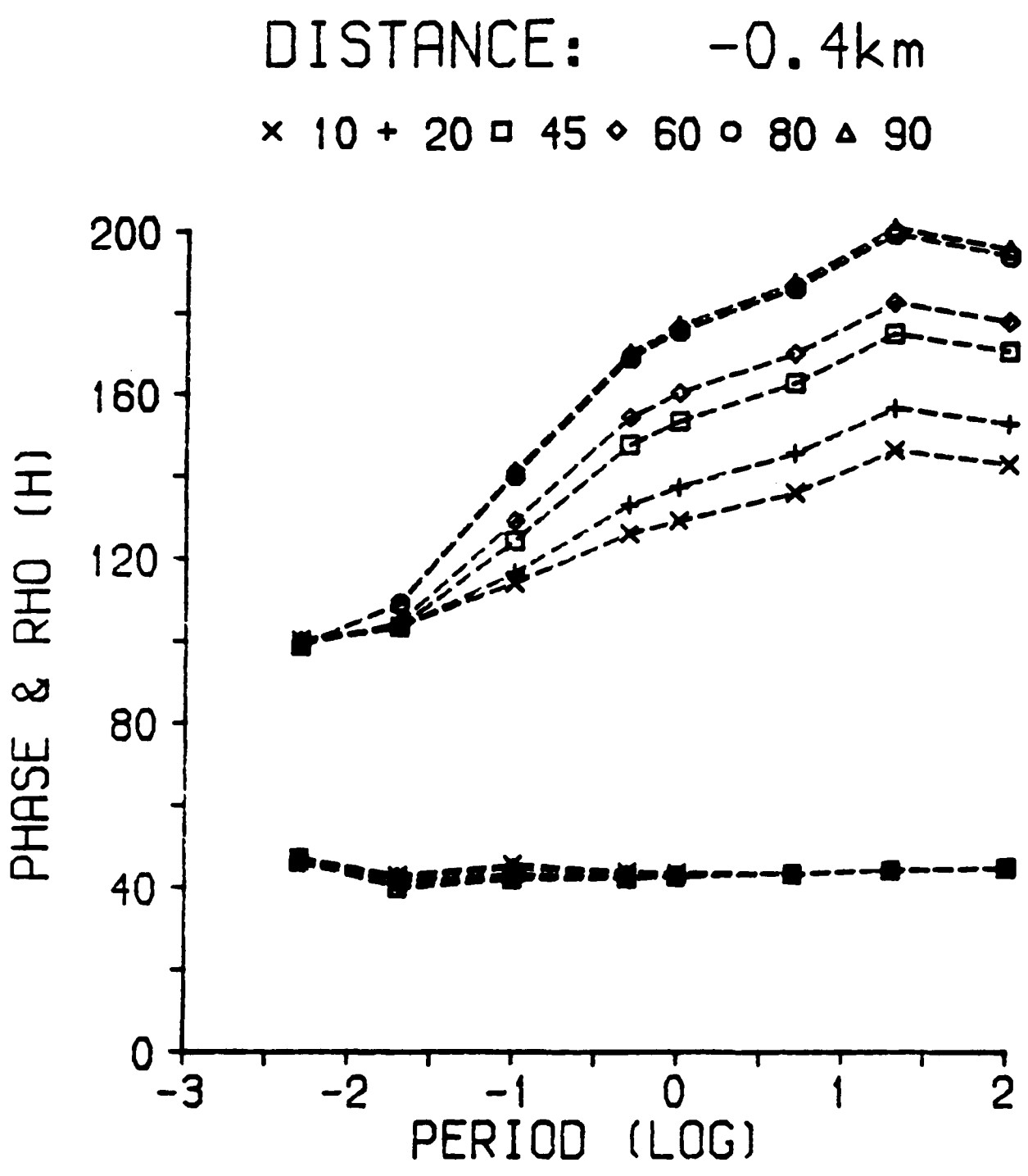
DISTANCE: -0.4km
× 10 + 20 □ 45 ◇ 60 ○ 80 △ 90
200
160
120
80
40
0
PHASE & RHO (H)
-3
-2
-1
0
1
2
PERIOD (LOG)

Figure V.6.c. Sounding curves for the H-polarization case at Y=-400m.

DISTANCE: 0.4km

× 10 + 20 □ 45 ◇ 60 ○ 80 △ 90

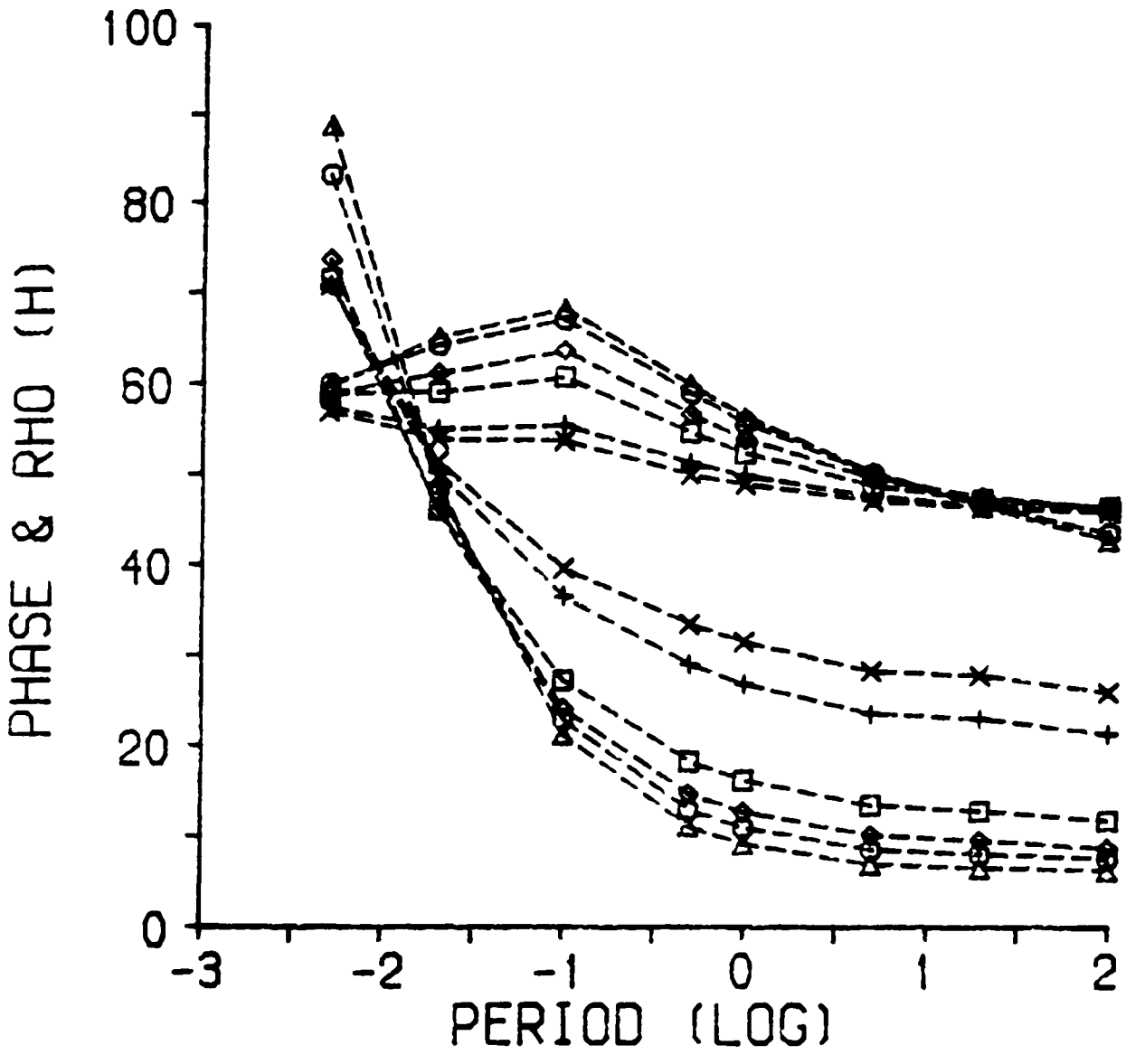

Figure V.6.d. Sounding curves for the H-polarization case at Y=400m.

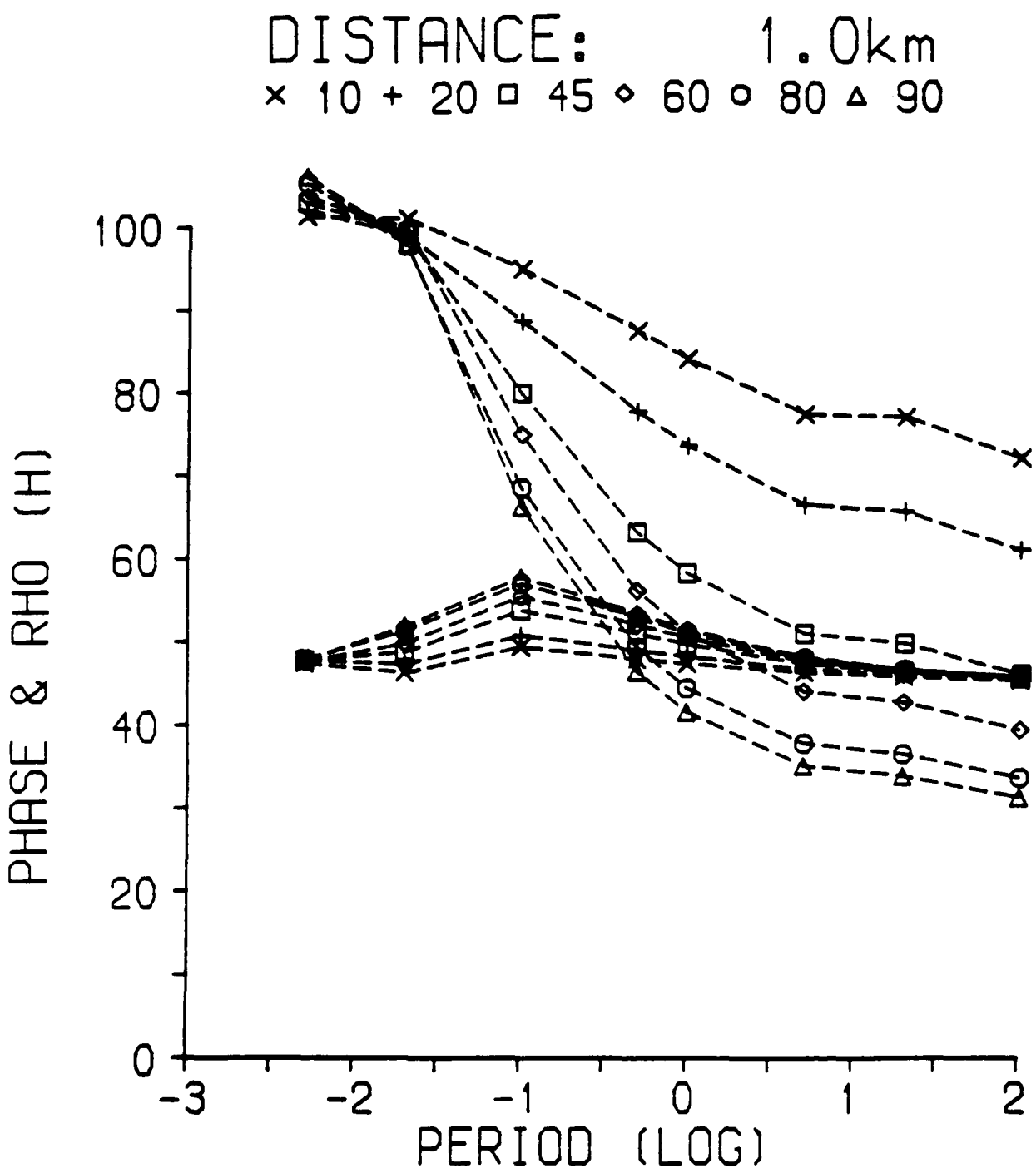
DISTANCE: 1.0km
× 10 + 20 □ 45 ◇ 60 ○ 80 △ 90
PHASE & RHO (H)
100
80
60
40
20
0
-3
-2
-1
0
1
2
PERIOD (LOG)

Figure V.6.e. Sounding curves for the H-polarization case at Y=1km.

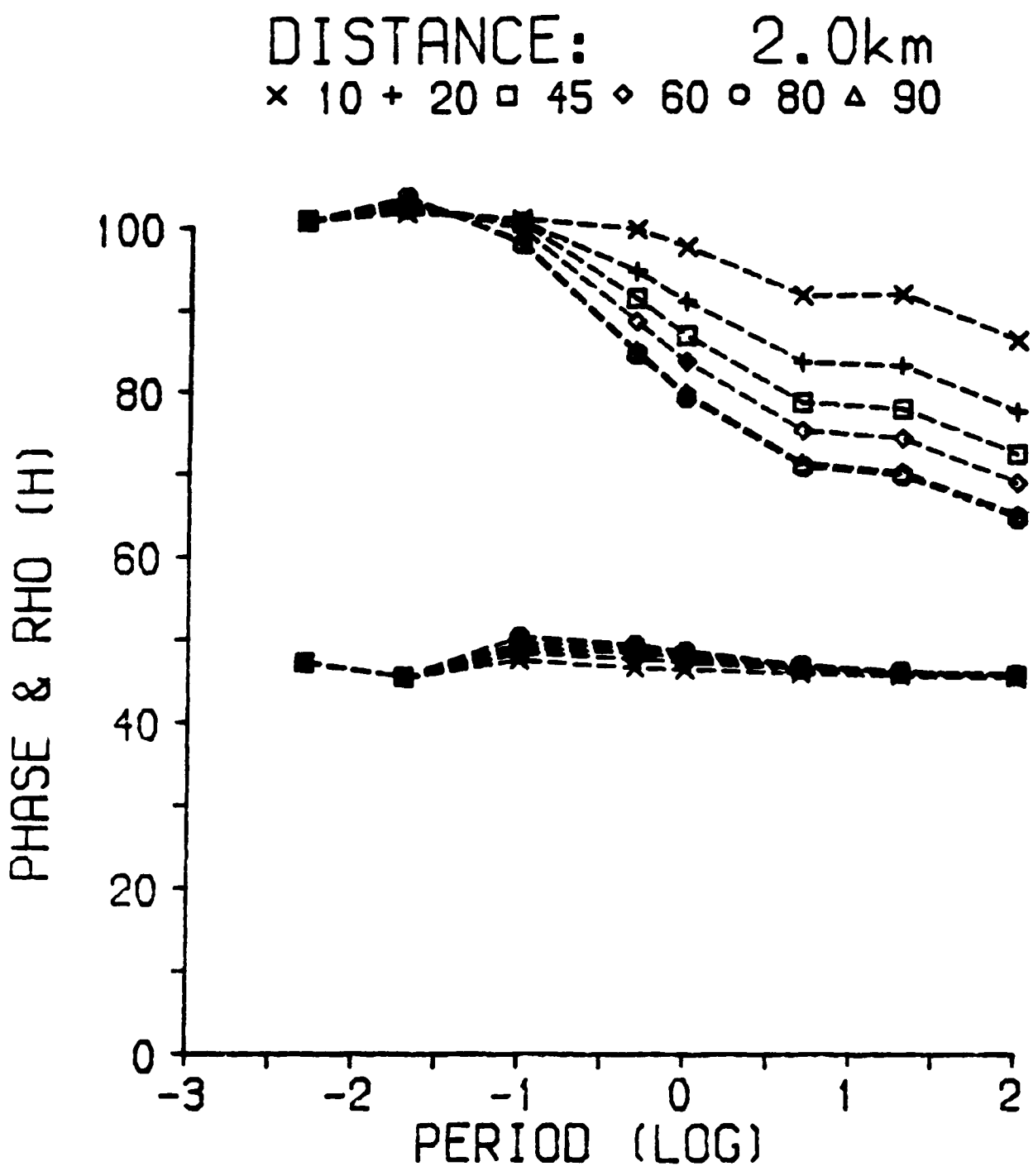
DISTANCE: 2.0km
× 10 + 20 □ 45 ◇ 60 ○ 80 △ 90
PHASE & RHO (H)
100
80
60
40
20
0
-3
-2
-1
0
1
2
PERIOD (LOG)

Figure V.6.f. Sounding curves for the H-polarization case at Y=2km.

The topographic distortions produce an apparent (false) thin layer over the half space; the greater the slope angle, the thinner this first layer becomes. Figure V.7 shows the thickness of the first layer against slope angle. The resistivity of the first apparent layer differs little from the true value, less than 5% on the lower side and up to 23% on the higher side. More interesting is the half-space beneath it. As shown in Figure V.8, the resistivity values for the second layer can be 63% from the true value. This is important since it suggests that even minor topographic slopes, e.g., 20° in figure V.8, can provide completely false geoelectric sections for the H-polarization case.

It is common practice to use invariant quantities constructed from combinations of the impedance tensor elements to derive invariant apparent resistivity and phase. They are often used in interpreting inhomogeneous structures with one dimensional models (Rokityansky, 1982, p.192). Thus it is worthwhile to repeat the last investigation using the invariant given by (III.67). The same two symmetrical points $|y|$=1km are used for this investigation. Inversions obtained using the invariant are less affected than for the H-polarization case. Figure V.9 shows that at y=-1km, values for the two layers always differ less than 15% from the true value. Nevertheless at y=1km the resistivity of the second layer is between 12% and 36% below the correct value. The second layer tends to be shallower than for the H-polarization case as shown in Figure V.10.

As described above, the H-polarization case is more affected by the presence of the slope. Distortions have a larger spatial wavelength and the level of distortion increases with period. This is a direct consequence of the way current lines adjust themselves beneath the slope surface. In the H-polarization case currents flow perpendicular to the strike, the current lines are brought together beneath the corner which marks the transition from the left (lower) side to the slope and are pulled apart beneath the corner at the transition slope to the right (higher) side. For the E-polarization case the same mechanism of focusing and dispersion of current lines applies but as currents flow parallel to the strike so the effect is very localized. An infinite depth to the basement has been simulated with the 2D models. One can regard those results as an upper limit to a finite depth to the basement case. The H-polarization topographic distortions for the infinite case are more drastic and act to greater distances than when the depth to basement is finite (Faradzhev et al., 1972; Thayer, 1975).

The above results demonstrate that the H-polarization is far

H-POLARIZATION

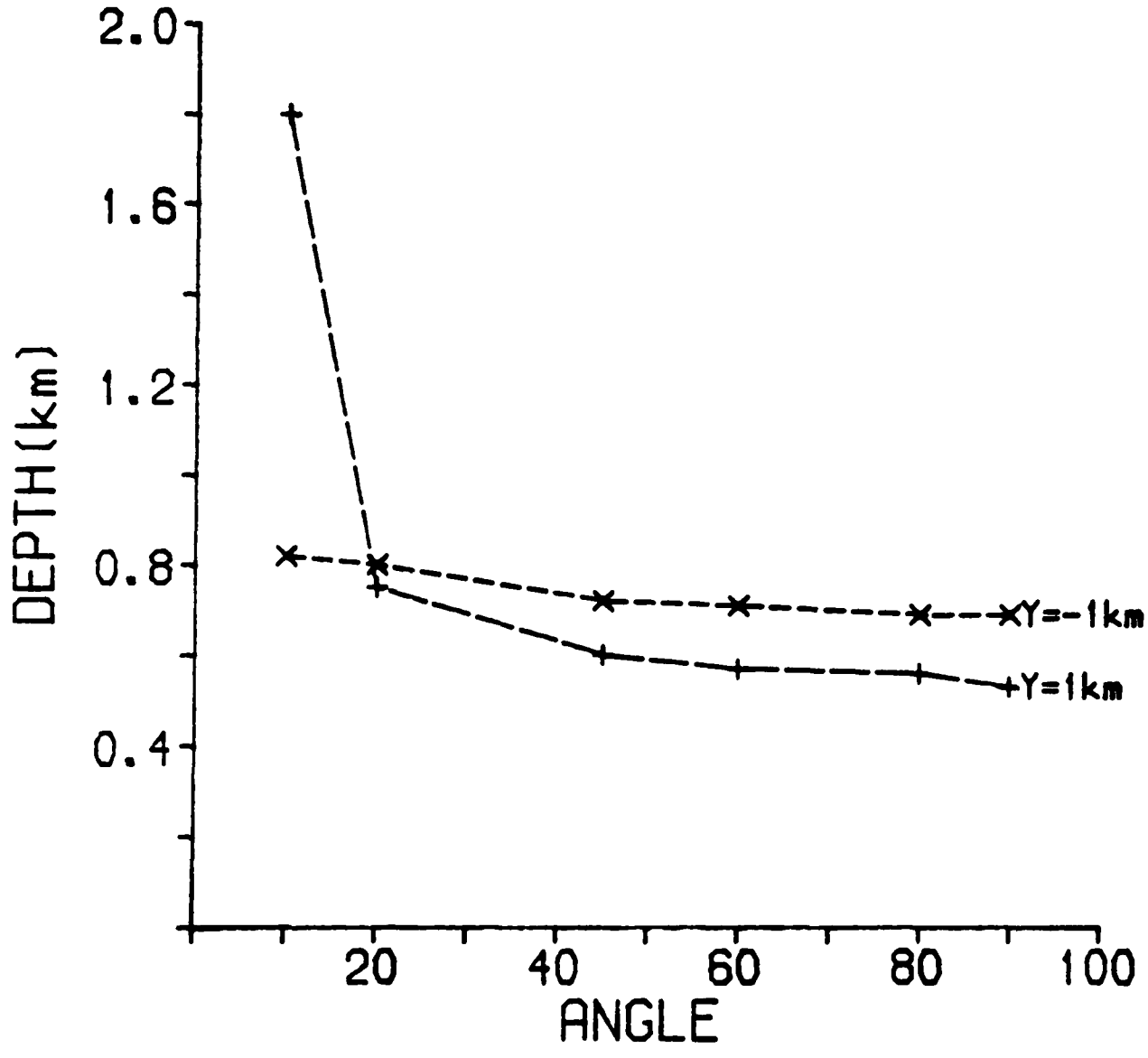

Figure V.7. Thickness (km) of the first layer against slope angle for the H-polarization case.

H-POLARIZATION

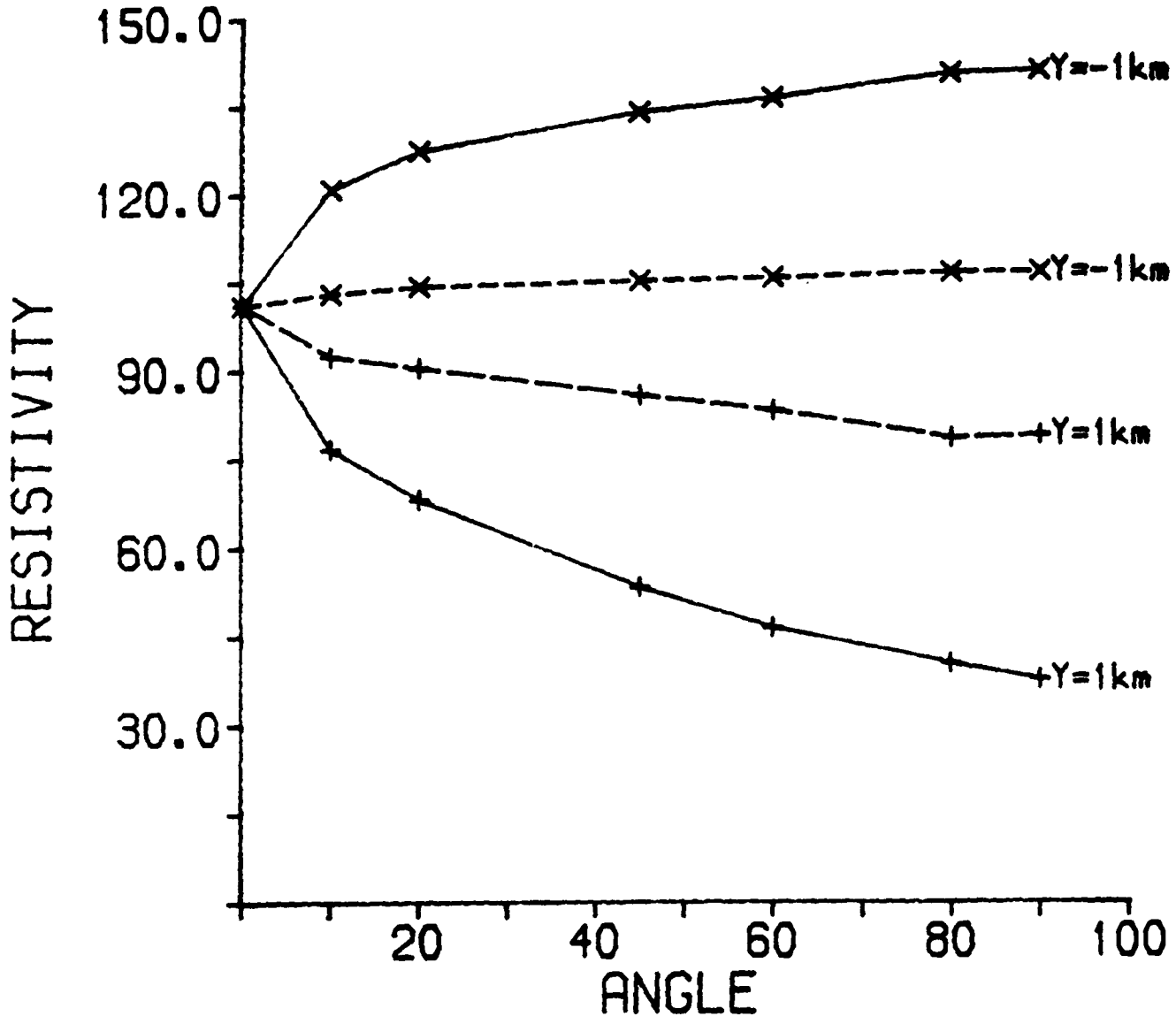

Figure V.8. Resistivity values (Ω.m) of the two fictitious layers against angle for H-polarization data. First layer values are shown with a dash line, a solid line is used for the second layer.

INVARIANT

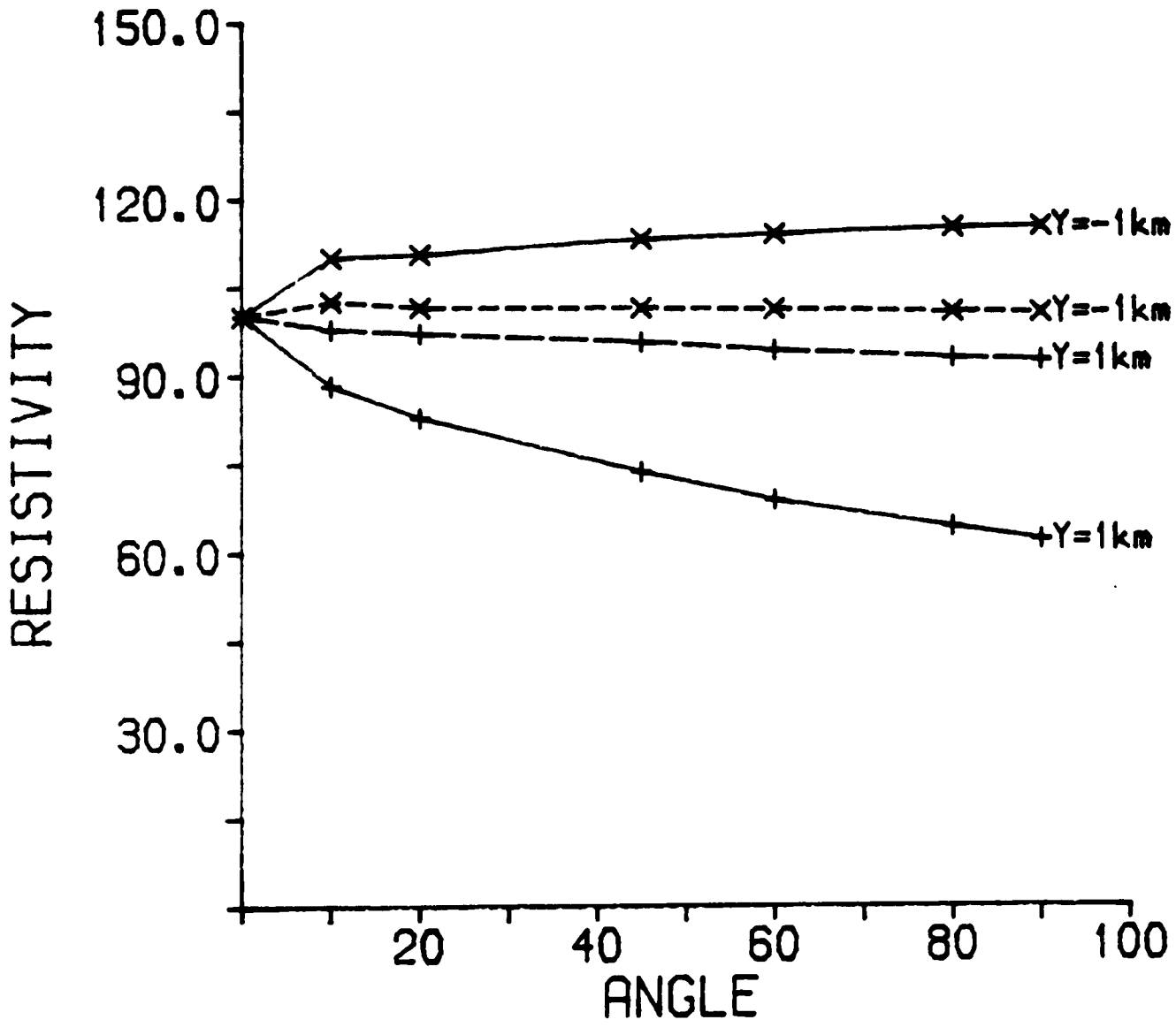
150.0
120.0
90.0
60.0
30.0
RESISTIVITY
20
40
60
80
100
ANGLE
Y=-1km
Y=-1km
Y=1km
Y=1km

Figure V.9. Resistivity values (Ω.m) of the two fictitious layers against angle for invariant data. First layer values are shown with a dash line, a solid line is used for the second layer.

INVARIANT

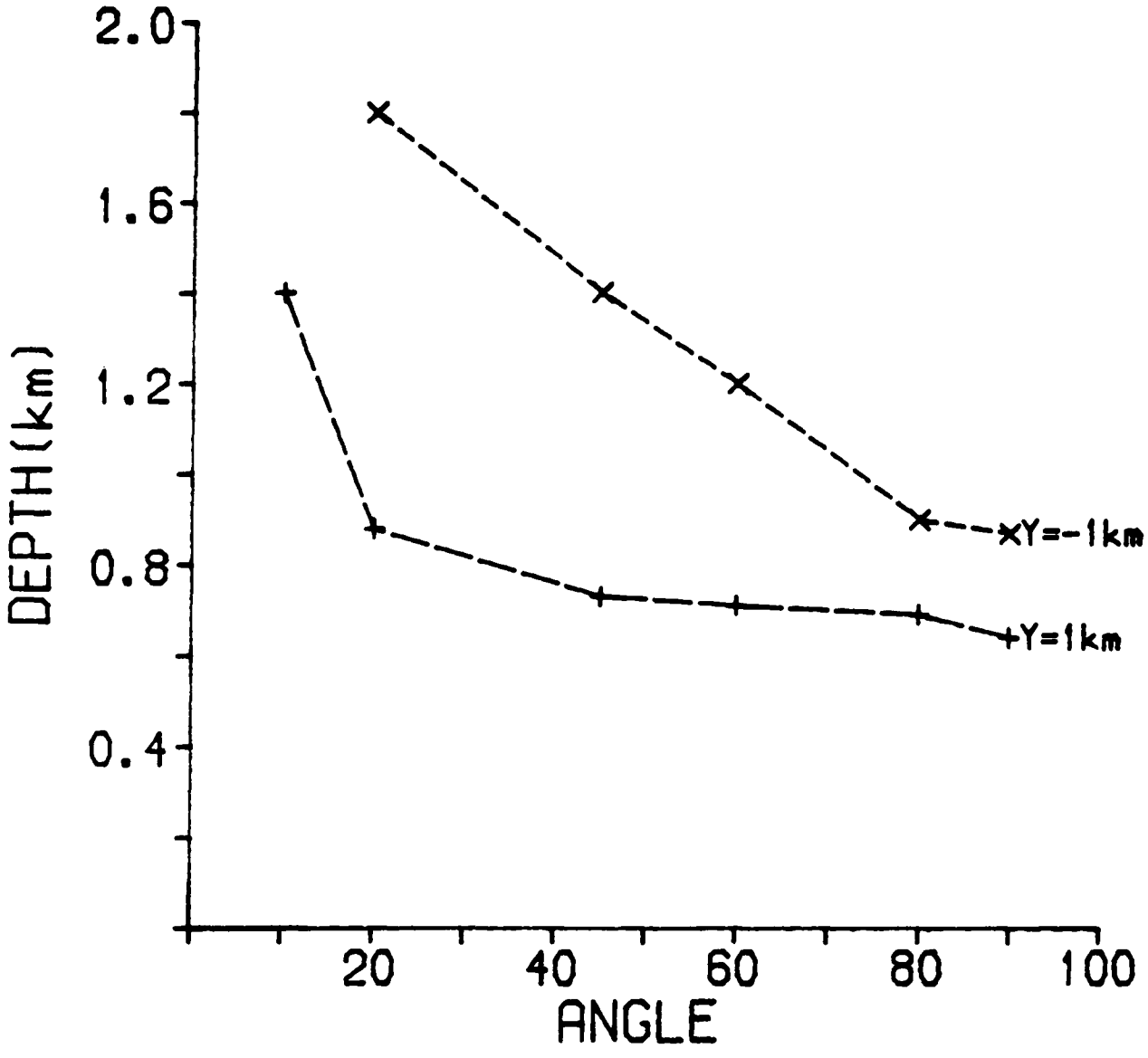

Figure V.10. Thickness (km) of the first layer against slope angle for the invariant data.

more affected than the E-polarization and phases are less affected than apparent resistivities. The longer the period the more affected the sounding curves are, and distortions are more drastic for the 90° model. These facts point to an upper limit to the distortions one should expect from an earth of uniform conductivity. However, the general case when the presence of subsurface structures which may couple with the topography provides a very difficult problem. These facts direct the solution to be either simple and generic or to be a rather complicated one, restricted to a particular situation. The point to be addressed in the generic case is, having the choice, how far from a topographic structure one should lay out the sensors in order to keep the topographic distortions to a minimum, say 10% or less? Equally important is to have a simple way of evaluating the distortions since the actual field problem may be so complicated that is not viable to solve it. Note also that the use of techniques like the ones for removing local superficial conductivity (Larsen, 1977), need such an extensive knowledge of the topography (Mozley, 1982), that is hardly of any practical use when applied to topographic distortions.

V.4. A Comparison with an Analytical Approximation

A simple analytical solution for telluric problems can be achieved using the Schwartz-Christoffel transform (Thayer, 1975; Harinarayana and Sarma, 1982). In this case telluric currents flow perpendicular to the strike between the surface and a perfect insulating basement. This solution, of course, is only valid for DC currents. The aim here is to show that the telluric solution is a good approximation to the limiting case in magnetotellurics.

The analytical model is a slope of height d and depth to the basement h. In order to conform with the previous models it is assumed $d<<h$; it is sufficient to set h=100, d=1. In what follows the results for the H-polarization case are used for the period T=100s. The analytical results were calculated by Harinarayana (1985) for all the angles used in this dissertation. Results for the left of the slope models are already published elsewhere (Harinarayana and Sarma, 1982). The electric fields are assumed parallel to the y-direction and the same sign convention, i.e. $y<0$ on the left and $y>0$ on the right of the slope, is used.

Let $E(y\to\infty)=E_h$ and $E(y\to-\infty)=E_\ell$ be the limiting analytical values. It is known that (Thayer, 1975)

$$\frac{E_1}{E_\ell} = \frac{h}{h+d}$$

but as d<<h, $E_h = E_\ell = E_\infty$. The field values are normalized as

$$\varepsilon = \frac{E}{E_\infty} \qquad (V.2)$$

For the numerical models the field at infinity is approximated by an average of field values at points at a sufficient distance to be considered unaffected by the presence of the slope, $\bar{E}$. Thus a numerical counterpart of definition (V.2) is given by

$$\varepsilon' = \frac{E'}{\bar{E}} \qquad (V.3)$$

where E' and $\bar{E}$ are numerical quantities. The comparison between ε and ε' is done assuming that they express similar quantities.

Figure V.11 shows the values for ε and ε' at points on the lower side, y<0. The two quantities agree reasonably well for all slope models except 10°, where some limited disagreement is apparent. Figure V.12 shows the same two quantities now on the higher side y>0. The two quantities now agree well only for 90° although ε and ε' tend to agree away from the slope. Discrepancies between ε and ε' are always less 10% at points y>1km. Analytical results tend to be more symmetrical than the numerical results when angles are small. As both analytical and numerical results agree well for the 90° model for which distortions are more drastic, it is possible to conclude that the analytical approximation agrees well with the upper limit of the topographic distortions. An interesting by-product of this investigation is that the comparison between ε and ε' provides an independent way of comparing the finite differences algorithm used in this work (Brewitt-Taylor and Weaver, 1976) with analytical results. Although the analytical results give only an approximation, both sets of results are in reasonable agreement.

V.5. Summary and Conclusions

In this chapter the topographic distortions caused by the presence of a slope have been analysed using 2D models. A finite difference algorithm is used to obtain both apparent resistivity and phase on the surface of an 100Ω.m homogeneous earth. Both E- and H-polarization cases are considered in the analysis. For all models the height difference between the two horizontal sides of the slope

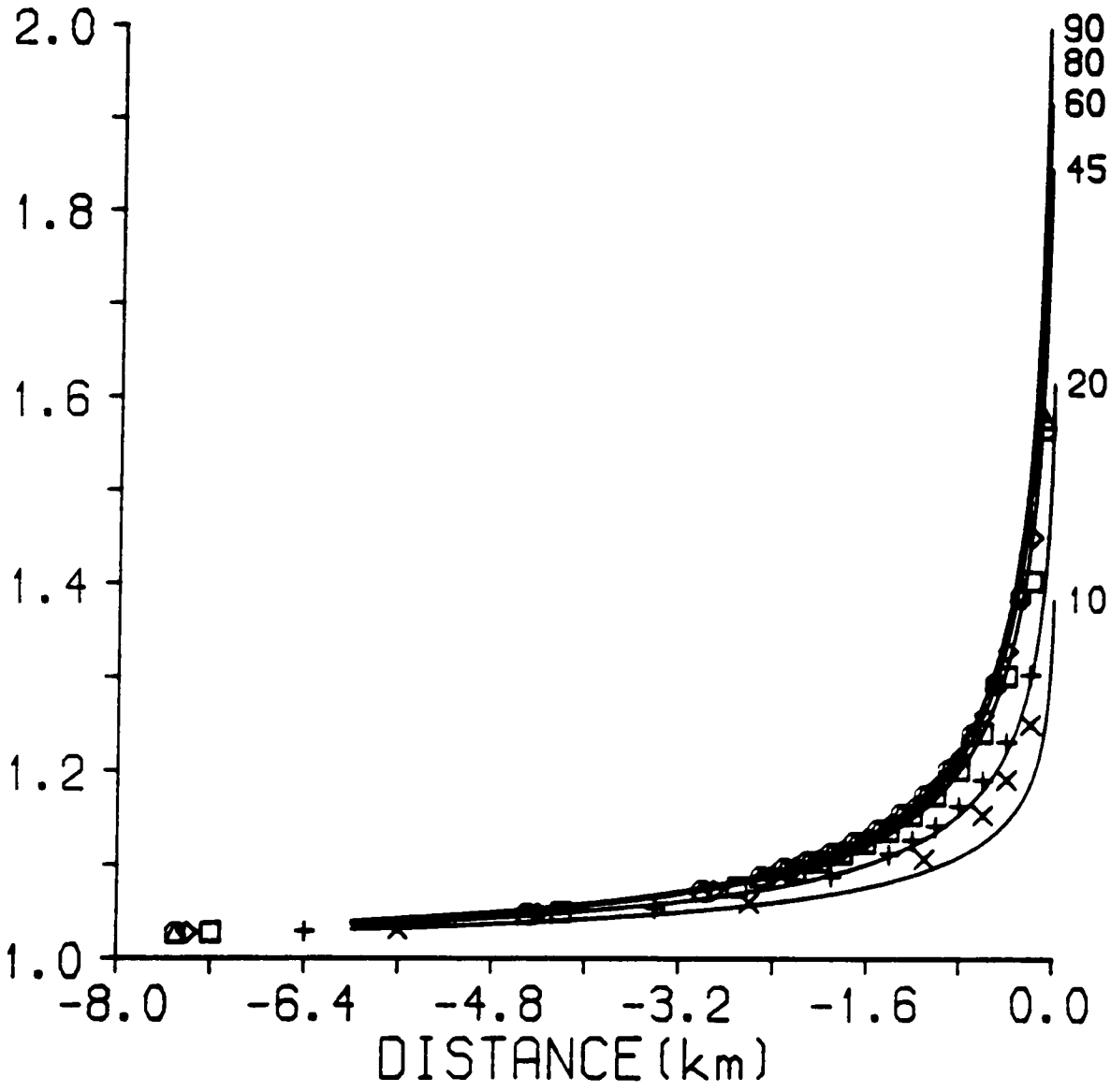
PERIOD: 100.000 s
× 10 + 20 □ 45 ◇ 60 ○ 80 △ 90
2.0
1.8
1.6
1.4
1.2
1.0
90
80
60
45
20
10
-8.0
-6.4
-4.8
-3.2
-1.6
0.0
DISTANCE(km)

Figure V.11. Comparison between ε (solid lines) and ε' (symbols) on the lower side.

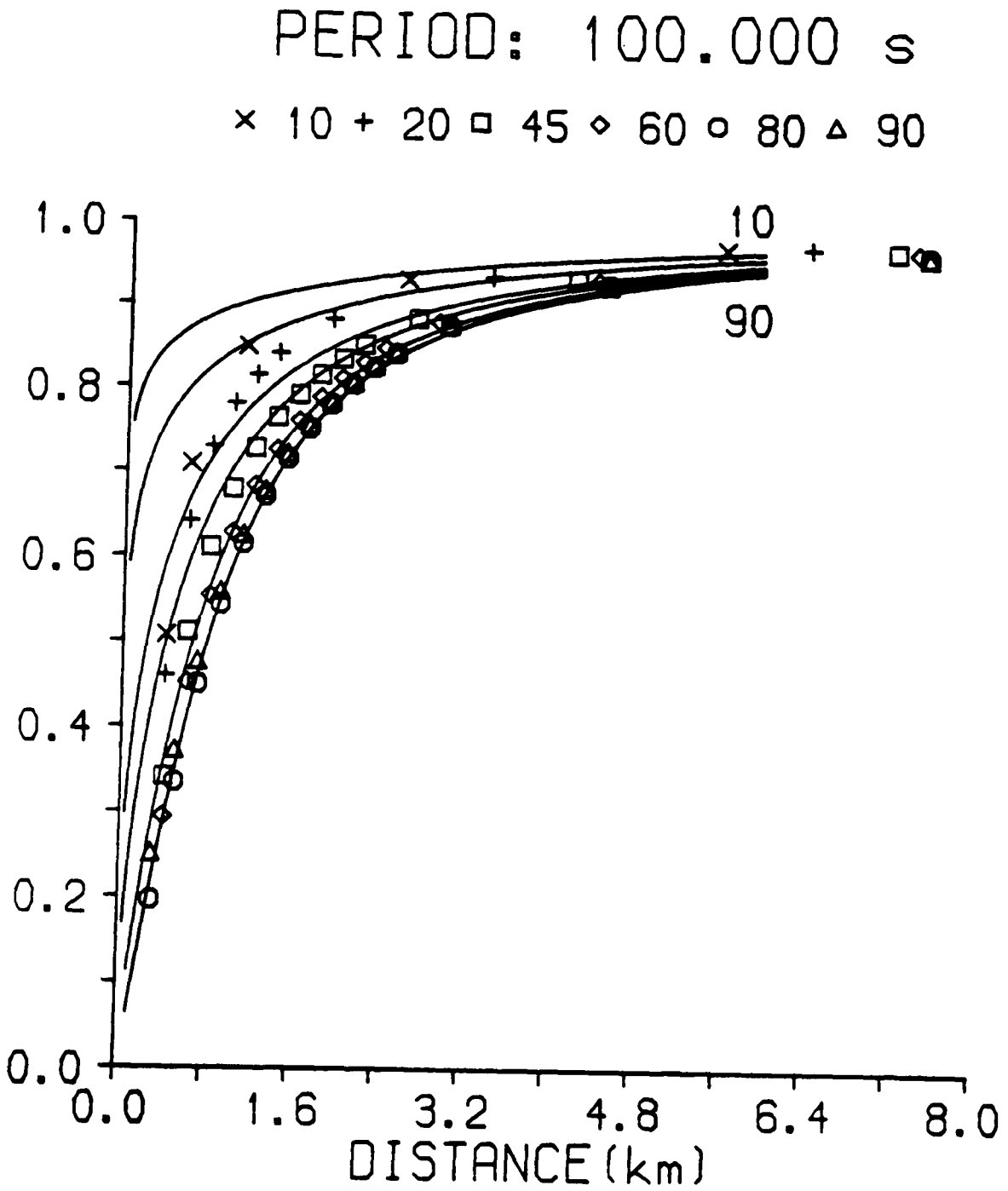
PERIOD: 100.000 s
× 10 + 20 □ 45 ◇ 60 ○ 80 △ 90
1.0
0.8
0.6
0.4
0.2
0.0
10
90
0.0
1.6
3.2
4.8
6.4
8.0
DISTANCE (km)

Figure V.12. Comparison between ε (solid lines) and ε' (symbols) on the higher side.

is kept constant while allowing angles to vary. Six models are analysed, each one characterized by its angle measured from the lower side: 10,20,45,60,80 and 90 degrees. A broadband period range is considered ranging from 0.005 to 100s. For the uniform earth considered these periods correspond to skin depths varying from 0.4 to 50.3km.

The same basic grid is used for all six models while allowing for changes in the geometry. In order to assess the quality of the chosen grid dimensions a half-space model is used to compare numerical values against the theoretical values, 100Ω.m for the apparent resistivity and 45 degrees for the phase. This comparison is done for the whole period range. Numerical and theoretical values agree well, the worst discrepancy being 0.3% at the longest period.

The topographic distortions due to the presence of the slope are analysed using two approachs. Distortions are analysed against the distance from the slope, the spatial distortions, or against period at selected sites, the sounding curve distortions. Spatial distortions may be limited to points $|y| \leq 8$km from the slope, since beyond this distance they are always under 10%. Sounding curve distortions are analysed for six selected sites with distances to the slope limited to $|y| \leq 2$km. The sounding curves from those sites are inverted in order to evaluate the effect of the topography on a 1D interpretation. The most drastically distorted case produced by the models is then compared against an analytical approximation.

For the E-polarization case the spatial distortions are greater for shorter periods. Distortions are limited to about 10% on the lower (left) side of the slope and on the higher (right) side of it at periods $T \geq 5$s. On the higher side distortions may reach 70% although this effect is very localized, dying out quickly with distance. Phase is very little affected on both sides of the slope. The E-polarization results are strongly frequency dependent in character and reflect the inductive nature of the distortion of this mode. Spatial distortions for the H-polarization case are more drastic than for the E-polarization case. The longer the period the more affected the apparent resistivity is. These distortions may reach values beyond 100% at the longer periods. Unlike the E-polarization case, distortions are strong on both sides of the slope. Phase distortions are noticeable and are affected in the same manner as the E-polarization distortions. Phase is affected above 10% only at those points on the higher side at periods $T < 1$s.

Six locations were chosen in order to analyse the distortions on sounding curves, |y|=0.4,1 and 2km. The E-polarization is less than 10% affected at the two extreme sites |y|=2km. At the other four sites the distortions reach 15% on the lower side and 50% on the higher side. The maximum distortion occurs on the higher side at periods which correspond to skin depths of the same order as the electromagnetic scale length of the slope. The H-polarization case displays a distorted behaviour at all 6 sites. On the lower side the phase is little affected but distortions on the apparent resistivities can reach 100%. On the higher side both phase and apparent resistivities are strongly affected. Phase distortions reach 58% at periods similar to the periods of maximum distortion for the E-polarization case. Apparent resistivities are strongly distorted at all sites.

The effect of the presence of the slope on the interpretation of MT data may be analysed by inverting the sounding curves. A 1D linearized inversion algorithm is used at two equidistant sites |y|=1km. The starting model for all inversions is a two layer model with a 10km thick first layer and assigning 100Ω.m for both layers. Inversions of the E-polarization data are very little affected by the slope. Nevertheless inversions of the H-polarization case produce a first layer with a thickness of the same order as the height difference between the two horizontal levels and resistivity values which differ from the true value as little as 5% on the lower side and 23% on the higher side. The resistivity of the half-space can differ from the true value as much as 44% on the lower side and 63% on the higher side. Inversions using invariant apparent resistivity and phase are also affected by the topography, although the distortions are not as strong as for the H-polarization case. On the lower side the two inverted resistivities differ less than 15% from the true value. On the other hand the resistivity of the second layer can be 36% below the correct value on the higher side. The first layer tends to be thicker than for the H-polarization inversions.

From the above results it is possible to conclude that there are two limiting cases for the distortions caused by the slope. At shorter periods the E-polarization apparent resistivity is significantly distorted on the higher side of the slope. These distortions are very localized dying out quickly with distance. Both apparent resistivity and phase are strongly distorted for the H-polarization case, the longer the period the stronger the distortions become. Moreover distortions are directly related to slope angle, i.e. greater angles produce stronger distortions.

Together, these facts single out the distortions on the H-polarization response produced by the 90 degrees slope at 100s as the limiting case for the topographic effect at any location. This limiting situation may be compared with an analytical approximation which is strictly valid only for DC currents. Both numerical and analytical results agree well, although the latter tend to underestimate the topographic effect if other angles are considered.

CHAPTER VI
Magnetotelluric Soundings in the Canadian Rocky Mountains

VI.1. Introduction

This chapter describes the work on a data set collected along a profile traversing the Rocky Mountains Trench near 53°N. This data set is part of a more extensive set acquired during 1982 along three profiles, as part of a collaborative work between the Universities of Alberta and Edinburgh. The work described here covers data selection and conditioning, data analysis, and data interpretation of a data set collected at 12 sites along the Small River (SR) Traverse. Part of this work contributed to a joint paper, accepted for publication in October 1986 (Hutton et al., 1987). Apart from the sounding curves which are the result of the data analysis, the work reported here does not repeat the material presented in the joint paper unless specifically stated. In addition, despite this chapter coming at the end of this dissertation, it describes work which was almost entirely done before chapters III and V. Only section VI.6 describes the work done after these two chapters and thus was not included in the joint paper. For the geophysical interpretation of the combined results from the three profiles the reader is referred to the joint paper.

VI.2. Structure of the Region

The Rocky Mountains Trench is a long and narrow intermontane valley which stretches for more than 1600km, with 0.9-1.8km high boundary walls separated by typical widths of 3 to 16km (Bennett et al., 1975). Almost everywhere the trench is covered by a layer of sediments with thicknesses ranging from 550m, from a Bouguer profile from 50°N to 53°N (Spence et al., 1977a), to 1-2km with an inferred resistivity value of roughly 10Ω.m (Dragert and Clarke, 1977). At the latitudes of this study the Trench separates the Eastern Metamorphic Belt, or Omineca Crystalline Belt and the Rocky Mountains Belt. The latter was formed by northeasterly thrusting and folding. Figure VI.1 shows the five distinct belts, each of them with its own history, that form the Canadian Cordillera (Monger et al., 1972). A review of the tectonic structure can be found elsewhere (Monger and Price, 1979). A comprehensive compilation of geophysical, geological and petrological results and their tectonic implications can also be found in the literature (Gough, 1986a).

Seismic refraction profiles near the study region, see figure VI.1, indicate a thick crust. Calculations show that P and S wave

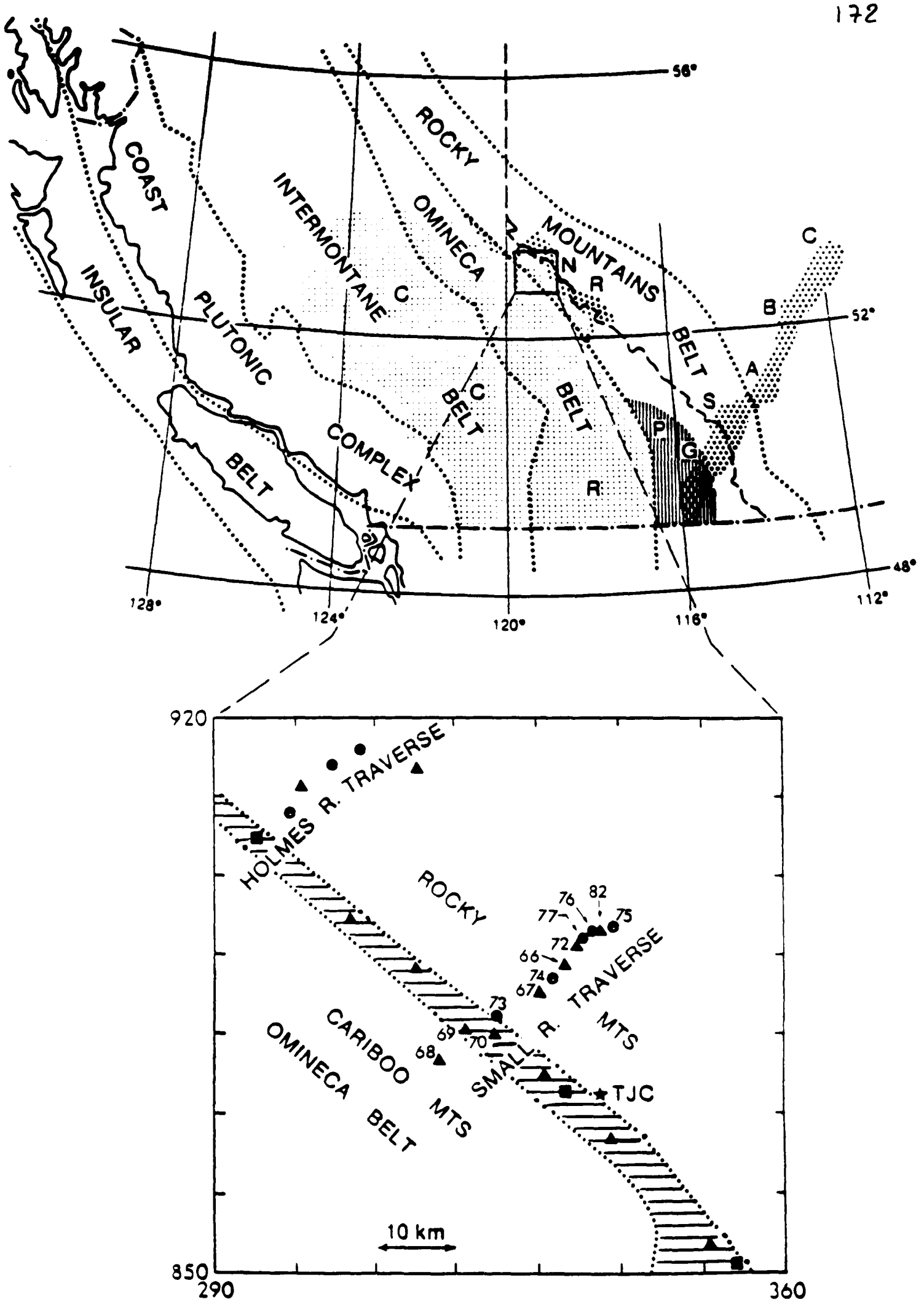
56°
52°
48°
128°
124°
120°
116°
112°
COAST
INSULAR
PLUTONIC
COMPLEX
INTERMONTANE
OMINECA
ROCKY
MOUNTAINS
BELT
A
B
C
R
S
P
G
920
850
290
360
HOLMES R.
TRAVERSE
ROCKY
MTS
CARIBOO
OMINECA
BELT
SMALL R.
TJC
66
67
68
69
70
72
73
74
75
76
77
82
10 km

Figure VI.1. Tectonic provinces of the Canadian cordillera. Conductive structures of the region are shown by stippling. They are: CCR, Canadian Cordillera Regional conductor; NR, Northern Rocky Mountains conductor; SABC, Southern Alberta-British Columbia conductor; and PG, Purcell Geanticline. Site locations are shown inside the box where the Rocky Mountains Trench appears shaded. Squares are sites covering 5000s-500Hz, triangles 100s-500Hz, and circles 10s-500Hz. TJC is Tête Jaune Cache. Only sites on the Small River Traverse are numbered. This figure except for the numbering is from another work (Hutton et al., 1986).

arrivals from the M discontinuity require a crust of the order of 50-60km (Bennett et al., 1975; Spence et al., 1977b; Mereu et al., 1977). Also an observed delay of 1.7s in a crustal phase has been explained in terms of the existence of a region with an anomalously hot mantle, possibly with melt intruding into the crust (Gough, 1986a). This is particularly interesting since the Canadian Cordillera Regional Conductor (CCR) as has been postulated (Gough, 1986a) may be related to partial melting in the upper mantle.

A schematic representation of the conductive structures within Western Canada is also shown in figure VI.1. The CCR and the Northern Rockies Conductor (NR) (Gough, 1986a) are in the region of the present study. In a large array study centred at Tête Jaune Cache (TJC), a highly conductive layer, probably in the lower crust with a conductive ridge rising into the upper crust, was found necessary to fit the data (Bingham et al., 1985). The conductive ridge rises near the edge of the conductive layer under the main ranges of the Rockies and is 50 to 80km wide. The existence of the CCR conductor was already known from earlier work (Dragert, 1973; Dragert and Clarke, 1977, Gough et al., 1982). Further south, at 37°N, a zone of enhanced conductivity in the upper mantle was also required to satisfy earlier observations of anomalous magnetic variation fields (Porath, 1971). The trench itself marks a transition zone where a change in horizontal conductivity was reported (Dragert, 1973).

The depth to the CCR conductor may be inferred from magnetotelluric soundings in south central British Columbia. MT sites along the southern border of British Columbia showed that the depth to a conductive layer of 10Ω.m is about 15km with a width in the region of 20-40km (Caner et al., 1969; Caner, 1971). Other workers tend to agree with these values postulating a layer with a resistivity of 5Ω.m and a thickness of 15-20km at depths of 40-50km (Dragert and Clarke, 1977), or postulate a highly resistive upper crust 15-25km thick over a conductive region (Dragert et al., 1980). Even further south, southeast of the SR traverse near Portland, Washington State, USA, evidence of a highly conductive lower crustal conductor of <5 Ω.m at depths varying from 15km downwards, has been presented (Stanley, 1984). This conductor is probably also overlain by highly resistive upper crustal rocks.

It is assumed that the CCR is associated with the occurrence of partial melting in the upper mantle, with a silicate melt as the most probable fluid, and highly saline mantle-derived water in the crust (Gough, 1986a). This water may have its origin in the

subduction of seafloor rocks containing brine (Gough, 1986b), as has been indicated beneath Vancouver Island (Kurtz et al., 1986). A good conductive layer as in the present case, somewhere near 15km, is accepted as being characteristic of lower crustal depths in tectonically active regions, most probably caused by the presence of free fluids (Shankland and Ander, 1983; Beamish and Smythe, 1986). In the general case it has been suggested that brine can be dragged towards the mantle by subduction (Gough, 1986c).

VI.3. Data Acquisition

Field sites are located along the SR traverse which is perpendicular to the Rocky Mountains Trench, near TJC. There are 12 sites on the SR traverse, with data from 7 sites covering the period range 100s to 500Hz while the remaining sites cover the range 10s to 500Hz. The sites along the traverse are shown with their identification numbers in figure VI.1. The other 13 sites which belong to the project are also shown in this same figure.

The automatic in-field analysis system SPAM MkI, developed in Edinburgh (Dawes, 1984), was used for the range 8s to 500Hz. Longer period data were recorded on cassette using a data logger. The SPAM is a battery operated digital AMT data acquisition and analysis system. Tensor analysis is performed in the field permitting both a check on data quality and adjustment of the signal dynamic range. Rejection criteria are applied in both the time-domain and frequency-domain analysis. An LSI-11/2 processor is used in this analysis. Two sets of induction coils are used to record the magnetic field, each one composed of three coils. Coils are laid out on the ground and shielded from the wind with a plastic cover. Non-polarizing $Cu\text{-}CuSO_4$ eletrodes encased in ceramic pots are used to measure the electric field. A typical telluric line length is 50m. Magnetic NS-EW directions are used as measuring directions whenever possible.

Data was recorded in four overlapping frequency bands as: from 1000Hz to <10Hz; from <100Hz to 1Hz; from <10Hz to 0.1Hz; and from <1Hz to <0.01Hz. These bands are numbered 1 to 4, respectively. Bands 1 to 3 are analysed by the SPAM main program, when the following steps are performed in the field: digitation of up to 5 component windows of 512 samples; checking of each component for saturation or low powers and adjusts amplification; FFT and tensor calculations; writing data on data cartridge. Data in these four decades, collected at the 12 sites of the SR traverse, were returned to Edinburgh for analysis. Decade 4 data was selected

later on a Dec PDP11 mini computer. The event selection of decade 4 was done visually using the following criteria: coherent magnetic and telluric activity; low degree of polarization; and low level of extraneous noise. The mainframe analysis of these four bands is described below.

VI.4. Data Analysis

Data from bands 1 to 4 were transfered to an ICL mainframe computer to be analysed. Data were transfered in time series form. Although there are obviously points in common with the data analysis described in chapter III, the data analysis described here is to a large extent independent of the one described earlier. Naturally the underlying principles described in chapter III remain the same. Here the standard package of programs used in the Department of Geophysics of the University of Edinburgh was employed. This package can be divided into three main parts: window analysis, window averaging and output of the final results. A window is a non-overlapping section of a time series containing 512 samples of each field component.

The window analysis stage performs individual analysis on each individual window. Long period linear trends are removed, the data series is then normalized to one standard deviation, and a cosine taper is applied to the first and last 10% data points. Data series are transformed to the frequency domain using FFT. A data window, now in the frequency domain, is then corrected for instrumental responses of the telluric pre-amplifiers and of the two sets of induction coils. In order to reduce the variance of the estimates, cross- and auto-spectral functions are averaged over fixed band lengths composed of 8 neighbouring frequencies. The 60Hz mains frequency and its odd harmonics as well as their possible aliasing effects are removed. The downward biased estimate of the impedance tensor $\underline{\underline{Z}}$, definition (III.20), is then calculated and the corresponding predicted coherences are estimated. The tipper is also calculated as well as the predicted tipper coherence. Polarization parameters are evaluated for both magnetic and electric fields. All the above quantities are estimated individually for each event.

These estimated quantities form the output of the first analysis phase. In the second phase, the variance of the resulting mean response functions is minimized averaging over all accepted events at each frequency. This, then, is a multi-event analysis phase in opposition to the first single event analysis. The

impedance tensor elements are averaged on a logarithmic scale assuming a log-normal distribution (Bentley, 1973), and one standard deviation error bars are calculated for the resultant mean estimates. The data selection is done by a number of acceptance criteria which are applied to the data in order to reject bad events. An initial rejection phase is applied to the data set before its conversion to a logarithm scale. Firstly an estimate is rejected if its predicted coherence is below a chosen threshold which depends on data quality at each site. For half of the sites, 0.7 is chosen as the minimum acceptable for the predicted coherence while for the other sites 0.8 is adopted. The coherence estimates are not bias corrected. Secondly a sign rejection criterion is applied. Tables with the estimates of the off-diagonal elements are constructed, preferred signs are found and estimates are rejected if signs disagree. Accepted estimates are then converted to a logarithmic scale. An additional test based on the signal-to-noise ratio is possible but was not used. Log-normal statistics are computed and data rejected if outside ± 2.2 standard deviations away from the mean. Statistics are then re-computed and the rejection process is repeated once more. For the whole data set considered, typical mean percentages of rejection in the selection criteria were: i)coherence rejection, 4-99%; ii)sign rejection, 0-20%; and iii)outlyer rejection, 0-30%.

VI.5. Results

The Rocky Mountains trench gives the predominant lineament direction in the region. This direction, 72°W magnetic, is then assumed to represent the predominant structural strike. In order to allow the interpretation of all sites along the traverse all sounding quantities are rotated to that direction, thus all sites are referred to the same coordinate system. The rotation of $\underline{\underline{Z}}$ is given by relation (III.63). Figure VI.2 sumarizes all the sounding results obtained along the SR traverse. In this figure, apparent resistivities and phases are shown in the major and minor directions, i.e. parallel and perpendicular to the strike. Also shown in the same figure are the skew, (III.68), the number of accepted estimates and the azimuth of rotation, (III.66). This last quantity is shown in the figure only for reference since all results are rotated to the structural strike direction. Other relevant information regarding site identification and data processing are also displayed in the same figure. The apparent resistivity curves along the major direction start at 10^{2}-10^{4} Ω.m at high frequencies and show a decreasing trend for all sites which at low frequencies reach values of the order of 1Ω.m for the majority of sites. Along

SITE : 268 TELLURIC

CHANNEL	20010	20020	20030	20040
BAND	1	2	3	4
COMPONENTS	1	1	1	5
SAMPLES/WINDOW	512	512	512	512
NUMBER WINDOWS	80	27	32	32
SAMPLE RATE HZ	2048	128	10	1
PLOT HPF	64.00	8.00	0.12	0.01
PLOT LPF	800.00	50.00	1.00	0.25
FREQS/DECADE	0	0	0	0
FREQS/BAND	0	0	12	13
MIN COHERENCY	0.00	0.00	0.00	0.00
REJECTION LOOPS	2	2	2	2

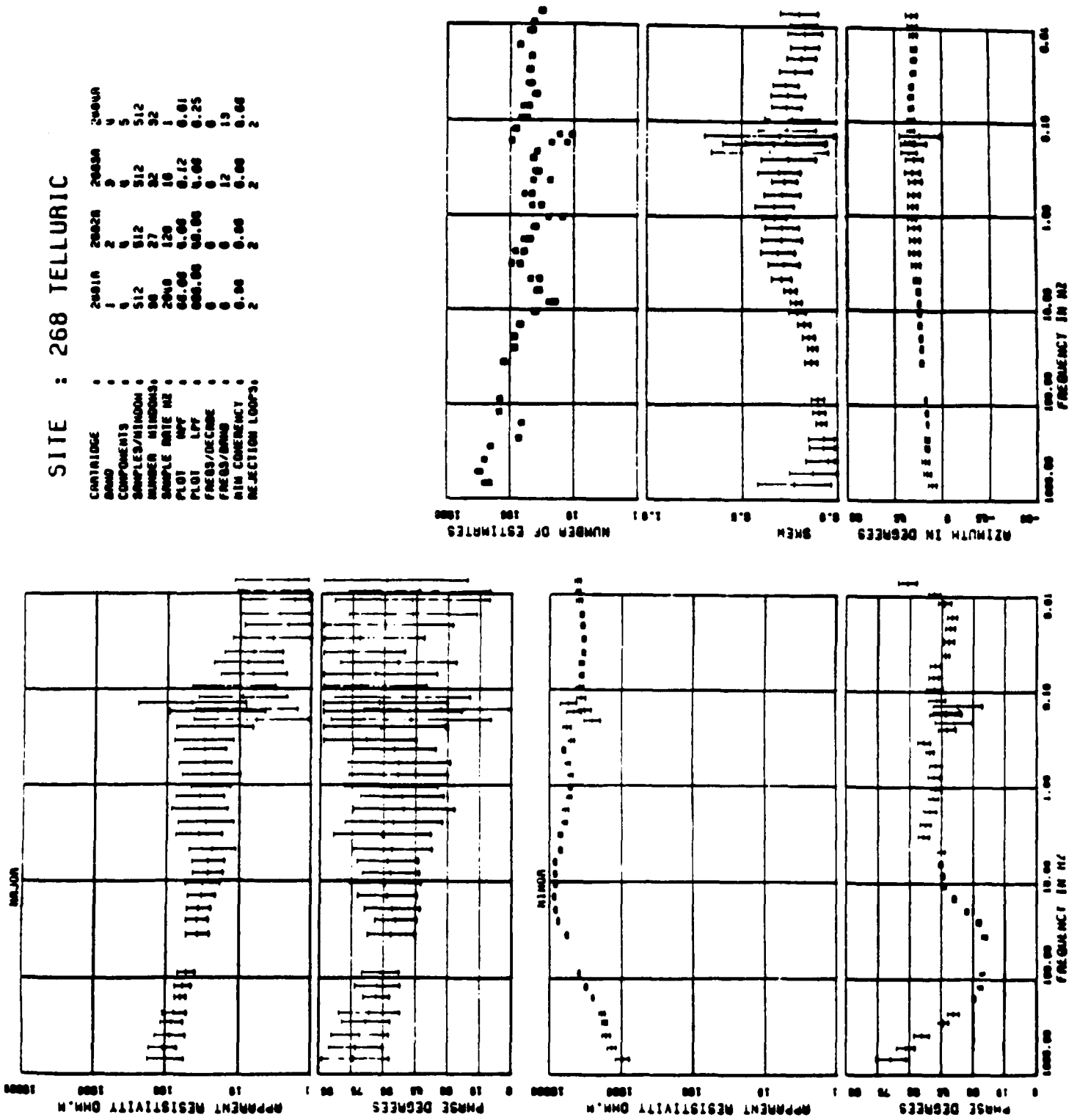

Figure VI.2. Results for all sites along the Small River Traverse. Apparent resistivities and phases are rotated to 72°W. The azimuth of the major at each site is shown for reference. Skew and number of accepted estimates are also shown. Additional information on site identification and on the statistics from the data processing are also displayed.

SITE : 269 TELLURIC

CARTRIDGE	20818	20828	20838
BAND	1	2	3
COMPONENTS	4	4	4
SAMPLES/WINDOW	512	512	512
NUMBER WINDOWS	64	80	48
SAMPLE RATE HZ	2048	128	16
PLOT MPP	80.00	1.00	0.12
PLOT LPF	800.00	10.00	1.00
FREQS/DECADE	8	8	8
FREQS/BAND	8	8	12
MIN COHERENCY	0.00	0.00	0.00
REJECTION LOOPS	2	2	2

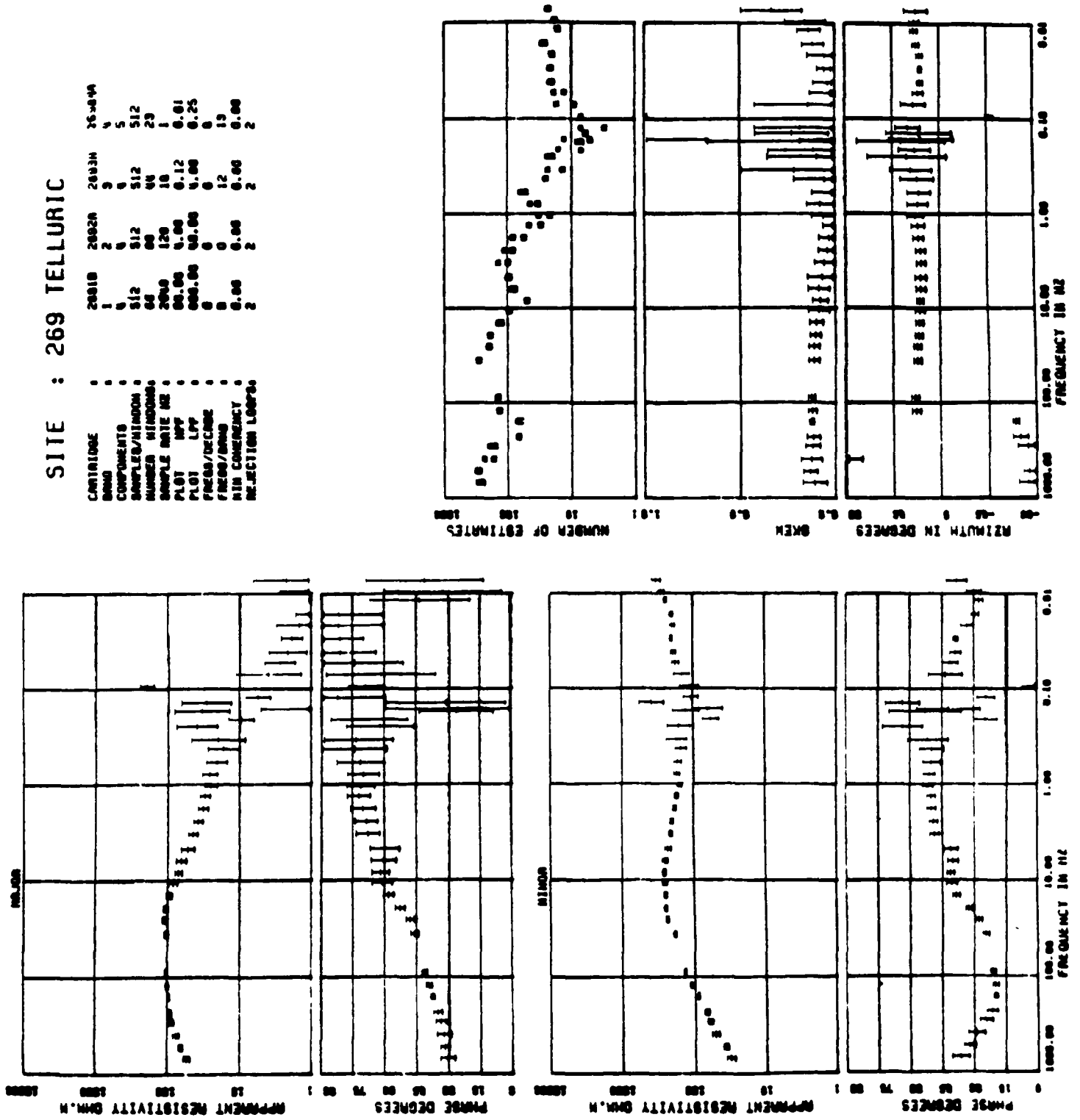

Figure VI.2. Continued (2).

SITE : 270 TELLURIC

	2701A	2702A	2703A	2704A
CARTRIDGE	1	2	3	4
BAND	1	1	1	1
COMPONENTS	5	5	5	5
SAMPLES/WINDOW	512	512	512	512
NUMBER WINDOWS	61	64	10	25
SAMPLE RATE HZ	2048	128	16	1
PLOT MPP	00.00	0.00	0.12	0.01
PLOT LPF	000.00	10.00	4.00	0.25
FREQS/DECADE	8	8	8	8
FREQS/BAND	8	8	12	13
MIN COHERENCY	0.00	0.00	0.00	0.00
REJECTION LOOPS	2	2	2	2

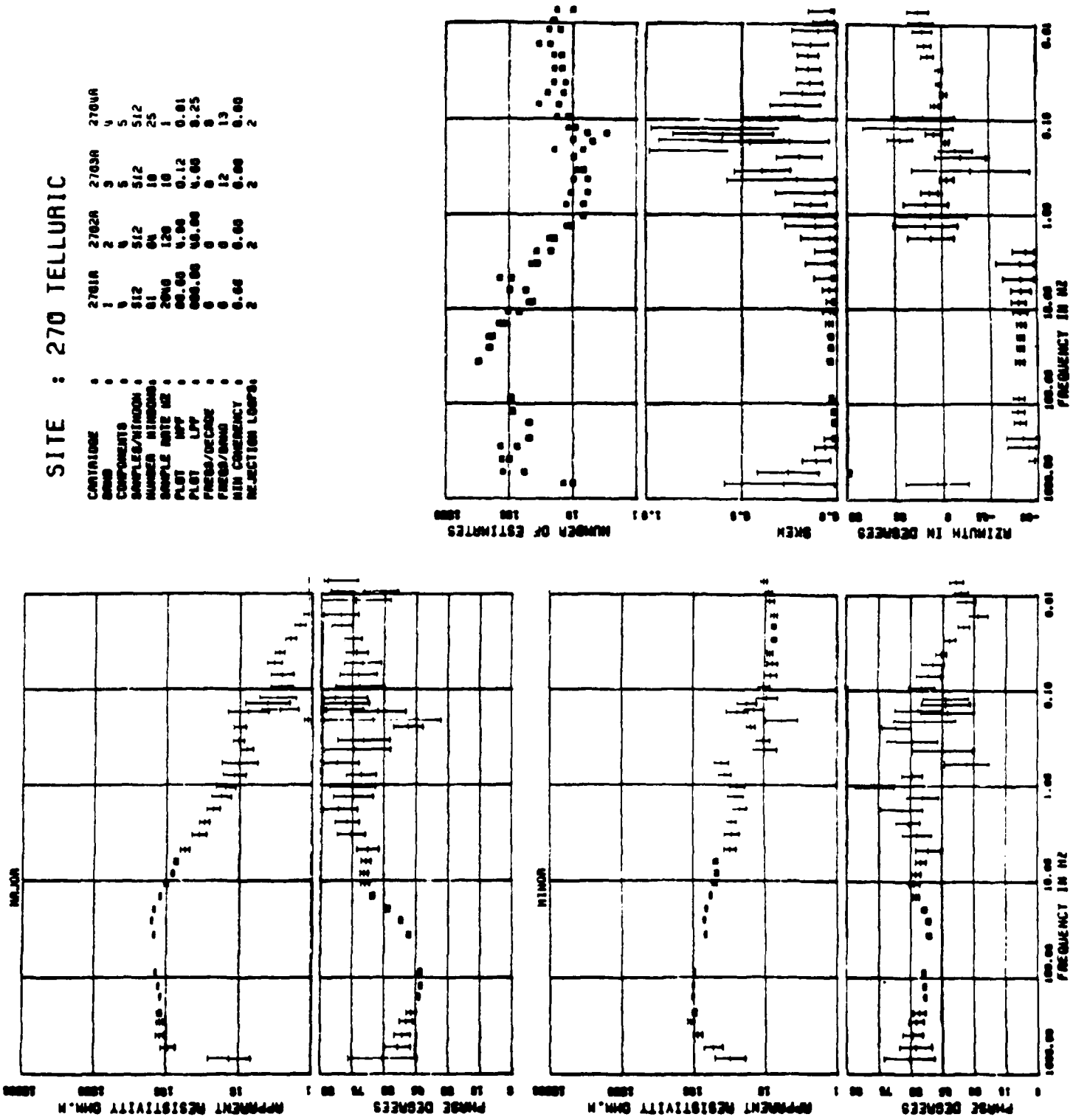

Figure VI.2. Continued (3).

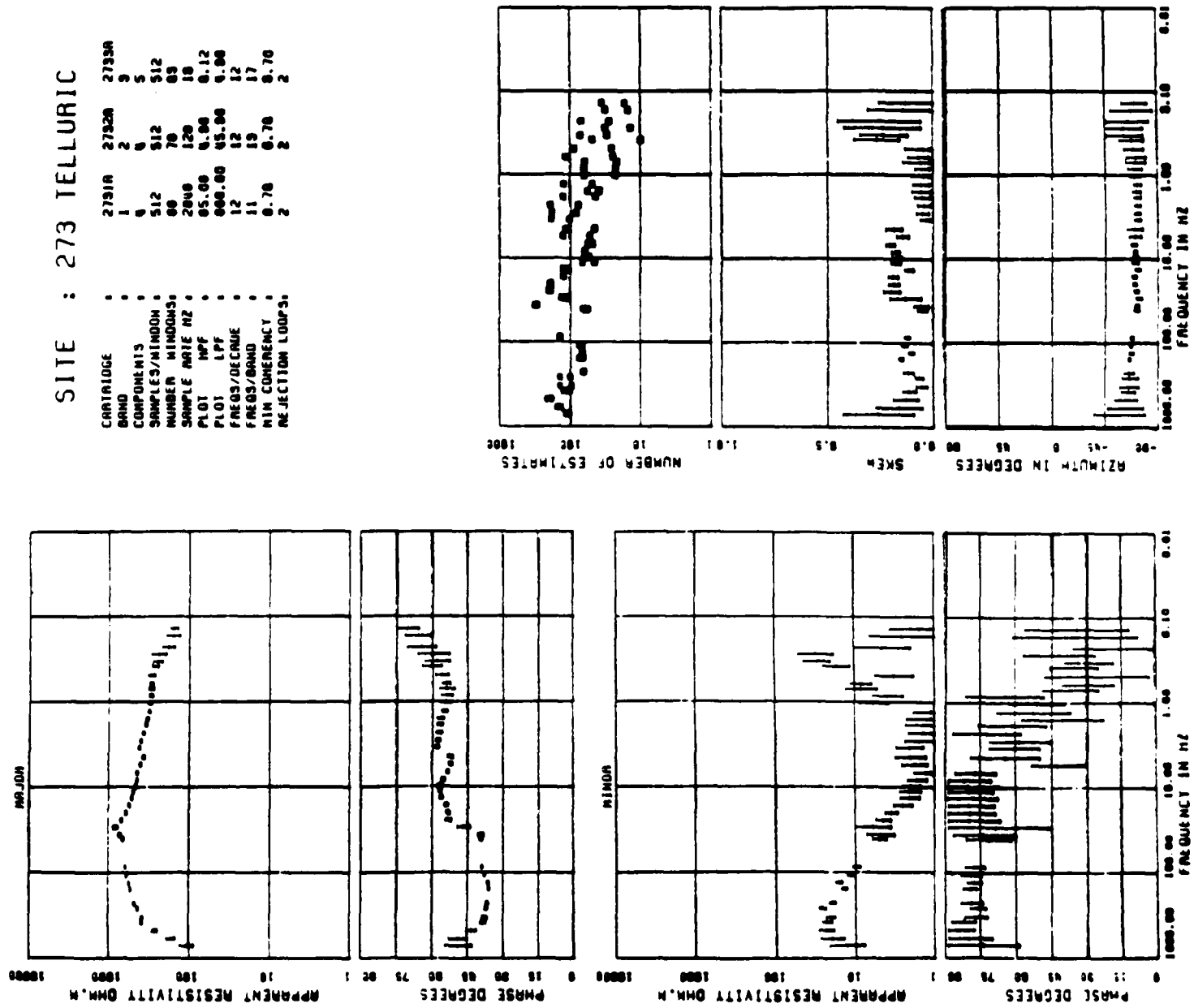
SITE : 273 TELLURIC
CARTRIDGE 27310 27320 27330
BAND 1 2 3
COMPONENTS 6 6 5
SAMPLES/WINDOW 512 512 512
NUMBER WINDOWS 80 70 83
SAMPLE RATE HZ 2048 128 10
PLOT HPF 85.00 0.06 0.12
PLOT LPF 000.00 45.00 0.06
FREQS/DECADE 12 12 12
FREQS/BAND 11 13 17
MIN COHERENCY 0.70 0.70 0.70
REJECTION LOOPS 2 2 2
NUMBER OF ESTIMATES
SKEW
AZIMUTH IN DEGREES
FREQUENCY
MAJOR
APPARENT RESISTIVITY OHM.M
PHASE DEGREES
MINOR
APPARENT RESISTIVITY OHM.M
PHASE DEGREES
FREQUENCY IN HZ

Figure VI.2. Continued (4).

SITE : 267 TELLURIC

	2671A	2672A	2673A	2674A
CARTRIDGE	1	2	3	4
BAND	4	4	4	5
COMPONENTS	512	512	512	512
SAMPLES/WINDOW	90	55	62	25
NUMBER WINDOWS	2048	128	16	1
SAMPLE RATE HZ	60.00	4.00	0.12	0.01
PLOT HPF	000.00	00.00	0.00	0.00
PLOT LPF	12	12	12	12
FREQS/DECADE	12	12	17	17
FREQS/BAND	0.70	0.70	0.70	0.70
MIN COHERENCY	2	2	2	2
REJECTION LOOPS				

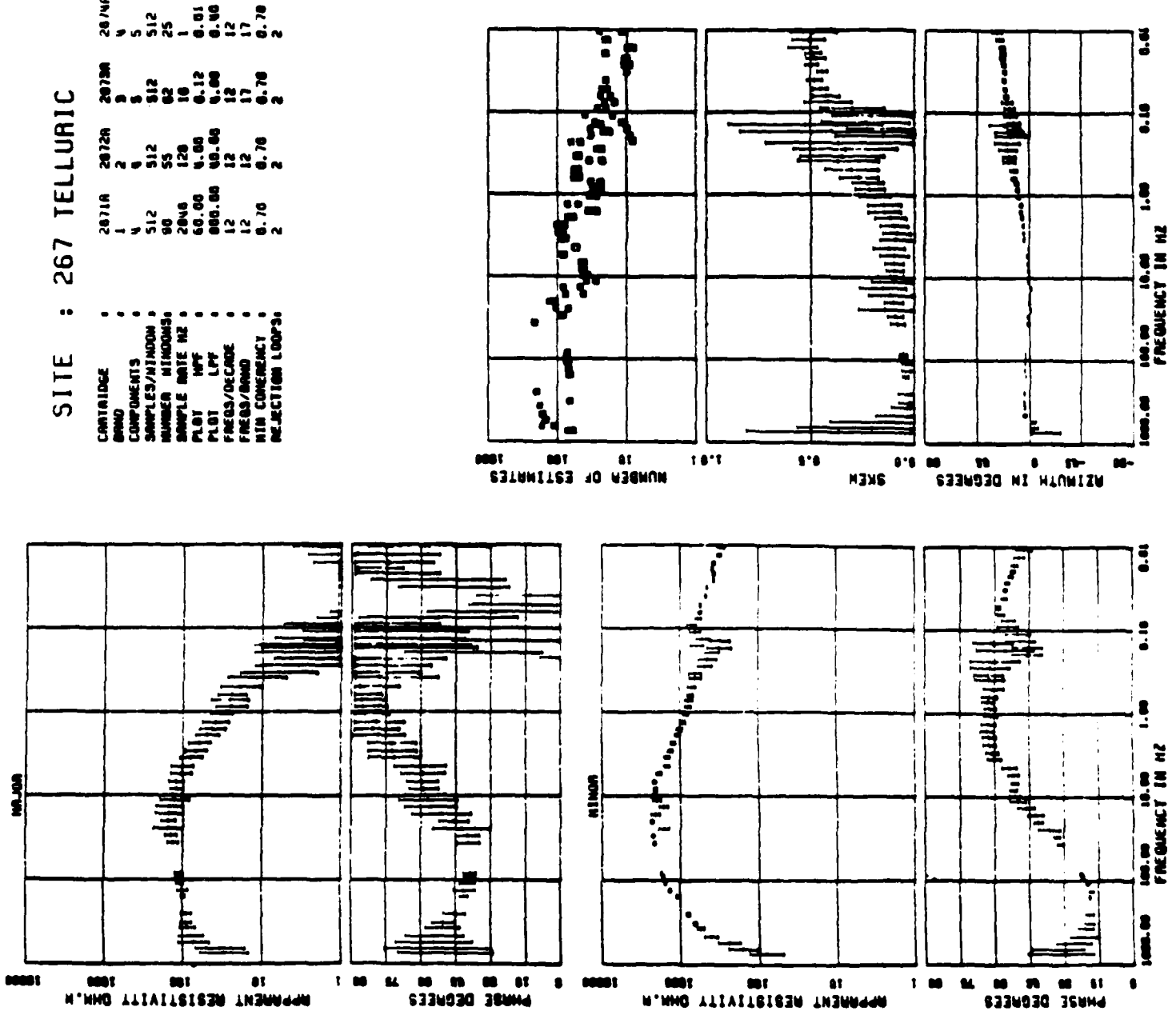

Figure VI.2. Continued (5).

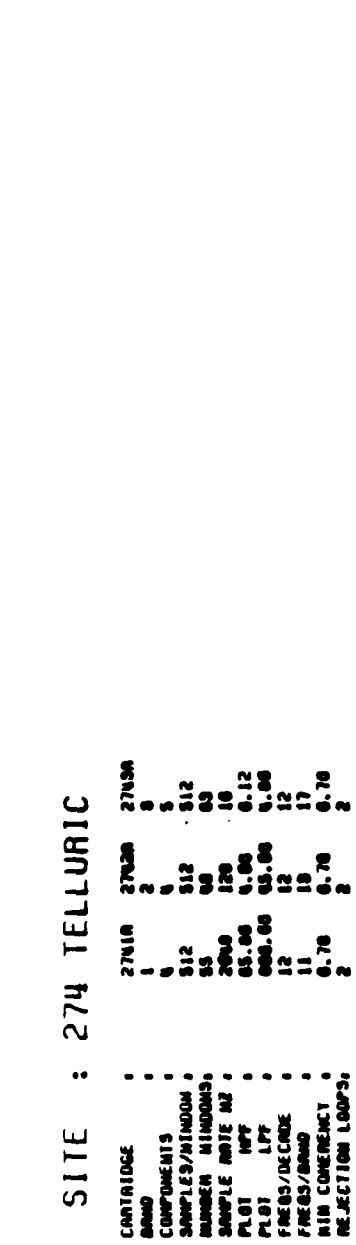
SITE : 274 TELLURIC
CANTRIDGE
BAND
COMPONENTS
SAMPLES/WINDOW
NUMBER WINDOWS
SAMPLE RATE HZ
PLOT HPF
PLOT LPF
FREQS/DECADE
FREQS/BAND
MIN COHERENCY
REJECTION LOOPS

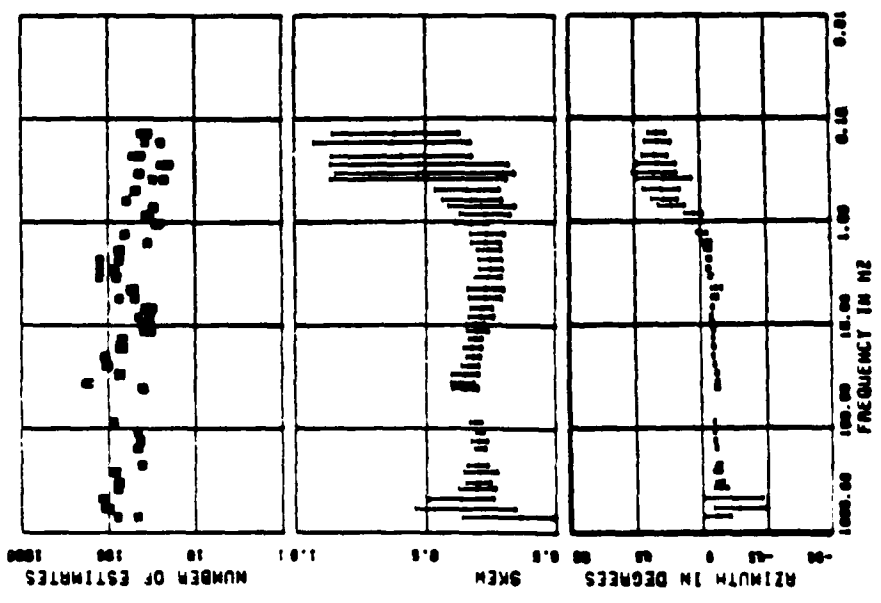
NUMBER OF ESTIMATES
SKEW
AZIMUTH IN DEGREES
FREQUENCY IN HZ

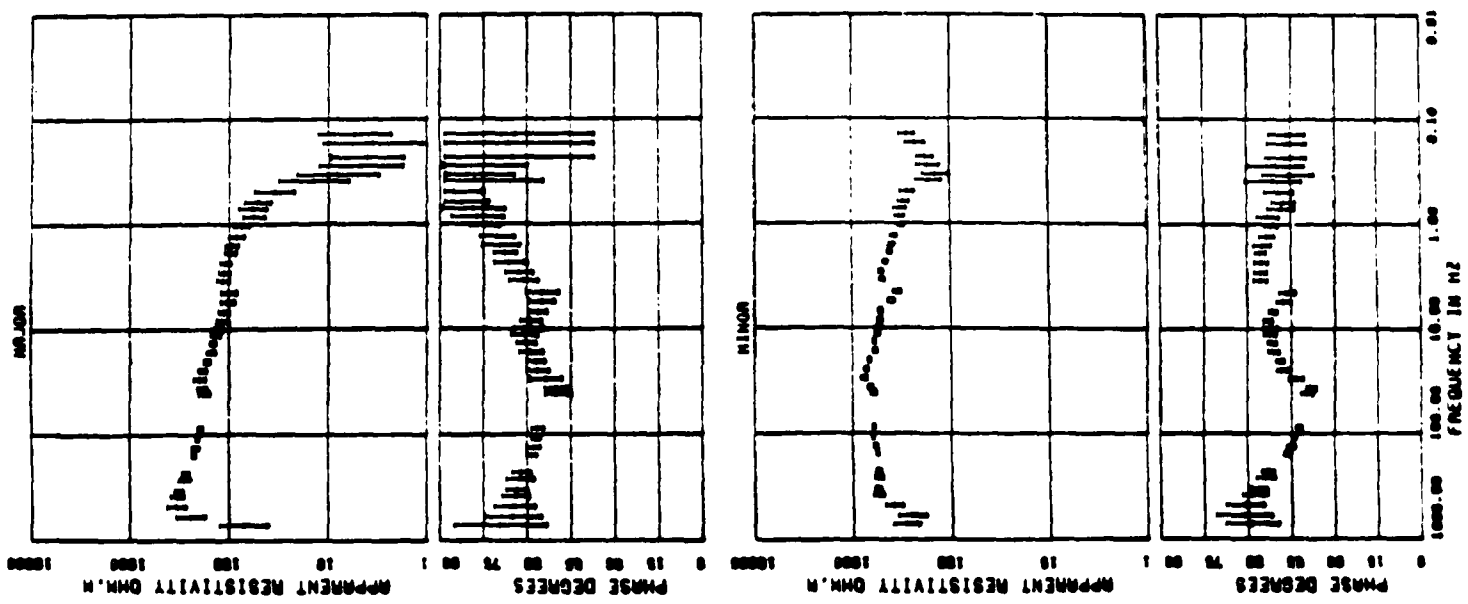
MAJOR
APPARENT RESISTIVITY OHM.M
PHASE DEGREES
MINOR
APPARENT RESISTIVITY OHM.M
PHASE DEGREES
FREQUENCY IN HZ

Figure VI.2. Continued (6).

SITE : 266 TELLURIC

CONTINUE	:	20010	20020	20030	200AA
BAND	:	1	2	3	4
COMPONENTS	:	1	1	1	1
SAMPLES/WINDOW	:	512	512	512	512
NUMBER WINDOWS	:	80	77	61	28
SAMPLE RATE HZ	:	2048	128	16	1
PLOT HPF	:	80.00	5.00	0.12	5.01
PLOT LPF	:	800.00	50.00	1.00	0.25
PHASE/DECADE	:	0	0	0	0
PHASE/BAND	:	0	0	12	13
BIN COHERENCY	:	0.00	0.00	0.00	0.00
REJECTION LOOPS	:	2	2	2	2

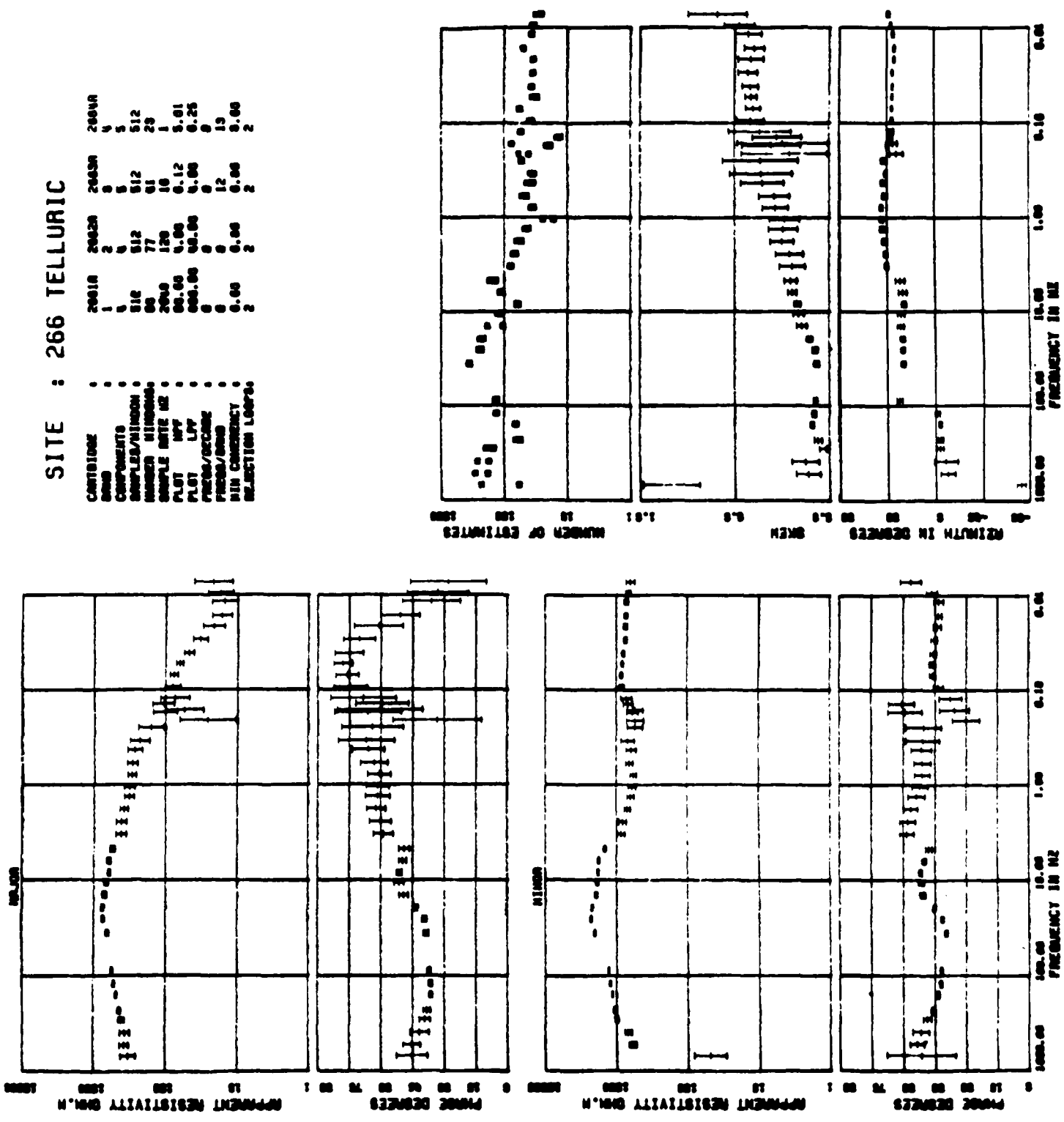

Figure VI.2. Continued (7).

SITE : 272 TELLURIC

CONTINUOUS	27218	2722A	2723A	2724A	
BAND	1	2	3	4	
COMPONENTS	6	6	5	5	
SAMPLES/WINDOW	512	512	512	512	
NUMBER WINDOWS	87	80	60	12	
SAMPLE RATE HZ	2048	128	16	1	
PLOT APP	60.00	0.00	0.12	0.01	
PLOT LPF	800.00	60.00	1.00	0.25	
FREQ/DECADE	0	0	0	0	
FREQ/BAND	0	0	12	13	
MIN COHERENCY	0.60	0.60	0.60	0.00	
REJECTION LOOPS	2	2	2	2	

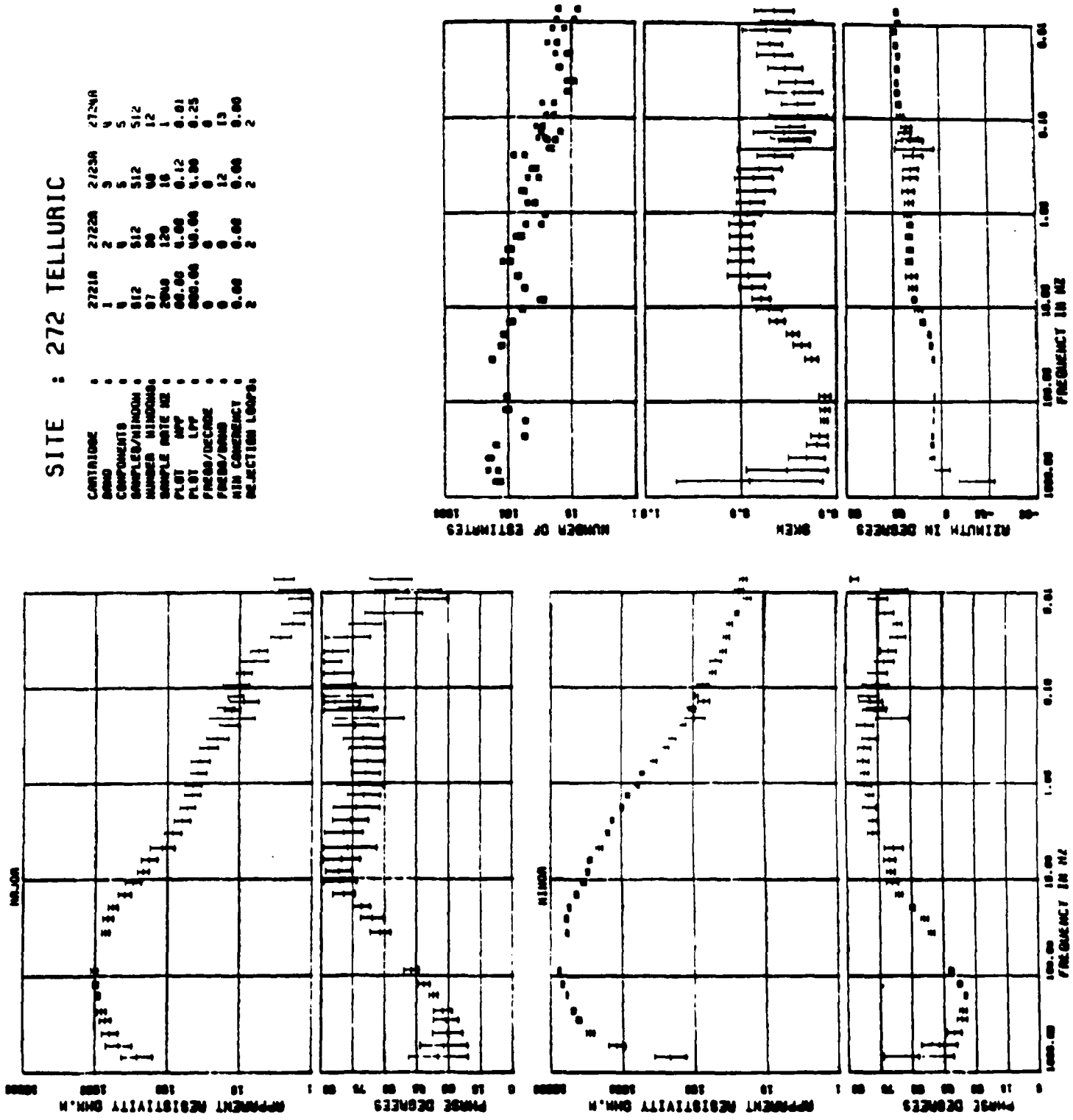

Figure VI.2. Continued (8).

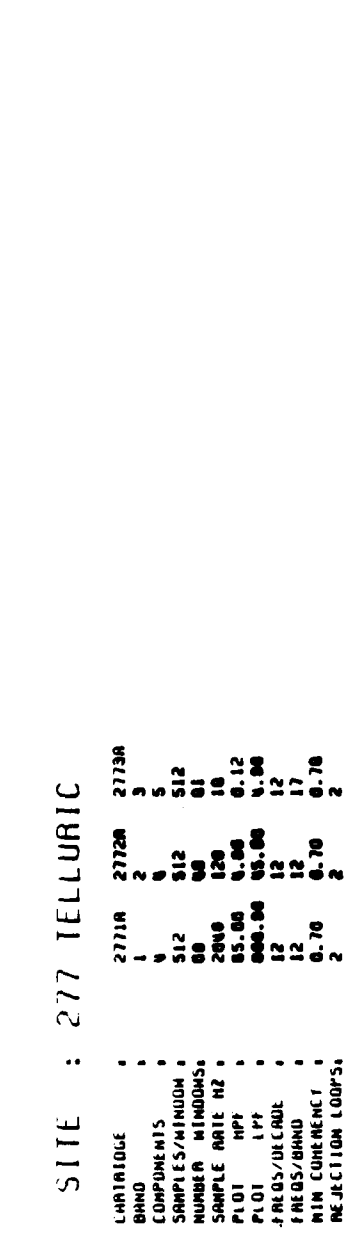
SITE : 277 TELLURIC
VARIABLE 27710 27720 27730
BAND 1 2 3
COMPONENTS 4 4 4
SAMPLES/WINDOW 512 512 512
NUMBER WINDOWS 80 80 81
SAMPLE RATE HZ 2048 128 10
PLOT HPF 85.00 0.06 0.12
PLOT LPF 800.00 55.00 1.00
FREQS/DECADE 12 12 12
FREQS/BAND 12 12 17
MIN COHERENCY 0.70 0.70 0.70
REJECTION LOOPS 2 2 2

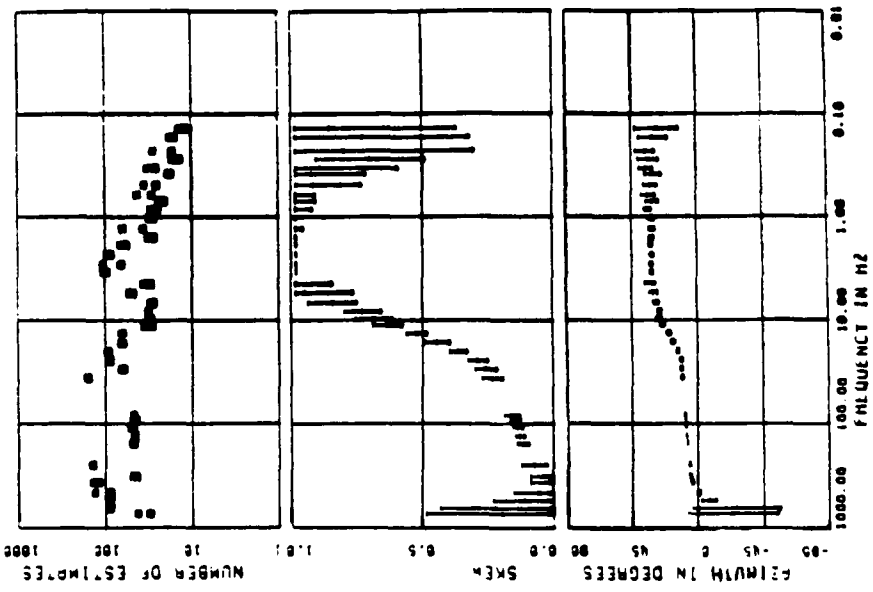
NUMBER OF ESTIMATES
SKEW
AZIMUTH IN DEGREES
FREQUENCY IN HZ

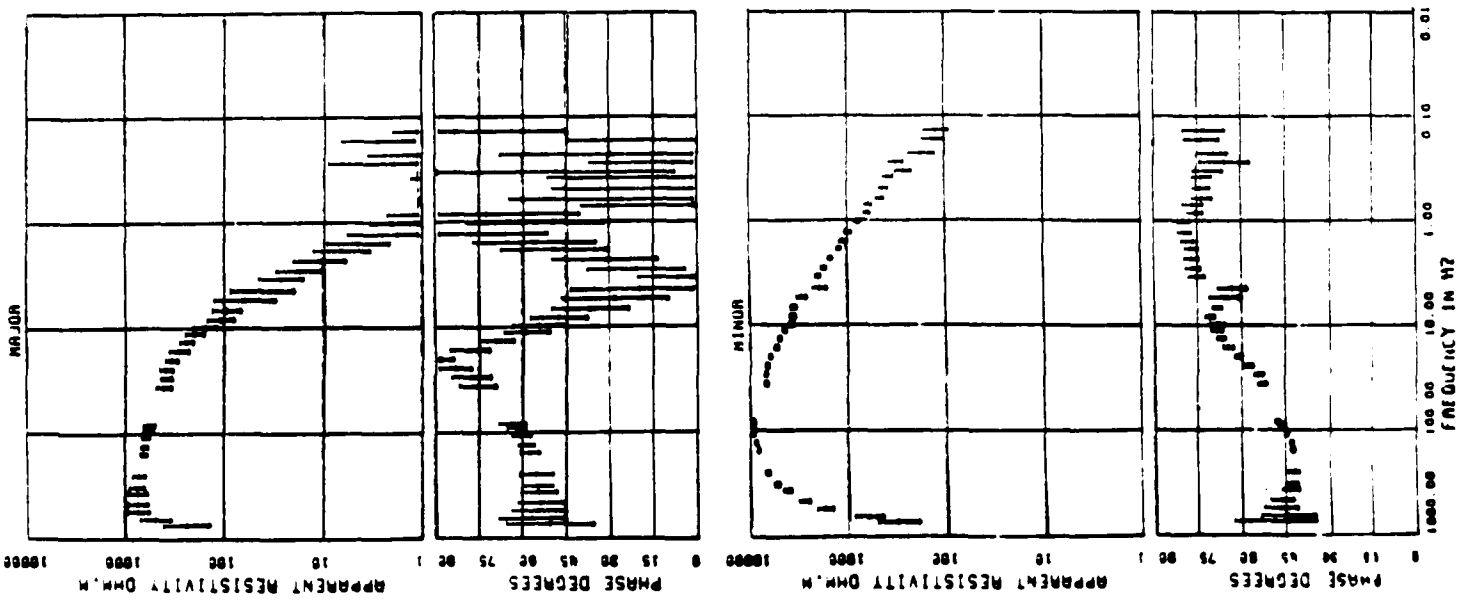
MAJOR
APPARENT RESISTIVITY OHM.M
PHASE DEGREES
MINOR
APPARENT RESISTIVITY OHM.M
PHASE DEGREES
FREQUENCY IN HZ

Figure VI.2. Continued (9).

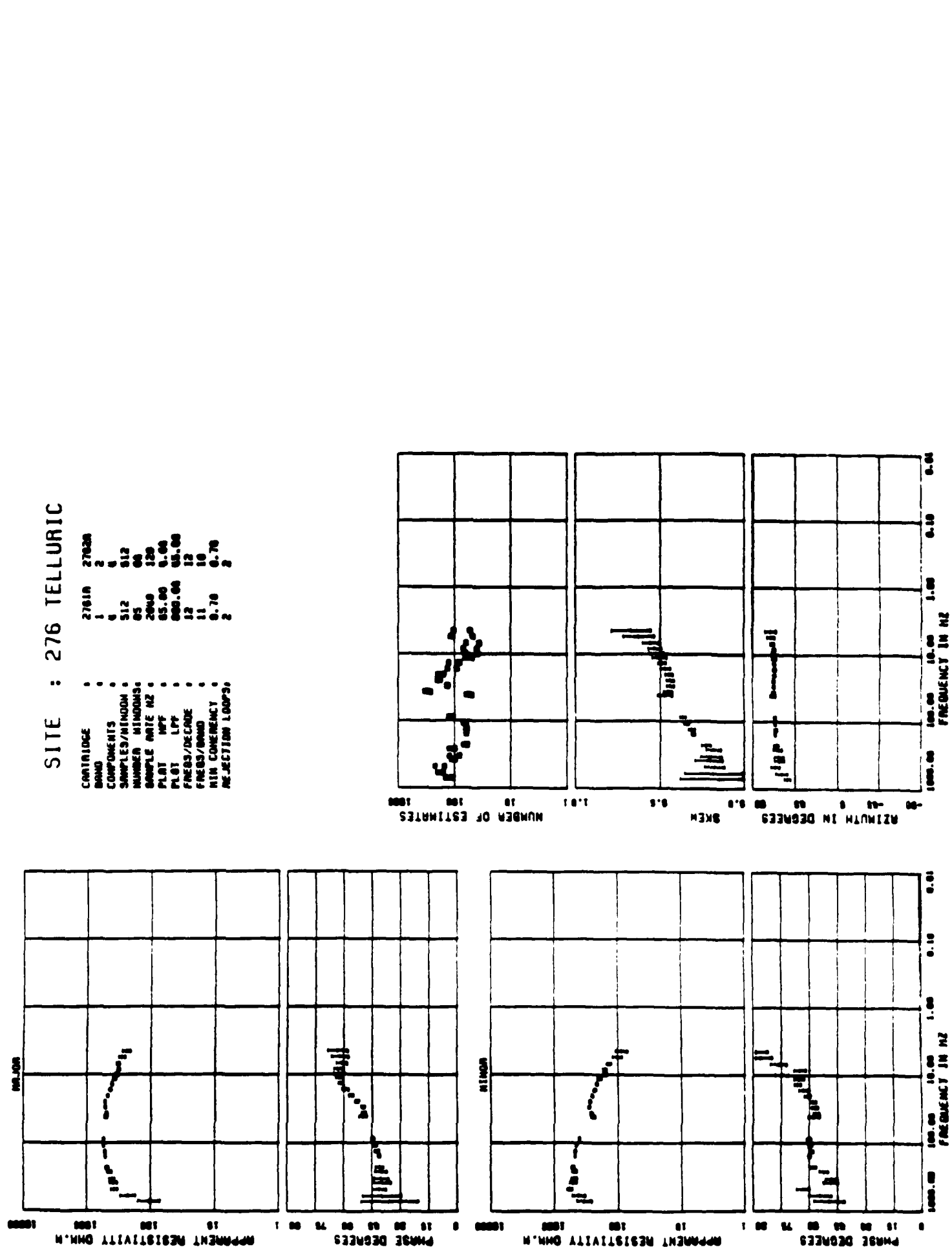
SITE : 276 TELLURIC
CARTRIDGE : 27
BOARD : 1
COMPONENTS : 6
SAMPLES/WINDOW : 512
NUMBER WINDOWS: 65
SAMPLE RATE HZ : 2048
PLOT HPF : 65.00
PLOT LPF : 800.00
FREQS/DECADE : 12
FREQS/BOARD : 11
MIN COHERENCY : 0.70
REJECTION LOOPS: 2
NUMBER OF ESTIMATES
SKEW
AZIMUTH IN DEGREES
FREQUENCY IN HZ
APPARENT RESISTIVITY OHM.M
PHASE DEGREES
MAJOR
MINOR

Figure VI.2. Continued (10).

SITE : 282 TELLURIC

CONFIGURE	2021A	2022A	2023A	2024A	
BOARD	1	2	3	4	
COMPONENTS	4	4	4	4	
SAMPLES/WINDOW	512	512	512	512	
NUMBER WINDOWS	76	63	63	20	
SAMPLE RATE MZ	2048	128	16	1	
FLOT HPF	65.00	1.00	0.12	0.01	
FLOT LPF	800.00	10.00	1.00	0.25	
FREQA/DECADE	0	0	0	0	
FREQB/DECADE	0	0	12	13	
MIN COHERENCY	0.60	0.60	0.60	0.60	
REJECTION LOOPS	2	2	2	2	

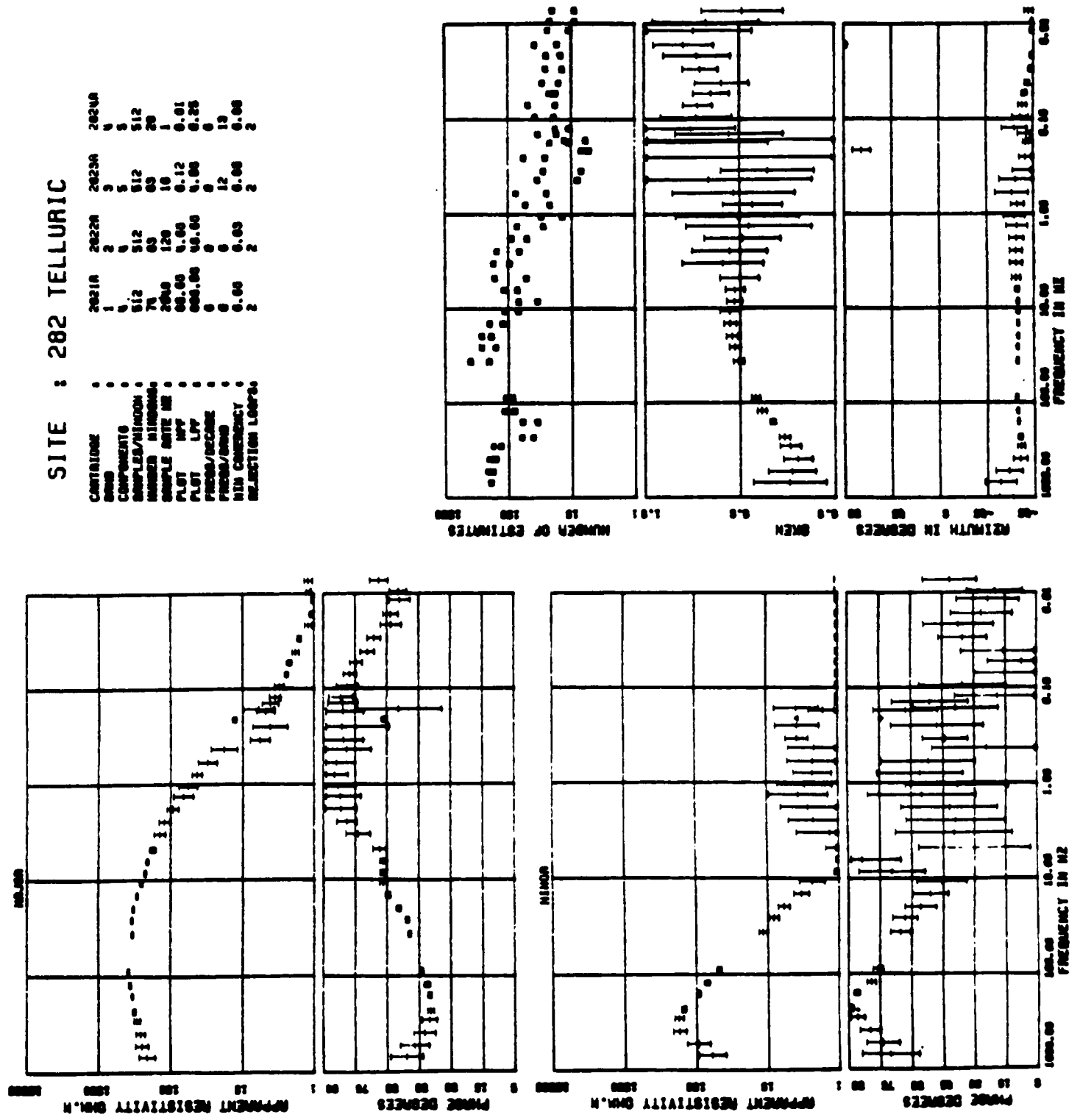

Figure VI.2. Continued (11).

SITE : 275 TELLURIC

CARTRIDGE	27518	27528
BAND	1	2
COMPONENTS	4	4
SAMPLES/WINDOW	512	512
NUMBER WINDOWS	10	64
SAMPLE RATE HZ	2048	128
PLOT HPF	65.00	8.00
PLOT LPF	000.00	05.00
FREQS/DECADE	12	12
FREQS/BAND	11	10
MIN COHERENCY	0.70	0.70
REJECTION LOOPS	2	2

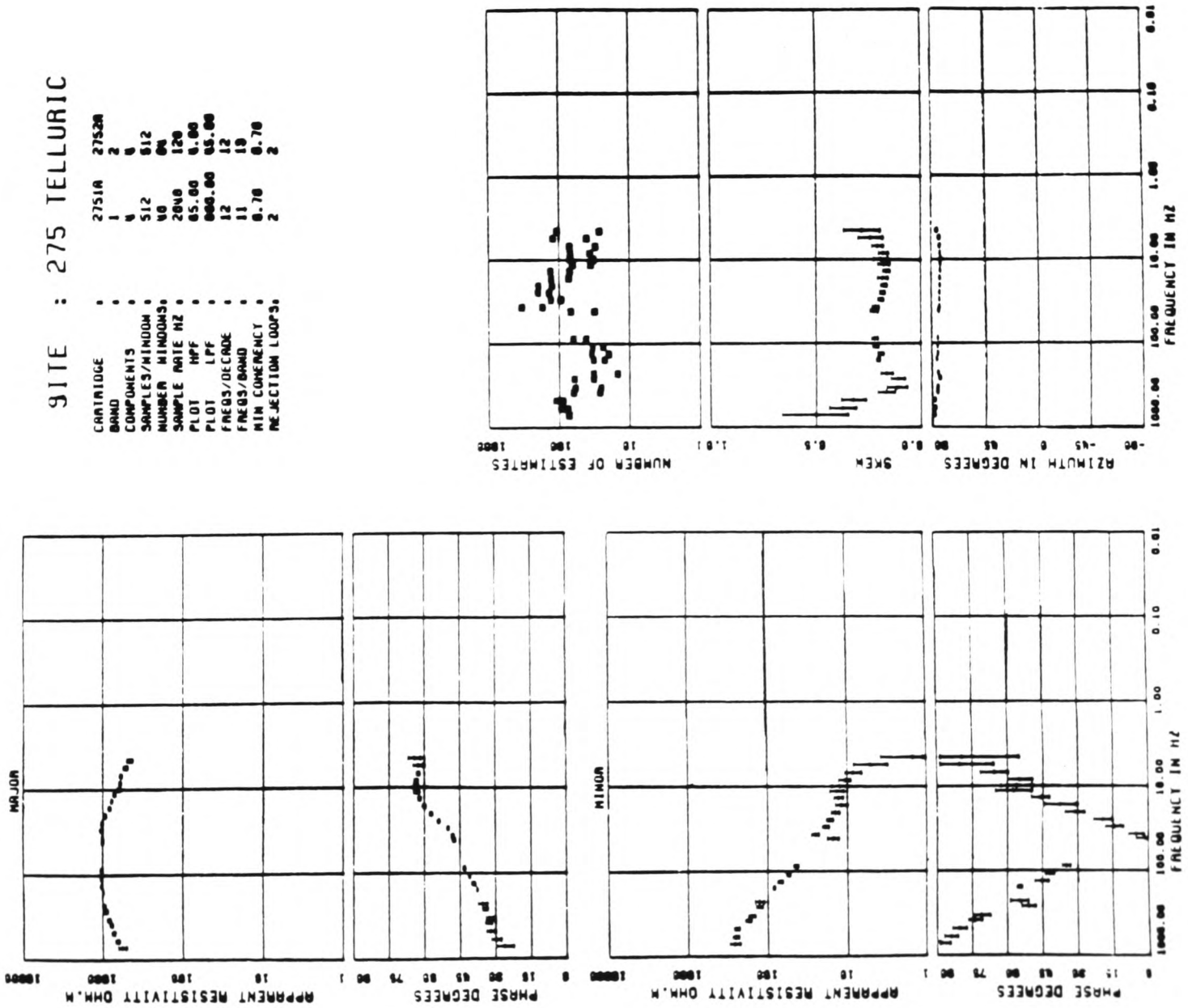

Figure VI.2. Final (12).

the minor direction most of the sites still show a similar decreasing trend. Azimuths are reasonably stable with respect to frequency for most of the sites. Anisotropy ratios show an increasing behaviour with frequency at all sites. Skew values increase not only with frequency but also away from the Rocky Mountains Trench.

There is very little data available on the vertical component. Six sites produced some vertical transfer functions for bands 3 and/or 4. At frequencies between 2 and 0.05Hz the real induction arrows at site 82 appear reversed with respect to the other available arrows along the trench. Analysing the induction arrows from all possible sites along the trench and along the two traverses it is possible to conclude that the main concentration of currents is under the Main Ranges of the Rockies and not under the Trench (Hutton et al., 1987).

VI.6. Interpretation

Interpretation in terms of pseudosections and geoelectric sections in which 1D inversions are brought together for all sites along the 2 traverses and the Rocky Mountains Trench profile, can be found elsewhere (Hutton et al., 1987). A Monte Carlo inversion scheme was used for the inversions of the invariant impedance (III.67) and of the E-polarization set of results. The Monte Carlo inversion algorithm is described in chapter IV. References to the above paper will be made whenever necessary.

Directional analysis

Assuming that the structure of the region is 2D or quasi two dimensional, the rotation to a gross structural strike, $\theta = 72^{\circ}W$, allows the association of the major and minor directions with the two polarization modes generated in 2D structures. Undoubtedly the Rocky Mountains Trench represents the main structural lineament in the region, thus it is reasonable to look for 2D effects in the major and minor directions. In principle a valid E-polarization response set would be characterised by the spatial continuity of the electric field component, and hence apparent resistivity, along the SR traverse. Therefore it should be possible to recognize the two polarization cases by comparing the smoothness of the major and minor sets of responses. This is not so straightforward since different frequencies may respond to different structures and these, in turn, depend on the relative site location. In addition both E- and H-polarization sounding curves may be strongly influenced by the

presence of 3D structures (e.g., Rokityansky, 1982, pp.220-225).

It is assumed here that the major direction which is parallel to the structural strike, represents the E-polarization set of responses. In order to assess the quality of this assumption an ideal 2D picture is employed. This is done with the aid of two different, although related, ways of viewing the response along the whole traverse. Firstly both apparent resistivities are plotted along the traverse at selected periods in the expectation of recognizing the E-polarization case by its smoothness, in opposition to a "jumpy" behaviour of the perpendicular H-polarization case (e.g., Schwarz et al.,1984). The results are shown in figure VI.3. As can be seen, this approach is of a very limited usefulness for the present data set since neither the major nor the minor provided smoothly varying values along the traverse.

A second approach uses the fact that in a strictly 2D situation the E-polarization apparent resistivity values along a traverse perpendicular to the strike must approach a common set of results, while the resistivities perpendicular to the strike may not (e.g., Hermance and Pedersen, 1980). In order to use this approach, sounding curves are plotted together for each polarization case. As in the first approach, this is done in the expectation of recognizing a relative behaviour between the two sets of curves. Figure VI.4 shows apparent resistivities and phases along the major direction for all sites along the SR traverse, whereas figure VI.5 shows the same quantities along the minor direction. The results shown indicate that the major apparent resistivity curves tend to cluster into a narrower range of values for almost all sites while the corresponding minor direction values tend to disperse, a behaviour that becomes even more conspicuous towards the lower frequencies. This fact supports the assumption that the major direction can be associated with the E-polarization case for the SR traverse.

Site Analysis

Before the information from all sites is brought together it is necessary to look critically at each site both individually and in relation to its neighbours. This qualitative analysis is done with the aid of some ancillary parameters such as anisotropy ratio, azimuth and skew. The necessary information is displayed in figure VI.2 for all sites along the traverse. It is worthwhile to stress

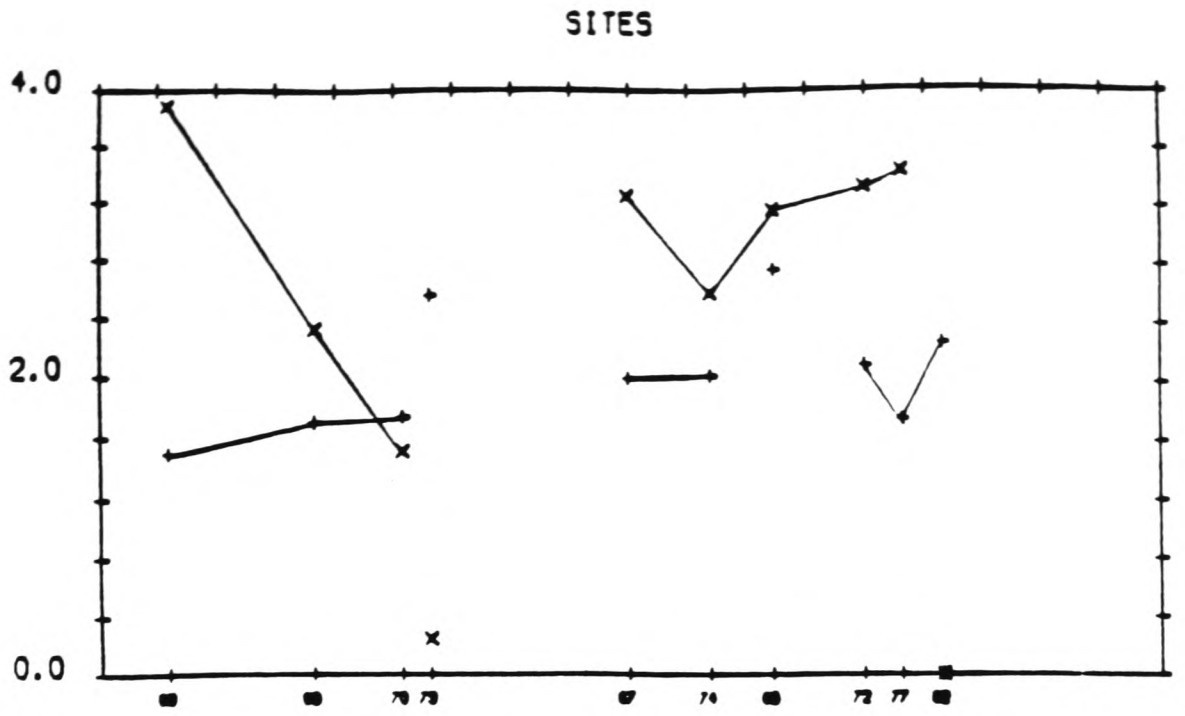

FREQUENCY: 5.00 Hz

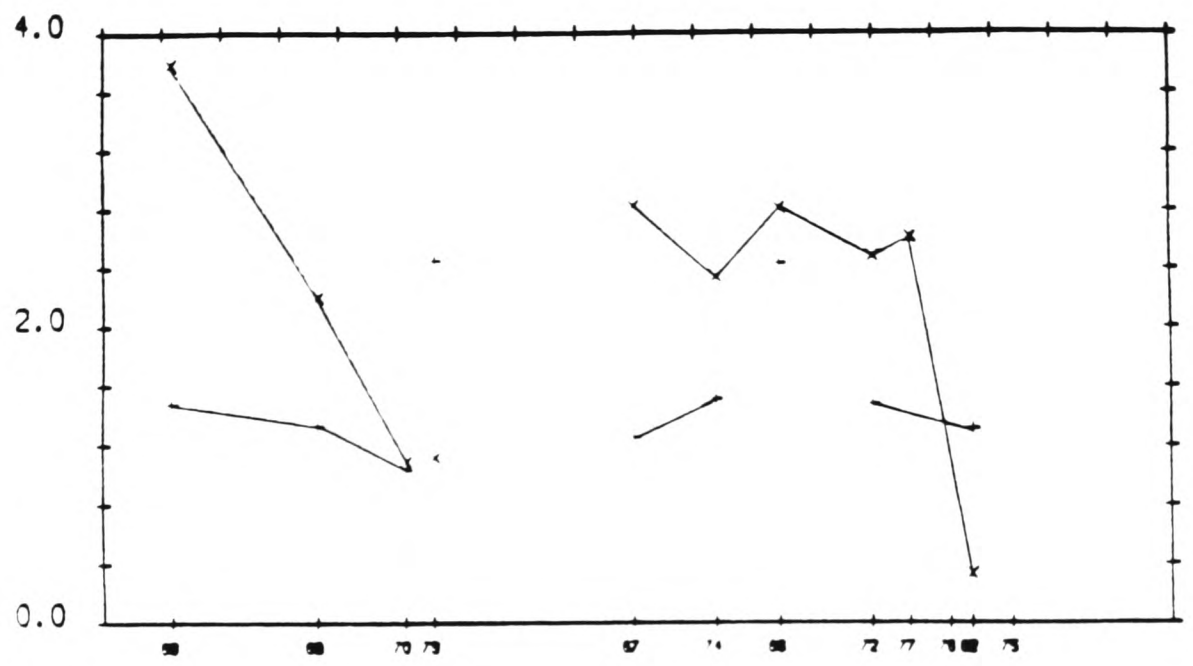

FREQUENCY: 0.50 Hz

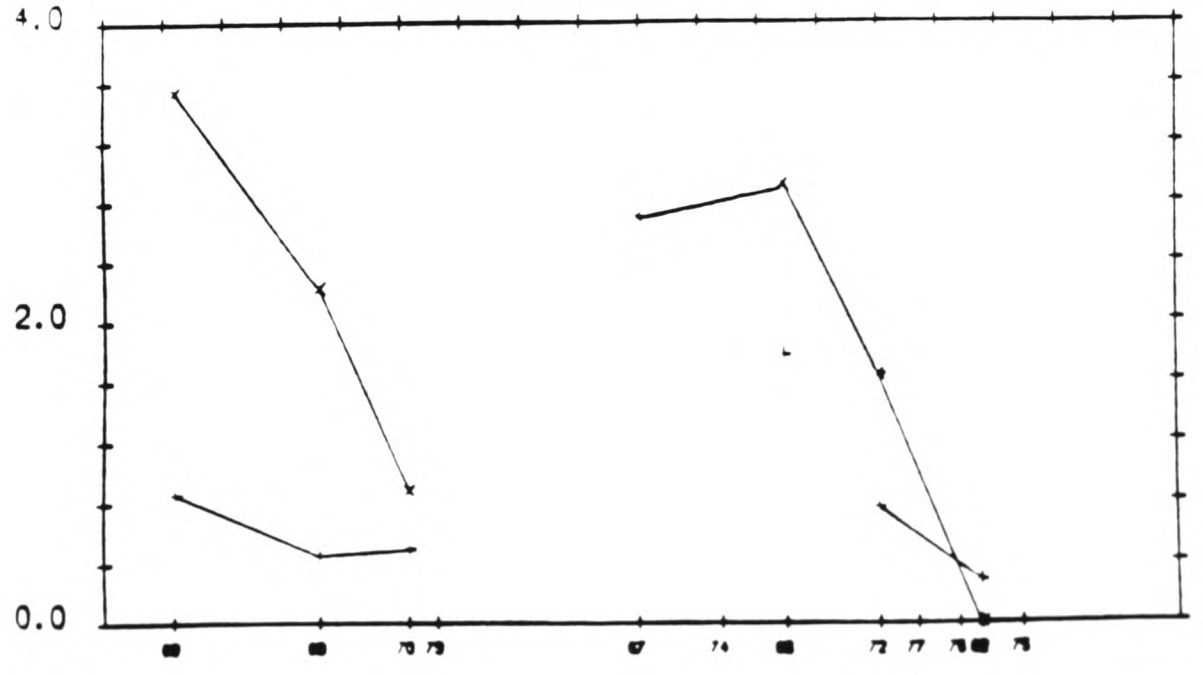

FREQUENCY: 0.05 Hz

SYMBOLS: + RHO1(MAJ), × RHO2(MIN)

Figure VI.3. Major (+) and minor (x) apparent resistivities along the SR traverse. Some symbols are linked with solid lines to highlight the relative continuity of the major. Resistivity values are shown in log(Ω.m).

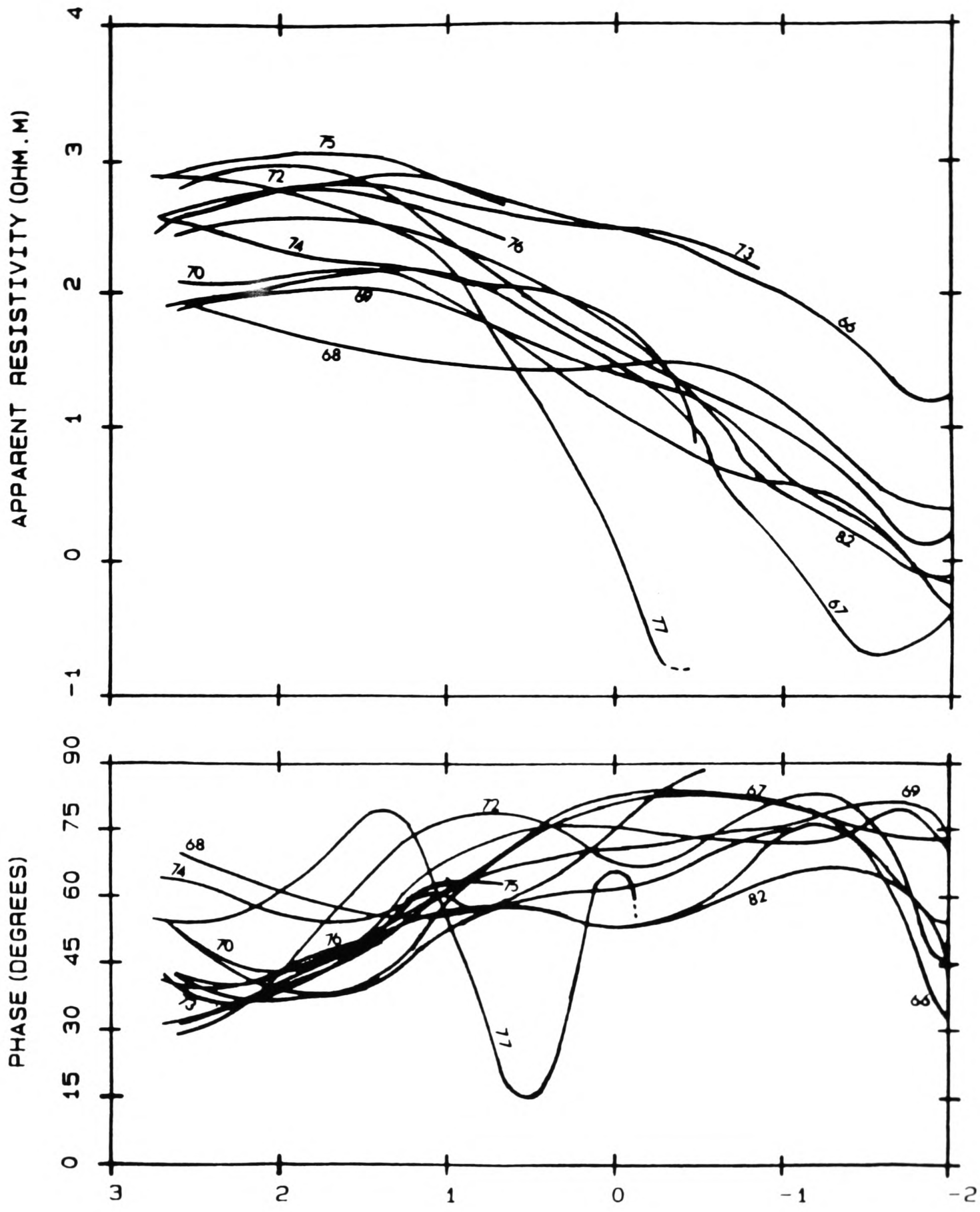
APPARENT RESISTIVITY (OHM.M)
4
3
2
1
0
-1
75
72
74
76
73
70
69
68
77
67
82
PHASE (DEGREES)
90
75
60
45
30
15
0
68
74
72
67
69
70
76
75
82
71
86
3
2
1
0
-1
-2

Figure VI.4. Apparent resistivity and phase curves along the major direction for all sites along the SR traverse. The apparent resistivity scale is logarithmic.

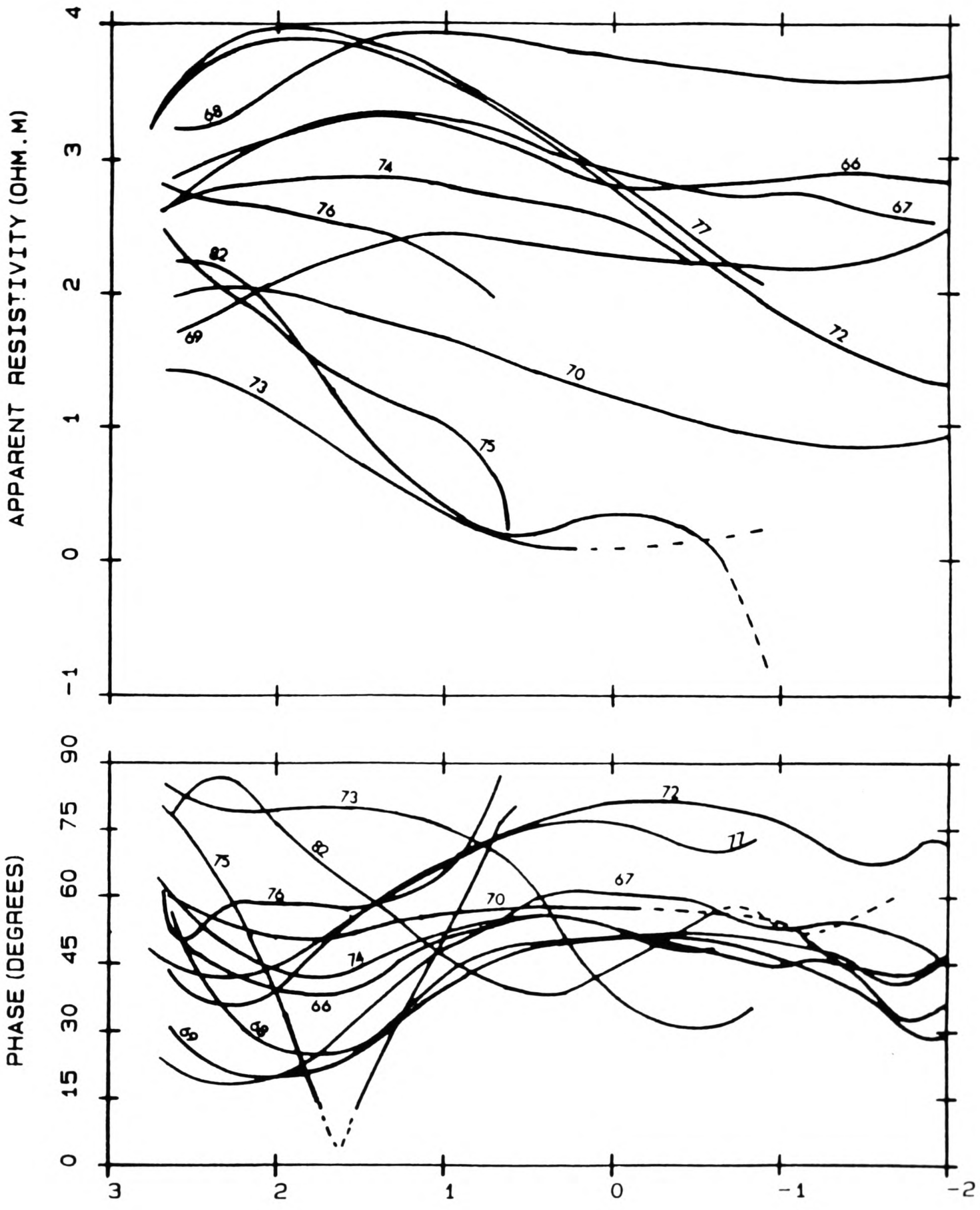
APPARENT RESISTIVITY (OHM.M)
4
3
2
1
0
-1
68
74
66
76
67
77
82
72
89
70
73
75
PHASE (DEGREES)
90
75
60
45
30
15
0
73
72
77
82
75
67
76
70
74
66
68
68
3
2
1
0
-1
-2

Figure VI.5. Apparent resistivity and phase sounding curves along the minor direction for all sites along the SR traverse. The apparent resistivity scale is logarithmic.

two points. Firstly the principal azimuth of rotation, (III.66), is independent of the rotated data set as all soundings curves are rotated to the structural strike direction, 72°W. Secondly the skew, definition (III.68), must be used with caution since it is essentially a non-reliable dimensionality indicator (Beamish, 1986b). A more reliable indicator is given by a set of inequality constraints which give the necessary conditions for the one-dimensionality of a site (Weidelt, 1972 and 1986). Nevertheless such constraints are invariant with respect to static effects (Larsen, 1981) which, as will be shown below, appear to affect many sites on the SR traverse. Moreover such constraints are likely to suffer numerical instability due to the error levels experienced at most of the sites.

Begin from the southwestern end of the SR traverse. Site 68 sits on a crystaline region and its response is strongly anisotropic with anisotropy ratios in excess of 1000. Its location probably is within or very close to a resistive region as suggested by the magnitude of both major and minor responses. This site shows stable azimuths 10°-30°E, with a gentle increasing trend with period. Its average azimuth direction is 20°E, which is perpendicular to a thrust fault indicated as f1 in figure VI.6. Skew values are moderate. Site 69 shares some of the characteristics of sites 68 and 70, its neighbours. The anisotropy ratio increases with period from 1 to 100. The azimuths start reflecting the strike direction and then rotate to values similar to those of site 68 below 100Hz. Skew values are less than for site 68 and are greater than those at site 70. Site 70 shows small anisotropy ratios, between 1 and 10, which are significantly above 1 only for periods above 10s. Azimuths now reflect the strike direction from the high frequencies down to 0.5Hz and again rotate to values similar to those at site 68 towards the end of the frequency range.

Site 70 appears to be the site that shows the best 1D characteristics in the SR traverse on the basis of the available information, although located close to the fault f1, see figure VI.6. Site 73 displays characteristics which are distinct from site 70 which is situated less than 1km away. Anisotropy ratios are in excess of 100. Azimuths reflect the strike direction for the whole frequency range in partial agreement with site 70 but skews are higher and less stable at site 73. The large disparity between resistivities at sites 70 and 73 may be caused by a very superficial heterogeneity. Elsewhere it has been reported that in the presence of a very shallow good conductor, sites only 500m apart may show large discrepancies in the amplitudes of $\underline{\underline{Z}}$ (Bahr, 1983).

The distance between sites 73 and 67 is in excess of 6km, the greatest along the SR traverse. Sites 67, 74, 66, 72, 77 and 76 share some important characteristics. Anisotropy ratios vary from above 1 to about 100 but, more important, the anisotropy does not vary much with respect to frequency, at least for frequencies between 100-1Hz. This behaviour appears to be caused by 3D inhomogeneities since phase values for the two polarization directions show values which are either not dissimilar or quasi-parallel for all sites except 66 and 77. Site 72 shows fairly constant anisotropy ratios at all frequencies below 100Hz and shows reasonable similar phase values for the two main directions for most of the frequency range. The possibility of 3D effects will be the subject of further investigation below. Azimuths show an increasing behaviour from small angles in the W or the E direction, to values just above 20° E, at sites 67 and 74 above 1s, or to 45° E, at sites 66, 72 and 77. Site 76 displays a fairly constant azimuth of 70° E. Skews are not small and show an increasing behaviour. The last two sites, 82 and 75, are very anisotropic, showing azimuths which are about $\pm$90° and large and scattered skew values. The sounding curves at those two sites indicate that they might be strongly influenced by either surface inhomogeneities or the topography.

The effect of topography

It is expected that the topography may influence certain sounding curves along the profile. In order to completely correct for the effect of the topography it would be necessary to construct a 3D topographical model (Mozley, 1982) which is beyond the scope of the present work. Nevertheless some insight into the effect of the topography in the direction of the SR traverse may be gained by a simplified 2D model. Such an approximate model, is better applied at sites where the topographic gradient is steeper and the sites closer together. Sites in the NE end of the traverse, from site 72 upstream, appear to be the best sites for this analysis. The topographic gradient becomes increasingly more pronounced towards the traverse NE end.

A 2D model of the topography in the direction of the SR traverse is shown in figure VI.6. The earth is considered to be of uniform resistivity of 100Ω.m. For the model calculations the whole frequency range is considered and the grid dimensions are 8x8 the largest skin depth. Model responses are calculated using a finite difference algorithm (Brewitt-Taylor and Weaver, 1976). Grid construction and modeling procedures are the same as described in chapter V. It was found from the responses of the model displayed

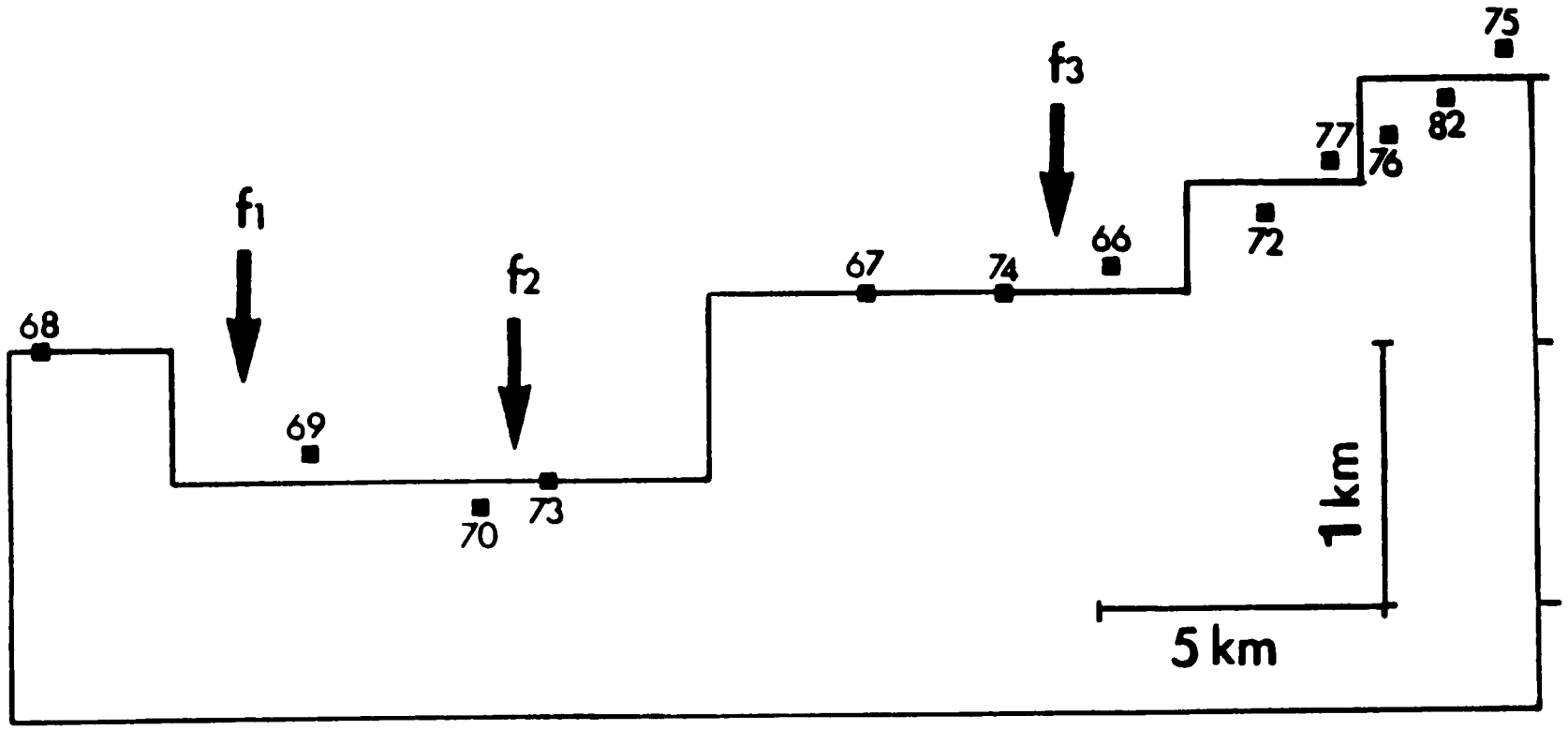
f1
f2
f3
68
69
70
73
67
74
66
72
77
76
82
75
1 km
5 km

Figure VI.6. Model of the topography showing site locations and heights. There are three faults: f1 and f3 are thrust faults and f2 is a normal fault. Hanging walls of the faults are on the SW (left) side.

in figure VI.6 that the topography alone, as modelled, is not sufficient to explain, even in part, the behaviour observed in the sounding curves. It was also found that the complete model responses can be obtained by sub-dividing the model into sections and analysing each step locally with the 90 degree step model described in chapter V. If a step model is used at each site, the results suggest that sites 82 and 75 display H-polarization "topographic" sounding curves which show some resemblance to the curves for a site on the higher side of a slope as shown in figure V.6.

Near surface inhomogeneities

Lateral inhomogeneities in the upper crust can cause local distortions of the MT fields. In particular, a depression filled with conductive sediments can introduce distortions on the apparent resistivity curves which appear as a frequency independent (static) shift or as a frequency dependent (inductive) distortion at high frequencies (Berdichevsky et al., 1984). A static effect may shift sounding curves either upwards or downwards. Such 3D distortions have been modelled for structures filled with conductive sediments in a conductor-resistor-conductor type of model (Berdichevsky and Dmitriev, 1976; Berdichevsky et al., 1984) and in more complicated models (Park et al., 1983; Park, 1985).

Three distortion mechanisms have been identified when analysing the 3D effects of a sediment-filled structure (Park, 1985). Identification of 3D effects is made possible by comparing the 3D results with their 2D and 1D "undisturbed" counterparts. The first is the vertical current distortion (VCD) which is a result of resistive coupling between the upper parts of the crust and mantle. The result of the VCD is a shifted resistivity curve which resembles the low frequency part of the 1D curve outside the inhomogeneity. The second mechanism is the horizontal current distortion (HCD) which results from the resistive coupling of upper crustal features. The result of the HCD is a parallel offset of the resistivity curves. The third mechanism is the local induction (LI) which appears as a frequency dependent offset of the 1D curve outside the inhomogeneity. Thus the two first mechanisms are responsible for static shifts of the resistivity curves, leaving the phase curve undistorted, while the third is responsible for inductive shifts. Frequency independent mechanisms appear as static shifts on apparent resistivity curves for both polarizations, leaving phases unaffected. Such 3D distortions can be severe and are unpredictable by 1D inversions or 2D modeling (Park, 1985). The higher

frequencies are expected to be least affected by static shift mechanisms as indicated by several examples in the literature (Berdichevsky and Dmitriev, 1976; Park et al., 1983; Berdichevsky et al., 1984; Park, 1985).

Such distortion mechanisms (Park, 1985) are particularly interesting since several sites along the SR traverse show characteristics which indicate that response curves may be static shifted and since both the Rocky Mountains Trench and the SR traverse are elongated structures filled with conductive sediments. Sites 66, 72, 77 and 76 show signs of this phenomenon, at least for part of the frequency range. Site 72 shows conspicuous signs of static shift, as shown in figure VI.7 where E- and H-polarization apparent resistivities and phases are shown together. At the latitude considered the trench is 5-10km wide, and is covered with conductive sediments ($\sim$10Ω.m) 550m to 2km thick (Dragert and Clarke, 1977; Spence et al., 1977a). These dimensions can be used to show that inductive mechanisms are not important either for the trench or for the traverse. Approximate formulae which estimate the minimum period range where LI is important (Berdichevsky et al., 1984; Park, 1985) give periods >500s for the trench which is beyond the periods considered here. Thus it is possible to assume that if any of the sites are affected by near surface inhomogeneities, the main distortion mechanisms will be generated by VCD and HCD.

The effect of the near surface distortion mechanisms on 1D interpretation is to produce a model where both resistivity and depth values of the layered structure are distorted since both apparent resistivity curves may be offset either downwards or upwards by an unknown amount. A synthetic model study of a superficial 3D structure over a layered earth has demonstrated that the low frequency portion of the 3D curves resemble the 1D curve obtained outside the inhomogeneity, i.e. reflecting the underlying layered structure, but were shifted with respect to the resistivity away from the 1D curve (Park et al., 1983; Park, 1985). It is reasonable to assume that near-surface effects may be compensated by shifting sounding curves (Park, 1985) thus preserving the information about the deeper structures. This can be done as long as the surface heterogeneities are sufficiently thin to produce static effects for a considerable part of the frequency range.

A complete parallel offset of a 1D resistivity curve with the phase preserved, can be represented by one member of the family of possible 1D models which fit the data at one site. In this particular case several models can fit the phase and produce an

SITE: 272C

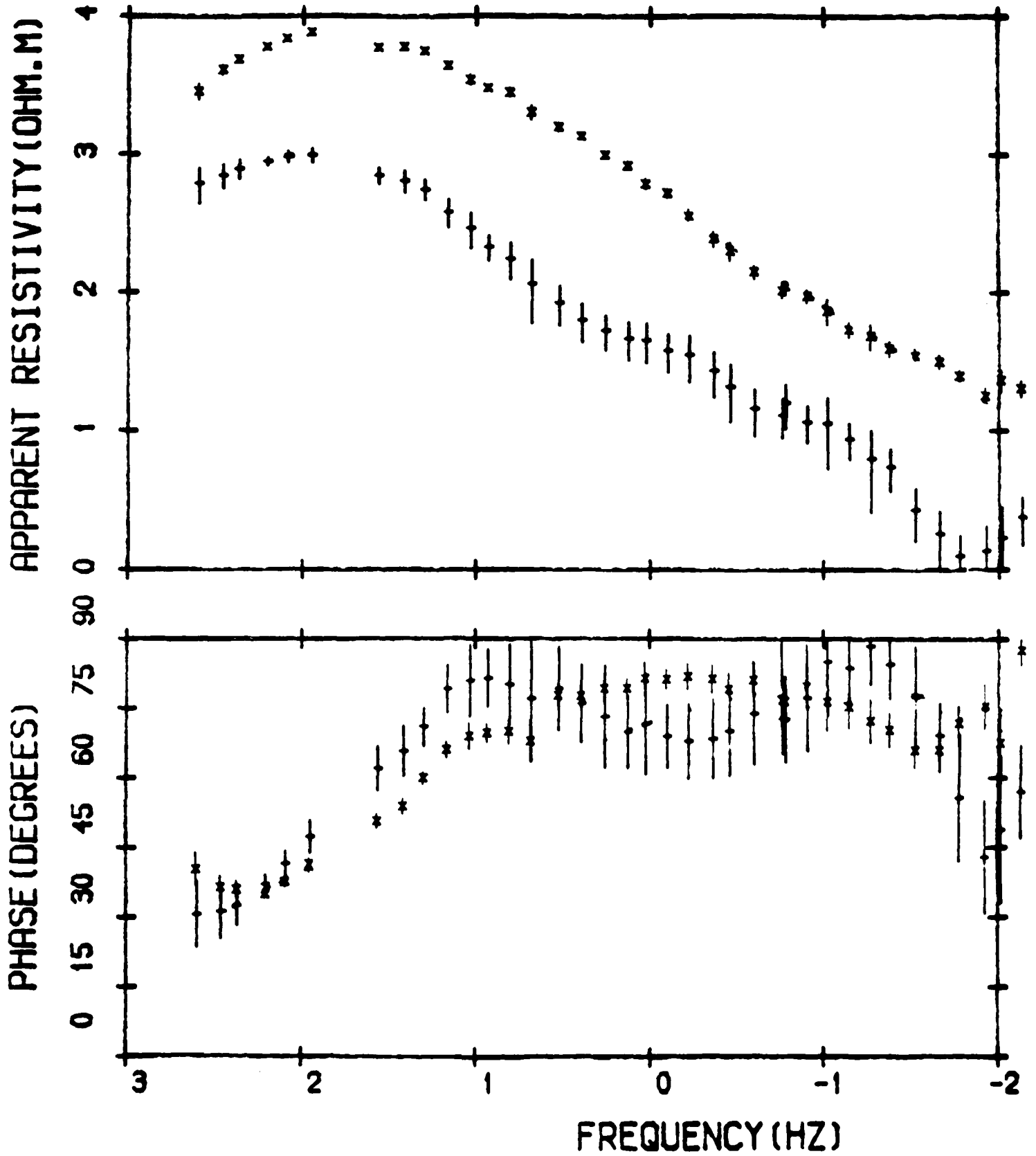
APPARENT RESISTIVITY(OHM.M)
0
1
2
3
4
PHASE(DEGREES)
0
15
30
45
60
75
90
3
2
1
0
-1
-2
FREQUENCY(HZ)

Figure VI.7. E- (+) and H-polarization (x) apparent resistivities and phases at site 72.

apparent resistivity curve which has the same shape but is parallel shifted in relation to the observed values. Of course this is a strict 1D case, in contrast to a 3D mechanism such as static shift. Nevertheless if it can be assumed that below a certain depth the structure is layered, one member of the family of 1D models will describe the earth below a certain frequency value.

Site 70 can be used to demonstrate how several 1D models can fit the data while producing shifted resistivities. Only the E-polarization responses are inverted. Site 70 is chosen because its data are of good quality and its sounding curves can be explained by a simple three-layer model. As shown in figure VI.8 this site has very low anisotropy ratios. The Monte Carlo algorithm, which is described in chapter IV, is used to produce the 1D inversions. This algorithm is used because it permits the specification of bounds for the initial model parameter permitting the user to restrict and direct the search in the model space. Figure VI.9 shows the 1D inversions of the E-polarization apparent resistivity and phase of site 70, obtained by specifying different bounds on the initial models. The three sets of models shown in the figure have different resistivity distributions which give the best fit found within the bounds and share similar phase responses. The model resistivity responses appear shifted, reflecting the different 1D models. The effect illustrated in figure VI.9 mimics, at least for some frequency range, the effects of a 1D inversion 3D data which suffers a parallel offset. For instance by inverting an E-polarization response curve which is static shifted, one would simply generate one member of a family as shown in figure VI.9. This may be the case at least for the low frequency sections of the sounding curves.

Data inversion and a resistivity section

Geoelectric sections can be constructed by putting together the result of 1D inversions along a profile. This is done in the expectation of finding an approximate image of the true resistivity distribution. Geoelectric sections for the SR traverse obtained using the E-polarization responses and the invariant, (II.67), can be found elsewhere (Hutton et al., 1987). In that paper 1D models for all sites shown in figure VI.1 were considered when constructing the geoelectric sections. The Monte Carlo algorithm was used for all inversions in that paper. The objective here is not to produce an interpretation for the SR traverse which is beyond the scope of this work, but rather to illustrate data characteristics. From this point of view a simplified geoelectric profile is now considered.

SITE: 270C

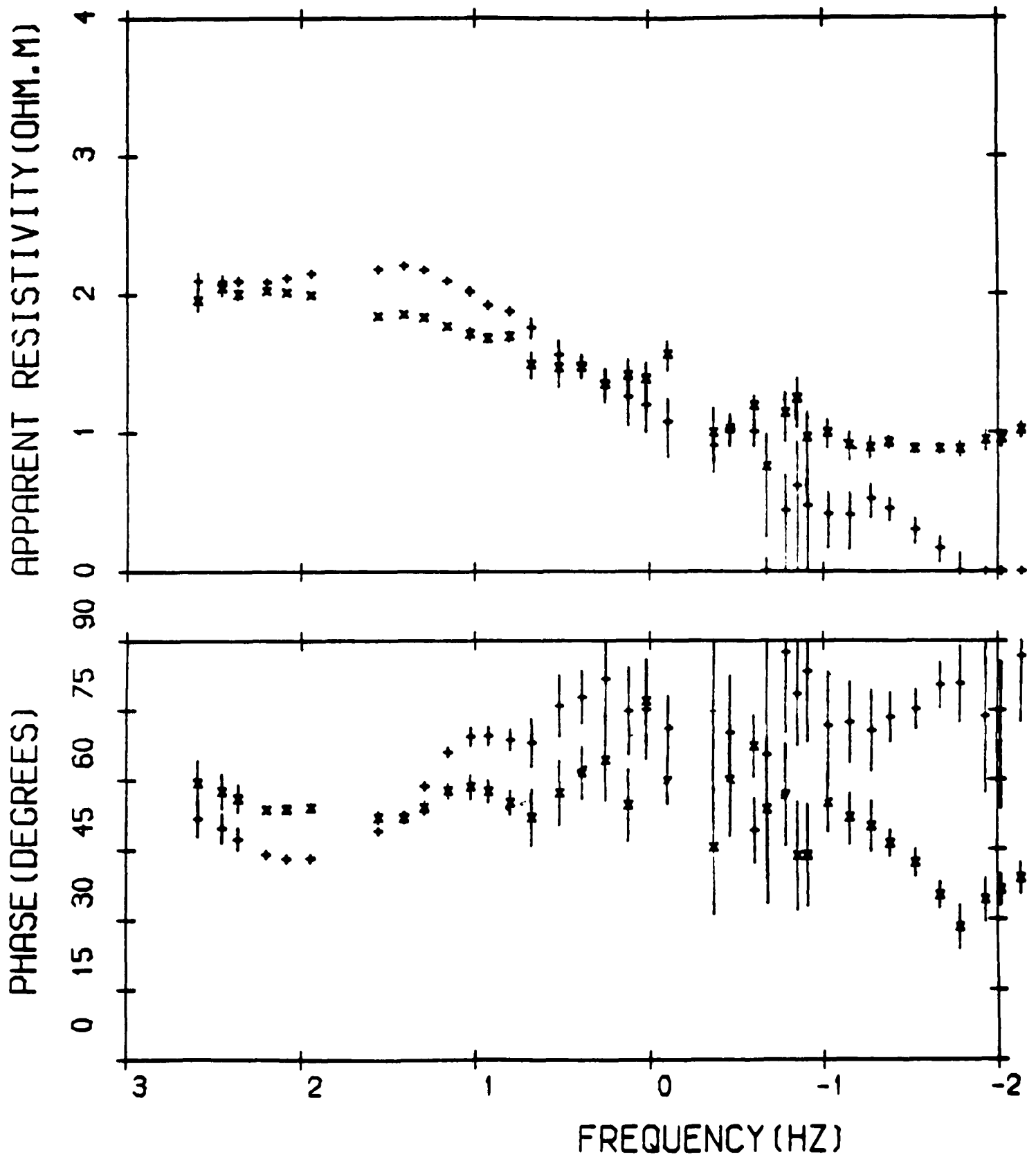
APPARENT RESISTIVITY(OHM.M)
0
1
2
3
4
PHASE(DEGREES)
0
15
30
45
60
75
90
3
2
1
0
-1
-2
FREQUENCY(HZ)

Figure VI.8. E- (+) and H-polarization (x) apparent resistivities and phases at site 70.

1D MODEL FOR SITE 270C

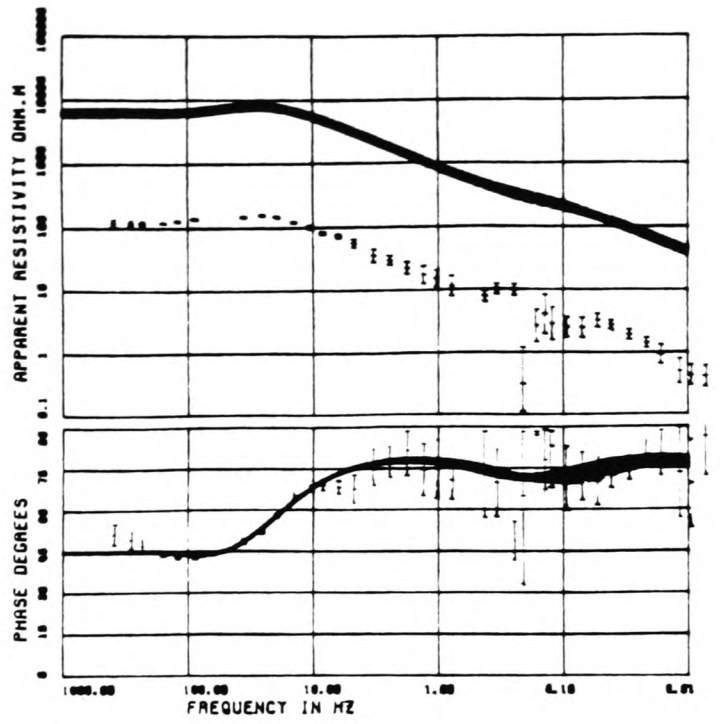

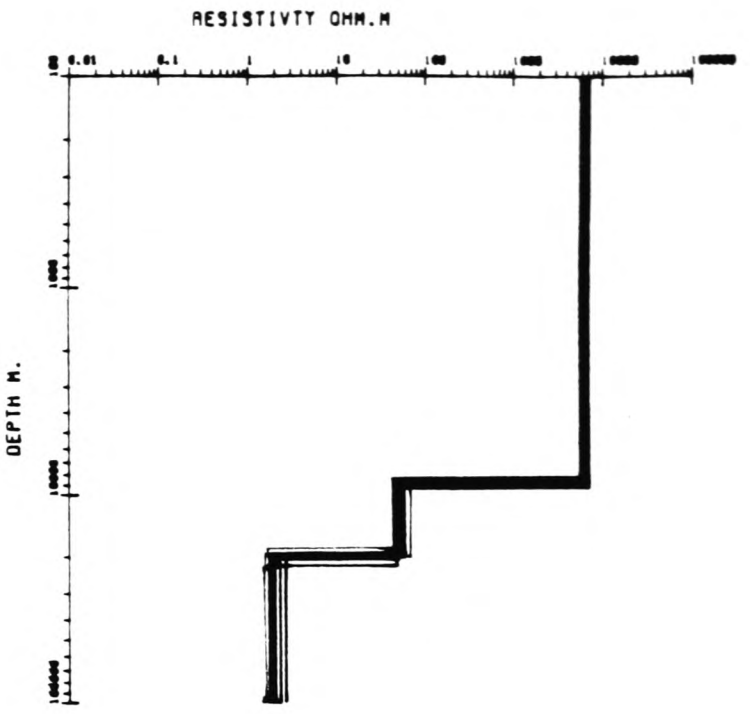

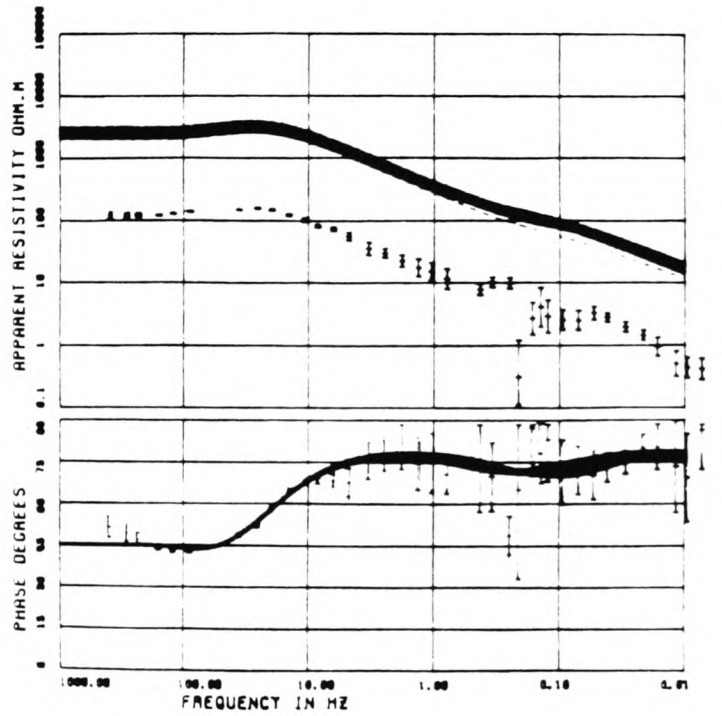

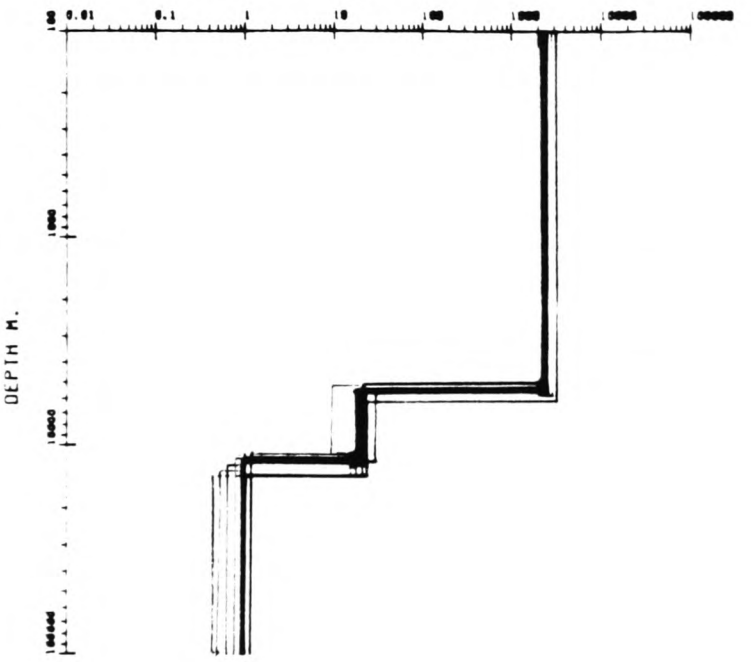

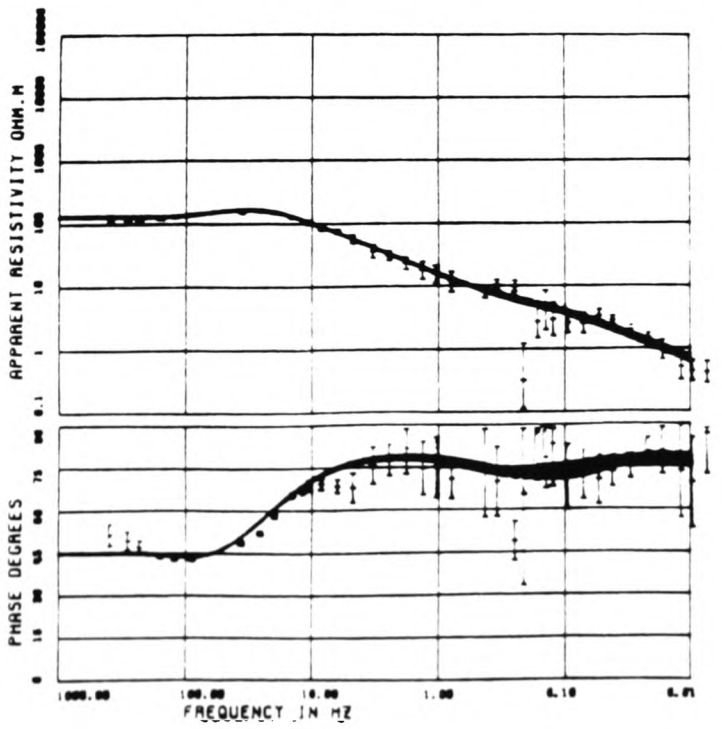

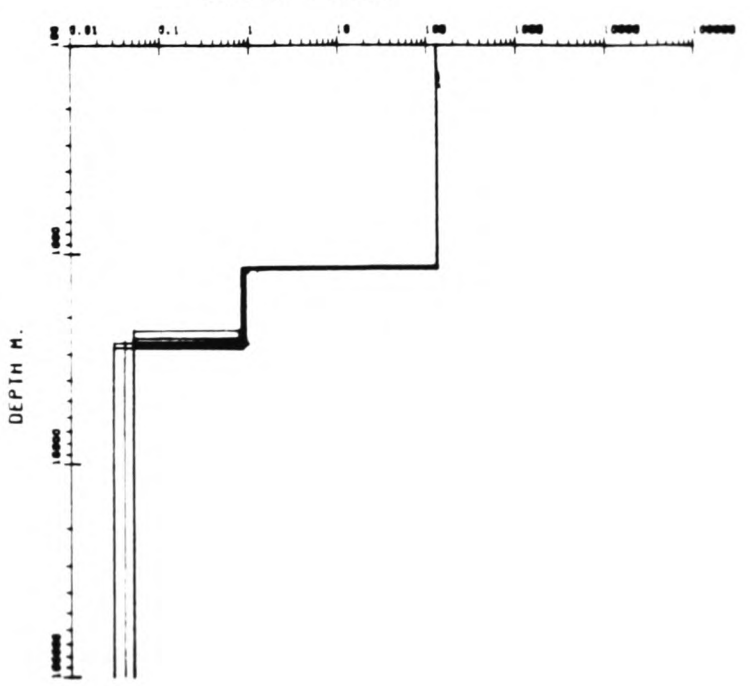

Figure VI.9. Monte Carlo 1D inversions of <u>both</u> apparent resistivity and phase for the E-polarization case at site 70. Different models are obtained specifying different bounds for the initial models.

The E-polarization responses, apparent resistivities and phase will be used for producing the 1D models. A linearized inversion algorithm is used for inverting the data; a brief description of this algorithm can be found in Chapter IV.

Due to the possible influence of distortions as discussed above, not all sites are considered in this investigation. This is done in the expectation of deriving a simpler and clearer profile using sites which appear less distorted. Site 73 is not used due to incompatibility of its response with sites 69 and 70. Site 77 is not used since its E-polarization phase displays an unrealistic behaviour, as shown in figure VI.2. Sites 82 and 75 are very anisotropic and may be severely distorted by surface effects and/or topography and are not used either. Sounding curves at sites 66, 72 and 76 are used in spite of the detected signs of near-surface distortions. All sites considered are inverted using the same starting model. This is a 6 layer model with all layers having the same resistivity value of 100Ω.m. The layers had depths of: 0.5, 1, 5, 10 and 50km.

The resulting 1D models are summarised in figure VI.10. Not all layers are used, the models are truncated where a layer is more than 3 skin depths thick. The boundaries of broad resistivity regions are delineated. Three regions are delineated with resistivities of 1, 100 and 1000Ω.m. The 1000Ω.m region beneath sites 66-76 may be grossly in error due to surface distortions. Figure VI.9 provides some insight on the type of error on both resistivity and depth values that may be expected due to parallel offsets of 1D curves. All the sites considered show very small resistivities ($\leq$1Ω.m) at depths of 1-4km, which is of the same order of magnitude as the observed sediment cover in the Rocky Mountains trench 0.5-3km (Dragert and Clarke, 1977; Spence et al., 1977a). The larger depths (>2km) occur beneath the most distorted sites and may be erroneous.

Another interesting characteristic of the data set is provided by the azimuths of rotation at sites 69, 70, 67, 74, 66, 72 and 77. These azimuths can be divided into two groups, sites 69 and 70 considered together and the five others sites in a second group. The azimuths at site 69 at higher frequencies are aligned with the strike direction and then rotate to values which are similar to those of site 68 for frequencies below 150Hz. The same behaviour is seen at site 70 but the rotation occurs for frequencies below 2Hz. A similar behaviour is observed at sites in the second group, but at these sites the azimuths rotate smoothly to a constant value around

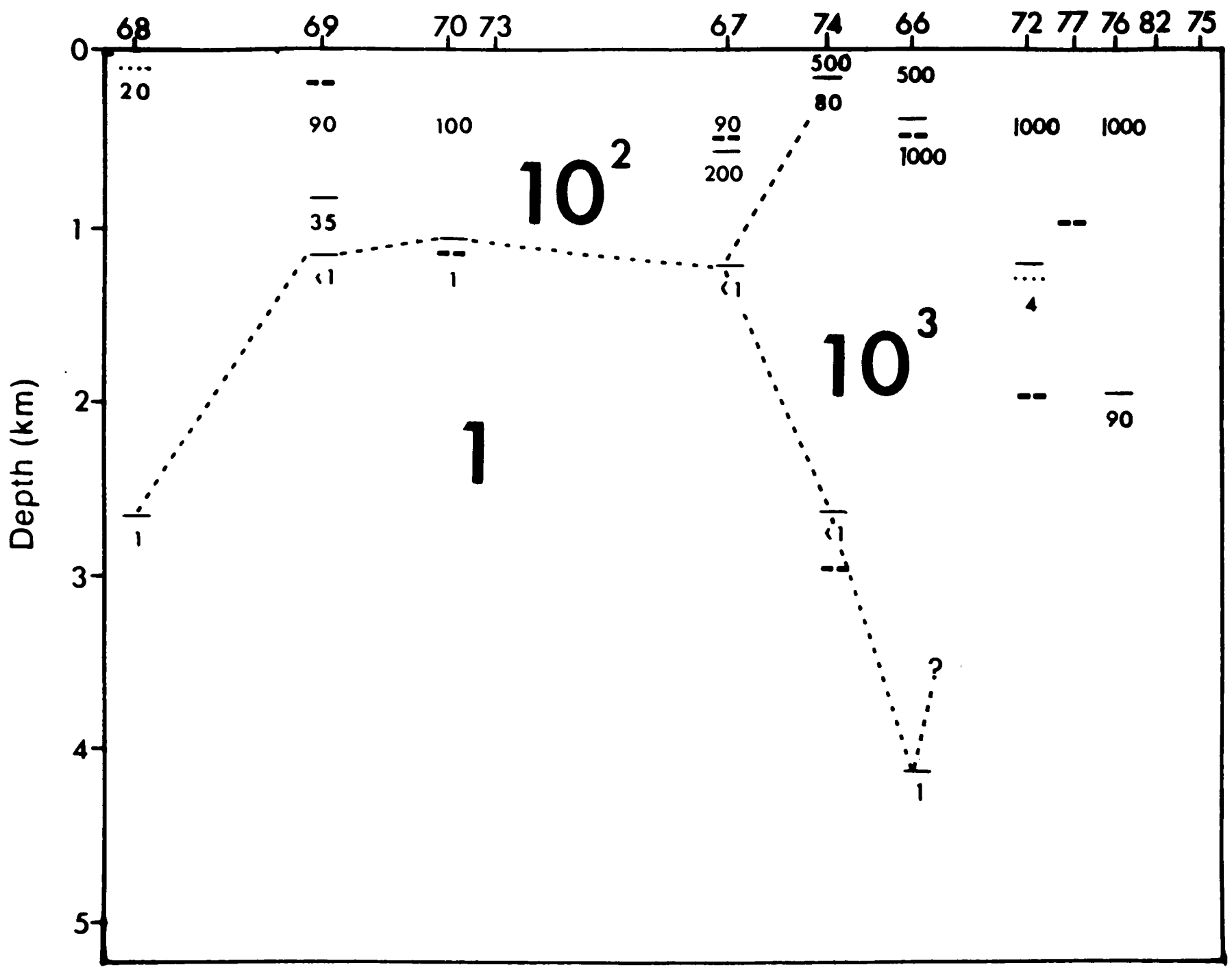
68
69
70 73
67
74
66
72 77 76 82 75
0
1
2
3
4
5
Depth (km)
20
90
100
35
<1
1
90
200
<1
500
80
500
1000
1000
1000
4
90
<1
1
?
10^2
10^3
1

Figure VI.10. Geoelectric section for the SR traverse. The 1D models are shown below each site. Solid thin lines are the layer boundaries. Layer boundaries which are considered dubious in the sense that they probably reflect the choice of the starting model are indicated by dotted lines. The lighter dashed lines delineate the resistivity regions. Heavy double dashes show the locations where an "azimuthal transition" occurs (see text).

45°E. In this case the frequency at which the "transition" occurs can be found by isolating the frequencies where the values change more rapidly and calculating the median.

Once the frequency, at which an azimuth "transition" occurs is found, it is possible to estimate the "depth", at which it occurs by calculating the Schmucker depth given by (IV.1). This transformation gives the depth to a perfect conductor and suits the data set considered since resistivities decrease with depth. These depths might reflect structural changes in the subsurface. Figure VI.10 also shows these "azimuthal depths" for the sites considered. Note that the "azimuthal depths" tend to correspond to the 1D inversion boundaries, although for some sites such as 69 and 66 they appear not to be related to any boundary. The significance of these depths and their discrepancies in relation to the 1D layer boundaries for the SR traverse need further work, which is beyond the scope of this dissertation.

VI.7. Summary and Conclusions

In this chapter data collected along a profile of sites along a traverse perpendicular to the Rocky Mountains Trench is described. The frequency range considered is from 100s to 500Hz. Part of the work described in this chapter is in a joint paper (Hutton et al., 1987). Here brief accounts of the geological structure of the region, data acquisition and data analysis are given. The results were obtained for all sites using a standard package of programs of data analysis. A section dealing with the interpretation of the results is given. The objective of this interpretation is to comment on the data characteristics which may hinder a "simple" geophysical interpretation. A simplified geoelectric profile is provided to further illustrate the difficulties in data interpretation. The reader is referred to the joint paper for a geophysical interpretation on the basis of 1D inversions and other geological and geophysical information.

For each site a group of results is presented in the form of plots or tables. The plots are presented in terms of both apparent resistivity and phase along two principal directions. The azimuth of rotation, the skew and the number of estimates are also plotted. The two principal directions are given by the structural strike represented by the direction of the Rocky Mountains Trench. The tables provide information on the details of the data analysis. Vertical transfer function results are briefly commented on.

The rotation of the impedance tensor to the strike direction is done in the expectation of interpreting the real structure as a quasi two dimensional structure. Two qualitative methods of assessing the choice of the angle of rotation are investigated. It was shown that E-polarization resistivity responses along the SR traverse approach a common set of values in contrast to the H-polarization responses. Another method based on the smoothness of the E-polarization resistivities along the profile proved to be of very limited usefulness.

The results at each site are analysed individually and in relation to its neighbours. Sounding curves, anisotropy ratio and azimuths are considered in this analysis. The skew is very little used. It was found that several sites show sounding curves which appear to indicate the presence of near-surface inhomogeneities. Synthetic studies show that sounding curves at sites affected by such 3D effects appear distorted in relation to the "undistorted" 1D or 2D counterparts. Two basic kinds of distortions are investigated, near-surface and topographic distortions. Several sites show signs of near-surface distortions and, in particular, site (72) shows parallel apparent resistivity curves and similar phases for almost the entire frequency range. Due to the dimensions of the trench, it is concluded that both vertical and horizontal current gathering possibly represent the principal mechanisms which are responsible for the observed shape of the sounding curves.

The effect of the topography along the traverse has been qualitatively investigated. A 2D model of the topography along the traverse is used for evaluating the topographical distortions. It was found that the 2D model is not sufficient to explain the behaviour of the sounding curves. In particular it has been found that the simpler single step model analysed in chapter V, may be used to obtain the distorted sounding curves at the steps of the model which approximates the topography along the SR traverse. By using the step model results it is possible to suggest that the topography may explain, to a limited extent, the observed H-polarization sounding curves at sites 82 and 75.

The distortions caused by near surface inhomogeneities are discussed using modeling results found in the literature. The effect of such distortions on 1D inversions are exemplified here using different 1D models which fit the data at one selected site (70). The case of a 1D effect which mimics the 3D distortions is warranted by the synthetic data studies which demonstrate that the lower frequency part of the 3D curves resembles the 1D curve

obtained outside the heterogeneity.

In order to further demonstrate the difficulties involved on the interpretation of the SR traverse data set, a simplified geoelectric profile is constructed bringing together selected 1D models along the traverse. Only E-polarization apparent resistivity and phases are inverted. This profile should be regarded as a highly simplified one and, again, the reader is referred to the joint paper for a complete interpretation using 1D models at all sites within the survey area. All inversions have a common starting model composed of 6 layers of 100Ω.m. The geoelectric profile shows the existence of three broad resistivity regions with 1, 100 and 1000Ω.m. The more conductive region lies across the bottom of the geoelectric section. The top of this region varies between 1 and 4km, but the deeper estimates (>2km) may be erroneous due to the existence of near-surface distortions. These considerations make the estimated depth to the conductive layer of the same order of magnitude as the previously reported thickness of the sediments along the Rocky Mountains Trench. This fact probably indicates that because the sediments are very conductive, the whole frequency range is not sufficient to penetrate the resistive basement below the sedimentary cover. Superimposed on the 1D geoelectric section the depths where "azimuthal transitions" occur are shown. These depths tend to correspond to the boundaries of the 1D models. Further study is needed to understand the geophysical meaning of these "azimuthal depths" for the SR traverse.

BIBLIOGRAPHY

Adam, A., L. Szarka., J. Vero, A. Wallner, R. Gutdeustsch, 1986. Magnetotellurics (MT) in mountains - noise, topography and crustal inhomogeneity effects. Phys. Earth Planet. Int., 42: 165-177.

Bahr, K., 1983. Joint interpretation of magnetotelluric and geomagnetic data and local telluric distortions. J. Geomag. Geoelectr. ,35: 555-566.

Bath, M., 1974. Spectral Analysis in Geophysics in Developments in Solid Earth Geophysics, vol 7. Elsevier, Amsterdam.

Beamish, D., J.C. Riddick, 1985a. TDP3 I. Background to the project. GRG-BGS Report N.85/21.

Beamish, D., J.C. Riddick, 1985b. TDP3 II. Magnetotelluric array instrumentation. BGS/GRG Report N.85/22.

Beamish, D., 1986a. Deep crustal geoelectric structure beneath the Nothumberland Basin. Geophys. J. R. astr. Soc., 84: 619-640.

Beamish, D., 1986b. Geoelectric structural dimensions from magnetotelluric data: methods of estimation, old and new. Geophys., 51, 6: 1298-1309.

Beamish, D., D.K. Smythe, 1986. Geophysical images of deep crust: the Iapetus suture. J. Geol. Soc., London, 143: 489-497.

Bendat, J.S., A.G. Piersol, 1971. Random Data: Analysis and Measurement Procedures. Wiley-Intercience, New York.

Bennett, G.T., R.M. Clowes, R.M. Ellis, 1975. A seismic refraction survey along the Rocky Mountains Trench, Canada. Bull. Seism. Soc. Am., 65, 1: 37-54.

Bentley, C.R., 1973. Error estimation in two-dimensional magnetotelluric analysis. Phys. Earth Plan. Int., 7: 423-430.

Berdichevsky, M.N., V.I. Dimitriev, 1976. Distortion of magnetic and electrical fields by surface lateral inhomogeneities. Acta Geod., Geophys. Mont. Acad. Sci. Hung., 11, 3-4: 447-483.

Berdichevsky, M.N., N.S. Golubtsova and A. Debabov, 1984. Magnetotelluric sounding above three-dimensional depressions. Izv., Earth Phys., 20, 12: 943-949.

Bingham, D.K., D.I. Gough, M.R. Ingham, 1985. Conductive structures under the Canadian Rocky Mountains. Can. J. Earth. Sci., 22: 384-398.

Booth, D.C., S. Crampin, R. Evans, J. Roberts, 1985. Shear-wave polarizations near the North Anatolian Fault-I. Evidence for anisotropy-induced shear-wave splitting. Geophys. J. R. astr. Soc., 83: 61-73.

Brewitt-Taylor, C.R., J.T. Weaver, 1976. On the finite difference solution of two-dimensional induction problems. Geophys. J. R. astr. Soc., 47: 375-396.

Brewitt-Taylor, C.R., P.B. Johns, 1980. Diakoptic solution of induction problems. J. Geomag. Geoelectr., 32, Suppl. I: SI73-SI78.

Brewitt-Taylor, C.R., J.T. Weaver, 1986. A computer program for the solution of electromagnetic induction problems. Depart. Phys., University of Victoria, Canada.

Cagniard, L., 1953. Basic theory of magnetotelluric method of geophysical prospecting. Geophys., 18: 605-635.

Caner, B., P.A. Camfield, F. Andersen, E.R. Niblett, 1969. A large-scale magnetotelluric survey in western Canada. Can. J. Earth Sci., 6: 1245-1261.

Caner, B., 1971. Quantitative interpretation of geomagnetic depth-sounding data in Western Canada. J. Geophys. Res., 76, 29: 7202-7215.

Carter, G.C., C.H. Knapp, A.H. Nuttal, 1973. Estimation of the magnitude-squared coherence function via overlapped Fast Fourier Transform Processing. IEEE Trans. Audio Electroacoust., AU-21, 4: 337-344.

Chave, A.D., R.P. von Herzen, K.A. Poehls, C.S. Cox, 1981. Electromagnetic induction fields in the deep ocean north-east of Hawaii: implications for mantle condutivity and source fields. Geophys. J. R. astr. Soc., 66: 379-406.

Clarke, J., T.D. Gamble, W.M. Goubau, R.H. Koch, R.F. Miracky, 1983. Remote reference magnetotellurics: equipment and procedures. Geophys. Prosp., 31: 149-170.

Crampin, S., D.C. Booth, 1985. Shear-wave polarizations near the North Anatolian Fault-II. Interpretation in terms of crack-induced anisotropy. Geophys. J. R. astr. Soc., 83: 75-92.

Crampin, S., R. Evans, S.B. Ucer, 1985. Analysis of records of local earthquakes: the Turkish Dilatancy Projects (TDP1 and TDP2). Geophys. J. R. astr. Soc., 83: 1-16.

Dawes, G.J.K., 1984. Short period automatic magnetotelluric (SPAM) system in A broadband tensorial magnetotelluric study in Travave-Radiocondili geothermal Field. Final report, by V.R.S. Hutton et al. EEC Report Series. EUR A2-031-UK.

Dekker, D.L., L.M. Hastie, 1981. Source of error and bias in a magnetotelluric depth sounding of the Bowen basin. Phys. Earth Planet. Int., 25: 219-225.

Dmitriev, V.I., M.N. Berdichevsky, 1979. The fundamental model of magnetotelluric sounding. Proc. IEEE, 67, 7: 1034-1044.

Dosso, H.W., W. Nienaber, 1986. A laboratory electromagnetic model study of the Juan de Fuca Plate region. Phys. Earth Planet. Inter., 43: 34-46.

Doucet, D., P.V. Ngoc, 1984. Generalisation et optimalisation de la methode des differences finies pour la modelisation en magnetotellurique (MT). Geophys. Prospect., 32: 292-316.

Dragert, H., 1973. A transfer function analysis of a geomagnetic depth sounding profile across central British Columbia. Can. J. Earth Sci., 10: 1089-1098.

Dragert, H., G.K.C. Clarke, 1977. A detailed investigation of the Canadian Cordillera geomagnetic transition anomaly. J. Geophys. Res., 42: 373-390.

Dragert, H., L.K. Law, P.O. Sule, 1980. Magnetotelluric soundings across the Pemberton Volcanic Belt, British Columbia. Can. J. Earth Sci., 17, 2: 161-167.

Eggers, D.E., 1982. An eigenstate formulation of magnetotelluric impedance tensor. Geophys., 47, 8: 1204-1214.

d'Erceville, I., G. Kunetz, 1962. The effect of a fault on the Earth's natural electromagnetic field. Geophys., 27, 5: 651-665.

Etheridge, M.A., V.J. Wall, R.H. Vernon, 1983. The role of the fluid phase during regional metamorphism and deformation. J. metamorphic Geol., 1: 205-226.

Faradzhev, A.S., K.K. Kakhramanov, G.A. Sarkisov, N.E. Khalilova, 1972. On effect of terrain on results of magnetotelluric soundings (MTS) and profiling (MTP). Izv., Earth Phys., 5: 92-94.

Filloux, J.H., 1980. North Pacific magnetotelluric experiments. J. Geomag. Geoelect., Kyoto, 32, Supp. I.: SI33-SI43.

Fisher, G., 1982. Magnetotelluric observational techniques on land. Geophys. Surv., 4: 373-393.

Fowler, R.A., B.J. Kotick, R.D. Elliott, 1967. Polarization analysis of natural and artificially induced geomagnetic micropulsations. J. Geophys. Res., 72, 11: 2871-2883.

Fyfe, W.S., 1986. Fluids in deep continental crust. Am. Geophys. Un., Geodyn. Ser. 14: 33-39.

Gamble, T.D., W.M. Goubau, J. Clarke, 1979a. Magnetotellurics with a remote reference. Geophys., 44, 1: 53-68.

Gamble, T.D., W.M. Goubau, J. Clarke, 1979b. Error analysis for remote reference magnetotellurics. Geophys., 44, 5: 959-968.

Gamble, T.D., W.M. Goubau, R. Miracky, J. Clarke, 1982. Magnetotelluric regional strike. Geophys. 47, 6: 932-937.

Goubau, W.M., T.D. Gamble, J. Clarke, 1978a. Magnetotellurics using lock-in signal detection. Geophys. Res. Letters, 5, 6: 543-546.

Goubau, W.M., T.D. Gamble, J. Clarke, 1978b. Magnetotelluric data analysis: removal of bias. Geophys., 43, 6:1157-1166.

Goubau, W.M., P.M. Maxton, R.H. Koch, J. Clarke, 1984. Noise correlation lengths in remote reference magnetotellurics. Geophys., 49, 4: 433-438.

Golub, G.H., C.F. van Loan, 1983. Matrix Computations, North Oxford Academic, Oxford.

Gough, D.I., D.K. Bingham, M.R. Ingham, A.O. Alabi, 1982. Conductive structure in south-western Canada: a regional magnetometer array study. Can. J. Earth Sci., 19: 1680-1690.

Gough, D.I., 1986a. Mantle upflow tectonics in the Canadian Cordillera. J. Geophys. Res., 91, B2: 1909-1919.

Gough, D.I., 1986b. Magnetotelluric evidence for subduction of seafloor sediments. Nature, 321: 566.

Gough, D.I., 1986c. Seismic reflectors, conductivity, water, and stress in the continental crust. Nature, 323: 143-144.

Gundel, A., 1977. Estimation of transfer functions with reduced bias in geomagnetic induction studies. Acta Geod., Geophys. Mont. Acad. Sci. Hung., 12(1-3): 345-352.

Harinarayana, T., S.V.S. Sarma, 1982. Topographic effects on telluric field measurements. PAGEOPH, 120: 778-783.

Harinarayana, T., 1985. Personal communication.

Harris, F.J., 1978. On the use of windows for harmonic analysis with the Discrete Fourier Transform. Proc. IEEE, 66, 1: 51-83.

Hermance, J.F., 1973. Processing of magnetotelluric data. Phys. Earth Plan. Int., 7: 349-364.

Hermance, J.F., R.E. Thayer, 1975. The telluric-magnetotelluric method. Geophys., 40, 4: 664-668.

Hermance, J.F., and J. Pedersen, 1980. Deep structure of the Rio Grande rift: a magnetotelluric interpretation. J. Geophys. Res., 85: 3899-3912.

Hutton, V.R.S., D.I. Gough, G.J.K. Dawes, J.M. Travassos, 1987. Magnetotelluric soundings in the Canadian Rocky mountains. Accepted for publication in Geophys. J. R. astr. Soc., 1986.

Jiracek, G.R., 1973. Numerical comparisons of a modified Rayleigh approach with other rough surface EM scattering solutions. IEEE Trans. Ant. Propagation, AP21, 3: 393-396.

Jones, A.G., 1977. Geomagnetic induction studies in Southern Scotland. PhD Dissertation, University of Edinburgh.

Jones, A.G., B. Olafsdottir, J. Tiikkainen, 1983. Geomagnetic induction studies in Scandinavia, III: magnetotelluric observations. J. Geophys., 54: 35-50.

Jones, F.W., L.J. Pascoe, 1971. A general computer program to determine the perturbation of alternating electric currents in a two-dimensional model of a region of uniform conductivity with an embedded inhomogeneity. Geophys. J. R. astr. Soc., 24: 3-30.

Jones, F.W., 1973. Induction in laterally non-uniform conductors: theory and numerical models. Phys. Earth and Planet. Int., 7: 282-293.

Jupp, D.L.B., K. Vozoff, 1975. Stable iterative methods for the inversion of geophysical data. Geophys. J. R. astr. Soc., 42: 957-976.

Jupp, D.L.B., K. Vozoff, 1977. Two-dimensional magnetotelluric inversion. Geophys. J. R. astr. Soc., 50: 333-352.

Jupp, D.L.B., 1978. Estimation of the magnetotelluric impedance functions. Phys. of the Earth and Plan. Int., 17: 75-82.

Kaikkonen, P., 1977. A finite element program package for eletromagnetic modeling. J. Geophys., 43: 179-192.

Kanasewich, E.R., 1975. Time Sequence Analysis in Geophysics. University of Alberta Press, Edmonton, Canada.

Kao, D.W., D. Rankin, 1977. Enhancement of signal-to-noise ratio in magnetotelluric data. Geophys., 42, 1: 103-110.

Kao, D., D. Orr, 1982. Magnetotelluric studies in the Market Weighton area of eastern England. Geophys. J. R. astr. Soc., 70: 323-327.

Keller, G.V., F.C. Frischknechkt, 1970. Electrical Methods in Geophysical Prospecting. Pergamon Press, Oxford.

Kerrich, R., T.E. la Tour, L. Willmore, 1984. Fluid participation in deep fault zones: evidence from geological, geochemical and O/ O relations. J. Geophys. Res., 89, B6: 4331-4343.

Kroger, P., H.J. Michel, R. Elsner, 1983. Comparison of errors in local and reference estimates of the magnetotelluric impedance tensor. J. Geophys., 52: 97-105.

Ku, C.C., M.S. Hsieh, S.H. Lim. 1973. The topographic effect in electromagnetic fields. Can. J. Earth Sci., 10: 645-650.

Kurtz, R.D., J.M. DeLaurier, J.C. Gupta, 1986. A magnetotelluric sounding across Vancouver Island detects the subducting Juan de Fuca plate. Nature, 321: 596-599

Larsen, J.C., 1975. Low frequency (0.1-6.0cpd) electromagnetic study of deep mantle electrical conductivity beneath the Hawaiian Islands. Geophys. J. R. astr. Soc., 43: 17-46.

Larsen, J.C., 1977. Removal of local surface conductivity effects from low frequency mantle response curves. Acta Geod., Geophys. Mont. Acad. Sci. Hung., 12(1-3): 183-186.

Larsen, J.C., 1980. Electromagnetic response functions from interrupted and noisy data. J. Geomag. Geoelect., Kyoto, 32, Suppl. I: 89-103.

Larsen, J.C., 1981. A new technique for layered earth magnetotelluric inversion. Geophys., 46, 9: 1247-1257.

Marquardt, D.W., 1963. An algorithm for least-squares estimation of non-linear parameters. J. Soc. Indust. Appl. Math., 11, 2: 431-441.

Menvielle, M., L. Szarka, 1986. Distortions of electromagnetic fields: topographic and man-made. Review paper at the 8th IAGA Workshop on Electromagnetic Induction, Neuchatel, 1986. To appear in Phys. of the Earth and Planet. Int.

Mereu, R.F., S.C. Majumdar, R.E. White, 1977. The structure of the crust and upper mantle under the highest ranges of the Canadian Rockies from a seismic refraction survey. Can. J. Earth. Sci.,

14: 196-208.

Monger, J.W.H., J.G. Souther, H. Gabrielse, 1972. Evolution of the Canadian Cordillera: a plate-tectonic model. Am. J. Sci., 272: 577-602.

Monger, J.W.H., R.A. Price, 1979. Geodynamic evolution of the Canadian Cordillera-progress and problems. Can. J. Earth Sci., 16: 770-791.

Mozley, E.C., 1982. An investigation of the conductivity distribution in the vicinity of a Cascade Volcano. PhD Dissertation, University of California, Berkeley.

Neves, A.S., 1957. The Generalized magnetotelluric method. PhD Thesis, Dept. of Geol. and Geophys., M.I.T. (Cited by Jupp and Vozoff, 1977).

Noponen, I., E. Nikkola, 1976. Detection of signal in the presence of noise. Geophysica 14, 1: 121-128.

Nuttall, A.H., G.C. Carter, 1976. Bias of the estimate of magnitude-squared coherence. IEEE Trans. Acoustics, Speech, and Signal Processing, ASSP-24: 582-583.

Oldenburg, D.W., 1979. One-dimensional inversion of natural source magnetotelluric observations. Geophys., 44, 7: 1218-1244.

Olhoeft, G.R., 1981. Electrical properties of granite with implications for the lower crust. J. Geophys. Res., 86, B2: 931-936.

Park, S.K., A.S. Orange, T.R. Madden, 1983. Effects of three-dimensional structure on magnetotelluric sounding curves. Geophys., 48, 10: 1402-1405.

Park, J., A.D. Chave, 1984. On the estimation of magnetotelluric response functions using the singular value decomposition. Geophys. J. R. astr. Soc., 77: 683-709.

Park, S.K., 1985. Distortion of magnetotelluric sounding curves by three-dimensional structures. Geophys., 50, 5: 785-797.

Parker, R.L., 1977. Understanding inverse theory. Ann. Rev. Earth Planet. Sci., 5: 35-64.

Parker, R.L., 1980. The inverse problem of electromagnetic induction: existence and construction of solutions based on incomplete data. J. Geophys. Res., 85: 4421-4428.

Parker, R.L., 1982. The existence of a region inaccessible to magnetotelluric sounding. Geophys. J. R. astr. Soc., 68: 165-170.

Parker, R.L., 1983. The magnetotelluric inverse problem. Geophys. Surv., 6: 5-25.

Parkinson, W.D., 1983. Introduction to Geomagnetism. Scottish Academic Press, Edinburgh.

Parry, J.R., S.H. Ward, 1971. Electromagnetic scattering from cylinders of arbitrary cross-section in a conductive half-space. Geophys., 36, 1: 67-100.

Payne, M.A., 1981. SI and CGS units, conventions and equations for use in geomagnetism. Phys. Earth Planet. Int., 26: P10-P16.

Pedersen, L.B., 1982. The magnetotelluric impedance tensor - its random and bias errors. Geophys. Prosp., 30: 188-210.

Pedersen, L.B., M. Svennekjaer, 1984. Extremal bias coupling in magnetotellurics. Geophys., 49, 11: 1968-1978.

Porath, H., 1971. Magnetic variation anomalies and seismic low-velocity zone in the western United States. J. Geophys. Res., 76: 2643-2648.

Price, A.T., 1962. The theory of magnetotelluric methods when the source fields is considered. J. Geophys. Res., 67: 1907-1918.

Rankin, D., 1962. The magnetotelluric effect of a dike. Geophys., 27: 666-676.

Reddig, R.P., G.R. Jiracek, 1984. Topographic modelling and correction in magnetotellurics. Extended abstract to the 54th SEG, Atlanta, USA.

Reddy, I.K., D. Rankin, 1974. Coherence functions for magnetotelluric analysis. Geophys., 39, 3: 312-320.

Reddy, I.K., D. Rankin, 1975. Magnetotelluric response of laterally inhomogeneous and anisotropic media. Geophys., 40, 6: 1035-1045.

Reddy, I.R., R.J. Phillips, J.H. Whitcomb, D.M. Cole, and R.A. Taylor, 1976. Monitoring of time dependent electrical resistivity by magnetotellurics. J. Geomag. Geoelectr., 28: 165-178.

Schwarz, G., V. Haak, E. Martinez, J. Bannister, 1984. The electrical conductivity of the Andean crust in northern Chile and Southern Bolivia as inferred from magnetotelluric measurements. J. Geophys., 55: 169-178.

Schmucker, V., 1970. Anomalies of geomagnetic variations in the southwestern United States. Bull. Scripps Inst. Oceanogr., University of California, San Diego, 13.

Sengor, A.M.C., K. Burke, J.F. Dewey, 1982. Tectonics of the North Anatolian transformation fault, in Multidisciplinary Approach to Earthquake Prediction, A. M. Isikara and A. Vogel (eds.), Veiweg, Wiesbadan: 3-22.

Shankland, T.J., 1975. Electrical conduction in rocks and minerals: parameters for interpretation. Phys. Earth Plan. Int., 10: 209-219.

Shankland, T.J., M.E. Ander, 1983. Electrical conductivity, temperatures, and fluids in the lower crust. J. Geophys. Res., 88, B11: 9475-9484.

Sims, W.E., F.X. Bostick, Jr., 1969. Methods of magnetotelluric analysis. Tech. Rep. 58, Univ. of Texas at Austin.

Sims, W.E., F.X. Bostick Jr., and H.W. Smith, 1971. The estimation of magnetotelluric impedance tensor elements from measured data. Geophys., 36, 5: 938-942.

Spence, G.D., R.M. Ellis, R.M. Cloves, 1977a. Gravity evidence against a high-angle fault crossing the Rocky Mountain Trench near Radium, British Columbia. Can. J. Earth Sci., 14: 25-31.

Spence, G.D., R.M. Clowes, R.M. Ellis, 1977b. Depth limits on the M discontinuity in the Southern Rock Mountains Trench, Canada. Bull. Seism. Soc. Am., 67, 2: 543-546.

Spies, B.R., D.E. Eggers, 1986. The use and misuse of apparent resistivity in electromagnetic methods. Geophys., 51, 7: 1462-1471.

Spitz, S., 1985. The magnetotelluric impedance tensor properties with respect to rotations. Geophys., 50, 10: 1610-1617.

Stanley, W.D., N.V. Frederick, 1979. U.S. Geological survey real-time MT system. USGS Open File 79-R27.

Stanley, W.D., 1984. Tectonic study of Cascade Range and Columbia Plateau in Washington State based upon magnetotelluric soundings. J. Geophys. Res., 89, B6: 4447-4460.

Swift, C.M., Jr., 1967. A magnetotelluric investigation of an electrical condutivity anomaly in the southwestern United States: PhD thesis M.I.T. (cited by Vozoff, 1972).

Swift, C.M., Jr., 1971. Theoretical magnetotelluric and turam response from two-dimensional inhomogeneities. Geophys., 36, 1: 38-52.

Thayer, R.E., 1975. Topographic distortion of telluric currents: a simple calculation. Geophys., 40, 1: 91-95.

Tikhonov, A.N., 1950. On investigation of electrical characteristics of deep strata of Earth's crust (in Russian). Dokl. Akad. Nauk. SSSR, 73: 295-297 (cited by Rokityansky, 1982).

Ting, S.C., G.W. Hohmann, 1981. Integral equation of the three-dimensional magnetotelluric response. Geophys., 46, 2: 182-197.

Vozoff, K., 1972. The magnetotelluric method in the exploration of sedimentary basins. Geophys., 37, 1: 98-141.

Wannamaker, P.E., J.A. Stodt, L. Rijo, 1986. Two-dimensional topographic responses in magnetotellurics modelled using finite elements. Geophys., 51, 11: 2131-2144.

Weaver, J.T., C.R. Brewitt-Taylor, 1978. Improved boundary conditions for the numerical solution of E-polarization problems in geomagnetic induction. Geophys. J. R. astr. Soc., 54: 309-317.

Weaver, J.T., B.V. Le Quang, G. Fischer, 1985. A comparison of analytic and numerical results for a two-dimensional control model in electromagnetic induction-I. B-polarization calculations. Geophys. J. R. astr. Soc., 82: 263-277.

Weaver, J.T., B.V. LeQuang, G. Fischer, 1986. A comparison of analytic and numerical results for a two-dimensional control model in electromagnetic induction-II. E-polarization calculations. Geophys. J. R. astr. Soc., (in press; cited by Brewitt-Taylor and Weaver, 1986).

Weidelt, P., 1972. The inverse problem of geomagnetic induction. Z. Geophys., 38: 247-289.

Weidelt, P., 1975. Eletromagnetic induction in three-dimensional structures. J. Geophys., 41: 85-109.

Weidelt, P.,1986. Discrete inequalities for magnetotelluric impendances of one-dimensional conductors. J. Geophys., 59: 171-176.

White, R.E., 1973. The estimation of signal spectra and related quantities by means of the multiple coherence function. Geophys. Prosp., 21:660-703.

Word, D.R., H.W. Smith, F.X. Bostick, Jr., 1970. An investigation of the magnetotelluric tensor method. Elect. Geophys. Res. Lab. Tech. Rep. 82, The Univ. Texas at Austin, Austin.

Wu, F.T., 1968. The inverse problem of magnetotelluric sounding. Geophys., 33: 972-979.

Yfantis, E.A., L.E. Borgman, 1981. Fast Fourier Transforms 2-3-5. Comp. Geosci., 7: 99-108.